Collider Phenomenology of Composite Higgs Models

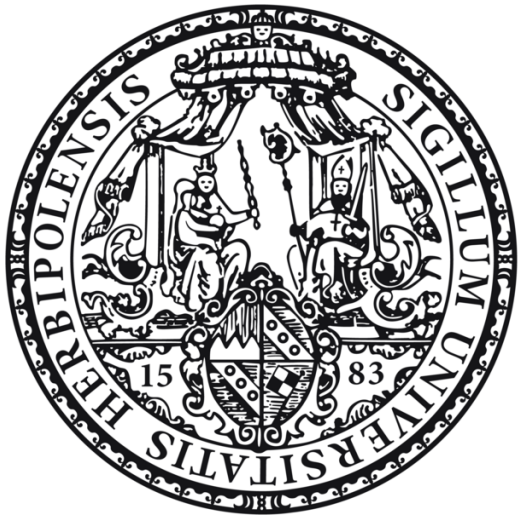

Dissertation zur Erlangung des naturwissenschaftlichen Doktorgrades
an der Fakultät für Physik und Astronomie
der Julius-Maximilians-Universität Würzburg

vorgelegt

von

Manuel Kunkel

aus Würzburg

Würzburg, im November 2024

Eingereicht bei der Fakultät für Physik und Astronomie am: _____

Gutachter der Dissertation
1. Gutachter: Prof. Dr. Werner Porod
2. Gutachter: Prof. Dr. Raimund Ströhmer
3. Gutachter: _____

Prüfer des öffentlichen Promotionskolloquiums
1. Prüfer: Prof. Dr. Werner Porod
2. Prüfer: Prof. Dr. Raimund Ströhmer
3. Prüfer: _____
4. Prüfer: _____
5. Prüfer: _____

Tag des öffentlichen Promotionskolloquiums:

_____

Doktorurkunde ausgehändigt am:

_____

Abstract

Composite Higgs models provide a well-motivated solution to the naturalness problem plaguing the Standard Model of particle physics. We study the collider phenomenology of a class of composite Higgs models with an underlying fermionic description. The Higgs appears as a pseudo Nambu-Goldstone boson (pNGB) originating from the spontaneous breaking of the global symmetry when the strongly interacting composite sector condenses. There will be further pNGBs, however, both colour singlets and coloured states. We collect and derive bounds on the masses of the coloured pNGBs for all popular cosets. For the purely electroweakly charged states we determine simplified model bounds on Drell-Yan pair production with decays into vector bosons or third generation quarks, covering all possible processes within this model class. As a complete model we study the SU(5)/SO(5) coset due to its rich particle content including a doubly charged scalar S^{++}. We first apply the simplified model bounds and then perform simulations of the full model to determine bounds on several mass scenarios. We show that this model features the process $pp \to S^{++}S^{--} \to W^+t\bar{b}W^-\bar{t}b$. We design a search proposal for this process employing deep learning techniques to train neural networks to separate signal from background events. The best performing network is a combination of a convolutional neural network using jet images and a multilayer perceptron on kinematic variables. We assess the discovery reach and expected exclusion limit for this process at the high-luminosity LHC. The models also contain colour triplet fermionic resonances, required to give mass to the top quark through the mechanism of partial compositeness. We systematically classify the production and decay channels and derive bounds on pair production for a few sample processes. Finally we turn to the spin-1 resonances, focusing on the coloured states. Among them there is a ubiquitous vector octet $\mathcal{V}_8$ that mixes with the gluon, allowing for single production. For all models, we calculate the relevant Lagrangian, derive bounds on $\mathcal{V}_8$ production, and explore which signatures can be expected from vector pair production at future colliders. This thesis is based on [1–3].

Zusammenfassung

Composite Higgs Modelle bieten eine gut motivierte Lösung des Natürlichkeitsproblems des Standardmodells der Teilchenphysik. Wir untersuchen die Beschleuniger-Phänomenologie einer Klasse von Composite Higgs Modellen mit zu Grunde liegender fermionischer Beschreibung. Das Higgs ist ein pseudo-Nambu-Goldstone-Boson (pNGB), das der spontanen Brechung der globalen Symmetrie entspringt, wenn der stark wechselwirkende Composite-Sektor kondensiert. Es gibt allerdings noch zusätzliche pNGBs, sowohl QCD-Singuletts als auch farbgeladene Zustände. Wir sammeln und bestimmen Ausschlussgrenzen auf die Massen der farbgeladenen pNGBs für alle Zustände in dieser Modellklasse. Für die nur elektroschwach geladenen Zustände bestimmen wir Beschränkungen auf vereinfachte Modelle für die Drell-Yan-Paarproduktion mit Zerfällen in Vektorbosonen oder Top- und Bottom-Quarks. Dabei decken wir alle in dieser Modellklasse möglichen Prozesse ab. Als konkretes Beispiel betrachten wir das SU(5)/SO(5) Modell, da es besonders viele Teilchen enthält, unter anderem einen doppelt geladenen Skalar S^{++}. Zuerst wenden wir die Beschränkungen auf vereinfachte Modelle an, dann führen wir Simulationen des ganzen Modells durch, um Beschränkungen in verschiedenen Massenszenarien zu bestimmen. Wir zeigen, dass dieses Modell auf den Prozess $pp \to S^{++}S^{--} \to W^+t\bar{b}W^-\bar{t}b$ führt. Wir schlagen eine Strategie zur Suche nach diesem Prozess vor. Diese verwendet Deep-Learning-Methoden um neuronale Netze zu trainieren, die die Signalevents von den Hintergründen trennen sollen. Das beste Netzwerk ist eine Kombination aus einem Convolutional-Neural-Network, das Jet-Bilder verwendet, und einem Multilayer-Perceptron basierend auf kinematischen Variablen. Wir arbeiten heraus bis zu welcher Masse des Skalars der Prozess am High-Luminosity-LHC entdeckt oder ausgeschlossen werden kann. Die Modelle enthalten zudem fermionische Farbtriplett-Resonanzen. Diese sind notwendig, um dem Top-Quark mit dem Partial-Compositeness-Mechanismus seine Masse zu geben. Wir klassifizieren systematisch deren Zerfallskanäle und bestimmen Beschränkungen auf die Paarproduktion für einige ausgewählte Prozesse. Schließlich betrachten wir die Spin-1 Resonanzen, wobei wir uns auf die farbgeladenen Zustände konzentrieren. Unter ihnen gibt es in allen Modellen ein Vektor-Oktett $\mathcal{V}_8$, das mit dem Gluon mischt und daher einzeln produziert werden kann. Wir berechnen für alle Modelle den relevanten Teil der Lagrange-Dichte, bestimmen Beschränkungen auf die $\mathcal{V}_8$ Produktion und diskutieren welche Signaturen von der Paarproduktion von Vektoren an zukünftigen Beschleunigern zu erwarten sind. Diese Arbeit basiert auf [1–3].

Contents

1 | Introduction

The discovery of the W and Z bosons in 1983 [4–7] has firmly cemented electroweak symmetry breaking (EWSB) [8–10] as an integral part of the Standard Model (SM) of particle physics. The $\mathrm{SU}(2)_L \times \mathrm{U}(1)_Y$ electroweak (EW) gauge symmetry is spontaneously broken to the $\mathrm{U}(1)_Q$ of quantum electrodynamics (QED) by the vacuum expectation value (VEV) of an elementary scalar, the Higgs field [11–13]. With the discovery of the corresponding Higgs boson in 2012 by the ATLAS and CMS experiments at CERN [14, 15], every particle predicted by the SM has been observed. Furthermore, the SM has passed a myriad of experimental tests, making it the most precisely validated theory in physics.

And yet, we know for a fact that the SM is incomplete: the SM neutrinos are massless while experiment shows that they are massive, and the SM offers no explanation for dark matter or the observed baryon asymmetry. Clearly, the SM must be extended. We should therefore view it as an effective field theory (EFT) and expect there to be an energy scale Λ_{SM} up to which the SM is a good description of Nature, but above which new physics sets in.

As with any EFT, the coefficients of the operators of dimension d are proportional to $\Lambda_{\mathrm{SM}}^{4-d}$. Since the Higgs mass is a relevant $d = 2$ operator, it appears as

$$c\Lambda_{\mathrm{SM}}^2 H^\dagger H \equiv \mu^2 H^\dagger H, \tag{1.1}$$

where c is a dimensionless coefficient and $|\mu^2| = m_h^2/2$ [16]. We know that $m_h = 125$ GeV, but Λ_{SM} may be as large as the GUT scale, requiring $|c| = |\mu^2|/\Lambda_{\mathrm{SM}}^2 \sim 10^{-28}$. That is, an EFT coefficient has to match the ratio of the EW-scale Higgs mass parameter to the EFT cutoff scale with enormous precision. The necessity for such large cancellations is considered unnatural and goes under the name of "naturalness problem" [17]. An illustrative approach to understanding the naturalness problem is to consider corrections to the Higgs mass, which are proportional to Λ_{SM}^2. We can separate the corrections into ones originating from energies below the cutoff, $\delta m_{h,\mathrm{SM}}^2$, and from higher energies, $\delta m_{h,\mathrm{BSM}}^2$, originating from beyond the Standard Model (BSM) physics [16]. Again we find that these two contributions which originate from distinct energy regimes have to cancel precisely to give the correct Higgs mass.

The naturalness problem is singled out from other theoretical problems of the SM, like the strong CP problem or the fermion mass hierarchy, by its deep impact on BSM model building. It is the primary motivation for two major schools of thought: supersymmetry (SUSY) and composite dynamics. In SUSY [18, 19], the quadratic divergence in m_h^2 is cancelled for each

particle by a contribution of a super partner with a different spin. SUSY models have been very popular over the last decades. However, the continued absence of experimental evidence despite an extensive search program at the Large Hadron Collider (LHC) has significantly decreased the viable parameter space. In this work, we therefore employ the second popular solution to the naturalness problem: replacing the ad-hoc Higgs potential from the SM with a new composite sector that dynamically breaks the EW symmetry when it condenses. The Higgs is then no longer an elementary scalar but a composite state from the new sector. This will naturally cut off corrections to m_h^2 at the Higgs compositeness scale, just like a proton is transparent to photons of wave length below the proton radius [16].

The idea of breaking the EW symmetry with composite dynamics has been around since the late 1970s. Early implementations go under the name of technicolor (TC) models [20, 21] and assume the new composite sector to be a scaled up version of quantum chromodynamics (QCD) which condenses around the EW scale $v = 246$ GeV [22]. TC models suffer from a number of phenomenological problems. Most crucially, they have trouble generating a large enough top quark mass while keeping flavour-changing neutral currents (FCNC) under control, and they predict a zoo of composite resonances with mass ~ 1 TeV which have not been observed. However, there is an extension of TC that avoids its phenomenological hurdles: composite Higgs models (CHMs).

In CHMs, first introduced by Kaplan and Georgi [23–25], the composite sector vacuum and the EWSB vacuum do not coincide but are misaligned by an angle $\theta \ll 1$. This creates a separation between the scale f where the composite sector condenses and the EW scale, $v = f \sin\theta$. This implies that in a CHM the composite sector resonances emerge at a much larger scale than in TC, thus evading experimental bounds. How is this compatible with a 125 GeV Higgs boson? As the composite sector condenses, its global symmetry group G is spontaneously broken to a subgroup H, implying $(\dim G - \dim H)$ massless Nambu-Goldstone bosons (NGBs) [26–28], and we take the Higgs boson to be one of them. Eventually we will also break G explicitly, for example by gauging the SM subgroup. This turns the NGBs into pseudo NGBs (pNGBs) and generates a potential for them which will trigger EWSB and give a mass to the Higgs. In short, the Higgs can be light because it is a pNGB and not a resonance. Finally, the issue of obtaining the large top quark mass is solved by requiring that the composite sector produce top partner resonances with the same quantum numbers as the top quark. This allows for mixing terms between the elementary and composite tops. Since the physical top quark is now a linear combination of an elementary and a composite state, this idea goes under the name of partial compositeness [29].

To study the pNGBs and the EWSB it is sufficient to choose the $G \to H$ breaking pattern and the irreducible representations (irreps) of the top partners. The smallest coset that accommodates a Higgs bidoublet is SO(5)/SO(4) which appears in holographic models [30]. In this work, we instead focus on CHMs with an underlying fermionic gauge theory. That is, we postulate a composite sector with hyperquarks that are charged under an asymptotically free hypercolour (HC) gauge group G_{HC}. In fact, the models we consider have two species ψ and χ

of hyperquarks in distinct irreps of G_{HC}. The ψ carry only EW quantum numbers while the χ carry QCD colour and hypercharge. This isolation of the QCD charged states allows us to treat the EW and colour sector separately in many cases. After applying a number of requirements (asymptotic freedom, having appropriate states for the Higgs and top partners, preserving custodial symmetry, etc) the vast model space can be reduced down to only 12 promising candidates [31–33], which in the following we dub the "Ferretti models". The purpose of this work is to contribute to the phenomenological investigations into these models: working out typical signatures, ascertaining the viable parameter space, and suggesting searches for key processes.

This thesis is structured as follows. In Chapter 2 we review the setup of a CHM, some calculational tools to describe the low-energy effective theory, and the partial compositeness construction. We then turn to the Ferretti models in Chapter 3. We summarise the steps to arrive at the 12 models and list the particle content of the models that is relevant to this thesis. In particular, there are some ubiquitous states that are present in all models, such as an electrically neutral colour octet vector resonance $\mathcal{V}_8$. We then explore a concrete model in detail, applying the tools from Chapter 2 to discuss the types of interactions that can appear in the Lagrangian. Finally, we use the hidden symmetry method to work out the phenomenologically relevant interactions of the coloured spin-1 resonances. This calculation shows that the $\mathcal{V}_8$ mixes with the gluon.

In the remaining chapters we study the phenomenology of the Ferretti models, beginning with the pNGBs in Chapter 4. After providing current mass bounds on the QCD pair production of coloured pNGBs, we turn to the EW states. We give an overview of the different production and decay channels and derive simplified model bounds on single and Drell-Yan pair production. Next, we apply them to a full model based on the SU(5)/SO(5) coset. We show that the simplified model bounds can compete with a full simulation in some scenarios, then we present recast bounds for a number of mass hypotheses. The SU(5)/SO(5) model features a doubly charged scalar that can decay as $S^{++} \to W^+ t\bar{b}$ leading to a $4t$-like signature from pair production. To close out our study of pNGBs, we propose a search for this process. We focus on the final state with two same-sign leptons which still leaves several light and b-jets. Due to the large jet multiplicity we employ deep learning techniques to differentiate the signal process from the SM backgrounds using a combination of jet images and kinematic data. We then derive the expected discovery reach and exclusion limit at the high-luminosity LHC.

In Chapter 5 we discuss the phenomenology of the fermionic resonances, focusing on the colour triplet states. We list all possible decay channels and derive recast bounds for several exotic channels. We then turn to the spin-1 resonances in Chapter 6, where we primarily study the decays of the octet $\mathcal{V}_8$ and derive bounds on its single production. As an outlook for future colliders, we also list the signatures that can be expected from pair production of two spin-1 states. Finally, we draw our conclusions and present an outlook for extending this work in Chapter 7.

We provide supplemental information in several appendices. We begin by summarising some commonly used embeddings and identities in Appendix A. In Appendix B we present

our simulation setup and detail how we extract upper limits on the cross sections from the various recasting tools. This is followed by details on the bounds on pNGB pair production in Appendix C. In Appendix D we review the fundamentals of deep learning, present the full neural network architectures used in Section 4.5, and justify our choice of training set and evaluation method. Finally, Appendix E documents `scangen`, a tool we have developed to simplify performing the simulations in this work.

2 | Composite Higgs models

So far, all experimental investigations of the Higgs boson are consistent with the elementary doublet predicted by the SM. Nevertheless, the wealth of questions left unanswered by the SM has motivated theorists to look for alternate explanations. Chief among these questions is the naturalness problem, which states that radiative corrections to the Higgs mass have to cancel each other with high precision despite originating from different sectors of the theory. This problem can be avoided by positing the Higgs bosons as a composite state.

In this chapter we review the theoretical groundwork for this thesis. We begin by retracing the path from technicolor to composite Higgs and discuss the setup of a CHM. We then go over the construction of the low-energy Lagrangian and finally discuss how to give a mass to the top quark via partial compositeness.

2.1 Idea and history

There is a compelling argument in favour of dynamical symmetry breaking via composite dynamics: It is the path that Nature has chosen once before, in the case of QCD [22]. Two-flavour QCD in the massless limit has a global $\mathrm{SU}(2)_L \times \mathrm{SU}(2)_R \times \mathrm{U}(1)_B$ flavour symmetry group, where B is the baryon number. Looking at QCD at decreasing energies, its coupling constant grows until it crosses a threshold around the scale $\Lambda_{\mathrm{QCD}} \approx 200$ MeV, above which the coupling becomes non-perturbative — QCD *condenses*. The quark bilinear operator $\bar{q}_R q_L$ receives a VEV,

$$\langle \bar{q}_{i,R}\, q_{j,L} \rangle = \Lambda_{\mathrm{QCD}}^3\, \delta_{ij} \tag{2.1}$$

the *chiral condensate*, which spontaneously breaks the chiral flavour group to its diagonal subgroup, $G \equiv \mathrm{SU}(2)_L \times \mathrm{SU}(2)_R \times \mathrm{U}(1)_B \to \mathrm{SU}(2)_D \times \mathrm{U}(1)_B \equiv H$. Thus, the chiral symmetry breaking in QCD is dynamically induced by the running of the coupling, rather than by an elementary scalar field. There are still scalars in the spectrum of course, but these are composite quark-quark bound states: massless pions, the NGBs due to the symmetry breaking. If we now gauge the EW subgroup $G_{\mathrm{EW}} \equiv \mathrm{SU}(2)_L \times \mathrm{U}(1)_Y$ of G with $Y = T_R^3 + B/2$, the pions will be eaten by the W and Z bosons, giving them a mass of $m_W = \frac{1}{2} g f_\pi \simeq 29$ MeV with the pion decay constant $f_\pi = 92$ MeV [22]. The custodial $\mathrm{SU}(2)_D \subset H$ even ensures that $\rho = m_W/(m_Z \cos\theta_W) = 1$ at tree level. While the scale is clearly off, this discussion shows that QCD can in principle describe EWSB.

At this point it is natural to wonder if a scaled up version of QCD might do the trick. This idea has been around since the 1970s [20,21] and goes under the name technicolor (TC). To be specific, we assume there is a new asymptotically free TC gauge group $G_{\mathrm{TC}} = \mathrm{SU}(N_{\mathrm{TC}})$ with N_D massless left- and right-chiral techniquarks $\psi^i_{L,R}$ in the fundamental irrep of G_{TC} [34]. We take $\psi^i_L = (U^i_L, D^i_L) \in \mathbf{2}$ of $\mathrm{SU}(2)_L$ while the right-chiral fields are $\mathrm{SU}(2)_L$ singlets, leading to a global flavour group of

$$G = \mathrm{SU}(2N_D)_L \times \mathrm{SU}(2N_D)_R \times \mathrm{U}(1)_T \tag{2.2}$$

containing the EW group, $G \supset \mathrm{SU}(2)_L \times \mathrm{SU}(2)_R \supset \mathrm{SU}(2)_L \times \mathrm{U}(1)_Y$. Analogously to QCD, the gauge coupling g_{TC} increases with decreasing energy until it hits a scale Λ_{TC} where the theory condenses. The global symmetry group is then spontaneously broken as $G \to H = \mathrm{SU}(2N_D)_D \times \mathrm{U}(1)_T$. This yields $4N_D^2 - 1$ technipion NGBs, three of which get absorbed by the W and Z bosons to give masses $m_W = \frac{1}{2} g f_{\mathrm{TC}} = m_Z \cos\theta_W$. This shows that in TC, $f_{\mathrm{TC}} = v$ and therefore $\Lambda_{\mathrm{TC}} = g_* f_{\mathrm{TC}} \sim 1$ TeV where g_* is a typical composite sector coupling.

Technicolour as discussed so far cannot give masses to the leptons and quarks. To this end, we have to extend the formalism, which leads us to the fittingly named extended technicolor (ETC) models [35,36]. Following [22,37], we enlarge the gauge group to $\mathrm{SU}(N_{\mathrm{ETC}}) \supset \mathrm{SU}(N_{\mathrm{TC}})$ and assume there is a scale Λ_{ETC} where the ETC group spontaneously breaks to $\mathrm{SU}(N_{\mathrm{TC}})$,

$$\mathrm{SU}(N_{\mathrm{ETC}}) \to \mathrm{SU}(N_{\mathrm{TC}}) \times G_{\mathrm{rem}}, \tag{2.3}$$

where the remainder G_{rem} might, for example, include $\mathrm{SU}(3)_c$. The techniquarks ψ and the SM fermions f are embedded in common irreps of $\mathrm{SU}(N_{\mathrm{ETC}})$, thus allowing for the vertices $\bar{\psi}\not{A}\psi$, $\bar{f}\not{A}f$, and $\bar{\psi}\not{A}f$ with the ETC gauge field A_μ. At the ETC breaking scale the diagrams exchanging an A_μ induce four-fermion operators, analogously to the Fermi interaction:

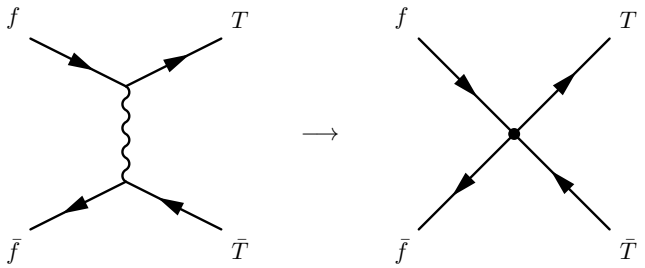

There are three relevant classes of four-fermion operators, which can be expressed as

$$\mathcal{L}_{\mathrm{int}} \supset \alpha_{ab} \frac{\bar{\psi} t^a \psi \, \bar{\psi} t^b \psi}{\Lambda^2_{\mathrm{ETC}}} + \beta_{ab} \frac{\bar{\psi}_L t^a \psi_R \, \bar{f}_R t^b f_L}{\Lambda^2_{\mathrm{ETC}}} + \gamma_{ab} \frac{\bar{f}_L t^a f_R \, \bar{f}_R t^b f_L}{\Lambda^2_{\mathrm{ETC}}}, \tag{2.4}$$

where t^a are the generators of $\mathrm{SU}(N_{\mathrm{ETC}})$, and the α, β, γ coefficients depend on the precise group structure. The α-terms generate masses for the technipions, while the β-terms yield the

desired SM fermion masses, which are roughly of size

$$m_f \approx \frac{\Lambda_{\mathrm{TC}}^3}{\Lambda_{\mathrm{ETC}}^2}. \tag{2.5}$$

The γ-terms in Eq. (2.4), however, are phenomenologically dangerous because they generally include flavour-changing neutral currents. For example, the operator

$$\gamma \frac{(\bar{s}\gamma_5 d)(\bar{d}\gamma_5 s)}{\Lambda_{\mathrm{ETC}}^2} \tag{2.6}$$

gives a contribution to the K_L–K_S mass difference Δm, which has been measured with a relative uncertainty of 0.17% [38]. To comply with this, the ETC scale has to be very high to suppress the FCNC operator.

Technicolour models face a number of phenomenological hurdles. For example, getting the correct kaon mass split requires $\Lambda_{\mathrm{ETC}} > 10^3$ TeV [37], while the estimate Eq. (2.5) implies $\Lambda_{\mathrm{ETC}} = \mathcal{O}(1\text{ TeV})$ to obtain $m_t = 173$ GeV. The FCNC can be reduced in "walking technicolor" models [39–44] which replace the QCD-like gauge dynamics with a scenario where the gauge coupling runs slowly — it "walks" — from Λ_{ETC} to Λ_{TC}. This enhances the techniquark condensate and thereby the α- and β-terms in Eq. (2.4) by a factor of $\sim \Lambda_{\mathrm{ETC}}/\Lambda_{\mathrm{TC}}$, while leaving the problematic γ-terms unaffected. While this approach can accommodate fermion masses of up to 1 GeV [37], the bottom and especially the top quark still remain out of reach. Simple TC models also have problems matching the EW precision observables S, T, U. Walking TC avoids this problem, albeit by virtue of there not being a way to estimate them [45]. Finally, the arguably strongest argument against TC is provided by the LHC: Since TC condenses around the weak scale, we would expect to see a zoo of resonances with mass of order 1 TeV, which simply have not been observed. Contrarily, we have observed a Higgs boson at 125 GeV, which TC does not predict [46]. Thus, TC has fallen out of favour in recent years. But the idea of dynamical symmetry breaking lives on in composite Higgs models.

The setup of a CHM [23–25] is similar to TC: We postulate a *composite sector* of hyperquarks Ψ charged under an asymptotically free hypercolour gauge group G_{HC}. We discuss concrete implementations of the composite sector in detail in Chapter 3 and only focus on general features of CHMs for now. The composite sector condenses at a scale Λ_{HC} as the hyperquark bilinear forms a condensate,

$$\left\langle \Psi^i \Psi^j \right\rangle = \Lambda_{\mathrm{HC}}^3 \Sigma_0^{ij}, \tag{2.7}$$

which breaks the global hyperquark flavour group $G \to H$. The specific breaking pattern and vacuum Σ_0 depend on the irreps of Ψ. Eventually, we would like to embed the SM gauge group in H, so we require $G_{\mathrm{EW}} \subset H$ (neglecting QCD for now). Actually, to protect the ρ-parameter, we should have $\mathrm{SU}(2)_L \times \mathrm{SU}(2)_R \subset H$ [47]. Finally, we demand that there is a Higgs candidate in the coset, $h \in G/H$. These constraints can be efficiently satisfied

with $G = \mathrm{SO}(5)$ and $H = \mathrm{SO}(4)$ since locally $\mathrm{SO}(4) \cong \mathrm{SU}(2)_L \times \mathrm{SU}(2)_R$, and corresponding models are called "minimal composite Higgs models" [30]. However, while the SO(5)/SO(4) coset famously appears in five-dimensional models [30], it cannot be obtained in the framework presented here. In this work, we study CHMs with an underlying fermionic description where the global symmetry of the composite sector is a flavour symmetry of the hyperquarks — and as such is always unitary. The minimal (i.e. with the fewest NGBs) coset is instead SU(4)/Sp(4) [48], and we will use it as an example later on.

Up to this point, the Higgs is massless, the EW symmetry remains unbroken, and the quarks and leptons are massless. To remedy this, we consider the second sector of the theory, the *elementary sector*, containing all SM fields (but the Higgs) along with their kinetic terms, but no Yukawa couplings. The full theory has to respect the SM gauge group, which is why we required $G_{\mathrm{EW}} \subset H$. However, by gauging only a subgroup of H, we explicitly break the global symmetry of the composite sector. This generates a potential for the now *pseudo* NGBs (pNGBs) in G/H, which includes the pNGB mass terms and triggers EWSB. There are two further potential sources of explicit symmetry breaking: mass terms for the hyperquarks and partial compositeness interactions of an elementary fermion with a composite partner [29]. The latter are the preferred way of generating fermion masses in CHMs, and are discussed in more detail in Section 2.3.

The vacuum $\Sigma_0 \equiv \Sigma_{\mathrm{EW}}$ in Eq. (2.7) preserves the EW symmetry, so what is the correct vacuum for the broken symmetry phase? In a TC model, it would be the vacuum Σ_{TC} that completely breaks G_{EW} to $\mathrm{U}(1)_Q$. In a CHM, however, we take

$$\Sigma_{\mathrm{CH}} = \cos\theta\, \Sigma_{\mathrm{EW}} + \sin\theta\, \Sigma_{\mathrm{TC}} \tag{2.8}$$

with $\sin\theta \ll 1$. This is known as *vacuum misalignment* [23] and marks one of the key differences between TC and CHMs. Furthermore, it highlights the fact that CHMs "smoothly interpolate between Higgs and technicolor dynamics" [24, p. 2]. We will see below that the misalignment angle connects the pion decay constant f with the Higgs VEV as

$$v = f \sin\theta. \tag{2.9}$$

A sufficiently small $\sin\theta$ creates a separation between the EW scale and the expected mass scale of composite resonances, thus avoiding TC's problem of predicting too light resonances.

2.2 The low-energy Lagrangian

In this section we review how to describe a CHM in the phase of broken global symmetry G, i.e. when the composite sector has condensed. We first give a general formulation, which also serves to set our notation for the model dependent calculations in Chapter 3. Then we illustrate the concepts for the case of a model with SU(4)/Sp(4) breaking.

2.2.1 Callan-Coleman-Wess-Zumino construction

Following the presentation in [16], we separate the generators $T^A = \{T^a, X^I\}$ of G into those preserving (T^a) and breaking (X^I) the vacuum Σ_0. From this definition we get

$$T^a\Sigma_0 + \Sigma_0(T^a)^T = 0, \qquad X^I\Sigma_0 - \Sigma_0(X^I)^T = 0. \tag{2.10}$$

The Lie algebra of the T^A splits as

$$[T^a, T^b] = if^{abc}T^c, \qquad [T^a, X^I] = if^{aIJ}X^J, \qquad [X^I, X^J] = if^{IJa}T^a. \tag{2.11}$$

The first commutator shows that H is a subgroup. No term proportional to X^K appears in the third commutator because we limit ourselves to symmetric cosets in this work. Finally, the second commutator shows that the X^I form a representation of H. Its dimension matches the number of broken generators, $\dim G - \dim H$, and it harbours the pNGBs,

$$\boldsymbol{\pi} = \pi^I X^I. \tag{2.12}$$

With the normalisation $\mathrm{Tr}\big(T^AT^B\big) = \frac{1}{2}\delta^{AB}$, we define the *Goldstone matrix*

$$U = \exp\left(\frac{\sqrt{2}i}{f}\,\boldsymbol{\pi}\right). \tag{2.13}$$

Under a global transformation $g \in G$, the Goldstone matrix transforms as

$$U(\pi) \to U(\pi') = g\,U(\pi)\,h^{-1}(g,\pi) \tag{2.14}$$

with a local element of the unbroken subgroup $h \in H$. This is the *non-linear realisation* of G acting on the pNGBs. If we transform U with an element $g_H \in H$, on the other hand, then $h(g_H, \pi) = g_H$, so U transforms linearly,

$$U(\pi) \to U(\pi') = g_H\,U(\pi)\,g_H^{-1}. \tag{2.15}$$

It is also instructive to study the effects of a transformation in the coset, $g_{G/H} \simeq \mathbb{1} + i\alpha^I X^I$. Considering for simplicity a coset $\mathrm{SO}(N)/\mathrm{SO}(N-1)$, Eq. (2.14) simplifies to

$$\pi_I \to \pi'_I + \frac{f}{\sqrt{2}}\,\alpha_I + \mathcal{O}\left(\alpha\sum_{n\geq 2}\frac{\pi^n}{f^{n-1}}\right). \tag{2.16}$$

This is known as the *shift symmetry*, which prohibits operators without pNGB (covariant) derivatives.

In 1969, Callan, Coleman, Wess, and Zumino (CCWZ) showed how to systematically construct the effective Lagrangian in a theory with spontaneous symmetry breaking (SSB) [49,50].

We define the *Maurer-Cartan form*

$$\Omega_\mu = i\,U^{-1}\left(\partial_\mu - iF_\mu^A T^A\right)U \equiv d_\mu^I X^I + e_\mu^a T^a = \mathbf{d}_\mu + \mathbf{e}_\mu \tag{2.17}$$

and divide it into the broken and unbroken components, the *CCWZ symbols* d_μ and e_μ [16]. At this stage, the F_μ^A are external sources, which we will eventually use to gauge the SM. Under a global transformation $g \in G$, the d- and e-symbols transform as

$$\mathbf{d}_\mu \to h(g,\pi)\,\mathbf{d}_\mu\,h^{-1}(g,\pi), \tag{2.18}$$

$$\mathbf{e}_\mu \to h(g,\pi)\,(\mathbf{e}_\mu + i\partial_\mu)\,h^{-1}(g,\pi). \tag{2.19}$$

Crucially, the transformation law is linear and only in terms of h. This allows us to construct the operators of the Lagrangian from the CCWZ symbols and derivatives in an H-invariant way, and G-invariance follows automatically — this is known as the CCWZ construction. The resulting operators are assigned a weight by the number of derivatives, or equivalently powers of momentum p, with $d_\mu, e_\mu, \partial_\mu = \mathcal{O}(p)$. For example, at $\mathcal{O}(p^2)$ we have $\mathrm{Tr}(\mathbf{d}_\mu\mathbf{d}^\mu)$, which is the unique $\mathcal{O}(p^2)$ operator as long as the pNGBs form an *irreducible* representation of H [16] — which is the case for the models considered below. To interpret it, we calculate the CCWZ symbols: By expanding the Maurer-Cartan form, we find [3]

$$\begin{aligned}\Omega_\mu = &-\frac{\sqrt{2}}{f}\,\partial_\mu\boldsymbol{\pi} + \frac{i}{f^2}[\boldsymbol{\pi},\partial_\mu\boldsymbol{\pi}] + \frac{\sqrt{2}}{3f^3}[\boldsymbol{\pi},[\boldsymbol{\pi},\partial_\mu\boldsymbol{\pi}]] + \cdots \\ &+ \mathbf{F}_\mu - \frac{\sqrt{2}i}{f}[\boldsymbol{\pi},\mathbf{F}_\mu] - \frac{1}{f^2}[\boldsymbol{\pi},[\boldsymbol{\pi},\mathbf{F}_\mu]] + \cdots .\end{aligned} \tag{2.20}$$

Splitting $\mathbf{F}_\mu = V_\mu^a T^a + A_\mu^I X^I$, we can use Eq. (2.11) to read off

$$\mathbf{d}_\mu = \mathbf{A}_\mu - \frac{\sqrt{2}}{f}\partial_\mu\boldsymbol{\pi} - \frac{\sqrt{2}i}{f}[\boldsymbol{\pi},\mathbf{V}_\mu] - \frac{1}{f^2}[\boldsymbol{\pi},[\boldsymbol{\pi},\mathbf{A}_\mu]] + \frac{\sqrt{2}}{3f^3}[\boldsymbol{\pi},[\boldsymbol{\pi},\partial_\mu\boldsymbol{\pi}]] + \cdots , \tag{2.21}$$

$$\mathbf{e}_\mu = \mathbf{V}_\mu - \frac{\sqrt{2}i}{f}[\boldsymbol{\pi},\mathbf{A}_\mu] + \frac{i}{f^2}[\boldsymbol{\pi},\partial_\mu\boldsymbol{\pi}] - \frac{1}{f^2}[\boldsymbol{\pi},[\boldsymbol{\pi},\mathbf{V}_\mu]] + \cdots . \tag{2.22}$$

We can now include the EW gauge interactions by setting the external sources equal to the gauge fields, $\mathbf{V}_\mu = g\mathbf{W}_\mu + g'\,\mathbf{B}_\mu$ and $\mathbf{A}_\mu = 0$. Then we have

$$\mathbf{d}_\mu = -\frac{\sqrt{2}}{f}\left(\partial_\mu\boldsymbol{\pi} - ig[\mathbf{W}_\mu,\boldsymbol{\pi}] - ig'[\mathbf{B}_\mu,\boldsymbol{\pi}]\right) + \cdots = -\frac{\sqrt{2}}{f}D_\mu\boldsymbol{\pi} + \cdots . \tag{2.23}$$

With the appropriate normalisation factor,

$$\mathcal{L}_{p^2} = \frac{f^2}{2}\,\mathrm{Tr}(\mathbf{d}_\mu\mathbf{d}^\mu) \supset \mathrm{Tr}(D_\mu\boldsymbol{\pi}D^\mu\boldsymbol{\pi}) = \frac{1}{2}(D_\mu\pi)^I(D^\mu\pi)^I, \tag{2.24}$$

the $\mathcal{O}(p^2)$ Lagrangian contains the kinetic terms of the pNGBs.

We now demonstrate the usefulness of the CCWZ construction with an explicit example. To this end we study the SU(4)/Sp(4) model following [48]. The EW preserving and breaking vacua are given by[1]

$$\Sigma_{\text{EW}} = \begin{pmatrix} i\sigma_2 & 0 \\ 0 & -i\sigma_2 \end{pmatrix}, \qquad \Sigma_{\text{TC}} = \begin{pmatrix} 0 & \mathbb{1} \\ -\mathbb{1} & 0 \end{pmatrix} \tag{2.25}$$

We can immediately write down the true vacuum with Eq. (2.8),

$$\Sigma_{\text{CH}} = \begin{pmatrix} \cos\theta\,(i\sigma_2) & \sin\theta\,\mathbb{1} \\ -\sin\theta\,\mathbb{1} & -\cos\theta\,(i\sigma_2) \end{pmatrix}, \tag{2.26}$$

but it turns out to be more convenient to start working with Σ_{EW} and introduce the misalignment later on. Eq. (2.10) yields the 10 unbroken generators, 6 of which form the $\text{SU}(2)_L \times \text{SU}(2)_R$ subgroup of Sp(4),

$$T_L^i = T^{1,2,3} = \frac{1}{2}\begin{pmatrix} \sigma_i & 0 \\ 0 & 0 \end{pmatrix}, \qquad T_R^i = T^{4,5,6} = \frac{1}{2}\begin{pmatrix} 0 & 0 \\ 0 & -\sigma_i^T \end{pmatrix}, \tag{2.27}$$

with the 4 remaining ones given by

$$T^{7,8,9} = \frac{1}{2\sqrt{2}}\begin{pmatrix} 0 & i\sigma_i \\ -i\sigma_i & 0 \end{pmatrix}, \qquad T^{10} = \frac{1}{2\sqrt{2}}\begin{pmatrix} 0 & \mathbb{1} \\ \mathbb{1} & 0 \end{pmatrix}. \tag{2.28}$$

The 5 broken generators span the pNGBs,

$$\boldsymbol{\pi} = \frac{1}{2\sqrt{2}}\begin{pmatrix} \pi_5 & 0 & \pi_1 + i\pi_2 & \pi_3 - i\pi_4 \\ 0 & \pi_5 & \pi_3 + i\pi_4 & -\pi_1 + i\pi_2 \\ \pi_1 - i\pi_2 & \pi_3 - i\pi_4 & -\pi_5 & 0 \\ \pi_3 + i\pi_4 & -\pi_1 - i\pi_2 & 0 & -\pi_5 \end{pmatrix}, \tag{2.29}$$

which form a $\mathbf{5}$ of Sp(4) and decompose as[2]

$$\mathbf{5} \to (\mathbf{2},\mathbf{2}) + (\mathbf{1},\mathbf{1}) \to \mathbf{3} + \mathbf{1} + \mathbf{1} \equiv \phi + h + \eta \tag{2.30}$$

under $\text{Sp}(4) \to \text{SU}(2)_L \times \text{SU}(2)_R \to \text{SU}(2)_D$. The custodial triplet $\phi = (\phi^{\pm}, \phi^0)$ corresponds to the longitudinal components of the W and Z bosons and is made up from $\pi_{1,2,3}$. The singlet $h = \pi_4$ from the bidoublet is the physical Higgs boson, while $\eta = \pi_5$ is a SM singlet. In unitary

[1] There is another inequivalent EW-preserving vacuum, $\text{diag}(i\sigma_2, i\sigma_2)$, which has been used in e.g. [51].

[2] Throughout this work the identities for products and decompositions of irreps are taken from [52].

gauge, $\pi_{1,2,3} = 0$, the pNGB matrix simplifies to

$$\boldsymbol{\pi} = \frac{1}{2\sqrt{2}} \begin{pmatrix} \eta & 0 & 0 & -ih \\ 0 & \eta & ih & 0 \\ 0 & -ih & -\eta & 0 \\ ih & 0 & 0 & -\eta \end{pmatrix}. \tag{2.31}$$

If we now define a rotation $\Omega(\theta)$ along the Higgs direction,

$$\Omega(\theta) = \exp\Big(\sqrt{2} i\theta X^h\Big), \qquad X^h = \frac{\partial \boldsymbol{\pi}}{\partial h}, \tag{2.32}$$

then the rotated generators

$$\tilde{T}^a = \Omega(\theta) T^a \Omega(\theta)^\dagger, \qquad \tilde{X}^I = \Omega(\theta) X^I \Omega(\theta)^\dagger \tag{2.33}$$

satisfy Eq. (2.10) with the misaligned vacuum $\Sigma_{\rm CH}$. Accordingly, the misaligned CCWZ symbols are defined along the rotated generators,

$$\tilde{\mathbf{d}}_\mu = 2\,\mathrm{Tr}\Big(\tilde{\Omega}_\mu \tilde{X}^I\Big)\tilde{X}^I, \qquad \tilde{\mathbf{e}}_\mu = 2\,\mathrm{Tr}\Big(\tilde{\Omega}_\mu \tilde{T}^a\Big)\tilde{T}^a. \tag{2.34}$$

Note that in the rotated Maurer-Cartan form, the SM vectors do not get misaligned,

$$\tilde{\Omega}_\mu = i\,U^{-1}(\tilde{\pi})\left(\partial_\mu - igW_\mu^i T_L^i - igB_\mu T_R^3\right) U(\tilde{\pi}), \tag{2.35}$$

because they generate the unbroken $G_{\rm EW}$ which corresponds to $\Sigma_{\rm EW}$. This mismatch leads to $\tilde{\mathbf{d}}_\mu$ containing a part of the EW gauge fields at $\mathcal{O}(f^0)$, see Eqs. (2.21) and (2.22), which will yield the W and Z masses. Indeed, we find

$$\begin{aligned} \frac{f^2}{2}\,\mathrm{Tr}\Big(\tilde{\mathbf{d}}_\mu \tilde{\mathbf{d}}^\mu\Big) \supset\ & \frac{1}{2}\partial_\mu h \partial^\mu h + \frac{1}{2}\partial_\mu \eta \partial^\mu \eta \\ & + \left(\frac{g^2 f^2 s_\theta^2}{8c_W^2} + \frac{g^2 f s_\theta c_\theta}{4c_W^2}\, h + \frac{g^2 c_{2\theta}}{8c_W^2}\, h^2 - \frac{g^2 s_\theta^2}{4}\,\eta^2\right)\left(Z_\mu Z^\mu + 2c_W^2 W_\mu^+ W^{-\mu}\right) \end{aligned} \tag{2.36}$$

where $c_W = \cos\theta_W$ and $s_\theta = \sin\theta$. The custodial symmetry enforces the fixed factor between the Z^2 and W^2 terms, and we read off

$$m_W = \frac{1}{2} g f \sin\theta, \qquad m_Z = \frac{m_W}{c_W}, \tag{2.37}$$

which confirms that with our normalisation, $v = f\sin\theta$. The further couplings

$$g_{hWW} = g m_W c_\theta = g_{hWW}^{\rm SM} c_\theta, \quad g_{hhWW} = \frac{1}{4} g^2 c_{2\theta} = g_{hhWW}^{\rm SM} c_{2\theta}, \quad g_{\eta\eta WW} = -\frac{1}{4} g^2 s_\theta^2, \tag{2.38}$$

highlight that in the limit $\theta \to 0$, the theory reduces to the SM.

2.2.2 Wess-Zumino-Witten term

While the CCWZ construction is a great tool, it does not capture all of the low-energy physics. In particular, it misses the anomalous Wess-Zumino-Witten (WZW) term [53–55], which plays an important role in the phenomenology of the pNGBs. We briefly summarise its origin following [56].

Consider a massless fermion ψ charged under a U(1) gauge theory. Classically, both $\psi \to e^{i\alpha}\psi$ and $\psi \to e^{i\alpha\gamma_5}\psi$ are symmetries of the theory and the corresponding vector and axial vector Noether currents are conserved,

$$j_V^\mu = \bar{q}\gamma^\mu q, \qquad j_A^\mu = \bar{q}\gamma^\mu\gamma_5 q, \qquad \partial_\mu j_{V/A}^\mu = 0. \tag{2.39}$$

However, in the quantised theory only the vector current remains conserved whereas the axial current famously satisfies

$$\partial_\mu j_A^\mu = -\frac{1}{16\pi^2}\,\epsilon^{\mu\nu\rho\sigma}F_{\mu\nu}F_{\rho\sigma}, \tag{2.40}$$

which is known as the *Adler-Bell-Jackiw (ABJ) anomaly* after its discoverers [57, 58]. Its origin can be understood in the path integral formalism, where the axial transformation leaves the action invariant, but not the path integral measure [59, 60]. This modifies the generating functional and thereby leads to Eq. (2.40).

A famous application of the ABJ anomaly is the decay of a neutral pion to two photons. Following [61], we consider three-flavour QCD where the non-abelian current $j_A^{\mu,a} = \bar{q}\gamma^\mu\gamma_5 t^a_{\mathbf{3}} q$ is anomalous analogously to Eq. (2.40). The Adler-Bardeen theorem states that the coefficient of an anomaly does not get renormalised [62]. Thus, by 't Hooft anomaly matching [17] there has to be a term in the low-energy Lagrangian that reproduces the anomaly exactly. This is the WZW term. We refer to [32, 63] for the formulation in terms of differential forms and focus on the result relevant for phenomenology here: After expanding the gauged WZW term, we find

$$\mathcal{L}_{\text{WZW}} \supset \frac{e^2}{32\pi^2 f_\pi}\,\pi^0\epsilon^{\mu\nu\rho\sigma}F_{\mu\nu}F_{\rho\sigma}, \tag{2.41}$$

which reproduces the ABJ anomaly and induces the decay $\pi^0 \to \gamma\gamma$ with the correct decay width. It is the latter point that marks the importance of the WZW term for phenomenology: It can open new decay channels for the pNGBs. For example, the η from the SU(4)/Sp(4) model receives the couplings [32]

$$\mathcal{L}_{\text{WZW}} \supset \frac{\dim(\Psi)}{16\pi^2 f}\,\cos\theta\,\eta\left(\frac{g^2 - g'^2}{2}Z_{\mu\nu}\tilde{Z}^{\mu\nu} + gg'F_{\mu\nu}\tilde{Z}^{\mu\nu} + g^2 W^+_{\mu\nu}\tilde{W}^{-\mu\nu}\right), \tag{2.42}$$

where we use the dual field strength tensor $\tilde{V}^{\mu\nu} = \frac{1}{2}\epsilon^{\mu\nu\rho\sigma}V_{\rho\sigma}$. Note that the WZW term depends only on the coset, except for the dimension of the hyperquark irrep under G_{HC} in the global prefactor.

2.2.3 Hidden gauge symmetry approach

The spectrum of a CHM also contains composite spin-1 resonances which emerge as bound states of the form $\mathcal{F}^\mu \sim \Psi\,\sigma^\mu\,\bar{\Psi}$. They can be described with the hidden gauge symmetry approach [64–68], see also [69]. It is based on the idea that the nonlinear sigma model for the coset G/H is gauge equivalent to a linear model with symmetry group $G \times H_{\text{local}}$, where H_{local} is gauged with gauge fields $\mathcal{F}^\mu$. We extend the group structure to $G \times G_{\text{local}}$ to also include axial vector states. The construction of the low-energy Lagrangian for the spin-1 resonances has been discussed in [70–72] and more recently in [73], whose presentation we follow here. However, we present the formalism for the case of a model with $\mathrm{SU}(3)_c \times \mathrm{U}(1)_X$ gauge theory which we will employ in Section 3.4, corresponding to the colour sector of the model class described in Chapter 3.

We begin with a CHM with global breaking pattern $G \to H$. We enlarge the global symmetry group to $G_0 \times G_1$, where a subset of G_0 is gauged by SM gauge fields

$$\mathbf{V}_\mu = \hat{g}_s \mathbf{G}_\mu + \hat{g}' \mathbf{B}_\mu. \tag{2.43}$$

Note that the gauge couplings do not correspond to the physical couplings due to mixing of the SM fields with the composite fields. The G_1 is completely gauged by the composite resonances,

$$\boldsymbol{\mathcal{F}}_\mu = \boldsymbol{\mathcal{V}}_\mu + \boldsymbol{\mathcal{A}}_\mu = \mathcal{V}_\mu^a T^a + \mathcal{A}_\mu^I X^I \tag{2.44}$$

with gauge coupling $\tilde{g}$. Note that this implies that there are $\dim H$ vector and $\dim G/H$ axial vector states[3]. The global symmetry is spontaneously broken to $H_0 \times H_1$, leading to two sets of pNGBs $\pi_{0,1}$. A linear combination of them gives mass to the $\boldsymbol{\mathcal{A}}_\mu$, while the orthogonal combination forms the physical pNGBs. Finally, the breaking of $H_0 \times H_1 \to H$ yields another set of pNGBs k, which are eaten to give mass to the vector states.

We define a Goldstone matrix

$$U_j = \exp\left(\frac{\sqrt{2}i}{f_j}\boldsymbol{\pi}_j\right) \tag{2.45}$$

and an associated Maurer-Cartan form

$$\Omega_{j,\mu} = i\,U_j^{-1} D_\mu U_j \tag{2.46}$$

for each sector, where the covariant derivatives read

$$D_\mu U_0 = (\partial_\mu - i\mathbf{V}_\mu)\,U_0, \tag{2.47}$$

$$D_\mu U_1 = (\partial_\mu - i\tilde{g}\boldsymbol{\mathcal{V}}_\mu - i\tilde{g}\boldsymbol{\mathcal{A}}_\mu)\,U_1. \tag{2.48}$$

[3] At this point the designation of vector and axial vector is arbitrary. They are only associated with vector and axial vector fermion currents in cosets of type $\mathrm{SU}(n) \times \mathrm{SU}(n)'/\mathrm{SU}(n)$.

From the Maurer-Cartan forms we define CCWZ symbols $\mathbf{d}_j^\mu$ and $\mathbf{e}_j^\mu$ in both sectors. The e-symbols are needed for the covariant derivative of the k pNGBs: Their Goldstone matrix

$$K = \exp\left(\frac{i}{f_K}\mathbf{k}\right) \tag{2.49}$$

transforms as

$$K \to h(g_0, \pi_0)\, K\, h^{-1}(g_1, \pi_1), \tag{2.50}$$

so the covariant derivative is given by

$$D_\mu K = \partial_\mu K - i\mathbf{e}_{0,\mu} K + iK\mathbf{e}_{1,\mu}. \tag{2.51}$$

Finally, we define the field strength tensors

$$\boldsymbol{\mathcal{F}}_{\mu\nu} = \partial_\mu \boldsymbol{\mathcal{F}}_\nu - \partial_\nu \boldsymbol{\mathcal{F}}_\mu - i\tilde{g}[\boldsymbol{\mathcal{F}}_\mu, \boldsymbol{\mathcal{F}}_\nu], \tag{2.52}$$

$$\mathbf{G}_{\mu\nu} = \partial_\mu \mathbf{G}_\nu - \partial_\nu \mathbf{G}_\mu - ig_s[\mathbf{G}_\mu, \mathbf{G}_\nu], \tag{2.53}$$

$$\mathbf{B}_{\mu\nu} = \partial_\mu \mathbf{B}_\nu - \partial_\nu \mathbf{B}_\mu. \tag{2.54}$$

Now we have all the ingredients to construct the most general Lagrangian at leading order,

$$\begin{aligned}\mathcal{L} = &-\frac{1}{2}\operatorname{Tr}\mathbf{G}_{\mu\nu}\mathbf{G}^{\mu\nu} - \frac{1}{2}\operatorname{Tr}\mathbf{B}_{\mu\nu}\mathbf{B}^{\mu\nu} - \frac{1}{2}\operatorname{Tr}\boldsymbol{\mathcal{F}}_{\mu\nu}\boldsymbol{\mathcal{F}}^{\mu\nu} \\ &+ \frac{f_0^2}{2}\operatorname{Tr}\mathbf{d}_{0,\mu}\mathbf{d}_0^\mu + \frac{f_1^2}{2}\operatorname{Tr}\mathbf{d}_{1,\mu}\mathbf{d}_1^\mu \\ &+ \frac{f_K^2}{2}\operatorname{Tr} D^\mu K (D_\mu K)^\dagger + r f_1^2\ \operatorname{Tr}\mathbf{d}_{0,\mu} K \mathbf{d}_1^\mu K^\dagger,\end{aligned} \tag{2.55}$$

which describes the pNGBs, the SM gauge fields, and the heavy spin-1 resonances. What is still missing are the fermions.

2.3 Partial compositeness

Finally in our exploration of CHMs we have to find a way to generate Yukawa couplings and give masses to the fermions, the most pressing being the top quark due to its large mass. In modern CHMs this is accomplished by the mechanism of *partial compositeness* (PC) [29], which posits that the physical top quark is an admixture of an elementary and a composite state. In this section we introduce PC following [16] and then discuss its phenomenological importance.

In Section 2.1 we saw that (extended) technicolor has difficulties generating a large enough top mass with a scalar operator,

$$\mathcal{L}_{\text{TC}} = -\lambda_t\, \bar{q}_L \mathcal{O}_{\text{TC}} t_R + \text{h.c.} \tag{2.56}$$

where $\mathcal{O}_{\rm TC}$ has the quantum numbers of the conjugate Higgs doublet. Instead, PC employs linear couplings to fermionic operators,

$$\mathcal{L}_{\rm PC} = -\lambda_L \bar{q}_L \mathcal{O}^L_{\rm PC} - \lambda_R \bar{t}_R \mathcal{O}^R_{\rm PC} + \text{h.c.}, \tag{2.57}$$

where schematically $\mathcal{O}^{L,R}_{\rm PC} = \Psi\bar{\Psi}\Psi$ and the operators have the same SM quantum numbers as q_L and t_R, respectively. Let's now evolve the coefficients down to $\Lambda_{\rm HC}$. Assuming that the theory remains near conformal during the renormalisation group (RG) evolution, we have

$$\lambda_{L,R}(\Lambda_{\rm HC}) \simeq \lambda_{L,R} \left(\frac{\Lambda_{\rm HC}}{\Lambda_{\rm 4F}}\right)^{[\mathcal{O}^{L,R}_{\rm PC}]-\frac{5}{2}}, \qquad \lambda_t(\Lambda_{\rm HC}) \simeq \lambda_t \left(\frac{\Lambda_{\rm HC}}{\Lambda_{\rm 4F}}\right)^{[\mathcal{O}_{\rm TC}]-1}, \tag{2.58}$$

where $\Lambda_{\rm 4F} \gg \Lambda_{\rm HC}$ is the scale where the four fermion interactions are generated. In both cases, a realistic top Yukawa can be obtained if the exponents are close to 0. In TC, this implies $[\mathcal{O}_{\rm TC}] \approx 1$ such that $|\mathcal{O}_{\rm TC}|^2$ is a relevant operator that leads to another naturalness problem. This also cannot be compensated by increasing $[\mathcal{O}_{\rm TC}]$ and instead choosing a large λ_t, which is bound by perturbativity. On the other side, there is no problem with $[\mathcal{O}^{L,R}_{\rm PC}] \approx 5/2$, the square of which is an irrelevant operator.

Below $\Lambda_{\rm HC}$, the operators $\mathcal{O}_{\rm PC}$ create fermionic resonances — so-called *top partners*. We start with the simplest case, $\mathcal{O}^L_{\rm PC} \to Q \in (\mathbf{3},\mathbf{2})_{1/6}$ and $\mathcal{O}^R_{\rm PC} \to T \in (\mathbf{3},\mathbf{1})_{2/3}$. Note that Q and T are Dirac states, i.e. both chiralities have the same quantum numbers. Thus, in contrast to the fermions in the SM, the top partners are not chiral but vector-like, and are often called vector-like quarks (VLQs). We can therefore give them a mass term. The PC Lagrangian can be conveniently formulated in terms of two-component spinors,

$$\mathcal{L} = -m_Q Q^c_L Q_L - m_T T^c_R T_R - \lambda_L Q^c_L q_L - \lambda_R T_R t^c_R + \text{h.c.}, \tag{2.59}$$

where

$$Q_L = \begin{pmatrix} T_L \\ B_L \end{pmatrix} \in (\mathbf{3},\mathbf{2})_{1/6}, \qquad Q^c_L = \begin{pmatrix} T^c_L \\ B^c_L \end{pmatrix} \in (\bar{\mathbf{3}},\mathbf{2})_{-1/6} \tag{2.60}$$

and $T = (T_R, \bar{T}^c_R)^T$. Note that the sub- and superscripts on the two-component spinors are part of the field names. Looking at the charge-2/3 states, we have a mass matrix

$$\mathcal{L}_{\rm mix} = -\mathcal{T}^c \mathcal{M}_{2/3} \mathcal{T} + \text{h.c.}, \quad \mathcal{M}_{2/3} = \begin{pmatrix} 0 & 0 & \lambda_R \\ \lambda_L & m_Q & 0 \\ 0 & 0 & m_T \end{pmatrix}, \quad \mathcal{T} = \begin{pmatrix} t_L \\ T_L \\ T_R \end{pmatrix}, \quad \mathcal{T}^c = \begin{pmatrix} t^c_R \\ T^c_L \\ T^c_R \end{pmatrix} \tag{2.61}$$

which is readily diagonalised:

$$m = 0: \qquad \hat{T}_1^c = \cos\theta_R\, t_R^c + \sin\theta_R T_R^c, \qquad \hat{T}_1 = \cos\theta_L\, t_L - \sin\theta_L T_L \tag{2.62}$$

$$m = \sqrt{\lambda_R^2 + m_T^2}: \qquad \hat{T}_2^c = -\sin\theta_R t_R^c + \cos\theta_R T_R^c, \qquad \hat{T}_2 = T_R \tag{2.63}$$

$$m = \sqrt{\lambda_L^2 + m_Q^2}: \qquad \hat{T}_3^c = T_L^c, \qquad \hat{T}_3 = \sin\theta_L t_L + \cos\theta_L T_L \tag{2.64}$$

with mixing angles

$$\sin\theta_L = \frac{\lambda_L}{\sqrt{\lambda_L^2 + m_Q^2}}, \qquad \sin\theta_R = \frac{\lambda_R}{\sqrt{\lambda_R^2 + m_T^2}}. \tag{2.65}$$

We identify the lightest Dirac state $t = (\hat{T}_1, \bar{\hat{T}}_1^c)^T$ with the physical top quark. It is a superposition of the elementary and composite states, thus *partially composite*.

The previous discussion illustrates the basic idea of PC but misses some crucial details. For one, we haven't actually given a mass to the top quark yet — t as defined above is massless. Secondly, in line with the formalism from Section 2.2.1, we should formulate the Lagrangian in a G-invariant way. We assume that both Q and T originate from the same irrep of H which is the case[4] for the models studied in Chapter 3. Schematically,

$$\Psi = \begin{pmatrix} Q_L \\ T_R \end{pmatrix}, \tag{2.66}$$

where in practice Ψ will contain further states that don't mix with the elementary fields. The elementary q_L and t_R^c are embedded in an *incomplete representation* of G, e.g.

$$q_L \to \zeta_L = (t_L, b_L, 0)^T, \qquad t_R^c \to \zeta_R^c = (0, 0, t_R^c)^T. \tag{2.67}$$

The ζ_L and ζ_R^c are referred to as *spurions*. For the purpose of constructing the Lagrangian, we are however free to treat them as full representations of G and only reduce them to incomplete ones when necessary. To couple the spurions to the top partners, we must promote Ψ — which transforms with H — to something that transforms with G. The correct tool for this job is the Goldstone matrix U, since we schematically have

$$U\Psi \overset{(2.14)}{\to} gUh^{-1}\, h\Psi = gU\Psi. \tag{2.68}$$

Thus, the proper partial compositeness Lagrangian reads

$$\mathcal{L}_{\text{PC}} = -m_\Psi \Psi^c \Psi - \lambda_L\, \zeta_L U \Psi^c - \lambda_R\, \zeta_R^c U \Psi + \text{h.c.}\,. \tag{2.69}$$

[4]Some models contain several states with the quantum numbers of top partners but we can always find a doublet and a singlet that come from the same H-irrep.

Note that while formally looking G-invariant, the spurions are in the end incomplete irreps and thus represent an explicit breaking of G, which also contributes to the pNGB potential. We recall that $U = \mathbb{1} + \sqrt{2}i\boldsymbol{\pi}/f + \mathcal{O}(\pi^2)$. The 0th order in the pNGBs corresponds to Eq. (2.59) and induces the mixing as discussed above. But now there are further terms, schematically

$$\frac{\lambda_R}{f}\, t_R^c\, \pi\, T_L \to \frac{\lambda_R}{f} \cos\theta_R \sin\theta_L\, t_R^c\, \pi\, t_L \supset \frac{\lambda_R}{f} \cos\theta_R \sin\theta_L\, t_R^c\, \frac{v+h}{\sqrt{2}}\, t_L, \tag{2.70}$$

where the arrow indicates a rotation to the mass eigenstates, and with a slight abuse of notation we retain the quark names on the right hand side. The π contains the Higgs field, thus finally generating a top Yukawa coupling, but other neutral pNGBs may also occur. Such couplings are phenomenologically important because if present, they open new decay channels for the pNGBs, $\pi \to t\bar{t}$. We can also assess the size of this coupling: it is proportional to $1/f$, and the product of λ_R and mixing angles determines the top mass, so we have

$$c\,\frac{m_t}{f}\, t_R^c t_L \pi \tag{2.71}$$

with an $\mathcal{O}(1)$ coefficient c [33]. The coupling to the bottom quark analogously scales with m_b/f.

In principle, we could repeat this process for all of the SM fermions f. In practice however, it is a tall order for a composite sector to produce a partner for every matter field. There is a much simpler solution: we take the TC approach, generating mass from the operators

$$ff\,\Psi\Psi. \tag{2.72}$$

Since the remaining fermions are orders of magnitude lighter than the top quark, the constraints discussed above are significantly weaker and mass generation via a bilinear operator is a valid option. Contrarily, such an operator for the top quark will only create a small contribution in the top left corner of $\mathcal{M}_{2/3}$ in Eq. (2.61) that will only mildly affect the mixing.

3 | The Ferretti models

Realisations of the composite Higgs idea in terms of an underlying model of hyperquarks as outlined in the previous chapter have been known since the origins of CHMs [25]. Implementations of partial compositeness are more difficult however, and have first appeared in 5D models in the 2000s [30, 74], which employ holographic techniques to relate the strongly coupled composite sector to a weakly coupled theory in five dimensions. Within the context of 4D models, the quest for ones with a fermionic UV theory that incorporates PC only started in the 2010s with SUSY CHMs [75, 76] and non-SUSY constructions [31, 77]. In particular, Ferretti and collaborators have made an effort to classify viable UV models [31–33], which has led to a list of 12 models that are considered promising candidates for a realistic CHM. This work is dedicated to studying the phenomenology of these models, which we dub the *Ferretti models*. In this chapter we first review the setup and define the Ferretti models. We then derive the particle content of the models and discuss typical couplings using the model M5 as a case study. Finally, we apply the hidden symmetry method to calculate the colour sector bosonic Lagrangian.

3.1 Models with an underlying fermionic description

In this section we retrace the key steps in reducing the infinite model space down to just a handful of models [31–33]. A guiding principle in this is the idea of *minimality*: wherever possible we will limit ourselves to the simplest cases. This begins already when we set out the base class of models that are even under consideration. We limit ourselves to simple and asymptotically free gauge groups G_{HC}. Besides the hypercolour gauge fields the field content is purely fermionic. Specifically, we assume hyperquarks in two distinct irreps of G_{HC}: in terms of left-handed Weyl fermions there are n_ψ copies of $\psi \in \mathbf{R}_\psi$ and n_χ copies of $\chi \in \mathbf{R}_\chi$. If the irrep is complex, we instead have $n_\psi \times (\psi, \tilde{\psi}) \in (\mathbf{R}_\psi, \bar{\mathbf{R}}_\psi)$ and analogously for χ. While the SM fermions are neutral under G_{HC}, the hyperquarks carry SM charges: we assign EW quantum numbers to the ψ, while the χ carry QCD colour and hypercharge. The global flavour group G of the hyperquarks is spontaneously broken to H when G_{HC} condenses.

We move on to the conditions that are placed on the models, starting with the phenomenological ones. Firstly, the global symmetry must allow for the following chain,

$$G \to H \supset G_{\text{cust}} \supset G_{\text{SM}}, \tag{3.1}$$

Ψ	Real	Pseudoreal	Complex
ψ :	SU(5)/SO(5)	SU(4)/Sp(4)	$SU(4)^2/SU(4)$
χ :	SU(6)/SO(6)	SU(6)/Sp(6)	$SU(3)^2/SU(3)$

Table 3.1: Minimal cosets in the EW (ψ) and colour sector (χ).

where $G_{\text{cust}} = \text{SU}(3)_c \times \text{SU}(2)_L \times \text{SU}(2)_R \times \text{U}(1)_X$ and $G_{\text{SM}} = \text{SU}(3)_c \times \text{SU}(2)_L \times \text{U}(1)_Y$. This is necessary since G_{SM} needs to be a gauge symmetry of the composite sector as well, so it must also be a global symmetry. We further need the custodial $\text{SU}(2)_L \times \text{SU}(2)_R$ to keep $\rho = 1$ at tree level. Finally, we require an additional $\text{U}(1)_X$ which becomes part of the hypercharge by $Y = T_R^3 + X$. Without it we wouldn't be able to satisfy our second criterion, the presence of three-hyperquark states Ψ^3 that function as top partners

$$Q_L^c \in (\bar{\mathbf{3}}, \mathbf{2})_{-1/6}, \qquad T_R \in (\mathbf{3}, \mathbf{1})_{2/3} \tag{3.2}$$

that can couple with q_L and t_R^c. Depending on the irreps, these will be of the form $\psi\chi\psi$ or $\chi\psi\chi$. We have a further requirement on the top partners: the Q_L must come in a $(\mathbf{2}, \mathbf{2})$ of $\text{SU}(2)_L \times \text{SU}(2)_R$ rather than $(\mathbf{2}, \mathbf{1})$ to protect the $Zb_L\bar{b}_L$ coupling [78]. Finally, among the pNGBs there must of course be a Higgs bidoublet,

$$G/H \ni (H, \tilde{H}) \equiv (\mathbf{1}, \mathbf{2}, \mathbf{2})_0 \quad \text{ of } G_{\text{cust}}. \tag{3.3}$$

Let us discuss some implications of these conditions. First, some more words on the symmetry breaking patterns are in order. As mentioned above, we use the two species of hyperquarks to separate EW and QCD quantum numbers. More precisely, we split the contributions to G_{cust} as

$$\psi : \qquad G_\psi \to H_\psi \supset \text{SU}(2)_L \times \text{SU}(2)_R, \tag{3.4}$$

$$\chi : \qquad G_\chi \to H_\chi \supset \text{SU}(3)_c \times \text{U}(1)_X. \tag{3.5}$$

Now assume ψ transforms under a real (R) or pseudoreal (PR) irrep of G_{HC}, then[1] $G_\psi = \text{SU}(n_\psi)$ and the condensate $\langle\psi\psi\rangle$ breaks it to $H_\psi = \text{SO}(n_\psi)$ for a real and $H_\psi = \text{Sp}(n_\psi)$ for a pseudoreal irrep. For a complex (C) irrep, we instead have two factors of $\text{SU}(n_\psi)$ that get broken to the diagonal subgroup, $\text{SU}(n_\psi)^2/\text{SU}(n_\psi)$. In order to accommodate both the custodial symmetry and the Higgs, we need $n_\psi \geq 5$ for R or $n_\psi \geq 4$ for PR/C, and minimality dictates that we take the lowest number in each category. For the χ hyperquarks the same discussion applies, with $n_\chi \geq 6$ for R/PR and $n_\chi \geq 3$ for C. The resulting cosets are listed in Tab. 3.1. We can take all 9 combinations of (ψ, χ) realities. However, in the cases (PR, PR), (PR, C), and (C, PR) it is not possible to form hypercolour singlet top partners, so only 6 combinations appear

[1] Technically, $G_\psi = \text{U}(n_\psi)$ — we will come back to the U(1) factors later.

in practice.

There are two subtleties associated with the U(1) factors. Firstly, we focus on a R/PR irrep and note that the global symmetry is actually $\mathrm{U}(n) \cong \mathrm{SU}(n) \times \mathrm{U}(1)$. Thus, the symmetry from both irreps is $\mathrm{SU}(n_\psi) \times \mathrm{U}(1)_\psi \times \mathrm{SU}(n_\chi) \times \mathrm{U}(1)_\chi$, where the U(1)s rotate all hyperquarks by the same phase. One linear combination of the U(1)s is ABJ anomalous while the orthogonal combination remains anomaly free, leaving a global $\mathrm{SU}(n_\psi) \times \mathrm{SU}(n_\chi) \times \mathrm{U}(1)$ symmetry. The second point concerns $\mathrm{U}(1)_X$ which is embedded in SO(6) and Sp(6) for R/PR irreps, but seems to be missing from the complex colour coset in Tab. 3.1. For a hyperquark in a complex irrep, the global symmetry is $\mathrm{U}(n) \times \mathrm{U}(n)' \cong \mathrm{SU}(n) \times \mathrm{SU}(n)' \times \mathrm{U}(1)_V \times \mathrm{U}(1)_A$. The axial $\mathrm{U}(1)_A$ again mixes to form an anomaly free U(1) while the vector-like $\mathrm{U}(1)_V$ remains unbroken. Therefore, a complex χ implies

$$\mathrm{SU}(3)^2 \times \mathrm{U}(1) \to \mathrm{SU}(3) \times \mathrm{U}(1) \equiv \mathrm{SU}(3)_c \times \mathrm{U}(1)_X, \tag{3.6}$$

which efficiently satisfies our requirements.

The symmetry breaking patterns discussed above are plausible but not guaranteed. In fact, the theory might condense in a way that breaks G_{HC} or $\mathrm{SU}(3)_c$. We exclude all models where this is predicted to happen by the maximally attractive channel (MAC) hypothesis [79], a heuristic for assessing which channels are likely to condense first. Finally, we impose a number of technical constraints: The theory must be free of gauge/global anomalies for a unitary/symplectic G_{HC}, and since we are going to gauge it, G_{SM} must not have 't Hooft anomalies. When considering the RG flow of the models, there is actually a contradiction: for PC to generate a large top Yukawa, the Ψ^3 operator needs to pick up a large anomalous dimension for which the running must be conformal. On the other hand, in a conformal theory the coupling cannot become strongly interacting in the infrared (IR). A possible solution is to look for non-conformal theories and rely on the fact that we can add additional hyperquarks of mass $\sim \Lambda_{\mathrm{HC}}$ to bring them into the conformal window [33]. We follow this approach and therefore require that our promising models are likely not conformal (unfortunately for this type of models a definitive test remains out of reach).

Now all that is left to do is to list the irreps of the viable hypercolour gauge groups and to check which of them fulfill all of our requirements, where we consider only the lowest dimensional irrep for each reality. This work has been done in [31–33] and has resulted in 12 promising models which are listed in Tab. 3.2. These models are the framework for all following phenomenological discussions in this work. The listed values for the hypercharge will be justified in Section 3.2.3. The baryon number of the χ is 1/6 in models with $\chi\psi\chi$ top partners and 1/3 in case of $\psi\chi\psi$. This is because Ψ^3 couples to quarks and we assign $B_\psi = 0$.

In the following we mostly take the masses of the BSM particles and the couplings as free parameters. We point out, however, that information about the spectrum can be obtained from holographic calculations [80–85]. Furthermore, several Lattice studies have been performed [86–101] to calculate masses and couplings for CHMs with HC gauge groups Sp(4) and SU(4).

G_{HC}	ψ	χ	Reality	Ψ^3	Y_χ	B_χ	N_{HC}	Name
$\text{SO}(N_{\text{HC}})$	$5 \times \mathbf{F}$	$6 \times \mathbf{Spin}$	R, R	$\chi\psi\chi$	$-1/3$	$1/6$	7, 9	M1, M2
$\text{SO}(N_{\text{HC}})$	$5 \times \mathbf{Spin}$	$6 \times \mathbf{F}$	R, R	$\psi\chi\psi$	$2/3$	$1/3$	7, 9	M3, M4
$\text{Sp}(2N_{\text{HC}})$	$5 \times \mathbf{A}_2$	$6 \times \mathbf{F}$	R, PR	$\chi\psi\chi$	$-1/3$	$1/6$	2	M5
$\text{SU}(N_{\text{HC}})$	$5 \times \mathbf{A}_2$	$3 \times (\mathbf{F}, \overline{\mathbf{F}})$	R, C	$\chi\psi\chi$	$-1/3$	$1/6$	4	M6
$\text{SO}(N_{\text{HC}})$	$5 \times \mathbf{F}$	$3 \times (\mathbf{Spin}, \overline{\mathbf{Spin}})$	R, C	$\chi\psi\chi$	$-1/3$	$1/6$	10	M7
$\text{Sp}(2N_{\text{HC}})$	$4 \times \mathbf{F}$	$6 \times \mathbf{A}_2$	PR, R	$\psi\chi\psi$	$2/3$	$1/3$	2	M8
$\text{SO}(N_{\text{HC}})$	$4 \times \mathbf{Spin}$	$6 \times \mathbf{F}$	PR, R	$\psi\chi\psi$	$2/3$	$1/3$	11	M9
$\text{SO}(N_{\text{HC}})$	$4 \times (\mathbf{Spin}, \overline{\mathbf{Spin}})$	$6 \times \mathbf{F}$	C, R	$\psi\chi\psi$	$2/3$	$1/3$	10	M10
$\text{SU}(N_{\text{HC}})$	$4 \times (\mathbf{F}, \overline{\mathbf{F}})$	$6 \times \mathbf{A}_2$	C, R	$\psi\chi\psi$	$2/3$	$1/3$	4	M11
$\text{SU}(N_{\text{HC}})$	$4 \times (\mathbf{F}, \overline{\mathbf{F}})$	$3 \times (\mathbf{A}_2, \overline{\mathbf{A}_2})$	C, C	$\psi\chi\psi$	$2/3$	$1/3$	5	M12

Table 3.2: Properties of the Ferretti models, adapted from [33]. The listed models pass all requirements mentioned in the text, including lying outside of the conformal window. The hyperquark irreps $\mathbf{F}$, $\mathbf{Spin}$, and $\mathbf{A}_2$ refer to the fundamental, spinorial, and two-index antisymmetric irreps of G_{HC}, respectively. The fourth column notes if the irreps are real (R), pseudoreal (PR), or complex (C), which determines the coset, see Tab. 3.1. Ψ^3 indicates the form of the top partners, and Y_χ and B_χ are the hypercharge and baryon number of the χ hyperquarks.

3.2 Particle content

Having defined the Ferretti models, our next task is to work out their phenomenology, starting with determining the particle content.

3.2.1 Pseudo Nambu-Goldstone bosons

We begin with the spin-0 states that are due to the spontaneous symmetry breaking, the pNGBs. We have seen in the previous section that for any model we can generically write the SSB as

$$G_\psi \times G_\chi \times \text{U}(1) \to H_\psi \times H_\chi, \tag{3.7}$$

which lays out the three sources of pNGBs: the EW coset G_ψ/H_ψ, the colour sector coset G_χ/H_χ, and the non-anomalous $\text{U}(1) \to \times$ which is also broken by the hyperquark condensates.

The global U(1)**.** The latter breaking leads to a SM neutral pNGB commonly named a, which is present in all models and can be very light. We do not study this state in this work and instead refer to [32, 33, 102–104] .

EW sector. The non-abelian sectors offer a much richer particle content. The EW pNGBs[2] form an irrep of H_ψ, which we decompose to $\mathrm{SU}(2)_L \times \mathrm{SU}(2)_R$ and $\mathrm{SU}(2)_L \times \mathrm{U}(1)_Y$:

$$\mathrm{SU}(5)/\mathrm{SO}(5): \quad \mathbf{14} \to (\mathbf{3},\mathbf{3}) + (\mathbf{2},\mathbf{2}) + (\mathbf{1},\mathbf{1}) \to \mathbf{3}_{\pm1} + \mathbf{3}_0 + \mathbf{2}_{\pm1/2} + \mathbf{1}_0 \tag{3.8}$$

$$\mathrm{SU}(4)/\mathrm{Sp}(4): \quad \mathbf{5} \to (\mathbf{2},\mathbf{2}) + (\mathbf{1},\mathbf{1}) \to \mathbf{2}_{\pm1/2} + \mathbf{1}_0 \tag{3.9}$$

$$\mathrm{SU}(4)^2/\mathrm{SU}(4): \quad \mathbf{15} \to (\mathbf{3},\mathbf{1}) + (\mathbf{1},\mathbf{3}) + (\mathbf{2},\mathbf{2}) + (\mathbf{2},\mathbf{2}) + (\mathbf{1},\mathbf{1}) \tag{3.10}$$

$$\to \mathbf{3}_0 + \mathbf{1}_\pm + \mathbf{1}'_0 + \mathbf{2}_{\pm1/2} + \mathbf{2}'_{\pm1/2} + \mathbf{1}_0 \tag{3.11}$$

As mentioned in Chapter 3, $\mathrm{SU}(4)/\mathrm{Sp}(4)$ is the minimal coset, featuring only the Higgs bidoublet and a SM singlet commonly denoted as η in the literature. Both of these are contained in the real and complex coset as well, in addition to three triplets for the real and a triplet, two doublets, and three singlets for the complex case.

Defining the pNGBs as eigenstates of $\mathrm{SU}(2)_L \times \mathrm{U}(1)_Y$ only makes sense with respect to the EW preserving vacuum Σ_{EW}. Following [105], we instead express them as custodial eigenstates since the $\mathrm{SU}(2)_D \subset \mathrm{SU}(2)_L \times \mathrm{SU}(2)_R$ remains unbroken after EWSB in the scalar sector. Thus:

$$\mathrm{SU}(5)/\mathrm{SO}(5): \quad (\mathbf{3},\mathbf{3}) + (\mathbf{2},\mathbf{2}) + (\mathbf{1},\mathbf{1}) \to (\mathbf{5}+\mathbf{3}+\mathbf{1}) + (\mathbf{3}+\mathbf{1}) + \mathbf{1} \tag{3.12}$$

$$\mathrm{SU}(4)/\mathrm{Sp}(4): \quad (\mathbf{2},\mathbf{2}) + (\mathbf{1},\mathbf{1}) \to (\mathbf{3}+\mathbf{1}) + \mathbf{1} \tag{3.13}$$

$$\mathrm{SU}(4)^2/\mathrm{SU}(4): \quad (\mathbf{3},\mathbf{1}) + (\mathbf{1},\mathbf{3}) + (\mathbf{2},\mathbf{2}) + (\mathbf{2},\mathbf{2}) + (\mathbf{1},\mathbf{1}) \tag{3.14}$$

$$\to (\mathbf{3}+\mathbf{3}) + (\mathbf{3}+\mathbf{1}) + (\mathbf{3}+\mathbf{1}) + \mathbf{1} \tag{3.15}$$

The parentheses around sums of irreps indicate states that derive from a common multiplet, with the exception of $\mathrm{SU}(4)^2/\mathrm{SU}(4)$, where the left and right triplets combine to two custodial triplets as $\frac{1}{\sqrt{2}}(l \pm r)$. We recall that a generic custodial quintuplet φ_5, triplet φ_3, and singlet φ_1 contain

$$\varphi_5 = (\varphi_5^{++}, \varphi_5^{+}, \varphi_5^{0}, \varphi_5^{-}, \varphi_5^{--}), \quad \varphi_3 = (\varphi_3^{+}, \varphi_3^{0}, \varphi_3^{-}), \quad \varphi_1 = \varphi_1^0, \tag{3.16}$$

where the superscript indicates the electric charge.

Colour sector. In this sector we have the additional complication that the underlying hyperquarks carry $\mathrm{U}(1)_X$ charges $X = Y_\chi$. Keeping the charge general for now, we have

$$\mathrm{SU}(6)/\mathrm{SO}(6): \quad \mathbf{20} \to \mathbf{8}_0 + \mathbf{6}_{2X} + \bar{\mathbf{6}}_{-2X} \tag{3.17}$$

$$\mathrm{SU}(6)/\mathrm{Sp}(6): \quad \mathbf{14} \to \mathbf{8}_0 + \mathbf{3}_{-2X} + \bar{\mathbf{3}}_{2X} \tag{3.18}$$

$$\mathrm{SU}(3)^2/\mathrm{SU}(3): \quad \mathbf{8}_0 \tag{3.19}$$

[2]Some of these pNGBs are complete SM singlets. Nevertheless we refer to all pNGBs that emerge from G_ψ/H_ψ as *electroweak* pNGBs, which should be read as a shorthand for "pNGBs emerging from the EW sector".

under $H_\chi \to \mathrm{SU}(3)_c \times \mathrm{U}(1)_X$, and we have omitted the unbroken U(1) in the complex coset. Since the coloured pNGBs are all $\mathrm{SU}(2)_L$ singlets, their electric charges Q match their X-charges. Thus, all models contain an electrically neutral colour octet pNGB, customarily denoted as π_8. The triplet π_3 only appears in M5 which has $Y_\chi = -1/3$ (see Tab. 3.2), so π_3 has $Q = 2/3$ and is comparable to a right-handed stop in SUSY. The charge of the colour sextet on the other hand depends on the model, being $-2/3$ in M1-2 and $4/3$ in M3-4 and M8-11. Since the coloured pNGBs are $\chi\chi$ bound states, their baryon numbers are $2B_\chi$, apart from the real color octet: $B(\pi_3) = \pm 1/3$, $B(\pi_6^{-2/3}) = \pm 1/3$, and $B(\pi_6^{4/3}) = \pm 2/3$. In Tab. 3.3 we group the models by properties of the χ and list all colour sector bosons.

3.2.2 Spin-1 resonances

We continue the discussion with the spin-1 resonances, which can also be neatly separated into EW and colour sector resonances. Assuming a (pseudo)real hyperquark irrep for simplicity, we generically have

$$\Psi\sigma^\mu\bar{\Psi} \sim \mathbf{F}_G \times \overline{\mathbf{F}}_G \ni \mathbf{Ad}_G \to \mathbf{Ad}_H + \mathbf{N}_H \equiv \mathcal{V}_\mu + \mathcal{A}_\mu \tag{3.20}$$

with $N = \dim G/H$. As discussed in Section 2.2.3, we separate the spin-1 states into ones along the unbroken subgroup $\mathcal{V}_\mu$ and ones along the coset $\mathcal{A}_\mu$. Starting again with the EW sector, we have

$$\begin{aligned}
\mathrm{SU}(5)/\mathrm{SO}(5): \quad & \mathbf{24}_{\mathrm{SU}(5)} \to \mathbf{10}_{\mathrm{SO}(5)} + \mathbf{14}_{\mathrm{SO}(5)} && (3.21)\\
\mathcal{V}_\mu: \quad & \mathbf{10}_{\mathrm{SO}(5)} \to (\mathbf{2},\mathbf{2}) + (\mathbf{3},\mathbf{1}) + (\mathbf{1},\mathbf{3}) && (3.22)\\
\mathcal{A}_\mu: \quad & \mathbf{14}_{\mathrm{SO}(5)} \to (\mathbf{3},\mathbf{3}) + (\mathbf{2},\mathbf{2}) + (\mathbf{1},\mathbf{1}) && (3.23)\\
\mathrm{SU}(4)/\mathrm{Sp}(4): \quad & \mathbf{15}_{\mathrm{SU}(4)} \to \mathbf{10}_{\mathrm{Sp}(4)} + \mathbf{5}_{\mathrm{Sp}(4)} && (3.24)\\
\mathcal{V}_\mu: \quad & \mathbf{10}_{\mathrm{Sp}(5)} \to (\mathbf{2},\mathbf{2}) + (\mathbf{3},\mathbf{1}) + (\mathbf{1},\mathbf{3}) && (3.25)\\
\mathcal{A}_\mu: \quad & \mathbf{5}_{\mathrm{Sp}(4)} \to (\mathbf{2},\mathbf{2}) + (\mathbf{1},\mathbf{1}) && (3.26)
\end{aligned}$$

We decompose the irreps to $\mathrm{SU}(2)_L \times \mathrm{SU}(2)_R$. The further decompositions have been given above. In the complex case, $H \cong G/H \cong \mathrm{SU}(4)$ and the identification with vector and axial vectors can be justified with corresponding fermion currents. Just as with the pNGBs,

$$\mathcal{V}_\mu/\mathcal{A}_\mu: \quad \mathbf{15}_{\mathrm{SU}(4)} \to (\mathbf{3},\mathbf{1}) + (\mathbf{1},\mathbf{3}) + (\mathbf{2},\mathbf{2}) + (\mathbf{2},\mathbf{2}) + (\mathbf{1},\mathbf{1}). \tag{3.27}$$

The vectors actually contain an additional singlet due to the unbroken U(1) in the complex coset. A first study of the EW spin-1 resonances has been performed in [73] focusing on the SU(4)/Sp(4) coset, whereas we conducted a more complete survey in [106].

In this work we focus on the coloured spin-1 states, which are derived analogously: From

	Models	χ	Y_χ	B_χ	π	$\mathcal{V}^\mu$	$\mathcal{A}^\mu$
C1	M1-2	R	$-1/3$	$1/6$	$\mathbf{8}_0$, $\mathbf{6}_{-2/3}$	$\mathbf{8}_0$, $\mathbf{1}_0$, $\mathbf{3}_{2/3}$	$\mathbf{8}_0$, $\mathbf{6}_{-2/3}$
C2	M3-4, M8-11	R	$2/3$	$1/3$	$\mathbf{8}_0$, $\mathbf{6}_{4/3}$	$\mathbf{8}_0$, $\mathbf{1}_0$, $\mathbf{3}_{-4/3}$	$\mathbf{8}_0$, $\mathbf{6}_{4/3}$
C3	M5	PR	$-1/3$	$1/6$	$\mathbf{8}_0$, $\mathbf{3}_{2/3}$	$\mathbf{8}_0$, $\mathbf{1}_0$, $\mathbf{6}_{-2/3}$	$\mathbf{8}_0$, $\mathbf{3}_{2/3}$
C4	M6-7	C	$-1/3$	$1/6$	$\mathbf{8}_0$	$\mathbf{8}_0$, $\mathbf{1}_0$	$\mathbf{8}_0$
C5	M12	C	$2/3$	$1/3$	$\mathbf{8}_0$	$\mathbf{8}_0$, $\mathbf{1}_0$	$\mathbf{8}_0$

Table 3.3: Grouping of the Ferretti models according to colour sector properties [3]. Besides the reality, hypercharge, and baryon number of the χ, we list the coloured pNGBs, the vector, and the axial vector states by their $\mathrm{SU}(3)_c \times \mathrm{U}(1)_Q$ quantum numbers. The conjugate of the complex states is implied. The colours of the resonances indicate the baryon number: $B = 0$ for black, $B = \pm 1/3$ for red, and $B = \pm 2/3$ for blue. The blue states can have B-conserving couplings to two quarks.

$\mathbf{35}_{\mathrm{SU}(6)} \to \mathbf{15}_{\mathrm{SO}(6)} + \mathbf{20}_{\mathrm{SO}(6)}$ we get

$$\mathcal{V}_\mu \equiv \mathbf{15}_{\mathrm{SO}(6)} \to \mathbf{8}_0 + \mathbf{3}_{-2X} + \bar{\mathbf{3}}_{2X} + \mathbf{1}_0, \qquad \mathcal{A}_\mu \equiv \mathbf{20}_{\mathrm{SO}(6)} \to \mathbf{8}_0 + \mathbf{6}_{2X} + \bar{\mathbf{6}}_{-2X} \tag{3.28}$$

of $\mathrm{SU}(3)_c \times \mathrm{U}(1)_X$ in the real coset. In the pseudoreal case, $\mathbf{35}_{\mathrm{SU}(6)} \to \mathbf{21}_{\mathrm{Sp}(6)} + \mathbf{14}_{\mathrm{Sp}(6)}$ leads to

$$\mathcal{V}_\mu \equiv \mathbf{21}_{\mathrm{Sp}(6)} \to \mathbf{8}_0 + \mathbf{6}_{2X} + \bar{\mathbf{6}}_{-2X} + \mathbf{1}_0, \qquad \mathcal{A}_\mu \equiv \mathbf{14}_{\mathrm{Sp}(6)} \to \mathbf{8}_0 + \mathbf{3}_{-2X} + \bar{\mathbf{3}}_{2X}, \tag{3.29}$$

and in the complex case we only have the octets and a singlet,

$$\mathcal{V}_\mu : \quad \mathbf{8}_0 + \mathbf{1}_0, \qquad \mathcal{A}_\mu : \quad \mathbf{8}_0. \tag{3.30}$$

The electric charges and baryon numbers of the spin-1 states follow analogously to the pNGBs and are indicated in Tab. 3.3, where the colour sector bosons are summarised. The table also groups the Ferretti models into several classes which we will come back to when we study the phenomenology of the coloured spin-1 resonances in Chapter 6.

3.2.3 Top partners

To determine the fermionic resonances we have to look at the Ψ^3 bound states. To illustrate the procedure, we work out the top partners in detail for the model M5 [107], which will serve as a case study in this work. Reading off from Tab. 3.2, the cosets are SU(5)/SO(5) and SU(6)/Sp(6) and the top partners are of type $\chi\psi\chi$. Starting with the colour sector, we have $\chi \in \mathbf{6}_{\mathrm{SU}(6)}$ and thus

$$\chi\psi\chi \in \mathbf{6}_{\mathrm{SU}(6)} \times \mathbf{6}_{\mathrm{SU}(6)} = \mathbf{15}_{\mathrm{SU}(6)} + \mathbf{21}_{\mathrm{SU}(6)} \to \mathbf{14}_{\mathrm{Sp}(6)} + \mathbf{1}_{\mathrm{Sp}(6)} + \mathbf{21}_{\mathrm{Sp}(6)}, \tag{3.31}$$

which decompose under $\mathrm{SU}(3)_c \times \mathrm{U}(1)_X$ as in Eq. (3.29). The same states can be obtained from

$$\chi\psi\bar{\chi} \in \mathbf{6}_{\mathrm{SU}(6)} \times \bar{\mathbf{6}}_{\mathrm{SU}(6)} = \mathbf{35}_{\mathrm{SU}(6)} + \mathbf{1}_{\mathrm{SU}(6)} \to \mathbf{21}_{\mathrm{Sp}(6)} + \mathbf{14}_{\mathrm{Sp}(6)} + \mathbf{1}_{\mathrm{Sp}(6)}. \tag{3.32}$$

In the EW sector there is only one $\psi \in \mathbf{5}_{\mathrm{SU}(5)} \to \mathbf{5}_{\mathrm{SO}(5)} \to (\mathbf{2},\mathbf{2}) + (\mathbf{1},\mathbf{1})$ of $\mathrm{SU}(2)_L \times \mathrm{SU}(2)_R$. The next step is to determine the hypercharge of the χ, for which we look at the colour triplet top partners:

$$\begin{aligned}(\mathbf{5},\mathbf{14})_H &\supset (\mathbf{2},\mathbf{2};\bar{\mathbf{3}}_{2X}) + (\mathbf{1},\mathbf{1};\mathbf{3}_{-2X}) && \text{of } G_{\mathrm{cust}} && (3.33)\\ &\supset (\bar{\mathbf{3}},\mathbf{2})_{1/2+2X} + (\mathbf{3},\mathbf{1})_{-2X} && \text{of } G_{\mathrm{SM}} && (3.34)\end{aligned}$$

The last two states have precisely the quantum numbers of Q_L^c and T_R if we choose $X = Y_\chi = -1/3$, as is indicated in Tab. 3.2. In fact, the argument above can be repeated for all models with top partners of type $\chi\psi\chi$, which is why they all share the same value of Y_χ. With the X-charge fixed, we can complete our classification of top partners in M5. From the $\mathbf{14}_{\mathrm{Sp}(6)}$ we get

$$\begin{aligned}(\mathbf{5},\mathbf{14}) &\to (\mathbf{2},\mathbf{2};\mathbf{8}_0) + (\mathbf{1},\mathbf{1};\mathbf{8}_0) + (\mathbf{2},\mathbf{2};\mathbf{3}_{2/3}) + (\mathbf{1},\mathbf{1};\mathbf{3}_{2/3}) + (\mathbf{2},\mathbf{2};\bar{\mathbf{3}}_{-2/3}) + (\mathbf{1},\mathbf{1};\bar{\mathbf{3}}_{-2/3}) && (3.35)\\ &\to (\mathbf{8},\mathbf{2})_{\pm 1/2} + (\mathbf{8},\mathbf{1})_0 + \big[(\mathbf{3},\mathbf{2})_{7/6} + (\mathbf{3},\mathbf{2})_{1/6} + (\mathbf{3},\mathbf{1})_{2/3} + cc\big] && (3.36)\end{aligned}$$

under $H \to G_{\mathrm{cust}} \to G_{\mathrm{SM}}$. After EWSB there will be one charged and one neutral colour octet Dirac fermion and one octet Majorana. Among the colour triplets is one state with charge 5/3, three with $Q = 2/3$, and one bottom-like state. Following the notation in [107], we denote these respectively as

$$\tilde{G}^{\pm},\ \tilde{G}^0,\ \tilde{g},\ X_{5/3},\ 3T,\ B. \tag{3.37}$$

From the Sp(6) singlet we get

$$(\mathbf{5},\mathbf{1}) \to (\mathbf{2},\mathbf{2};\mathbf{1}_0) + (\mathbf{1},\mathbf{1};\mathbf{1}_0) \to (\mathbf{1},\mathbf{2})_{\pm 1/2} + (\mathbf{1},\mathbf{1})_0 \to \tilde{h}^{\pm},\ \tilde{h}^0,\ \tilde{B}, \tag{3.38}$$

where $\tilde{B}$ is a Majorana spinor. Finally, the $\mathbf{21}_{\mathrm{Sp}(6)}$ yields

$$\begin{aligned}(\mathbf{5},\mathbf{21}) &\to (\mathbf{2},\mathbf{2};\mathbf{8}_0) + (\mathbf{1},\mathbf{1};\mathbf{8}_0) + (\mathbf{2},\mathbf{2};\mathbf{1}_0) + (\mathbf{1},\mathbf{1};\mathbf{1}_0)\\ &\quad + \big[(\mathbf{2},\mathbf{2};\mathbf{6}_{-2/3}) + (\mathbf{1},\mathbf{1};\mathbf{6}_{-2/3}) + cc\big] && (3.39)\\ &\to (\mathbf{8},\mathbf{2})_{\pm 1/2} + (\mathbf{8},\mathbf{1})_0 + (\mathbf{1},\mathbf{2})_{\pm 1/2} + (\mathbf{1},\mathbf{1})_0\\ &\quad + \big[(\mathbf{6},\mathbf{2})_{-1/6} + (\mathbf{6},\mathbf{2})_{-7/6} + (\mathbf{6},\mathbf{1})_{-2/3} + cc\big] && (3.40)\end{aligned}$$

The octets and singlet match the ones from Eq. (3.36), and we find sextets with charges 1/3, $-5/3$, and three states with charge $-2/3$.

Models	$\mathbf{1}_0^M$	$\mathbf{1}_0$	$\mathbf{1}_1$	$\mathbf{3}_{-\frac{4}{3}}$	$\mathbf{3}_{-\frac{1}{3}}$	$\mathbf{3}_{\frac{2}{3}}$	$\mathbf{3}_{\frac{5}{3}}$	$\mathbf{3}_{\frac{8}{3}}$	$\mathbf{6}_{-\frac{5}{3}}$	$\mathbf{6}_{-2/3}$	$\mathbf{6}_{\frac{1}{3}}$	$\mathbf{8}_0^M$	$\mathbf{8}_0$	$\mathbf{8}_1$
M1-2, M5-7	✓	✓	✓		✓	✓	✓		✓	✓	✓	✓	✓	✓
M3-4				✓	✓	✓	✓	✓						
M8-12					✓	✓	✓							

Table 3.4: Overview of the top partner field content in the Ferretti models. We list the $\mathrm{SU}(3)_c \times \mathrm{U}(1)_Y$ eigenstates and denote Majorana states with a superscript M. A checkmark indicates that the Ψ^3 combination that yields the top partners contains the respective state.

In the model M5, the fermionic resonances come in the $\mathbf{1}, \mathbf{3}, \mathbf{6}$, and $\mathbf{8}$ of colour. This is actually the case for all models with top partners of type $\chi\psi\chi$, see Tab. 3.4. There we show which mass eigenstates are contained within the Ψ^3 top partners. If these are of the form $\psi\chi\psi$, the top partners only come in colour triplets. The electric charges then depend on the coset: In M3-4, the larger $\mathbf{5}_{\mathrm{SU}(5)} \ni \psi$ leads to a plethora of states, among them $\mathrm{SU}(2)_L$ triplets with hypercharges $5/3$ and $-1/3$, which after EWSB yield the exotic states

$$X_{8/3} \in \mathbf{3}_{8/3}, \qquad X_{-4/3} \in \mathbf{3}_{-4/3} \qquad \text{of } \mathrm{SU}(3)_c \times \mathrm{U}(1)_Q. \tag{3.41}$$

In models with $\chi\psi\chi$, on the other hand, the top partners always come in $(\mathbf{2},\mathbf{2}) + (\mathbf{1},\mathbf{1})$ of $\mathrm{SU}(2)_L \times \mathrm{SU}(2)_R$ and therefore always lead to the states indicated in the first row of Tab. 3.4. We note that the only universal states are colour triplets of charges $5/3$, $2/3$, and $-1/3$.

3.3 A case study: the model M5

We now study a concrete model in some detail, the model M5. This section serves two purposes: we can put the abstract concepts of the previous chapter to use and show their application in practice, and we set the notation and perform some calculations that will be important in later chapters. In this section we follow our previous work [107], where we performed an in-depth study of M5.

3.3.1 Embeddings

The vacua

$$\Sigma_{0,\psi} = \begin{pmatrix} & i\sigma_2 & \\ -i\sigma_2 & & \\ & & 1 \end{pmatrix}, \qquad \Sigma_{0,\chi} = \begin{pmatrix} 0 & -\mathbb{1}_3 \\ \mathbb{1}_3 & 0 \end{pmatrix} \tag{3.42}$$

break the global symmetry as

$$\mathrm{SU}(5) \times \mathrm{SU}(6) \times \mathrm{U}(1) \to \mathrm{SO}(5) \times \mathrm{Sp}(6) \equiv H. \tag{3.43}$$

Now we embed the generators of G_{cust} in the unbroken subgroup. We take

$$T_L^i = \frac{1}{2}\begin{pmatrix} \mathbb{1}_2 \otimes \sigma^i & \\ & 0 \end{pmatrix}, \qquad T_R^i = \frac{1}{2}\begin{pmatrix} \sigma^i \otimes \mathbb{1}_2 & \\ & 0 \end{pmatrix}, \tag{3.44}$$

for the $\mathrm{SU}(2)_L \times \mathrm{SU}(2)_R$ and

$$T_G^a = \frac{1}{\sqrt{2}}\begin{pmatrix} t_{\mathbf{3}}^a & \\ & -(t_{\mathbf{3}}^a)^T \end{pmatrix}, \qquad T_X = \frac{1}{3}\begin{pmatrix} -\mathbb{1}_3 & \\ & \mathbb{1}_3 \end{pmatrix} \tag{3.45}$$

for $\mathrm{SU}(3)_c \times \mathrm{U}(1)_X$, where the $t_{\mathbf{3}}^a = \frac{1}{2}\lambda^a$ are the SU(3) generators in the fundamental irrep. Having fixed the generators, we can embed the fields in irreps of H. We recall from Section 3.2.1 that the colour sector pNGBs are the neutral octet π_8 and a triplet π_3 with charge 2/3. Belonging to the adjoint and two-index antisymmetric irreps of $\mathrm{SU}(3)_c$ respectively, we write them as

$$\boldsymbol{\pi}_8 = \pi_8^a\, t_{\mathbf{3}}^a, \qquad \boldsymbol{\pi}_3 = \pi_3^i\, L^i \quad \text{with } [L^i]^{jk} = \frac{1}{\sqrt{2}}\epsilon^{ijk}, \tag{3.46}$$

and the full pNGB matrix reads

$$\boldsymbol{\pi}_\chi = \frac{1}{\sqrt{2}}\begin{pmatrix} \boldsymbol{\pi}_8 & \boldsymbol{\pi}_3^\dagger \\ \boldsymbol{\pi}_3 & \boldsymbol{\pi}_8^T \end{pmatrix}. \tag{3.47}$$

The normalisations are chosen such that $\mathrm{Tr}\big(\boldsymbol{\pi}^\dagger\boldsymbol{\pi}\big) = \frac{1}{2}\pi_8^a\pi_8^a + \pi_3^{*,i}\pi_3^i$. Turning to the spin-1 states, the axial vectors exactly match the pNGBs while the vectors consist of a neutral octet and singlet and a sextet with charge $-2/3$, embedded into Sp(6) as

$$\boldsymbol{\mathcal{V}}^\mu = \frac{1}{\sqrt{2}}\begin{pmatrix} \boldsymbol{\mathcal{V}}_8^\mu + \frac{1}{\sqrt{6}}\boldsymbol{\mathcal{V}}_1^\mu & \boldsymbol{\mathcal{V}}_6^\mu \\ \boldsymbol{\mathcal{V}}_6^{\mu,\dagger} & -\boldsymbol{\mathcal{V}}_8^{\mu,T} - \frac{1}{\sqrt{6}}\boldsymbol{\mathcal{V}}_1^\mu \end{pmatrix}, \qquad \boldsymbol{\mathcal{A}}^\mu = \frac{1}{\sqrt{2}}\begin{pmatrix} \boldsymbol{\mathcal{A}}_8^\mu & \boldsymbol{\mathcal{A}}_3^{\mu,\dagger} \\ \boldsymbol{\mathcal{A}}_3^\mu & \boldsymbol{\mathcal{A}}_8^{\mu,T} \end{pmatrix}. \tag{3.48}$$

The singlet matrix is $\boldsymbol{\mathcal{V}}_1^\mu = \mathcal{V}_1\,\mathbb{1}_3$ and for the sextet we have $\boldsymbol{\mathcal{V}}_6^\mu = \mathcal{V}_6^{\mu,s}K^s$ with symmetric 3×3 matrices K^s. Explicit forms for K^s can be found in Appendix A, along with an overview of the colour sector embeddings employed in this work.

We turn to the EW sector. We refer to [106] for the spin-1 states and instead focus on the pNGBs. The states are listed in Eq. (3.12) and are embedded in SO(5) as

$$\boldsymbol{\pi}_\psi = \frac{1}{2}\begin{pmatrix} \frac{\eta}{\sqrt{10}}\mathbb{1}_2 + \boldsymbol{\pi}_0 & \boldsymbol{\pi}_+ & H \\ \boldsymbol{\pi}_- & \frac{\eta}{\sqrt{10}}\mathbb{1}_2 - \boldsymbol{\pi}_0 & -\tilde{H} \\ H^\dagger & -\tilde{H}^\dagger & -\frac{4}{\sqrt{10}}\eta \end{pmatrix}, \tag{3.49}$$

where $\pi_{\pm,0}$ are the triplets with hypercharges $\pm 1, 0$ with matrix embeddings

$$\boldsymbol{\pi}_0 = \frac{1}{\sqrt{2}}\pi_0^i \sigma^i, \qquad \boldsymbol{\pi}_\pm = \pi_\pm^i \sigma^i, \tag{3.50}$$

H is the Higgs doublet

$$H = \begin{pmatrix} \phi^+ \\ \frac{1}{\sqrt{2}}(h + i\phi^0) \end{pmatrix} \tag{3.51}$$

and $\tilde{H} = i\sigma^2 H^*$ its dual. Here h is the physical Higgs, $\phi^{\pm,0}$ are the longitudinal components of the $W^\pm$ and Z bosons, and finally η is a SM singlet. As discussed above, we prefer to express the pNGB as custodial eigenstates,

$$\mathbf{14} \to (\mathbf{3},\mathbf{3}) + (\mathbf{2},\mathbf{2}) + (\mathbf{1},\mathbf{1}) \to (\mathbf{5}+\mathbf{3}+\mathbf{1}) + (\mathbf{3}+\mathbf{1}) + \mathbf{1} \tag{3.52}$$

$$\equiv (\eta_5 + \eta_3 + \eta_1) + (\phi + h) + \eta. \tag{3.53}$$

The relation between the π_i and the η_i is

$$\pi_+^+ = \eta_5^{++}, \quad \pi_+^0 = \frac{i\eta_3^+ - \eta_5^+}{\sqrt{2}}, \quad \pi_0^+ = -\frac{i\eta_3^+ + \eta_5^+}{\sqrt{2}}, \tag{3.54}$$

$$\pi_0^0 = \frac{\eta_1^0 - \sqrt{2}\eta_5^0}{\sqrt{3}}, \quad \pi_+^- = \frac{\sqrt{2}\eta_1^0 + \eta_5^0}{\sqrt{6}} + i\frac{\eta_3^0}{\sqrt{2}}, \tag{3.55}$$

and $\pi_-^- = (\pi_+^+)^*$, $\pi_-^0 = (\pi_+^0)^*$, $\pi_-^+ = (\pi_+^-)^*$, and $\pi_0^- = (\pi_0^+)^*$ [105]. In both sectors we exponentiate the $\boldsymbol{\pi}_{\psi/\chi}$ to the Goldstone matrices $U_{\psi/\chi}$ with separate decay constants $f_{\psi/\chi}$.

We now come to the top partners, which have been discussed in detail in Section 3.2.3. While both $\chi\psi\chi$ and[3] $\chi\bar{\psi}\bar{\chi}$ lead to the same resonances, the physics is quite different. In the first case, the top partners proper emerge from the $\mathbf{15} = \mathbf{A}_2$ of SU(6), as opposed to the $\mathbf{35} = \mathbf{Ad}$ in the second case. This impacts the spurion irreps of the elementary quarks, which in turn affects the couplings. In this work, we consider the case where the top partners come from the $\mathbf{A}_2$. The couplings to quarks will therefore involve the $(\mathbf{5},\mathbf{14})_H$ and $(\mathbf{5},\mathbf{1})_H$, which are embedded in the colour sector by

$$(\mathbf{5},\mathbf{14})_H \equiv \Psi_{\mathbf{14}} = \frac{1}{\sqrt{2}}\begin{pmatrix} -\boldsymbol{Q}_3^c & -\boldsymbol{Q}_8 \\ \boldsymbol{Q}_8^T & -\boldsymbol{Q}_3 \end{pmatrix}, \qquad (\mathbf{5},\mathbf{1})_H \equiv \Psi_{\mathbf{1}} = Q_1 \Sigma_{0,\chi}. \tag{3.56}$$

For the fermions we use the same colour sector matrices as for the bosons, i.e. $\boldsymbol{Q}_8 = Q_8^a\, t_{\mathbf{3}}^a$ and

[3] We recall that these are two-component spinors. The operator will couple to q_L and t_R^c, so the number of barred spinors must be even. Thus, the second operator reads $\chi\bar{\psi}\bar{\chi}$ rather than $\chi\psi\bar{\chi}$.

$\boldsymbol{Q}_3 = Q_3^i L^i$. Note that all Q_r are quintuplets of SO(5), embedded as

$$Q_3 = (X_{5/3}, X_{2/3}, T_L, B_L, iT_R)^T, \qquad Q_8 = (\tilde{G}_u^+, \tilde{G}_u^0, \tilde{G}_d^0, \tilde{G}_d^-, i\tilde{g})^T, \tag{3.57}$$

$$Q_3^c = (B_L^c, -T_L^c, -X_{2/3}^c, X_{5/3}^c, -iT_R^c)^T, \qquad Q_1 = (\tilde{h}_u^+, \tilde{h}_u^0, \tilde{h}_d^0, \tilde{h}_d^-, i\tilde{B})^T. \tag{3.58}$$

Here the first two and the third and fourth components both form doublets while the last component is a singlet. For example, $(\tilde{G}_u^+, \tilde{G}_u^0)^T \in \mathbf{2}_{1/2}$ and $(\tilde{G}_d^0, \tilde{G}_d^-)^T \in \mathbf{2}_{-1/2}$. We now dress the top partners to obtain operators that transform as $(\mathbf{5}, \mathbf{15})$ of G:

$$\mathcal{O}_{\mathbf{14}} = U_\chi \left(U_\psi \cdot \Psi_{\mathbf{14}}\right) U_\chi^T, \qquad \mathcal{O}_{\mathbf{1}} = U_\chi \left(U_\psi \cdot \Psi_{\mathbf{1}}\right) U_\chi^T. \tag{3.59}$$

Finally, the elementary quarks have to be embedded in the conjugate irrep, $\zeta_{L/R} \in (\bar{\mathbf{5}}, \overline{\mathbf{15}})$. These are given by

$$\zeta_L = \frac{1}{\sqrt{2}} \begin{pmatrix} \boldsymbol{\xi}_L & 0 \\ 0 & 0 \end{pmatrix}, \qquad \boldsymbol{\xi}_L = \xi_L^i L^i, \qquad \xi_L = (b_L, -t_L, 0, 0, 0)^T, \tag{3.60}$$

$$\zeta_R^c = \frac{1}{\sqrt{2}} \begin{pmatrix} 0 & 0 \\ 0 & \boldsymbol{\xi}_R^c \end{pmatrix}, \qquad \boldsymbol{\xi}_R^c = \xi_R^{c,i} L^i, \qquad \xi_R^c = (0, 0, 0, 0, -it_R^c)^T. \tag{3.61}$$

With all of the definitions out of the way, we now turn to constructing the Lagrangian.

3.3.2 The Lagrangian

We can divide the model Lagrangian into several sectors as follows:

$$\begin{aligned} \mathcal{L}_{\text{M5}} = \mathcal{L}_{\text{h.s.}}^{\text{EW}} + \mathcal{L}_{\text{h.s.}}^{\text{colour}} + \mathcal{L}_{\text{WZW}} - V_{\text{pNGB}} \\ + \sum_f f i\sigma^\mu D_\mu \bar{f} + \sum_\Psi \left(\Psi i\sigma^\mu D_\mu \bar{\Psi} - m_Q \Psi\Psi\right) + \mathcal{L}_{\text{der}} + \mathcal{L}_{\text{mix}} + \text{h.c.} \end{aligned} \tag{3.62}$$

This splits roughly into bosons in the first row and fermions in the second. The hidden symmetry Lagrangians $\mathcal{L}_{\text{h.s.}}^i$ contain kinetic terms for the pNGBs and spin-1 resonances. In the EW sector for example [1],

$$\mathcal{L}_{\text{h.s.}}^{\text{EW}} \supset \text{Tr}(D_\mu \boldsymbol{\pi}_\psi D^\mu \boldsymbol{\pi}_\psi) \tag{3.63}$$

$$\supset \left(2ieA^\mu + ig\frac{c_{2w}}{c_w} Z^\mu\right) \eta_5^{--} \overleftrightarrow{\partial_\mu} \eta_5^{++} + \left(\frac{ig}{\sqrt{2}} W^{-\mu} (c_\theta \eta_3^- - i\eta_5^-) \overleftrightarrow{\partial_\mu} \eta_5^{++} + \text{h.c.}\right). \tag{3.64}$$

Here we highlight the couplings that are relevant for the pair production of the doubly charged η_5^{++} or mixed production of a doubly and singly charged state, which we will make use of in Chapter 4. The remaining couplings are listed in Appendix C.1. On the side of the spin-1 resonances, $\mathcal{L}_{\text{h.s.}}$ induces a mixing between elementary and composite spin-1 states, which we will explore in detail in Section 3.4 for the colour sector. Finally, the hidden symmetry

Lagrangian also determines the couplings between the spin-1 states and the pNGBs.

From the anomalous global U(1) we get the WZW term which couples a (pseudo-)scalar to two gauge bosons. For the ubiquitous colour octet π_8, it is given by

$$\mathcal{L}^{\pi_8}_{\mathrm{WZW}} = \frac{g_s^2 \dim\chi}{16\pi^2 f_\chi}\frac{1}{2}d^{abc}\,\pi_8^a\,\epsilon^{\mu\nu\rho\sigma}G^b_{\mu\nu}G^c_{\rho\sigma} + \frac{g_s g' \dim\chi}{16\pi^2 f_\chi}\,Y_\chi\,\pi_8^a\epsilon^{\mu\nu\rho\sigma}G^a_{\mu\nu}B_{\rho\sigma}, \tag{3.65}$$

where $G^a_{\mu\nu}$ and $B_{\mu\nu}$ are the $\mathrm{SU}(3)_c$ and $\mathrm{U}(1)_Y$ field strength tensors, respectively [33]. Both couplings are proportional to $\dim\chi$, which in M5 is $\dim\mathbf{F}_{\mathrm{Sp}(4)} = 4$. The d^{abc} is the fully symmetric tensor of SU(3), and $Y_\chi = -1/3$ in M5.

Similarly to Eq. (3.65), the EW pNGBs in $\eta_{5,3,1}$ obtain couplings to W, Z, and the photon. At leading order in v/f, these all originate from just one operator [1],

$$\pi_0^i\,\epsilon^{\mu\nu\rho\sigma}\,W^i_{\mu\nu}B_{\rho\sigma} = \pi_0^i\,\epsilon^{\mu\nu\rho\sigma}\,W^i_{\mu\nu}\,(c_W A_{\rho\sigma} - s_W Z_{\rho\sigma})\,. \tag{3.66}$$

For the singly charged states, this means that the coupling to the photon is larger than the coupling to Z by a factor of $\cot\theta_W$. Furthermore, there are no couplings to WW for the η_i^0 and η_5^{++}. The latter can be relaxed when including higher order terms: With two Higgs insertions we can write

$$\frac{1}{f_\psi^2}\,\pi_+^i\,\epsilon^{\mu\nu\rho\sigma}\,W^i_{\mu\nu}W^j_{\rho\sigma}\,\tilde{H}\sigma^j\tilde{H} + \mathrm{h.c.}\,. \tag{3.67}$$

This gives a coupling of η_5^{++} to W^-W^- which is however suppressed by v^2/f_ψ^2.

The final of the purely bosonic terms in the Lagrangian is the scalar potential. It is generated by all sources of explicit breaking of the global symmetry: the gauging of the G_{SM} subgroup of H, the potential mass terms for the hyperquarks, and the incomplete spurion irreps of the quarks in the partial compositeness interactions. The potential induces the EWSB, gives masses to the pNGBs, and contains multi-pion interactions that may be important for cascade decays. We do not have the means to calculate the potential. In a previous work [108] we instead classified all operators that can contribute by means of a spurion analysis. This revealed that the number of operators and associated independent coefficients is too large for a phenomenological analysis. We will instead take the pNGB masses as free parameters in this work.

We turn to the fermion terms in the second line of Eq. (3.62). In the first term, the sum runs over all quarks and leptons and D_μ is the regular SM covariant derivative. For the composite fermions Ψ this is more complicated. We recall that the CCWZ symbol e_μ transforms like an adjoint and therefore plays the role of a generalised gauge field [16],

$$D_\mu\Psi = (\partial_\mu - i\mathbf{e}_\mu)\,\Psi = (\partial_\mu - i\tilde{g}\boldsymbol{\mathcal{V}}_\mu - c_1[\boldsymbol{\pi},\boldsymbol{\mathcal{A}}_\mu] - c_2[\boldsymbol{\pi},\partial_\mu\boldsymbol{\pi}] + \cdots)\,\Psi, \tag{3.68}$$

where we are deliberately not going into detail about the coefficients, which we will fix in the following section. For now, we note that we have a coupling with $\mathcal{V}_\mu$ acting like a regular gauge

field, along with operators containing an increasing number of pNGBs and spin-1 fields.

In $\mathcal{L}_{\rm der}$ we have the derivative couplings, so called because they couple two top partners to a derivative of a pNGB at leading order. For the present case,

$$\mathcal{L}_{\rm der} = ia_1\, \Psi_{\mathbf{14}}\sigma^\mu\bar{\Psi}_{\mathbf{14}}\, \mathbf{d}_\mu + ia_2\, \Psi_{\mathbf{14}}\sigma^\mu\bar{\Psi}_{\mathbf{1}}\, \mathbf{d}_\mu + \text{h.c.}\,, \tag{3.69}$$

where all index contractions are implicit. Expanding the second term to first order in π_χ yields

$$\mathcal{L}_{\rm der} \supset -\frac{ia_2}{2f_\chi}\,\mathrm{Tr}\big(\Psi_{\mathbf{14}}\sigma^\mu\bar{\Psi}_{\mathbf{1}}\,\partial_\mu\boldsymbol{\pi}_\chi\big) + \text{h.c.} \tag{3.70}$$

$$\supset \frac{ia_2}{4f_\chi}\,\Big(Q_8^a\sigma^\mu\bar{Q}_1\,\partial_\mu\pi_8^a + Q_3^c\sigma^\mu\bar{Q}_1\partial_\mu\pi_3 + Q_3\sigma^\mu\bar{Q}_1\partial_\mu\pi_3^\dagger\Big) + \text{h.c.}, \tag{3.71}$$

with

$$Q_8^a\sigma^\mu\bar{Q}_1 = \tilde{G}_u^{+,a}\sigma^\mu\bar{\tilde{h}}_u^+ + \tilde{G}_u^{0,a}\sigma^\mu\bar{\tilde{h}}_u^0 + \tilde{G}_d^{0,a}\sigma^\mu\bar{\tilde{h}}_d^0 + \tilde{G}_d^{-,a}\sigma^\mu\bar{\tilde{h}}_d^- + \tilde{g}\sigma^\mu\bar{\tilde{B}}, \tag{3.72}$$

$$Q_3\sigma^\mu\bar{Q}_1 = X_{5/3}\sigma^\mu\bar{\tilde{h}}_u^+ + X_{2/3}\sigma^\mu\bar{\tilde{h}}_u^0 + T_L\sigma^\mu\bar{\tilde{h}}_d^0 + B_L\sigma^\mu\bar{\tilde{h}}_d^- + T_R\sigma^\mu\tilde{B}. \tag{3.73}$$

We note that the d-symbol also contains the axial vectors, leading to operators like

$$\mathrm{Tr}\big(\Psi_{\mathbf{14}}\sigma^\mu\bar{\Psi}_{\mathbf{14}}\boldsymbol{\mathcal{A}}_\mu\big) \supset \alpha_1 Q_3\sigma_\mu\bar{Q}_3\mathcal{A}_8^\mu \tag{3.74}$$

coupling two triplet top partners to the axial octet. More details about the derivative couplings can be found in [108].

Finally, we discuss the partial compositeness interactions in $\mathcal{L}_{\rm mix}$. For the chosen embeddings, we have

$$\mathcal{L}_{\rm mix} = -\lambda_L\mathcal{O}_{\mathbf{14}}\zeta_L - \lambda'_L\mathcal{O}_{\mathbf{1}}\zeta_L - \lambda_R\mathcal{O}_{\mathbf{14}}\zeta_R^c - \lambda'_R\mathcal{O}_{\mathbf{1}}\zeta_R^c + \text{h.c.}, \tag{3.75}$$

which are readily expanded to [107]

$$\mathcal{O}_{\mathbf{14}}\zeta_L = \frac{1}{2}Q_3^c\xi_L - \frac{i}{\sqrt{2}f_\chi}\pi_3^\dagger\boldsymbol{Q}_8\xi_L - \frac{i}{\sqrt{2}f_\chi}Q_3^c\boldsymbol{\pi}_8\xi_L + \mathcal{O}(\pi_\psi,\pi_\chi^2), \tag{3.76}$$

$$\mathcal{O}_{\mathbf{1}}\zeta_L = \frac{i}{f_\chi}\pi_3^\dagger\xi_L Q_1 + \mathcal{O}(\pi_\psi,\pi_\chi^2), \tag{3.77}$$

$$\mathcal{O}_{\mathbf{14}}\zeta_R^c = \frac{1}{2}\xi_R^c Q_3 - \frac{i}{\sqrt{2}f_\chi}\xi_R^c\boldsymbol{Q}_8\pi_3 - \frac{i}{\sqrt{2}f_\chi}\xi_R^c\boldsymbol{\pi}_8 Q_3 + \mathcal{O}(\pi_\psi,\pi_\chi^2), \tag{3.78}$$

$$\mathcal{O}_{\mathbf{1}}\zeta_R^c = \frac{i}{f_\chi}\pi_3\xi_R^c Q_1 + \mathcal{O}(\pi_\psi,\pi_\chi^2). \tag{3.79}$$

The SO(5) products are

$$Q_3^c \xi_L = T_L^c t_L + B_L^c b_L, \qquad Q_8 \xi_L = \tilde{G}_u^+ b_L - \tilde{G}_u^0 t_L, \qquad \xi_L Q_1 = \tilde{h}_u^+ b_L - \tilde{h}_u^0 t_L, \tag{3.80}$$

$$\xi_R^c Q_3 = t_R^c T_R, \qquad \zeta_R^c Q_8 = t_R^c \tilde{g}, \qquad \xi_R^c Q_1 = t_R^c \tilde{B}, \tag{3.81}$$

in the limit $\theta \to 0$. We see that the desired mixing terms between elementary quarks and top partners are indeed generated. The terms with one pNGB are phenomenologically important as well: the third term in Eq. (3.76) for example includes $T_L^c \pi_8 t_L$, which induces the decay $\pi_8 \to t\bar{t}$ after mixing. The EW pNGBs obtain couplings to third generation quarks analogously.

3.3.3 Baryon or lepton number violation

If the colour triplet pNGB is heavier than at least some of the top partners, it can decay into them as well as a quark, e.g. $\pi_3 \to t\tilde{B}$. We studied this case in detail in [107] and there are hints from holographic calculations suggesting that the coloured pNGBs may be rather heavy [80,81]. In this section we instead consider the case where the π_3 is the lightest state, expanding on the brief discussion in [107]. Looking at the Lagrangian in the previous section, there is then no decay channel for the π_3. Being a colour triplet, it can however not be stable. This forces us to include either baryon or lepton number violating terms — but not both to avoid proton decay.

Beginning with baryon number violation, the simplest possibility would be

$$\mathcal{L}_{\Delta B} = c_{\Delta B}\, \pi_3 bs + \text{h.c.} = c_{\Delta B}\, \epsilon_{ijk}\, \pi_{3,i} b_j s_k + \text{h.c.} \tag{3.82}$$

with the bottom b and the strange quark s. By writing out the colour indices we see why we cannot couple $\pi_3 bb$: the operator is antisymmetric in the colour indices. We could have chosen any combination of two different down-type quarks but decided on the heaviest states in analogy to the partial compositeness couplings.

While the baryon number violating terms were added ad hoc, the lepton number violation can be incorporated in a much more comprehensive manner. We recall that the singlet top partners contain a $(\tilde{h}_d^0, \tilde{h}_d^-) \in \mathbf{2}_{-1/2}$ and a $\tilde{B} \in \mathbf{1}_0$, which can be interpreted as partners of the lepton doublet and a right handed neutrino, respectively. We can use this to write down partial compositeness interactions for the third generation leptons $\ell_L = (\nu, \tau_L^-)$. To this end, we embed the leptons analogously to the quarks,

$$\xi_\ell = (\tau_L^-, -\nu, 0, 0, 0)^T, \qquad \zeta_\ell = \xi_\ell \Sigma_{\chi,0} \tag{3.83}$$

and we can write

$$\mathcal{L}_{\Delta L} = -\lambda_\ell\, \mathcal{O}_{\mathbf{1}} \zeta_\ell + \text{h.c.} \tag{3.84}$$

$$= 6\lambda_\ell \left(-\tilde{h}_u^+ \tau_L^- + s_{\theta/2}^2\, \tilde{h}_d^0 \nu + c_{\theta/2}^2 \tilde{h}_u^0 \nu - \frac{s_\theta}{\sqrt{2}}\, \tilde{B}\nu + \text{h.c.} \right) + \mathcal{O}(\pi_\psi) + \text{h.c.}\,. \tag{3.85}$$

Combining this with the composite sector mass term[4]

$$-\frac{1}{2}M_1\, Q_1 Q_1 = M_1(\tilde{h}_u^0\tilde{h}_d^0 - \tilde{h}_u^+\tilde{h}_d^-) + \frac{1}{2}M_1\tilde{B}\tilde{B}, \tag{3.86}$$

we get the mass matrices

$$\frac{1}{2}(\nu, \tilde{B}, \tilde{h}_u^0, \tilde{h}_d^0)\begin{pmatrix} 0 & \frac{3}{\sqrt{2}}\lambda_\ell s_\theta & 6\lambda_\ell c_{\theta/2}^2 & 6\lambda_\ell s_{\theta/2}^2 \\ \frac{3}{\sqrt{2}}\lambda_\ell s_\theta & M_1 & 0 & 0 \\ 6\lambda_\ell c_{\theta/2}^2 & 0 & 0 & M_1 \\ 6\lambda_\ell s_{\theta/2}^2 & 0 & M_1 & 0 \end{pmatrix}\begin{pmatrix} \nu \\ \tilde{B} \\ \tilde{h}_u^0 \\ \tilde{h}_d^0 \end{pmatrix} - (\tilde{h}_u^+)\Big(6\lambda_\ell, M_1\Big)\begin{pmatrix} \tau_L^- \\ \tilde{h}_d^- \end{pmatrix}. \tag{3.87}$$

In the charged sector we get a massless Weyl spinor (the physical τ_L) and a massive Dirac spinor with mass $\sqrt{M_1^2 + 36\lambda_\ell^2}$. The neutral mass matrix also yields one Dirac state with the same mass (up to $\mathcal{O}(\theta^2)$) and two Majorana states:

$$m = 0 + \mathcal{O}(\theta^2): \qquad \hat{\nu}_L = \mathcal{N}_L\left(-\frac{M_1}{6\lambda_\ell}\nu_L + \frac{\theta}{2\sqrt{2}}\tilde{B} + \tilde{h}_d^0 + \mathcal{O}(\theta^2)\right), \tag{3.88}$$

$$m = M_1: \qquad \hat{\nu}_R = \mathcal{N}_R\left(\left(-\frac{2\sqrt{2}}{\theta} - \frac{\sqrt{2}\theta}{3}\right)\tilde{B} + \tilde{h}_u^0 + \tilde{h}_d^0 + \mathcal{O}(\theta^2)\right), \tag{3.89}$$

which we identify as the left- and right-handed neutrinos, respectively. Coming back to the issue of decay channels for the π_3, if we take into account the $(T_L, B_L) \leftrightarrow (t_L, b_L)$ mixing and the mixing in the lepton sector, then Eq. (3.71) induces

$$\pi_3 \to t\bar{\nu},\, b\tau^+, \tag{3.90}$$

which violates lepton number by one unit.

3.4 Calculation of the colour sector spin-1 resonances

Having gained an overview of the Lagrangian of the model M5 in the previous section, we now focus on a specific sector. We would like to calculate the terms that are relevant for the phenomenology of the coloured spin-1 resonances, which are (mostly) contained in $\mathcal{L}_{\text{h.s.}}^{\text{colour}}$, the colour sector hidden symmetry Lagrangian. Over the course of this calculation we work with the SU(6)/Sp(6) coset of M5, but the results can easily be extended to the other cosets, which we will discuss at the end of this section. This section is based on [3].

We briefly recap the setup: we extend the global symmetry to $\mathrm{SU}(6)_0 \times \mathrm{SU}(6)_1$ which gets broken to $\mathrm{Sp}(6)_0 \times \mathrm{Sp}(6)_1$ by two sets of pNGBs $\pi_{0,1}$. After a further breaking step mediated by NGBs k, the remaining symmetry group is the diagonal Sp(6). In terms of the Goldstone

[4] In principle, one could introduce a mass split between the underlying doublet and singlet hyperquarks [105], which would lead to a mass split between the $\tilde{h}$ and B. For simplicity we neglect this at this point.

matrix K of the k, their kinetic term reads

$$\operatorname{Tr} D_\mu K (D^\mu K)^\dagger, \qquad D_\mu K = \partial_\mu K - i\mathbf{e}_{0,\mu} K + iK\mathbf{e}_{1,\mu}. \tag{3.91}$$

The k are would-be NGBs that give mass to the $\mathcal{V}_\mu$. Thus, in unitary gauge we have $K = \mathbb{1}$, and the kinetic term simplifies to

$$\operatorname{Tr} D_\mu K (D^\mu K)^\dagger = \operatorname{Tr} \mathbf{e}_{0,\mu}\mathbf{e}_0^\mu + \operatorname{Tr} \mathbf{e}_{1,\mu}\mathbf{e}_1^\mu - 2\operatorname{Tr} \mathbf{e}_{0,\mu}\mathbf{e}_1^\mu. \tag{3.92}$$

With this, the hidden symmetry Lagrangian Eq. (2.55) is given by

$$\begin{aligned}\mathcal{L} = &-\frac{1}{2}\operatorname{Tr}\mathbf{G}_{\mu\nu}\mathbf{G}^{\mu\nu} - \frac{1}{2}\operatorname{Tr}\mathbf{B}_{\mu\nu}\mathbf{B}^{\mu\nu} - \frac{1}{2}\operatorname{Tr}\boldsymbol{\mathcal{F}}_{\mu\nu}\boldsymbol{\mathcal{F}}^{\mu\nu} \\ &+ \frac{f_0^2}{2}\operatorname{Tr}\mathbf{d}_{0,\mu}\mathbf{d}_0^\mu + \frac{f_1^2}{2}\operatorname{Tr}\mathbf{d}_{1,\mu}\mathbf{d}_1^\mu + r f_1^2\ \operatorname{Tr}\mathbf{d}_{0,\mu}\mathbf{d}_1^\mu \\ &+ \frac{f_K^2}{2}\operatorname{Tr}\mathbf{e}_{0,\mu}\mathbf{e}_0^\mu + \frac{f_K^2}{2}\operatorname{Tr}\mathbf{e}_{1,\mu}\mathbf{e}_1^\mu - f_K^2\operatorname{Tr}\mathbf{e}_{0,\mu}\mathbf{e}_1^\mu.\end{aligned} \tag{3.93}$$

From Eqs. (2.21) and (2.22) we have in the composite sector

$$\mathbf{d}_{1,\mu} = \tilde{g}\boldsymbol{\mathcal{A}}_\mu - \frac{\sqrt{2}}{f_1}D_\mu\boldsymbol{\pi}_1 - \frac{\tilde{g}}{f_1^2}[\boldsymbol{\pi}_1,[\boldsymbol{\pi}_1,\boldsymbol{\mathcal{A}}_\mu]] + \frac{\sqrt{2}}{3f_1^3}[\boldsymbol{\pi}_1,[\boldsymbol{\pi}_1,\partial_\mu\boldsymbol{\pi}_1]] + \cdots, \tag{3.94}$$

$$\mathbf{e}_{1,\mu} = \tilde{g}\boldsymbol{\mathcal{V}}_\mu - \frac{\sqrt{2}i\tilde{g}}{f_1}[\boldsymbol{\pi},\boldsymbol{\mathcal{A}}_\mu] + \frac{i}{f_1^2}[\boldsymbol{\pi}_1,\partial_\mu\boldsymbol{\pi}_1] - \frac{\tilde{g}}{f_1^2}[\boldsymbol{\pi}_1,[\boldsymbol{\pi}_1,\boldsymbol{\mathcal{V}}_\mu]] + \cdots, \tag{3.95}$$

where

$$D_\mu\boldsymbol{\pi}_1 = \partial_\mu\boldsymbol{\pi}_1 - i\tilde{g}[\boldsymbol{\mathcal{V}}_\mu,\boldsymbol{\pi}_1]. \tag{3.96}$$

In the elementary sector we do not have axial vectors, and the vector states are

$$\mathbf{V}_\mu = \hat{g}_s\mathbf{G}_\mu + \hat{g}'\mathbf{B}_\mu, \tag{3.97}$$

where the hats on the couplings are there to remind us that these are not the physical $\mathrm{SU}(3)_c$ and $\mathrm{U}(1)_Y$ gauge couplings, as we will see below. With this, the CCWZ symbols of the elementary sector are

$$\mathbf{d}_{0,\mu} = -\frac{\sqrt{2}}{f_0}D_\mu\boldsymbol{\pi}_0 + \frac{\sqrt{2}}{3f_0^3}[\boldsymbol{\pi}_0,[\boldsymbol{\pi}_0,\partial_\mu\boldsymbol{\pi}_0]] + \cdots, \tag{3.98}$$

$$\mathbf{e}_{0,\mu} = \hat{g}_s\mathbf{G}_\mu + \hat{g}'\mathbf{B}_\mu + \frac{i}{f_0^2}[\boldsymbol{\pi}_0,\partial_\mu\boldsymbol{\pi}_0] - \frac{1}{f_0^2}[\boldsymbol{\pi}_0,[\boldsymbol{\pi}_0,\hat{g}_s\mathbf{G}_\mu + \hat{g}'\mathbf{B}_\mu]] + \cdots. \tag{3.99}$$

Now we have all the pieces in place to expand Eq. (3.93) and explore its consequences.

3.4.1 Masses and mixing of the spin-1 states

As a first step we determine the physical spin-1 states. To this end, we look for all terms in the Lagrangian that can give us contributions to the mass matrices. This is straightforward for the axial vectors,

$$\frac{f_1^2}{2}\,\mathrm{Tr}\,\mathbf{d}_{1,\mu}\mathbf{d}_1^\mu \supset \frac{\tilde{g}^2 f_1^2}{2}\,\mathrm{Tr}(\boldsymbol{\mathcal{A}}_\mu\boldsymbol{\mathcal{A}}^\mu) = \frac{1}{2}m_{\mathcal{A}}^2\,\mathcal{A}_\mu^I\mathcal{A}^{I,\mu} \tag{3.100}$$

with

$$m_{\mathcal{A}} = \frac{\tilde{g}f_1}{\sqrt{2}}. \tag{3.101}$$

For the vector states we look at the e^2 terms,

$$\mathrm{Tr}(\mathbf{e}_{0,\mu}\mathbf{e}_0^\mu) \supset \hat{g}_s^2\,\mathrm{Tr}(\mathbf{G}_\mu\mathbf{G}^\mu) + \hat{g}'^2\,\mathrm{Tr}(\mathbf{B}_\mu\mathbf{B}^\mu) = \frac{1}{2}\hat{g}_s^2 G_\mu^a G^{\mu,a} + \frac{1}{2}\hat{g}'^2 B_\mu B^\mu, \tag{3.102}$$

$$\mathrm{Tr}(\mathbf{e}_{1,\mu}\mathbf{e}_1^\mu) \supset \tilde{g}^2\,\mathrm{Tr}(\boldsymbol{\mathcal{V}}_\mu\boldsymbol{\mathcal{V}}^\mu) = \frac{1}{2}\tilde{g}^2\mathcal{V}_\mu^a\mathcal{V}^{a,\mu}, \tag{3.103}$$

$$\mathrm{Tr}(\mathbf{e}_{0,\mu}\mathbf{e}_1^\mu) \supset \mathrm{Tr}((g_s\mathbf{G}_\mu + g'\mathbf{B}_\mu)\tilde{g}\boldsymbol{\mathcal{V}}^\mu) = \frac{1}{2}\hat{g}_s\tilde{g}\,G_\mu^a\mathcal{V}_8^{a,\mu} + \frac{1}{2}\hat{g}'\tilde{g}\,B_\mu\mathcal{V}_1^\mu. \tag{3.104}$$

In Eq. (3.103) we can split the $\mathcal{V}_\mu^a$ into

$$\mathcal{V}_\mu^a\mathcal{V}^{a,\mu} = \mathcal{V}_{8,\mu}^a\mathcal{V}_8^{a,\mu} + \mathcal{V}_{1,\mu}\mathcal{V}_1^\mu + 2\mathcal{V}_{6,\mu}^c\mathcal{V}_6^\mu \tag{3.105}$$

from which we can immediately read off

$$m_{\mathcal{V}_6} = \frac{\tilde{g}f_K}{\sqrt{2}}. \tag{3.106}$$

For the colour octet and singlet, Eq. (3.104) represents a mixing term, which leads to the octet mass term

$$\frac{1}{2}V_{8,\mu}^{a,T}\,\mathcal{M}_8^2\,V_8^{a,\mu}, \qquad V_{8,\mu}^a = \begin{pmatrix} G_\mu^a \\ \mathcal{V}_{8,\mu}^a \end{pmatrix}, \qquad \mathcal{M}_8^2 = \frac{f_K^2}{2}\begin{pmatrix} \hat{g}_s^2 & -\hat{g}_s\tilde{g} \\ -\hat{g}_s\tilde{g} & \tilde{g}^2 \end{pmatrix}. \tag{3.107}$$

The eigenvalues and -vectors of the mass matrix are

$$m_G = 0: \qquad \frac{1}{\sqrt{\tilde{g}^2+\hat{g}_s^2}}\begin{pmatrix}\tilde{g}\\ \hat{g}_s\end{pmatrix} \equiv \begin{pmatrix}\cos\beta_8\\ \sin\beta_8\end{pmatrix}, \tag{3.108}$$

$$m_{\mathcal{V}_8} = \frac{f_K}{\sqrt{2}}\sqrt{\tilde{g}^2+\hat{g}_s^2}: \quad \frac{1}{\sqrt{\tilde{g}^2+\hat{g}_s^2}}\begin{pmatrix}-\hat{g}_s\\ \tilde{g}\end{pmatrix} \equiv \begin{pmatrix}-\sin\beta_8\\ \cos\beta_8\end{pmatrix}, \tag{3.109}$$

and we identify the massless state with the physical gluon. We will show just below that the physical strong coupling g_s is given by

$$g_s = \hat{g}_s \cos\beta_8 = \tilde{g} \sin\beta_8. \tag{3.110}$$

With a slight abuse of notation we can switch to the physical mass eigenstates by replacing

$$\begin{pmatrix} G^a_\mu \\ \mathcal{V}^a_{8,\mu} \end{pmatrix} \to \begin{pmatrix} \cos\beta_8 & -\sin\beta_8 \\ \sin\beta_8 & \cos\beta_8 \end{pmatrix} \begin{pmatrix} G^a_\mu \\ \mathcal{V}^a_{8,\mu} \end{pmatrix}. \tag{3.111}$$

In principle the same analysis can be repeated for the colour singlet states. However, there will be further contributions to that mixing from the EW sector [73], and a combined calculation is required for reliable results. We leave that for future work.

3.4.2 Couplings to quarks

The vector octet plays a special role for the phenomenology due to its mixing with the gluon. To see why, we consider the kinetic terms of the quarks:

$$\mathcal{L} \supset i\bar{q}\not{D}q \supset \hat{g}_s\, \bar{q}\, \not{G}^a t^a_{\mathbf{3}}\, q \xrightarrow{\text{phys}} \hat{g}_s \cos\beta_8\, \bar{q}\, \not{G}^a t^a_{\mathbf{3}}\, q - \hat{g}_s \sin\beta_8\, \bar{q}\, \not{\mathcal{V}}^a_8 t^a_{\mathbf{3}}\, q \tag{3.112}$$

where a sum over q is implied. We can read off Eq. (3.110) from the first term after the mixing since the physical gluon has to couple to the quarks with the physical g_s. The second term couples the heavy vector to two quarks with the prefactor

$$C_{qq} = -\hat{g}_s \sin\beta_8 = -g_s \tan\beta_8 \tag{3.113}$$

independent of the quark family. In particular, this couples the $\mathcal{V}_8$ to two light quarks, thus opening up the Drell-Yan single production channel. Generally, the single production cross section falls off much slower with mass than for pair production. The LHC phenomenology of the model will therefore be dominated by the single production of $\mathcal{V}_8$.

3.4.3 Couplings to gluons

Despite the prominence of $\mathcal{V}_8$ single production, we now turn to the kinetic terms of the vectors to calculate the couplings relevant for pair production. The reason is that while pair production of vectors will likely be out of reach at the LHC, these couplings are interesting for a study at future colliders. We begin with

$$\mathcal{L} \supset -\frac{1}{2} \operatorname{Tr} \mathbf{G}_{\mu\nu} \mathbf{G}^{\mu\nu} - \frac{1}{2} \operatorname{Tr} \boldsymbol{\mathcal{V}}_{\mu\nu} \boldsymbol{\mathcal{V}}^{\mu\nu} \tag{3.114}$$

where we need

$$\boldsymbol{\mathcal{V}}_{\mu\nu} = \partial_\mu \boldsymbol{\mathcal{V}}_\nu - \partial_\nu \boldsymbol{\mathcal{V}}_\mu - \sqrt{2} i\tilde{g}[\boldsymbol{\mathcal{V}}_\mu, \boldsymbol{\mathcal{V}}_\nu] \tag{3.115}$$

to keep the normalisation fixed, see Appendix A for details. At $\mathcal{O}(g^0)$ we have the abelian kinetic terms

$$\mathcal{L}_{g^0} = -\frac{1}{4}(\partial_\mu G^a_\nu - \partial_\nu G^a_\mu)^2 - \frac{1}{4}(\partial_\mu \mathcal{V}^a_{8,\nu} - \partial_\nu \mathcal{V}^a_{8,\mu})^2 - \frac{1}{2}\left|\partial_\mu \mathcal{V}_{6,\nu,s} - \partial_\nu \mathcal{V}_{6,\mu,s}\right|^2 . \tag{3.116}$$

At order $\mathcal{O}(g^1)$ each term comes with one derivative of a vector,

$$\begin{aligned}\mathcal{L}_g = &-\frac{1}{2}\hat{g}_s\, f^{abc}\,(\partial_\mu G^a_\nu - \partial_\nu G^a_\mu)\, G^b_\mu G^c_\nu \\ &+2i\tilde{g}\Big[(\partial_\mu \mathcal{V}^a_{8,\nu} - \partial_\nu \mathcal{V}^a_{8,\mu})\mathcal{V}^{b,\mu}_8 \mathcal{V}^{c,\nu}_8 \operatorname{Tr}\big(t^a_{\mathbf{3}} t^b_{\mathbf{3}} t^c_{\mathbf{3}}\big) \\ &\quad + (\partial_\mu \mathcal{V}^a_{8,\nu} - \partial_\nu \mathcal{V}^a_{8,\mu})\mathcal{V}^\mu_{6,s}\mathcal{V}^{c\nu}_{6,t} \operatorname{Tr}\big(t^a_{\mathbf{3}} K^s K^t\big) \\ &\quad + \big((\partial_\mu \mathcal{V}_{6,\nu,s} - \partial_\nu \mathcal{V}_{6,\mu,s})\mathcal{V}^{c\mu}_{6,t}\mathcal{V}^{a,\nu}_8 \operatorname{Tr}\big(K^s K^t t^a_{\mathbf{3}}\big) + \text{h.c.}\big)\Big],\end{aligned} \tag{3.117}$$

where from Appendix A we have

$$\operatorname{Tr}\big(t^a_{\mathbf{3}} t^b_{\mathbf{3}} t^c_{\mathbf{3}}\big) = \frac{1}{4}(d^{abc} + i f^{abc}), \qquad \operatorname{Tr}\big(K^s K^t t^a_{\mathbf{3}}\big) = \frac{1}{2}[t^a_{\mathbf{6}}]^{ts}. \tag{3.118}$$

Taking a closer look at the $\mathcal{V}_8^3$ term,

$$\begin{aligned} d^{abc}(\partial_\mu \mathcal{V}^a_{8,\nu} - \partial_\nu \mathcal{V}^a_{8,\mu})\mathcal{V}^{b,\mu}_8 \mathcal{V}^{c,\nu}_8 &= d^{abc}\partial_\mu \mathcal{V}^a_{8,\nu}\mathcal{V}^{b,\mu}_8 \mathcal{V}^{c,\nu}_8 - d^{abc}\partial_\mu \mathcal{V}^a_{8,\nu}\mathcal{V}^{b,\nu}_8 \mathcal{V}^{c,\mu}_8 && (3.119)\\ &= d^{abc}\partial_\mu \mathcal{V}^a_{8,\nu}\mathcal{V}^{b,\mu}_8 \mathcal{V}^{c,\nu}_8 - d^{abc}\partial_\mu \mathcal{V}^a_{8,\nu}\mathcal{V}^{c,\nu}_8 \mathcal{V}^{b,\mu}_8 = 0, && (3.120)\end{aligned}$$

we see that due to symmetry only the f^{abc} contributes, leaving us with

$$\begin{aligned}\mathcal{L}_g = &-\frac{1}{2}\hat{g}_s\, f^{abc}\,(\partial_\mu G^a_\nu - \partial_\nu G^a_\mu)\, G^b_\mu G^c_\nu - \frac{1}{2}\tilde{g}\, f^{abc}\,(\partial_\mu \mathcal{V}^a_{8,\nu} - \partial_\nu \mathcal{V}^a_{8,\mu})\mathcal{V}^{b,\mu}_8 \mathcal{V}^{c,\nu}_8 \\ &+ \tilde{g}\Big[i(\partial_\mu \mathcal{V}^a_{8,\nu} - \partial_\nu \mathcal{V}^a_{8,\mu})\mathcal{V}^\mu_{6,s}\mathcal{V}^{c\nu}_{6,t}\,[t^a_{\mathbf{6}}]^{ts} + \big(i(\partial_\mu \mathcal{V}_{6,\nu,s} - \partial_\nu \mathcal{V}_{6,\mu,s})\mathcal{V}^{c\mu}_{6,t}\mathcal{V}^{a,\nu}_8\,[t^a_{\mathbf{6}}]^{ts} + \text{h.c.}\big)\Big].\end{aligned} \tag{3.121}$$

Lastly, we have the quartic terms at $\mathcal{O}(g^2)$ where we find

$$\begin{aligned}\mathcal{L}_{g^2} = &-\frac{\hat{g}_s^2}{4}\, f^{abc} f^{ade}\, G^b_\mu G^c_\nu G^{d,\mu} G^{e,\nu} - \frac{\tilde{g}^2}{4}\, f^{abe} f^{cde}\, \mathcal{V}^a_{8,\mu}\mathcal{V}^b_{8,\nu}\mathcal{V}^{c,\mu}_8\mathcal{V}^{d,\nu}_8 && (3.122)\\ &+ \tilde{g}^2\Big[i\,\mathcal{V}^a_{8,\mu}\mathcal{V}^b_{8,\nu}\mathcal{V}^\mu_{6,s}\mathcal{V}^{c\nu}_{6,t}\, f^{abd}\,[t^d_{\mathbf{6}}]^{ts} + (\mathcal{V}^c_{6,\mu,t}\mathcal{V}^a_{8,\nu} - \mathcal{V}^c_{6,\nu,t}\mathcal{V}^a_{8,\mu})\mathcal{V}^\mu_{6,s}\mathcal{V}^{b,\nu}_8\,[t^b_{\mathbf{6}} t^a_{\mathbf{6}}]^{ts}\Big]. && (3.123)\end{aligned}$$

So far we have written the Lagrangians in terms of the purely elementary and composite fields. The next step is to transform the octets to the physical fields by means of Eq. (3.111). For simplicity we limit ourselves to the terms of up to two heavy vectors. The $\mathcal{O}(g^0)$ Lagrangian

remains unaffected, of course. At linear order we find

$$\begin{aligned}\mathcal{L}_g \xrightarrow{\text{phys}} &-\frac{1}{2}g_s\, f^{abc}\,(\partial_\mu G^a_\nu - \partial_\nu G^a_\mu)G^{b,\mu}G^{c,\nu}\\ &-\frac{1}{2}g_s\, f^{abc}\,(\partial_\mu G^a_\nu - \partial_\nu G^a_\mu)\mathcal{V}_8^{b,\mu}\mathcal{V}_8^{c,\nu} - g_s f^{abc}(\partial_\mu \mathcal{V}^a_{8,\nu} - \partial_\nu \mathcal{V}^a_{8,\mu})G^{b,\mu}\mathcal{V}_8^{c,\nu}\\ &+ ig_s(\partial_\mu G^a_\nu - \partial_\nu G^a_\mu)\mathcal{V}^\mu_{6,s}\mathcal{V}^{c\nu}_{6,t}\,[t^a_{\mathbf{6}}]^{ts} + g_s\big(i(\partial_\mu \mathcal{V}_{6,\nu,s} - \partial_\nu \mathcal{V}_{6,\mu,s})\mathcal{V}^{c\mu}_{6,t}G^{a,\nu}[t^a_{\mathbf{6}}]^{ts} + \text{h.c.}\big).\end{aligned} \tag{3.124}$$

Note that the contributions to the $\mathcal{V}_8$-G-G coupling cancel. This means there will be no $gg \to \mathcal{V}_8$ contribution to the single production. Finally, the $\mathcal{O}(g^2)$ terms become

$$\mathcal{L}_{g^2} \xrightarrow{\text{phys}} -\frac{g_s^2}{4}\, f^{abc}f^{ade}\, G^b_\mu G^c_\nu G^{d,\mu}G^{e,\nu} \tag{3.125}$$

$$\begin{aligned}&-\frac{g_s^2}{2}\, f^{abe}f^{cde}\left(G^a_\mu G^b_\nu \mathcal{V}_8^{c,\mu}\mathcal{V}_8^{d,\nu} + G^a_\mu \mathcal{V}^b_{8,\nu}G^{c,\mu}\mathcal{V}_8^{d,\nu} + G^a_\mu \mathcal{V}^b_{8,\nu}\mathcal{V}_8^{c,\mu}G^{d,\nu}\right)\\ &+ ig_s^2\, G^a_\mu G^b_\nu \mathcal{V}^\mu_{6,s}\mathcal{V}^{c\nu}_{6,t}\, f^{abd}\,[t^d_{\mathbf{6}}]^{ts} + g_s^2(\mathcal{V}^c_{6,\mu,t}G^a_\nu - \mathcal{V}^c_{6,\nu,t}G^a_\mu)\mathcal{V}^\mu_{6,s}G^{b,\nu}\,[t^b_{\mathbf{6}}t^a_{\mathbf{6}}]^{ts}.\end{aligned} \tag{3.126}$$

We note that couplings $G\mathcal{V}_8^3$ also exist,

$$\mathcal{L}_{g^2} \supset -\frac{1}{2}g_s(\tilde{g}c_8^3 - \hat{g}_s s_8^3)\, f^{abe}f^{cde}\left(G^a_\mu \mathcal{V}^b_{8,\nu}\mathcal{V}_8^{c,\mu}\mathcal{V}_8^{d,\nu} + \mathcal{V}^a_{8,\mu}G^b_\nu \mathcal{V}_8^{c,\mu}\mathcal{V}_8^{d,\nu}\right), \tag{3.127}$$

where the coupling is not fixed by gauge invariance but dependens on $\tilde{g}$ [109].

3.4.4 Identifying the physical pNGBs

Before we can calculate the couplings of the vectors to the pNGBs, we need to determine the physical scalars. To this end we turn to the d-symbols since

$$\mathbf{d}_{i,\mu} = -\frac{\sqrt{2}}{f_i}D_\mu \boldsymbol{\pi}_i + \cdots . \tag{3.128}$$

The $d_{i,\mu}$ appear squared in the Lagrangian as

$$\mathcal{L} = \frac{f_i^2}{2}\,\mathrm{Tr}\,\mathbf{d}_{i,\mu}\mathbf{d}_i^\mu \supset \mathrm{Tr}\, D_\mu \boldsymbol{\pi}_i D^\mu \boldsymbol{\pi}_i \tag{3.129}$$

and as a mixing term

$$\mathcal{L} \supset r f_1^2\,\mathrm{Tr}\,\mathbf{d}_{0,\mu}\mathbf{d}_1^\mu \supset 2r\frac{f_1}{f_0}\,\mathrm{Tr}\, D_\mu \boldsymbol{\pi}_0 D^\mu \boldsymbol{\pi}_1. \tag{3.130}$$

All in all we have

$$\mathcal{L} \supset \mathrm{Tr}\left(D_\mu \boldsymbol{\pi}_0 D^\mu \boldsymbol{\pi}_0 + D_\mu \boldsymbol{\pi}_1 D^\mu \boldsymbol{\pi}_1 + 2r\frac{f_1}{f_0}D_\mu \boldsymbol{\pi}_0 D^\mu \boldsymbol{\pi}_1\right) \tag{3.131}$$

$$\equiv \mathrm{Tr}(D_\mu \boldsymbol{\pi}_A D^\mu \boldsymbol{\pi}_A + D_\mu \boldsymbol{\pi}_B D^\mu \boldsymbol{\pi}_B). \tag{3.132}$$

In the second line we have introduced decoupled and canonically normalised fields π_A and π_B, which are given by

$$\pi_0 = \frac{\pi_A}{\sqrt{2}\sqrt{1 + r\, f_1/f_0}} - \frac{\pi_B}{\sqrt{2}\sqrt{1 - r\, f_1/f_0}}, \tag{3.133}$$

$$\pi_1 = \frac{\pi_A}{\sqrt{2}\sqrt{1 + r\, f_1/f_0}} + \frac{\pi_B}{\sqrt{2}\sqrt{1 - r\, f_1/f_0}}. \tag{3.134}$$

The $\pi_{A,B}$ are still not the physical fields π_P, since a linear combination π_U of them is eaten by the $\mathcal{A}_\mu$. We therefore introduce another linear transformation,

$$\pi_A = \cos\alpha\, \pi_P - \sin\alpha\, \pi_U, \qquad \pi_B = \sin\alpha\, \pi_P + \cos\alpha\, \pi_U, \tag{3.135}$$

where

$$\tan\alpha = -\sqrt{\frac{1 + r\, f_1/f_0}{1 - r\, f_1/f_0}}. \tag{3.136}$$

We can combine both redefinitions into

$$\pi_0 = \pi_P \frac{1}{\sqrt{1 - R^2}}, \qquad \pi_1 = \pi_U - \pi_P \frac{R}{\sqrt{1 - R^2}} \tag{3.137}$$

with

$$R = r\frac{f_1}{f_0}. \tag{3.138}$$

The unphysical modes π_U vanish in the unitary gauge, which we will use throughout this section. The physical $\pi_P \equiv \pi$ are the usual SU(6)/Sp(6) pNGBs. Their decay constant f_χ is a combination of f_0 and f_1,

$$f_\chi = \sqrt{f_0^2 - r^2 f_1^2}. \tag{3.139}$$

3.4.5 Couplings to pNGBs

We now collect all interactions of one $\mathcal{V}_\mu$ or $\mathcal{A}_\mu$ with up to three pNGBs. It turns out that the lowest dimensional couplings are to two π for the vectors and three π for the axial vectors[5], which matches the situation in QCD. The corresponding operators can always be reduced[6] to only one independent form each,

$$\mathcal{O}_V = i\,\mathrm{Tr}([\boldsymbol{\pi}, \partial_\mu \boldsymbol{\pi}]\boldsymbol{V}^\mu), \qquad \mathcal{O}_\mathcal{A} = \mathrm{Tr}([\boldsymbol{\pi}, [\boldsymbol{\pi}, \partial_\mu \boldsymbol{\pi}]]\boldsymbol{\mathcal{A}}^\mu), \tag{3.140}$$

where $V = \mathcal{V}, G, B$ denotes a generic vector, and we introduce a factor of i so that both operators are hermitian. We take a two-step approach with the states, keeping the unphysical

[5] The operator for a $\mathcal{A}\pi\pi$ coupling would be of the form $\mathrm{Tr}\big[X^I, X^J\big]X^K \sim \mathrm{Tr}\, T^a X^K = 0$.

[6] with $\mathrm{Tr}(\partial_\mu\boldsymbol{\pi}[\boldsymbol{\pi}, \boldsymbol{V}^\mu]) = -\,\mathrm{Tr}([\boldsymbol{\pi}, \partial_\mu\boldsymbol{\pi}]\boldsymbol{V}^\mu)$ and $\mathrm{Tr}([\boldsymbol{\pi}, [\boldsymbol{\pi}, \partial\boldsymbol{\pi}]]\boldsymbol{\mathcal{A}}) = -\,\mathrm{Tr}([\boldsymbol{\pi}, \partial\boldsymbol{\pi}][\boldsymbol{\pi}, \boldsymbol{\mathcal{A}}]) = \mathrm{Tr}(\partial\boldsymbol{\pi}[\boldsymbol{\pi}, [\boldsymbol{\pi}, \boldsymbol{\mathcal{A}}]])$.

vectors for now but working with the physical pNGBs from the start. Since we work in unitary gauge, π_0 and π_1 are both proportional to the physical π, only differing in the prefactor, see Eq. (3.137). We therefore have to keep track of which sector the factors of π in Eq. (3.140) stem from,

$$\mathcal{O}_V^{k,l} = \left(\frac{1}{\sqrt{1-R^2}}\right)^k \left(-\frac{R}{\sqrt{1-R^2}}\right)^l i\,\mathrm{Tr}([\boldsymbol{\pi}, \partial_\mu \boldsymbol{\pi}]\boldsymbol{V}^\mu), \tag{3.141}$$

$$\mathcal{O}_{\mathcal{A}}^{k,l} = \left(\frac{1}{\sqrt{1-R^2}}\right)^k \left(-\frac{R}{\sqrt{1-R^2}}\right)^l \mathrm{Tr}([\boldsymbol{\pi}, [\boldsymbol{\pi}, \partial_\mu \boldsymbol{\pi}]]\boldsymbol{\mathcal{A}}^\mu). \tag{3.142}$$

With the definitions settled, we can start collecting terms. The relevant contributions originate from the d^2 and e^2 terms, and we begin with the former:

$$\frac{f_0^2}{2}\,\mathrm{Tr}(\mathbf{d}_{0,\mu}\mathbf{d}_0^\mu) \supset \mathrm{Tr}(D_\mu \boldsymbol{\pi}_0 D^\mu \boldsymbol{\pi}_0) \tag{3.143}$$

$$\supset 2i\hat{g}_s\,\mathrm{Tr}(\partial_\mu \boldsymbol{\pi}_0[\boldsymbol{\pi}_0, \mathbf{G}^\mu]) + 2i\hat{g}'\,\mathrm{Tr}(\partial_\mu \boldsymbol{\pi}_0[\boldsymbol{\pi}_0, \mathbf{B}^\mu]) \tag{3.144}$$

$$= -2\hat{g}_s\,\mathcal{O}_G^{2,0} - 2\hat{g}'\,\mathcal{O}_B^{2,0}, \tag{3.145}$$

in the elementary sector, and analogously in the composite one,

$$\begin{aligned}\frac{f_1^2}{2}\,\mathrm{Tr}(\mathbf{d}_{1,\mu}\mathbf{d}_1^\mu) &\supset 2i\tilde{g}\,\mathrm{Tr}(\partial_\mu \boldsymbol{\pi}_1[\boldsymbol{\pi}_1, \boldsymbol{\mathcal{V}}^\mu]) + \frac{\sqrt{2}\tilde{g}}{3f_1}\,\mathrm{Tr}([\boldsymbol{\pi}_1, [\boldsymbol{\pi}_1, \partial_\mu \boldsymbol{\pi}_1]]\boldsymbol{\mathcal{A}}^\mu) \\ &\quad + \frac{\sqrt{2}\tilde{g}}{f_1}\,\mathrm{Tr}(\partial_\mu \boldsymbol{\pi}_1[\boldsymbol{\pi}_1, [\boldsymbol{\pi}_1, \boldsymbol{\mathcal{A}}^\mu]])\end{aligned} \tag{3.146}$$

$$= 2i\tilde{g}\,\mathrm{Tr}(\partial_\mu \boldsymbol{\pi}_1[\boldsymbol{\pi}_1, \boldsymbol{\mathcal{V}}^\mu]) + \frac{4\sqrt{2}\tilde{g}}{3f_1}\,\mathrm{Tr}([\boldsymbol{\pi}_1, [\boldsymbol{\pi}_1, \partial_\mu \boldsymbol{\pi}_1]]\boldsymbol{\mathcal{A}}^\mu) \tag{3.147}$$

$$= -2\tilde{g}\,\mathcal{O}_{\mathcal{V}}^{0,2} + \frac{4\sqrt{2}\tilde{g}}{3f_1}\,\mathcal{O}_{\mathcal{A}}. \tag{3.148}$$

Then there is the $d_0 d_1$ mixed term,

$$rf_1^2\ \mathrm{Tr}(\mathbf{d}_{0,\mu}\mathbf{d}_1^\mu) \tag{3.149}$$

$$\begin{aligned}&\supset rf_1^2\ \mathrm{Tr}\left(\frac{2i\tilde{g}}{f_0 f_1}\partial_\mu \boldsymbol{\pi}_0[\boldsymbol{\pi}_1, \boldsymbol{\mathcal{V}}^\mu] + \frac{\sqrt{2}\tilde{g}}{f_0 f_1^2}\partial_\mu \boldsymbol{\pi}_0[\boldsymbol{\pi}_1, [\boldsymbol{\pi}_1, \boldsymbol{\mathcal{A}}^\mu]]\right. \\ &\qquad \left. - \frac{2i}{f_0 f_1}[\boldsymbol{\pi}_0, (\hat{g}_s \mathbf{G}_\mu + \hat{g}'\mathbf{B}_\mu)]\partial^\mu \boldsymbol{\pi}_1 + \frac{\sqrt{2}\tilde{g}}{3f_0^3}[\boldsymbol{\pi}_0, [\boldsymbol{\pi}_0, \partial_\mu \boldsymbol{\pi}_0]]\boldsymbol{\mathcal{A}}^\mu\right)\end{aligned} \tag{3.150}$$

$$= rf_1^2\left(-\frac{2\tilde{g}}{f_0 f_1}\,\mathcal{O}_{\mathcal{V}}^{1,1} + \frac{\sqrt{2}\tilde{g}}{f_0 f_1^2}\,\mathcal{O}_{\mathcal{A}}^{1,2} + \frac{2\hat{g}_s}{f_0 f_1}\,\mathcal{O}_G^{1,1} + \frac{2\hat{g}'}{f_0 f_1}\,\mathcal{O}_B^{1,1} + \frac{\sqrt{2}\tilde{g}}{3f_0^3}\,\mathcal{O}_{\mathcal{A}}^{3,0}\right). \tag{3.151}$$

The remaining contributions come from e^2-terms, with

$$\frac{f_K^2}{2}\,\mathrm{Tr}(\mathbf{e}_{0,\mu}\mathbf{e}_0^\mu) \supset \frac{f_K^2}{2f_0^2}\,\mathrm{Tr}(2i(\hat{g}_s \mathbf{G}_\mu + \hat{g}'\mathbf{B}_\mu)[\boldsymbol{\pi}_0, \partial^\mu \boldsymbol{\pi}_0]) = \frac{f_K^2}{f_0^2}\left(\hat{g}_s\,\mathcal{O}_G^{2,0} + \hat{g}'\,\mathcal{O}_B^{2,0}\right) \tag{3.152}$$

in the elementary sector,

$$\frac{f_K^2}{2}\operatorname{Tr}(\mathbf{e}_{1,\mu}\mathbf{e}_1^\mu) \supset \frac{f_K^2}{2f_1^2}\operatorname{Tr}\left(2i\tilde{g}\boldsymbol{\mathcal{V}}_\mu[\boldsymbol{\pi}_1,\partial^\mu\boldsymbol{\pi}_1]+\frac{2\sqrt{2}\tilde{g}}{f_1}[\boldsymbol{\pi}_1,\partial_\mu\boldsymbol{\pi}_1][\boldsymbol{\pi}_1,\boldsymbol{\mathcal{A}}^\mu]\right) \tag{3.153}$$

$$=\frac{f_K^2}{f_1^2}\left(\tilde{g}\,\mathcal{O}_{\mathcal{V}}^{0,2}-\frac{\sqrt{2}\tilde{g}}{f_1}\,\mathcal{O}_{\mathcal{A}}^{0,3}\right) \tag{3.154}$$

in the composite sector, and

$$-f_K^2\operatorname{Tr}(\mathbf{e}_{0,\mu}\mathbf{e}_1^\mu) \supset -f_K^2\operatorname{Tr}\left(\frac{i}{f_1^2}\mathbf{V}_\mu[\boldsymbol{\pi}_1,\partial_\mu\boldsymbol{\pi}_1]+\frac{i\tilde{g}}{f_0^2}[\boldsymbol{\pi}_0,\partial_\mu\boldsymbol{\pi}_0]\boldsymbol{\mathcal{V}}^\mu+\frac{\sqrt{2}\tilde{g}}{f_0^2f_1}[\boldsymbol{\pi}_0,\partial_\mu\boldsymbol{\pi}_0][\boldsymbol{\pi}_1,\boldsymbol{\mathcal{A}}^\mu]\right) \tag{3.155}$$

$$=-f_K^2\left(\frac{\hat{g}_s}{f_1^2}\,\mathcal{O}_G^{0,2}+\frac{\hat{g}'}{f_1^2}\,\mathcal{O}_B^{0,2}+\frac{\tilde{g}}{f_0^2}\,\mathcal{O}_{\mathcal{V}}^{2,0}-\frac{\sqrt{2}\tilde{g}}{f_0^2f_1}\,\mathcal{O}_{\mathcal{A}}^{2,1}\right) \tag{3.156}$$

from the mixed terms.

Now we add all contributions and take into account the vector mixing. This results in the following Lagrangian for the decays into pNGBs:

$$\mathcal{L}_{\text{decays}} = C_{\mathcal{A}}\mathcal{O}_{\mathcal{A}} + C_{\mathcal{V}_8}\mathcal{O}_{\mathcal{V}_8} + C_{\mathcal{V}_6}\mathcal{O}_{\mathcal{V}_6} \tag{3.157}$$

with coefficients

$$C_{\mathcal{V}_6} = \tilde{g}(r^2-1)\,\frac{f_K^2}{f_\chi^2} \equiv g_{\rho\pi\pi}, \tag{3.158}$$

$$C_{\mathcal{V}_8} = g_{\rho\pi\pi}\,(\cos\beta_8+\tan\beta_8\sin\beta_8) + 2\frac{1+R^2}{1-R^2}\,\hat{g}_s\sin\beta_8, \tag{3.159}$$

$$C_{\mathcal{A}} = \frac{\sqrt{2}\tilde{g}r}{3}(1-r^2)(f_1^2-3f_K^2). \tag{3.160}$$

The $g_{\rho\pi\pi}$ — named in analogy to QCD — is the coupling of the vectors to the pNGBs with the elementary sector decoupled, $\beta_8 \to 0$. Indeed,

$$\lim_{\beta_8\to 0} C_{\mathcal{V}_8} = g_{\rho\pi\pi}. \tag{3.161}$$

Now all that's left is to calculate the operators, where we limit ourselves to the $\mathcal{V}_8$ whose phenomenology we will study later on. Inserting the embeddings in Eqs. (3.47) and (3.48), we

find

$$\mathcal{O}_{\mathcal{V}_8} = \mathrm{Tr}([\boldsymbol{\pi}, \partial_\mu \boldsymbol{\pi}]\boldsymbol{\mathcal{V}}_8^\mu) = \frac{1}{\sqrt{2}}\,\mathrm{Tr}\Big(\boldsymbol{\pi}_8 \overleftrightarrow{\partial_\mu} \boldsymbol{\pi}_8 \boldsymbol{\mathcal{V}}_8^\mu + \boldsymbol{\pi}_3^c \overleftrightarrow{\partial_\mu} \boldsymbol{\pi}_3 \boldsymbol{\mathcal{V}}_8^\mu\Big) \tag{3.162}$$

$$= \frac{1}{\sqrt{2}}\,\pi_8^a \overleftrightarrow{\partial_\mu} \pi_8^b\, \mathcal{V}_8^c\ \mathrm{Tr}\big(t_{\mathbf{3}}^a t_{\mathbf{3}}^b t_{\mathbf{3}}^c\big) - \frac{1}{\sqrt{2}}\,\pi_{3,i}^c \overleftrightarrow{\partial_\mu} \pi_{3,j}\, \mathcal{V}_8^a\ \mathrm{Tr}\big(L^i L^j t_{\mathbf{3}}^a\big) \tag{3.163}$$

$$= \frac{i}{4\sqrt{2}}\,\pi_8^a \overleftrightarrow{\partial_\mu} \pi_8^b\, \mathcal{V}_8^c\, f^{abc} - \frac{1}{2\sqrt{2}}\,\pi_{3,i}^c \overleftrightarrow{\partial_\mu} \pi_{3,j}\, \mathcal{V}_8^a\, [t_{\mathbf{3}}^a]^{ij}, \tag{3.164}$$

where we made use of some trace identities listed in Appendix A.

3.4.6 Independent parameters

We recap the parameters involved in the hidden symmetry calculation and fix a minimal set of independent parameters, neglecting the singlet as explained above. The Lagrangian contains the parameters f_0, f_1, f_K, r, $\hat{g}_s$, and $\tilde{g}$. The mixing angle depends only on $\tilde{g}$ through Eq. (3.110),

$$\sin\beta_8 = \frac{g_s}{\tilde{g}}. \tag{3.165}$$

We can trade two f-scales for masses,

$$f_1 = \frac{\sqrt{2} m_{\mathcal{A}}}{\tilde{g}}, \qquad f_K = \frac{\sqrt{2} m_{\mathcal{V}_6}}{\tilde{g}} = \frac{\sqrt{2} m_{\mathcal{V}_8}}{\sqrt{\tilde{g}^2 + \hat{g}_s^2}}. \tag{3.166}$$

Note that only one vector mass is independent. Rather than the two masses we prefer to work with one mass and a relative mass parameter

$$\xi = \frac{m_{\mathcal{A}}}{m_{\mathcal{V}_8}}. \tag{3.167}$$

We rewrite the remaining parameters f_0 and r in terms of two more physical ones, the coupling $g_{\rho\pi\pi}$ and the decay constant of the physical pNGBs f_χ, by means of

$$f_0 = \sqrt{\frac{f_1^2 f_\chi^2}{f_K^2} \frac{g_{\rho\pi\pi}}{\tilde{g}} + f_1^2 + f_\chi^2}, \qquad r = \sqrt{1 + \frac{f_\chi^2 g_{\rho\pi\pi}}{f_K^2 \tilde{g}}}. \tag{3.168}$$

This leaves us with five independent parameters from the hidden symmetry calculation:

$$\tilde{g}, \quad g_{\rho\pi\pi}, \quad m_{\mathcal{V}_8}, \quad \xi, \quad f_\chi. \tag{3.169}$$

There is however one further source of parameters.

3.4.7 Couplings from partial compositeness

The phenomenology of the spin-1 resonances is mostly described by the hidden symmetry Lagrangian, but not entirely. Looking back to Eq. (3.68), the kinetic terms of the top partners contain

$$\bar{\Psi}\,\not{\mathcal{V}}\,\Psi \supset \bar{T}\,\not{\mathcal{V}}_8\,T \xrightarrow{\text{phys}} \bar{t}\,\not{\mathcal{V}}_8\,t, \tag{3.170}$$

where we made use of the PC mixing in the last step. More precisely, the $\mathcal{V}_8$ couple to the top and bottom quarks,

$$\mathcal{L} \supset \bar{t}\,\not{\mathcal{V}}_8^a t_{\mathbf{3}}^a \left(g_{\mathcal{V}tt}^L P_L + g_{\mathcal{V}tt}^R P_R\right) t + \bar{b}\,\not{\mathcal{V}}_8^a t_{\mathbf{3}}^a \left(g_{\mathcal{V}bb}^L P_L\right) b \tag{3.171}$$

where we can estimate the couplings as

$$g_{\mathcal{V}tt}^L = g_{\mathcal{V}bb}^L = \tilde{g}\cos\beta_8\, s_L^2, \qquad g_{\mathcal{V}tt}^R = \tilde{g}\cos\beta_8\, s_R^2 \tag{3.172}$$

with PC mixing angles $s_{L,R}$. That is, while the light quarks couple to the $\mathcal{V}_8$ solely due to the vector mixing, the third generation quarks receive additional contributions from PC.

While in the SU(6)/Sp(6) coset, the $\mathcal{V}$ in Eq. (3.170) also contains a sextet, it has baryon number 1/3 so it cannot couple to two quarks. We instead consider the models M3-4 and M8-11 which have SU(6)/SO(6) breaking and the $\mathcal{V}_3$ has charge $-4/3$ and baryon number 2/3. This allows for couplings

$$\mathcal{L} \supset g_{\mathcal{V}tt}^{LR}\,\overline{t^c}\not{\mathcal{V}}_3 t + \text{h.c.} \tag{3.173}$$

with

$$g_{\mathcal{V}tt}^{LR} = \tilde{g} s_R^2 \sin\theta. \tag{3.174}$$

where the PC mixing angle is right handed because the operator originates from a singlet top partner. Furthermore, the coupling is suppressed by $\sin\theta$ due the presence of a left handed and right handed top partner, one of which has a suppressed mixing with the top quark.

Couplings to third generation quarks can also be found for the axial vectors, induced by the derivative couplings, see Eq. (3.74). All models feature the octet $\mathcal{A}_8$ whose couplings match the ones of $\mathcal{V}_8$ but without the $\cos\beta_8$. Note however that the $\mathcal{A}_8$ does not couple to light quarks, since it does not mix with the gluon. Focusing on the same models as for the $\mathcal{V}_3$, we also have an $\mathcal{A}_6$ with charge 4/3, which can couple to two top quarks

$$\mathcal{L} \supset g_{\mathcal{A}tt}^{LR}\,\bar{t}\not{\mathcal{A}}_6 t^c + \text{h.c.} \tag{3.175}$$

with $g_{\mathcal{A}tt}^{LR} = g_{\mathcal{V}tt}^{LR}$.

3.4.8 Generalisation to other cosets

In this section we presented the hidden symmetry calculation for the SU(6)/Sp(6) coset. These results can be straightforwardly generalised to SU(6)/SO(6) and $\mathrm{SU}(3)^2/\mathrm{SU}(3)$: the $\mathcal{V}_8$ and $\mathcal{V}_1$ are present in all models and their couplings remain the same. In the complex coset there is no further vector state, while the real coset features a $\mathcal{V}_3$ rather than a $\mathcal{V}_6$, and an $\mathcal{A}_6$ instead of the $\mathcal{A}_3$. The couplings can be recovered by replacing $\phi_6 \leftrightarrow -\phi_3^c$ and $\phi_6^c \leftrightarrow \phi_3$ for generic triplet/sextet fields $\phi_{3/6}$, where the relative sign comes from the fact that the $\mathbf{6}_{\mathrm{SU}(3)}$ is symmetric while the $\mathbf{3}_{\mathrm{SU}(3)}$ is antisymmetric. Furthermore, we have to exchange $t^a_{\mathbf{3}} \leftrightarrow t^a_{\mathbf{6}}$.

4 | Phenomenology of pseudo Nambu-Goldstone bosons

Any realistic composite Higgs model will feature an extended scalar sector with additional pNGBs beyond the Higgs boson. In the model class described in Chapter 3, these can be separated into QCD charged states coming from the $\chi\chi$-condensate and the ones emerging from the EW sector. For brevity we refer to the latter states as EW pNGBs. The coloured pNGBs come in the irreps **3**, **6**, and **8** of $\mathrm{SU}(3)_c$, while the EW sector scalars come as triplets, doublets, and singlets of $\mathrm{SU}(2)_L$. In this chapter we study the phenomenology of both types of pNGBs, assuming that they are lighter than the fermionic and spin-1 resonances.

We begin with the coloured pNGBs, describing their production and decay channels and then deriving the current mass bounds. The phenomenology of the electroweak pNGBs is more involved. In Section 4.2 we give an overview of the various production and decay channels and establish a fermiophilic and a fermiophobic scenario as two benchmarks. We then derive simplified model bounds for both scenarios in Section 4.3. As an application, we study the phenomenology of the pNGBs in the SU(5)/SO(5) coset. We demonstrate both the usefulness and the limitations of applying the simplified model bounds to a full model, and derive exclusion bounds on the masses for a variety of mass hierarchies. Sections 4.2 to 4.4 are based on [1].

During our study of the simplified model bounds on EW pNGBs, we found that decays into quarks are relatively weakly constrained. A dedicated search may discover these processes or significantly extend the exclusion limits. To this end, we design a search strategy for a $4t$-like signature in Section 4.5: the pair production of two doubly charged scalars undergoing a three-body decay, $pp \to S^{++}S^{--} \to W^+t\bar{b}W^-\bar{t}b$. The proposed search makes use of deep learning techniques to differentiate the signal process from the SM backgrounds. We derive the discovery reach and expected exclusion limit at the high-luminosity LHC (HL-LHC). Section 4.5 is based on [2].

4.1 Coloured states

In the Ferretti models, coloured pNGBs come in three colour representations: octets π_8, sextets π_6, and triplets π_3. We begin this section by summarising their interactions as outlined in Chapter 3. We then derive the current mass bounds from pair production.

4.1.1 Production and decay channels

The colour octet, which is present in all 12 models, has two interactions which facilitate decays: an anomalous coupling to gg, $g\gamma$, and gZ through the WZW term in Eq. (3.65), and couplings to top and bottom quarks from partial compositeness,

$$\pi_8 \to gg,\, g\gamma,\, gZ;\, t\bar{t},\, b\bar{b}. \tag{4.1}$$

The relative branching ratios of the diboson channels are fixed: $\pi_8 \to gg$ accounts for 94% (80%) of all decays for models with $Y_\chi = 1/3$ ($Y_\chi = 2/3$) and for a scalar mass of 1 TeV [33]. Nevertheless, the photon channel leads to interesting signatures which have been studied in [110, 111]. To simplify the analysis we do not study the $g\gamma$ and gZ decay channels in this work. For the decays into quarks, we generically expect the coupling to top quarks to dominate over bottom quarks by a factor of m_t/m_b. This leaves us with two main decay modes of the π_8,

$$\pi_8 \to gg;\, t\bar{t}. \tag{4.2}$$

The anomalous coupling to gluons Eq. (3.65) is a dimension-5 operator and as such comes with a suppression of $1/f_\chi$. It was shown in [110] that despite that, there are models where the coupling to top quarks is naturally small compared to the gluon coupling, so we consider both options.

The colour sextet is present in models with the SU(6)/SO(6) coset. Using the model classes defined in Tab. 3.3, π_6 has electric charge $Q = -2/3$ and baryon number $B = -1/3$ in C1 and $Q = 4/3$ and $B = 2/3$ in C2. From the charges, the possible decay channels read

$$\text{C1}: \qquad \pi_6 \to bb, \tag{4.3}$$

$$\text{C2}: \qquad \pi_6 \to tt. \tag{4.4}$$

The decay in C2 conserves baryon number and can therefore be generated by partial compositeness. In C1 however, we have to add a baryon number violating ($\Delta B = 1$) coupling for π_6 to have a decay channel. Note that we choose to couple π_6 to the bottom quark, but couplings to light quarks would also be possible. The π_6 coupling to top quarks was studied in [112].

Finally, the colour triplet is only present in the model M5 featuring the SU(6)/Sp(6) coset. It has $Q = 2/3$ and $B = 1/3$ and we have to add either baryon number or lepton number violating terms to avoid a stable π_3 [107]. Keeping with the typical flavour hierarchy, we have

$$\Delta B = 1: \qquad \pi_3 \to \bar{b}\bar{s}, \tag{4.5}$$

$$\Delta L = 1: \qquad \pi_3 \to t\bar{\nu},\, b\tau^+. \tag{4.6}$$

Note that $\pi_3 \to \bar{b}\bar{b}$ is absent due to $\mathrm{SU}(3)_c$ antisymmetrisation. The lepton number violating decays can be obtained by extending the idea of partial compositeness to the third generation

leptons as discussed in Section 3.3.3. We follow this approach, which implies $\mathrm{Br}(\pi_3 \to t\bar{\nu}) = \mathrm{Br}(\pi_3 \to b\tau^+) = 50\%$ up to kinematic differences in the decay products.

To summarise the discussion so far, we formulate simplified models for the coloured pNGBs, following the notation introduced in [113]. Apart from the universal kinetic and mass terms, we have couplings to vector bosons and SM fermions,

$$\mathcal{L}_{\mathrm{int}} = \mathcal{L}_{\pi V\tilde{V}} + \mathcal{L}_{\pi ff}. \tag{4.7}$$

Since we only study the dominant $\pi_8 \to gg$ diboson decay, the first term simply reads

$$\mathcal{L}_{\pi V\tilde{V}} = \frac{g_s^2}{16\pi^2 f_\chi} \tilde{K}_{gg}^{\pi_8}\, d^{abc}\, \pi_8^a G_{\mu\nu}^b \tilde{G}^{\mu\nu,c} \tag{4.8}$$

with $\tilde{G}^{\mu\nu} = \frac{1}{2}\epsilon^{\mu\nu\rho\sigma} G_{\rho\sigma}$. The couplings to fermions are given by

$$\begin{aligned}
\mathcal{L}_{\pi ff} = {} & \bar{t}\,\pi_8\,(\kappa_t^{\pi_8} + i\tilde{\kappa}_t^{\pi_8}\gamma_5)t \\
& + \bar{t}\,\pi_6^{4/3}\,(\kappa_t^{\pi_6^{4/3}} + i\tilde{\kappa}_t^{\pi_6^{4/3}}\gamma_5)C\bar{t}^T + b^T\,\pi_6^{2/3}\,(\kappa_t^{\pi_6^{2/3}} + i\tilde{\kappa}_t^{\pi_6^{2/3}}\gamma_5)Cb + \mathrm{h.c.} \\
& + \bar{t}\,\pi_3\,(\kappa_{t\nu,L}^{\pi_3} P_L + \kappa_{t\nu,R}^{\pi_3} P_R)\nu + \bar{b}\,\pi_3\,(\kappa_{b\tau,L}^{\pi_3} P_L + \kappa_{b\tau,R}^{\pi_3} P_R)\tau + \mathrm{h.c.} \\
& + b^T\,\pi_3\,(\kappa_{bs,L}^{\pi_3} P_L + \kappa_{bs,R}^{\pi_3} P_R)Cs,
\end{aligned} \tag{4.9}$$

where C is the charge conjugation matrix, the superscript of the π_6 indicates the electric charge, and contractions of colour indices are implicit.

The coloured pNGBs can be QCD pair produced at the LHC. The corresponding cross section is model independent, being purely determined by the $\mathrm{SU}(3)_c$ irreps. For the octet we calculate the cross section at next-to-leading order (NLO) with the publicly available `sgluons` Universal FeynRules Output (UFO) library [114], setting the scales to $\mu_R = \mu_F = m_\pi$ and using the `NNPDF` 2.3 parton distribution function (PDF) set. With this scale choice, the K-factor turns out to be close to 1. We therefore expect that our cross sections of the π_6 calculated with a leading order (LO) UFO [115, 116] — no NLO calculations are available — will also only see minor loop corrections. For the π_3, precise calculations for decoupled stop pair production are available at the approximate next-to-next-to-leading order (NNLO) including the next-to-next-to-leading log (NNLL) [117–119]. The resulting cross sections are shown in grey in Fig. 4.1. The π_6 has the largest cross section, closely followed by the π_8, while the π_3 lies about an order of magnitude below that.

The pair production combined with the decay channels discussed above leads to the signatures $4t/4g$ for π_8, $4t/4b$ for π_6, and $\bar{b}\bar{s}bs/q_3\bar{l}_3\bar{q}_3 l_3$ for π_3, where $q_3 = t, b$ and $l_3 = \tau^-, \nu$. Feynman diagrams for π_8 are shown in Fig. 4.2. For the octet and sextet, there is another production channel: tt- or bb-associated single production, shown in the right panel of Fig. 4.2 for π_8. These processes also lead to a $4t/4b$ signature, albeit with different kinematics. The single production cross section depends on the couplings to quarks and typically dominates over pair production for large masses. Due to its model dependence, we do not study it further.

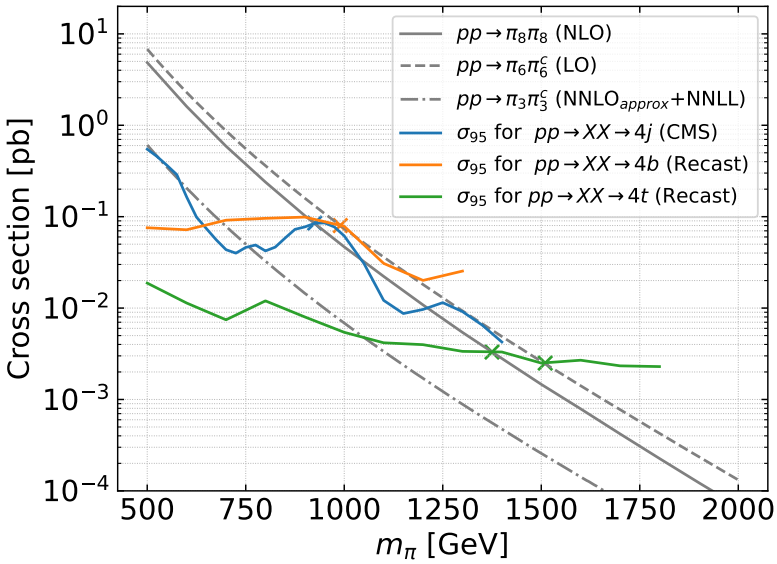

Figure 4.1: QCD pair production of coloured pNGBs. The grey lines show the cross sections calculated at a centre-of-mass energy $\sqrt{s} = 13$ TeV with the precision indicated in parentheses. The coloured lines are 95% CL upper limits on cross section times branching ratio into the respective decay channels. The limits are taken from [120] for $4j$, and obtained from recasts of [121, 122]/[123, 124] for $4t/4b$.

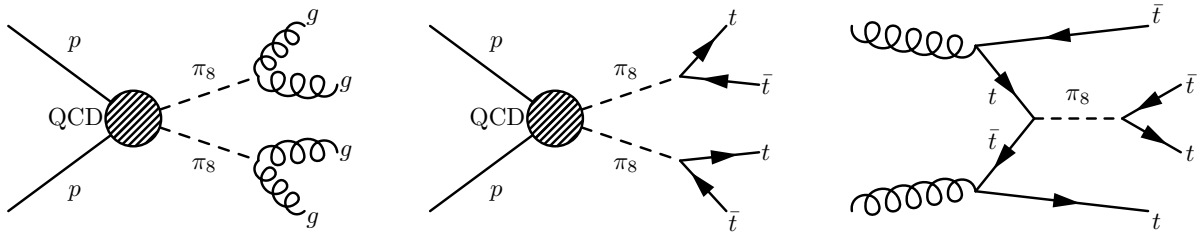

Figure 4.2: Feynman diagrams for $4g$- and $4t$ production via π_8.

4.1.2 Mass bounds

We now make use of the universality of the pair production cross section to set lower limits on the masses of the coloured pNGBs for each decay channel. The results are summarised in Tab. 4.1. We begin with the colour triplet, for which direct searches apply: the baryon number violating decay is covered by a CMS search for pairs of dijet resonances [120], $pp \to XX \to (jj)(jj)$. Masses between 500 and 770 GeV are excluded at 95% confidence level (CL), except for the region 520-580 GeV which is still barely allowed. Note that while the search is for $\tilde{t} \to \bar{d}\bar{s}$, it does not veto b-jets and can therefore also be applied to the $\pi_3 \to \bar{b}\bar{s}$. The lepton number violating decay is constrained by ATLAS searches for scalar leptoquarks decaying into third generation fermions [125–127] which have been statistically combined in [128], yielding a mass bound of 1340 GeV for equal branching ratio into $t\bar{\nu}$ and $b\tau^+$. For the colour octet, the decay into gluons is again covered by [120]. From the upper limit σ_{95} on the cross section at 95% CL, shown as a blue line in Fig. 4.1 assuming an acceptance of 10%, masses below 925 GeV are excluded. Furthermore, the region 1040 GeV $\leq m_{\pi_8} \leq$ 1210 GeV is excluded also.

For the remaining channels, no dedicated searches have been performed at 13 TeV. We

Process	Mass bound [GeV]	Constraining searches
$\pi_8\pi_8 \to 4t$	1375	ATLAS SUSY searches [121, 122]
$\pi_8\pi_8 \to 4g$	925	CMS search $XX \to 4j$ [120]
$\pi_6\pi_6^c \to 4t$	1510	ATLAS SUSY searches [121, 122]
$\pi_6\pi_6^c \to 4b$	990	ATLAS searches for b-squarks [124] and general new phenomena [123]
$\pi_3\pi_3^c \to \bar{b}\bar{s}bs$	770	CMS search $XX \to 4j$ [120]
$\pi_3\pi_3^c \to q_3\bar{l}_3\bar{q}_3l_3$	1340	Stat. combination of ATLAS LQ searches [128]

Table 4.1: Mass bounds from QCD pair production of coloured pNGBs assuming 100% branching ratio into each channel. The leptoquark (LQ) channel of π_3 has $\mathrm{Br}(\pi_3 \to t\bar{\nu}) = \mathrm{Br}(\pi_3 \to b\tau^+) = 50\%$ up to mass effects.

therefore determine the upper limits from recast searches. Our procedure and the toolchain are presented in Appendix B. We use publicly available UFO libraries for the octet [129–131] and sextet [115, 116] to generate leading order events. The strongest constraints on the $XX \to 4t$ signature are obtained from two ATLAS SUSY searches, both using 139 fb^{-1} of data and implemented in `CheckMATE`: a search for R-parity violating SUSY in final states with leptons and many jets [121], and a search focusing on final states with missing transverse momentum and ≥ 3 b-jets [122]. Since the searches are not charge-sensitive, the limits apply equally to $\pi_8 \to t\bar{t}$ and $\pi_6 \to tt$, and we read off $m_{\pi_8} \geq 1375$ GeV and $m_{\pi_6} \geq 1510$ GeV. To our knowledge, these are the strongest recasting bounds for these channels in the literature, improving the limit on m_{π_8} obtained in [131] by about 120 GeV. In the ATLAS analysis [132] the results of a search for $t\bar{t}H/A \to 4t$ are applied to $\pi_8\pi_8 \to 4t$, yielding a slightly weaker bound of 1330 GeV. Finally, we find a bound of 990 GeV for the $\pi_6 \to bb$ decay channel. Here, the constraining analyses are an ATLAS search for bottom squarks using 139 fb^{-1} [124] and a general search for new phenomena based on only 3.2 fb^{-1} but with a large number of signal regions [123].

4.2 Overview of electroweak states

The electroweak pNGBs come with electric charges ± 2, ± 1, and 0. When discussing them in a model independent way, we denote them as $S^{\pm\pm}$, $S^{\pm}$, and S^0, respectively. Being colour singlets, they lack the large and model independent QCD pair production channel of their colour sector counterparts. In this section, we discuss their possible production and decay channels.

The phenomenology of the EW pNGBs is determined by three types of couplings:

- $\mathcal{L}_{SSV} + \mathcal{L}_{SSVV}$: gauge couplings to one or two EW gauge bosons coming from the covariant derivative,
- $\mathcal{L}_{SVV}$: anomalous couplings to two EW gauge bosons via the WZW term,

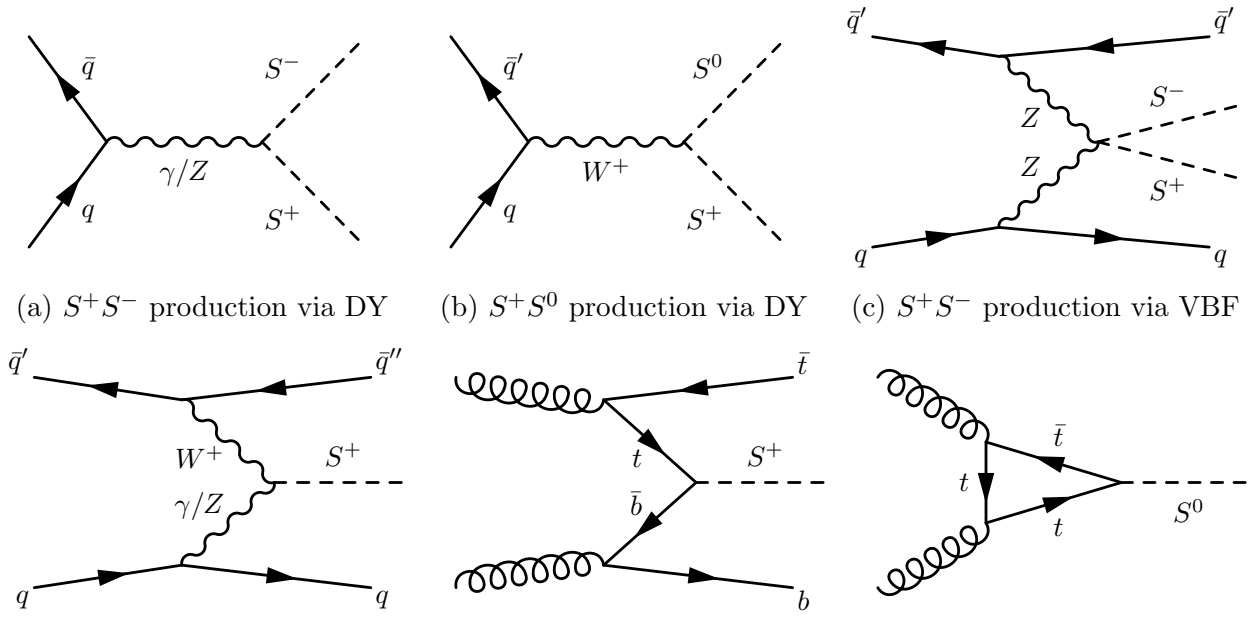

(a) S^+S^- production via DY (b) S^+S^0 production via DY (c) S^+S^- production via VBF

(d) S^+ production via VBF (e) S^+tb associated production (f) S^0 production via ggF

Figure 4.3: Feynman diagrams for the pair and single production of electroweak pNGBs via (a,b) Drell-Yan, (c,d) vector boson fusion, (e) quark associated production, and (f) gluon-gluon-fusion (ggF).

- $\mathcal{L}_{Sff}$: couplings to third generation quarks via partial compositeness.

Of those, the gauge couplings are always present, although the specific values are model dependent. The anomaly and quark couplings do not necessarily appear and we discuss them below. For now, we assume all couplings are present. This leads to a variety of production channels, as illustrated in Fig. 4.3 for a generic singly charged scalar S^+. The first row highlights the production channels due to gauge couplings: Fig. 4.3a shows S^+S^- Drell-Yan (DY) production. Since the pNGBs come in multiplets of $\mathrm{SU}(2)_L$, there can also be mixed channels, e.g. S^+S^0 in Fig. 4.3b. A second mode for pair production is vector boson fusion (VBF) via the $SSVV$-couplings in the covariant derivative as in Fig. 4.3c. It was shown in [105] that DY production dominates over VBF. The anomaly coupling of a scalar to two vector bosons allows for VBF single production as shown in Fig. 4.3d. However, since the coupling is suppressed by a large scale, the corresponding cross section is quite small. This is not the case for the second single production mode: the S^+ can be produced in association with a top and bottom quark as depicted in Fig. 4.3e. Finally, the coupling of the neutral scalar to top quarks allows for single production by gluon-gluon-fusion (see Fig. 4.3f) analogous to the SM Higgs. The cross sections for both associated production and gluon-gluon-fusion depend quadratically on the scalar-quark coupling.

We now turn to the decay channels of the EW pNGBs. The first thing to note is that the gauge couplings in $\mathcal{L}_{SSV}$ allow for cascade decays of the form

$$S_1 \to S_2 V^{(*)} \tag{4.10}$$

if $m_{S_1} > m_{S_2}$ with a fitting vector boson $V = W^{\pm}, Z$. Depending on the mass splitting, the vector boson may be off-shell. Cascade decays play an important role when studying the phenomenology of a full model, as we will see in Section 4.4. For now we only look at the decays of the lightest scalars, for which there are two options: decays into fermions or into vector bosons.

If couplings of the pNGBs to third generation quarks are generated (*fermiophilic scenario*), we expect them to dominate over the anomaly couplings to vector bosons. The dominant decay channels are

$$S^+ \to t\bar{b}, \tag{4.11}$$

$$S^0 \to t\bar{t};\, b\bar{b}. \tag{4.12}$$

The $S^0 b\bar{b}$-coupling is suppressed by m_b/m_t compared to the top coupling. Therefore, the $S^0 \to b\bar{b}$ channel is only relevant if the decay into top quarks is kinematically forbidden, i.e. $m_{S^0} < 2m_t$. Note that the coupling to the top quarks also induces the decay

$$S^0 \to \gamma\gamma \tag{4.13}$$

via a top loop. While being significantly suppressed compared to diquark decays, its clean signature makes this decay channel important when searching for S^0 as proven by the Higgs boson. Finally, the doubly charged scalar cannot decay into two quarks due to its charge. Instead, its dominant decay in the fermiophilic scenario is a three body decay mediated by an off-shell S^+,

$$S^{++} \to W^+ S^{+,*} \to W^+ t\bar{b}. \tag{4.14}$$

In the SU(5)/SO(5) model — the only coset to feature a doubly charged scalar — this decay dominates over the $S^{++} \to W^+W^+$ anomaly decay despite the phase space suppression [1]. The size of the couplings to quarks depends on the specific model, but as explained in Section 2.3 we can estimate $c\, m_q/f_\psi$, with an order-1 coupling c and $f_\psi \gtrsim 1$ TeV.

There are also models where at least some of the pNGBs do not couple to quarks [133]. In the absence of couplings to quarks (*fermiophobic scenario*), the suppressed decays into vector bosons become important. The electric charges allow for the following decays:

$$S^{++} \to W^+W^+, \tag{4.15}$$

$$S^+ \to W^+\gamma,\, WZ, \tag{4.16}$$

$$S^0 \to W^+W^-,\, \gamma\gamma,\, \gamma Z,\, ZZ. \tag{4.17}$$

The anomaly couplings are fully determined by the coset and are listed in [133]. We show the branching ratios for the EW pNGBs appearing in the Ferretti models in Fig. 4.4. For

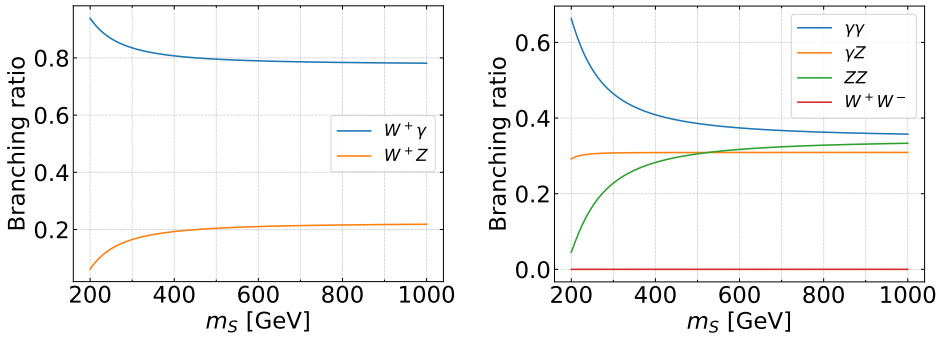

(a) $\eta^+_{3/5}$ in SU(5)/SO(5) (b) $\eta^0_{1/5}$ in SU(5)/SO(5)

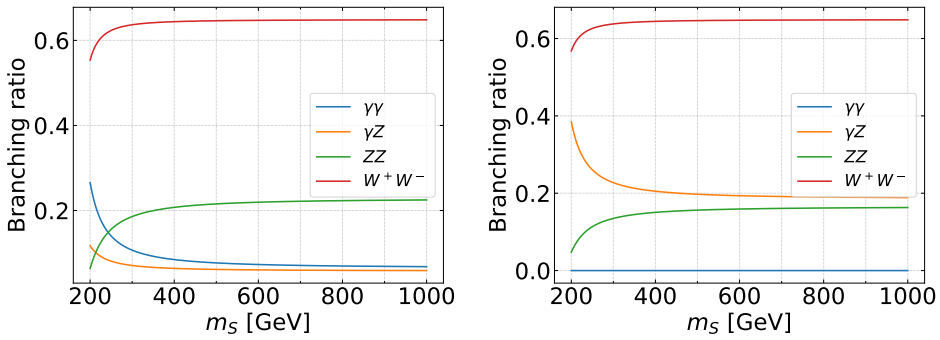

(c) η in SU(5)/SO(5) (d) η in SU(4)/Sp(4)

Figure 4.4: Branching ratios of EW pNGBs in the Ferretti models. The misalignment angle was taken as $\theta = 0$, in which case the singly charged and neutral states in the real coset have the same branching ratios. The η in the $SU(4)^2/SU(4)$ coset has identical couplings to its counterpart in SU(4)/Sp(4).

simplicity we have taken the limit[1] $\theta \to 0$ in which case the branching ratios of η_3^+ and η_5^+ coincide (Fig. 4.4a), as do the ones of η_1^0 and η_5^0 (Fig. 4.4b). For $\eta^0_{1/5}$, the decay into W^+W^- is negligibly small. For the gauge singlet η on the other hand, W^+W^- is the dominant decay channel. This is true both for the real coset (Fig. 4.4c) as well as the pseudoreal and complex cosets (Fig. 4.4d), both of which have the same branching ratios of η. For the latter cosets, the η does not couple to $\gamma\gamma$.

There are a few notable absences in Fig. 4.4. In the SU(5)/SO(5) coset, the η_3^0 does not couple to the anomaly. In the fermiophobic scenario, it will undergo three body decays via off-shell pNGBs as discussed in detail in Section 4.4. In the $SU(4)^2/SU(4)$ coset, the η is even the only state with anomaly couplings. If the remaining pNGBs also do not couple to fermions then at first glance they cannot decay. In practice however, we always expect at least a small mass splitting between the states which leads to cascade decays to the lightest state, mediated either by gauge couplings or by the scalar potential. The lightest pNGB can then decay to gauge bosons via two (potentially off-shell) η.

[1]Taking a vanishing θ only changes the branching ratios by $\mathcal{O}(1\%)$ compared to a more realistic $\theta \sim 0.1$.

4.3 Simplified model bounds

In the previous section we noted that Drell-Yan is the dominant pair production mode, while the pNGBs can be singly produced in association with two third generation quarks or via gluon-gluon-fusion for the case of neutral scalars. As a next step, we would like to assess to which extent the EW pNGBs have been excluded by LHC data. This was straightforward for the coloured pNGBs due to the model independent QCD pair production, whereas both single and pair production of EW pNGBs depend on model specific couplings: the W and Z couplings for DY and the quark couplings for single production. Our aim will therefore be to derive limits on production cross section times branching ratio rather than mass bounds. That is, instead of constraining a specific model we derive bounds on simplified models [1]. This way, our results are applicable to a wide class of models with extended scalar sectors, not just composite Higgs models.

4.3.1 Simplified models

We employ the simplified model for extended scalar sectors that was introduced in [113], extending the SM by four scalars: S^0, $S^{0\prime}$, S^+, and S^{++}. The new scalars are colour singlets and are labeled by the electric charge, i.e. they are mass eigenstates. Note that we have included two neutral scalars which we assume to have opposite parity. This is necessary to have a coupling of two neutral scalars to the Z boson. We assume that the state even under charge-parity (CP) does not obtain a VEV. Besides the kinetic and mass terms, the BSM Lagrangian splits into three parts,

$$\mathcal{L}_{\text{int}} = \mathcal{L}_{SSV} + \mathcal{L}_{SVV} + \mathcal{L}_{Sff}, \tag{4.18}$$

as discussed in the previous section.

We begin with the scalar-scalar-vector couplings,

$$\begin{aligned}\mathcal{L}_{SSV} = &\frac{ie}{s_W} W^{-\mu} \left(K_W^{S^0 S^+} S^0 \overleftrightarrow{\partial_\mu} S^+ + K_W^{S^{0\prime} S^+} S^{0\prime} \overleftrightarrow{\partial_\mu} S^+ + K_W^{S^- S^{++}} S^- \overleftrightarrow{\partial_\mu} S^{++} \right) + \text{h.c.} \\ &+ \frac{ie}{s_W c_W} Z^\mu \left(K_Z^{S^0 S^{0\prime}} S^0 \overleftrightarrow{\partial_\mu} S^{0\prime} + K_Z^{S^+ S^-} S^+ \overleftrightarrow{\partial_\mu} S^- + K_Z^{S^{++} S^{--}} S^{++} \overleftrightarrow{\partial_\mu} S^{--} \right) \\ &- ieA^\mu \left(S^+ \overleftrightarrow{\partial_\mu} S^- + 2 S^{++} \overleftrightarrow{\partial_\mu} S^{--} \right) ,\end{aligned} \tag{4.19}$$

where $\phi_1 \overleftrightarrow{\partial_\mu} \phi_2 \equiv \phi_1(\partial_\mu \phi_2) - (\partial_\mu \phi_1)\phi_2$. These couplings are generated by the covariant derivative terms in a full model. Note that the photon couplings are fixed by QED, while the couplings to the W and Z bosons depend on the model, specifically the $\mathrm{SU}(2)_L \times \mathrm{U}(1)_Y$ irreps of the pNGBs and the mass mixing. The K_V^{SS} parameters determine the production cross section, with $\sigma(pp \to S_1 S_2) \propto |K_V^{S_1 S_2}|^2$.

Secondly we have the scalar-vector-vector couplings facilitating the decays into gauge bosons,

$$\begin{aligned}\mathcal{L}_{SVV} = \frac{e^2}{16\pi^2 v}\Bigg[& S^0\left(\tilde{K}^{S^0}_{\gamma\gamma}F_{\mu\nu}\tilde{F}^{\mu\nu} + \frac{2}{s_W c_W}\tilde{K}^{S^0}_{\gamma Z}F_{\mu\nu}\tilde{Z}^{\mu\nu} + \frac{1}{s_W^2 c_W^2}\tilde{K}^{S^0}_{ZZ}Z_{\mu\nu}\tilde{Z}^{\mu\nu}\right.\\ & \left. + \frac{2}{s_W^2}\tilde{K}^{S^0}_{WW}W^+_{\mu\nu}\tilde{W}^{-\mu\nu}\right)\\ & + S^{0\prime}\left(K^{S^{0\prime}}_{\gamma\gamma}F_{\mu\nu}F^{\mu\nu} + \frac{2}{s_W c_W}K^{S^{0\prime}}_{\gamma Z}F_{\mu\nu}Z^{\mu\nu} + \frac{1}{s_W^2 c_W^2}K^{S^{0\prime}}_{ZZ}Z_{\mu\nu}Z^{\mu\nu}\right.\\ & \left. + \frac{2}{s_W^2}K^{S^{0\prime}}_{WW}W^+_{\mu\nu}W^{-\mu\nu}\right)\\ & + \left(S^+\left(\frac{2}{s_W}\tilde{K}^{S^+}_{\gamma W}F_{\mu\nu}\tilde{W}^{-\mu\nu} + \frac{2}{s_W^2 c_W}\tilde{K}^{S^+}_{ZW}Z_{\mu\nu}\tilde{W}^{-\mu\nu}\right) + \text{h.c.}\right)\\ & + S^{++}\frac{1}{s_W^2}\tilde{K}^{S^{++}}_{W^-W^-}W^-_{\mu\nu}\tilde{W}^{-\mu\nu} + \text{h.c.}\Bigg], \end{aligned} \tag{4.20}$$

which are dimension-5 operators. The dual field strength tensor reads $\tilde{F}^{\mu\nu} = \frac{1}{2}\epsilon^{\mu\nu\rho\sigma}F_{\rho\sigma}$. We write the couplings with $F\tilde{F}$ since that is the form of the WZW term. Only for the CP-even $S^{0\prime}$ we have to take the combination FF. This does not affect the kinematics of the decay.

Finally we have the fermiophilic couplings induced by partial compositeness,

$$\begin{aligned}\mathcal{L}_{Sff} = & S^0\left[i\tilde{\kappa}_t^{S^0}\,\bar{t}\gamma_5 t + i\tilde{\kappa}_b^{S^0}\,\bar{b}\gamma_5 b\right] + S^{0\prime}\left[\kappa_t^{S^0}\,\bar{t}t + \kappa_b^{S^0}\,\bar{b}b\right]\\ & + S^+\,\bar{t}\left(\kappa^{S^+}_{tb,L}P_L + \kappa^{S^+}_{tb,R}P_R\right)b + \text{h.c.}\,. \end{aligned} \tag{4.21}$$

As with $\mathcal{L}_{SVV}$, we write the couplings to S^0 as a pseudoscalar and $S^{0\prime}$ as a scalar. For the singly charged state we allow chiral interactions.

4.3.2 Bounds on single production

In the fermiophilic scenario, S^0 and S^+ can be singly produced from their couplings to third generation quarks. One option is production in association with two quarks,

$$pp \to S^0 t\bar{t} \to t\bar{t}t\bar{t}, \qquad pp \to S^{\pm} tb \to tbtb\,. \tag{4.22}$$

Furthermore, the S^0 can be produced by gluon-gluon-fusion, leading to

$$pp \to S^0 \to t\bar{t}, \qquad pp \to S^0 \to \gamma\gamma\,. \tag{4.23}$$

Fortunately, there are direct searches applicable to each of these processes. Our approach in this section is to compare the limits on the cross sections obtained from the direct searches with estimates of realistic cross sections in composite Higgs models.

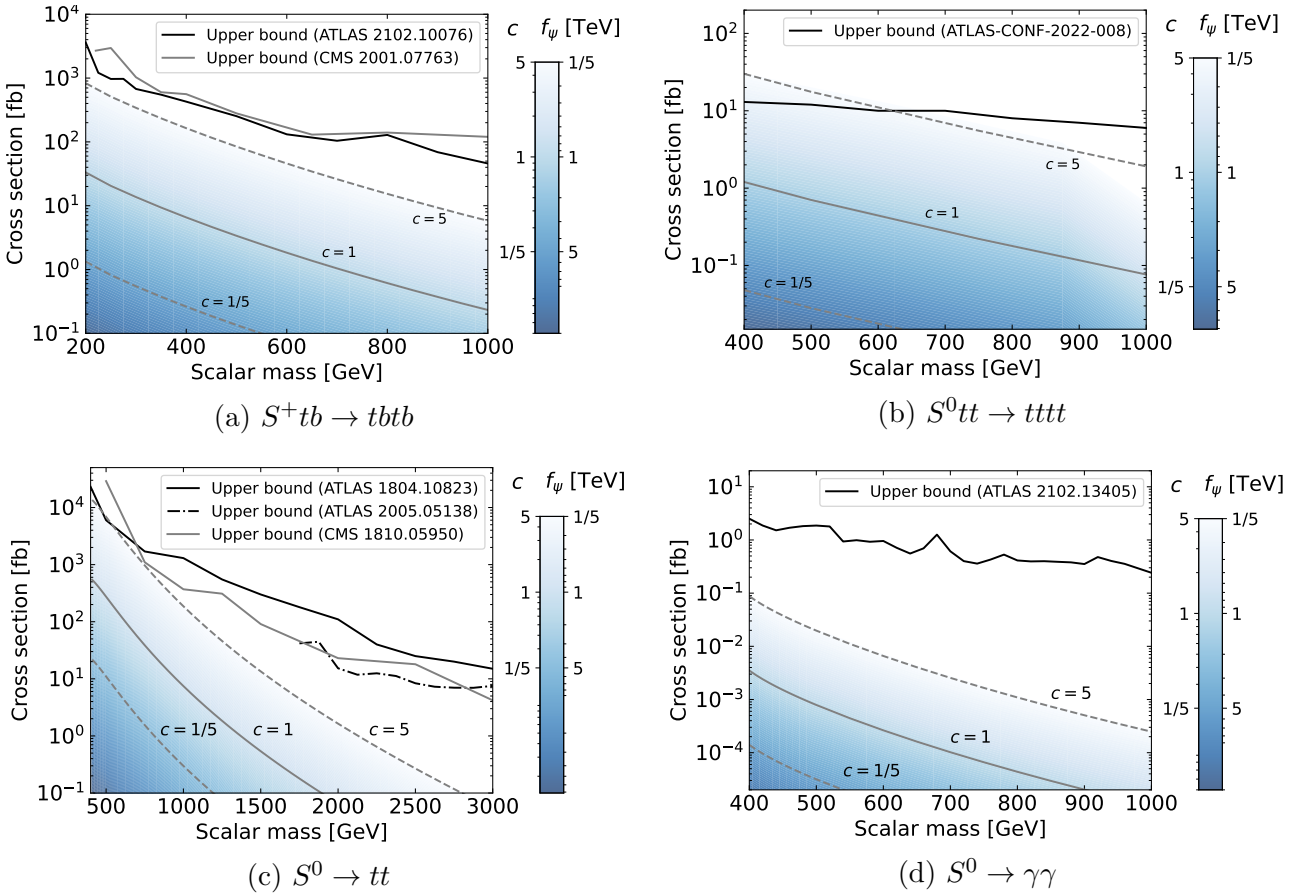

(a) $S^+tb \to tbtb$ (b) $S^0tt \to tttt$

(c) $S^0 \to tt$ (d) $S^0 \to \gamma\gamma$

Figure 4.5: Bounds on the single production of EW pNGBs (a,b) in association with two third generation quarks and (c,d) via gluon-gluon-fusion. The area shaded in blue indicates typical cross sections assuming that only one scalar is present. The coupling to the quarks is given by $c\, m_t/f_\psi$ and the side band maps the blue shade to the corresponding value of c (for $f_\psi = 1$ TeV) and f_ψ (for $c = 1$). The darker regions are theoretically more favourable (see text).

We recall that the couplings in Eq. (4.21) involving a top quark can be written as

$$\kappa_i = c_i \frac{m_t}{f_\psi} \tag{4.24}$$

with an $\mathcal{O}(1)$ constant c_i and $f_\psi \gtrsim 1$ TeV. In Fig. 4.5 we show the cross sections for the single production processes for reference values $c = 1/5$, 1, and 5, assuming a fixed $f_\psi = 1$ TeV. To obtain the cross section for arbitrary values of c and f_ψ we can rescale the $c = 1$ line by $(c/f_\psi)^2$ with f_ψ in TeV. For Fig. 4.5a we calculate the cross section at leading order using the public `eVLQ` UFO model presented in [113]. We use the `NNPDF` 2.3 PDF set and set the renormalisation and factorisation scales to $\mu_R = \mu_F = (m_t + m_b + m_{S^+})/3$, as this results in a K-factor very close to 1 [134]. For the remaining three processes, calculations by the Higgs Xsection working group are available [135, 136], so we use these and rescale the Yukawa coupling accordingly. Lower cross section values are shaded in a darker blue to indicate that this is the more favourable region of parameter space from a model building point of view. The reason is that the f_ψ can always be chosen larger than 1 TeV, whereas couplings $c > 5$ are unrealistic, making the lightly

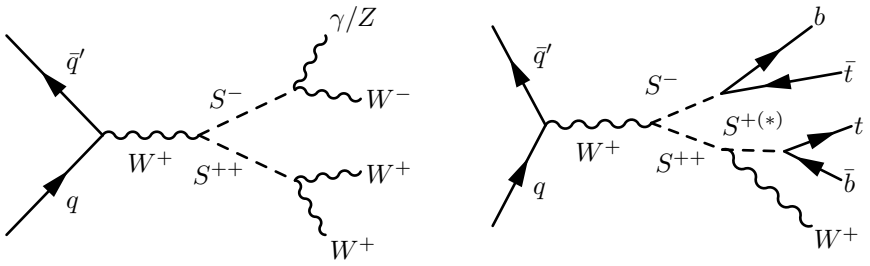

Figure 4.6: Examples of di-scalar channels from pair production via Drell-Yan processes with subsequent decays into SM particles in the (left) fermiophobic and (right) fermiophilic case.

shaded and white regions of the plots hard to reach.

The cross sections are to be compared with the experimental searches for (a) $pp \to S^{\pm}tb \to tbtb$ [137, 138], (b) $pp \to (H/A)t\bar{t} \to t\bar{t}t\bar{t}$ [139], (c) $pp \to Z' \to t\bar{t}$ [140–142], and (d) $pp \to S^0 \to \gamma\gamma$ [143]. For each search we show the upper limit on the cross section of the respective process. The only process that yields a bound is S^0tt associated production in Fig. 4.5b, which can be excluded up to 640 GeV for $c = 5$ and $f_\psi = 1$ TeV. Looking at the shaded regions, the area where an exclusion is reached is a rather small part of the parameter space.

Even for a specific model, the couplings to quarks c_i depend on unknown mixing angles between top quark and top partners, making it impossible to derive specific bounds on the scalar mass in a given model. However, if a model contains several scalars of the same charge, all states will populate the signal regions of the constraining analyses, thus enlarging the parameter space that leads to an exclusion.

4.3.3 Bounds on Drell-Yan pair production

We now turn to the pair production of EW pNGBs via DY processes. The possible scalar pairs that can be produced at the LHC are

$$pp \to S^{\pm\pm}S^{\mp},\ S^{\pm}S^{0\prime},\ S^{++}S^{--},\ S^{+}S^{-},\ S^{0}S^{0\prime}. \tag{4.25}$$

We refer to a scalar pair combined with its first tier decays into SM particles as a *di-scalar channel*, while reserving the term *final state* for the detector-level objects. Two examples for di-scalar channels are shown in Fig. 4.6. In Tabs. 4.2 and 4.3 we list all di-scalar channels in the fermiophobic and fermiophilic scenarios, of which there are 24 and 8, respectively. Note that charge conjugated processes belong to the same di-scalar channel.

Our goal is to determine upper limits σ_{95} on the di-scalar channel cross sections, i.e. limits on the product of the Drell-Yan production cross sections with the branching ratios into SM particles. For the single production described in the previous section, there were experimental searches for all processes of interest, from which we could extract the σ_{95}. The search coverage for the di-scalar channels is significantly worse. To the best of our knowledge, only two channels have been directly searched for: $S^{++}S^{--} \to WWWW$ and $S^{\pm\pm}S^{\mp} \to WWWZ$ in [144]. A reason why these channels are an exception is that the doubly charged scalar cannot be

fermiophobic	$S^{++}S^{--}$	$S^{\pm\pm}S^{\mp}$	$S^{+}S^{-}$	$S^{\pm}S^{0(\prime)}$	$S^{0}S^{0\prime}/S^{0\prime}S^{0}$
$WWWW$	$W^+W^+W^-W^-$	-	-	-	$W^+W^-W^+W^-$
$WWW\gamma$	-	$W^\pm W^\pm W^\mp\gamma$	-	$W^\pm\gamma W^+W^-$	-
$WWWZ$	-	$W^\pm W^\pm W^\mp Z$	-	$W^\pm Z W^+W^-$	-
$WW\gamma\gamma$	-	-	$W^+\gamma W^-\gamma$	-	$W^+W^-\gamma\gamma$
$WWZ\gamma$	-	-	$W^\pm\gamma W^\mp Z$	-	$W^+W^-\gamma Z$
$WWZZ$	-	-	W^+ZW^-Z	-	W^+W^-ZZ
$W\gamma\gamma\gamma$	-	-	-	$W^\pm\gamma\gamma\gamma$	-
$WZ\gamma\gamma$	-	-	-	$W^\pm\{Z\gamma\}\gamma$	-
$WZZ\gamma$	-	-	-	$W^\pm\{Z\gamma\}Z$	-
$WZZZ$	-	-	-	$W^\pm ZZZ$	-
$\gamma\gamma\gamma\gamma$	-	-	-	-	$\gamma\gamma\gamma\gamma$
$Z\gamma\gamma\gamma$	-	-	-	-	$Z\gamma\gamma\gamma$
$ZZ\gamma\gamma$	-	-	-	-	$Z\{Z\gamma\}\gamma$
$ZZZ\gamma$	-	-	-	-	$ZZZ\gamma$
$ZZZZ$	-	-	-	-	$ZZZZ$

Table 4.2: Classification of the 24 di-scalar channels in the fermiophobic scenario in terms of the 5 pair production cases (columns) and the 15 combinations of gauge bosons (rows) from decays. Bosons of the same colours are resonantly produced. The notation $\{Z\gamma\} = Z\gamma + \gamma Z$ indicates the two permutations. The charge conjugated channels are also included.

fermiophilic	$S^{++}S^{--}$	$S^{++}S^{-}$	$S^{+}S^{-}$	$S^{+}S^{0(\prime)}$	$S^{0}S^{0\prime}/S^{0\prime}S^{0}$
$tttt$	-	-	-	-	$t\bar{t}t\bar{t}$
$ttt\bar{b}$	-	-	-	$t\bar{b}t\bar{t}$	-
$tt\bar{b}\bar{b}$	-	-	$t\bar{b}b\bar{t}$	-	$t\bar{t}b\bar{b}$
$t\bar{b}\bar{b}\bar{b}$	-	-	-	$t\bar{b}b\bar{b}$	-
$\bar{b}\bar{b}\bar{b}\bar{b}$	-	-	-	-	$b\bar{b}b\bar{b}$
$Wtt\bar{b}\bar{b}$	-	$W^+t\bar{b}b\bar{t}$	-	-	-
$WWtt\bar{b}\bar{b}$	$W^+t\bar{b}W^-b\bar{t}$	-	-	-	-

Table 4.3: Classification of the 8 di-scalar channels in the fermiophilic scenario in terms of the 5 pair production cases (columns) and the 5 combinations of top and bottom from decays (rows). In cases with one or two doubly charged scalars, one always obtains $tt\bar{b}\bar{b}$ with one or two additional W bosons, respectively. The charge conjugated channels are also included.

singly produced with a considerable cross section, thus motivating a search for pair production. Besides that, several searches have been performed for processes that are similar to ours: di-Higgs production leads to $WW^{(*)}\gamma\gamma$, $WW^{(*)}WW^{(*)}$ and $bbbb$ channels [145–150], but searches for them are strongly focused on scalar masses of 125 GeV and study different production mechanisms. There are searches for non-Higgs scalar pair production in the $WWWW$ [151] and $bbbb$ [152] channels, but these consider resonant production. Due to the different kinematics and/or limitation to the Higgs mass, these searches have limited applicability to the di-scalar channels at hand.

Since only 2 out of 32 di-scalar channels have been constrained by experiments, it is necessary to reinterpret existing analyses to derive bounds on the scalar pair production. To this end, a comprehensive recasting study is in order, which we performed in [1]. The basis for our simulations is the public `eVLQ` UFO model presented in [113], which implements the simplified

models presented in Section 4.3.1 and is capable of NLO calculations in QCD. We extended the model by an additional neutral scalar $S^{0\prime}$ to allow for $S^0 S^{0\prime}$ production. For channels involving two different scalars, we assume them to be mass degenerate. We generate signal events for DY production and decay to SM particles at a centre-of-mass energy of $\sqrt{s} = 13$ TeV at NLO in QCD. We then scan over the mass and generate 10^5 Monte Carlo events per parameter point using `MadGraph5_aMC@NLO`. The events are then passed to `MadAnalysis5`, `CheckMATE`, and `Rivet/Contur` for evaluation, see Appendix B for details. From each available recast analysis, we extract the upper limit on the di-scalar cross section at 95% CL and finally save the strongest bound as the result for that scan point.

The resulting simplified model bounds are displayed in Fig. 4.7:

(a) We begin with the fermiophilic decays in Fig. 4.7a, which yield several third generation quarks and W bosons if the S^{++} is involved. The $4t$(-like) channels are constrained the strongest, while channels with multiple bottom quarks are less so. In Section 4.5, we propose a search strategy for one of these channels, $S^{++}S^{--} \to W^+ t\bar{b} W^- \bar{t} b$.

(b) First among the fermiophobic channels we show the ones featuring an S^{++} in Fig. 4.7b. We also show the limits of the two direct searches [144], which are naturally stronger than the recast bounds.

(c) In Fig. 4.7c we show the three channels resulting from S^+S^- production. The bounds show a clear hierarchy dictated by the number of photons appearing, with $W\gamma W\gamma$ being constrained the strongest and $WZWZ$ the weakest.

(d) Next, we show the limits on the $S^\pm S^0$ channels in Fig. 4.7d. This reaffirms that photon-rich channels are more strongly constrained.

(e) To help with readability we split the $S^0 S^{0\prime}$ channels into two panels, starting with those with ≥ 2 photons in Fig. 4.7e, all of which are quite strongly constrained.

(f) Finally, Fig. 4.7f shows the bounds on the $S^0 S^{0\prime}$ channels with at most 1 photon.

The bounds in Fig. 4.7 have been derived from recasts of [121, 123, 124, 144, 153–164]. More detailed information about which searches provide the strongest bounds for which di-scalar channels is given in Tabs. C.1 and C.2 in Appendix C.3. The full numerical results displayed in Fig. 4.7 are available on `https://github.com/manuelkunkel/scalarbounds`.

Before concluding our study of the simplified model bounds, some comments about the advantages and limitations of our results are in order. The key advantage of the simplified model bounds lies in their ease of use. Using the upper limits in Fig. 4.7 requires calculating cross sections and branching ratios but completely eliminates the need for recasting, thus saving on computation time and simplifying the technical setup.

The simplified model approach comes with some downsides however. We recall that — apart from the di-scalar channels featuring $S^{\pm\pm} \to W^\pm W^\pm$ covered by [144] — the bounds presented

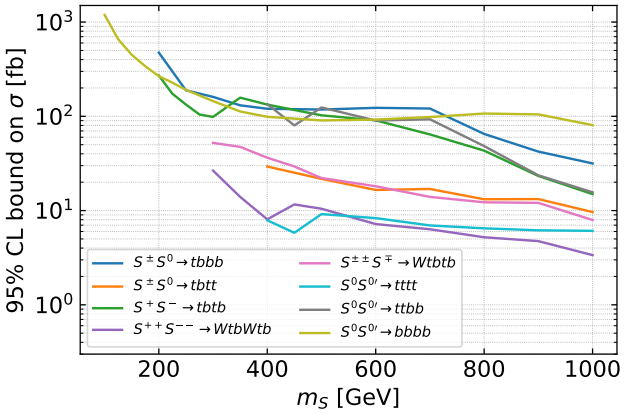

(a) Scalar pair with decays to quarks

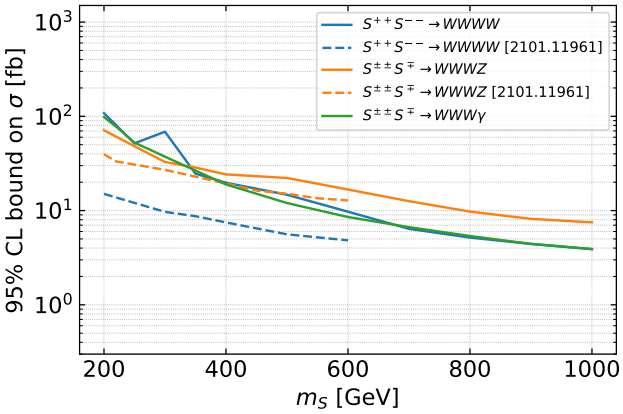

(b) $S^{++}S^{--}$ and $S^{\pm\pm}S^{\mp}$ with di-boson decays

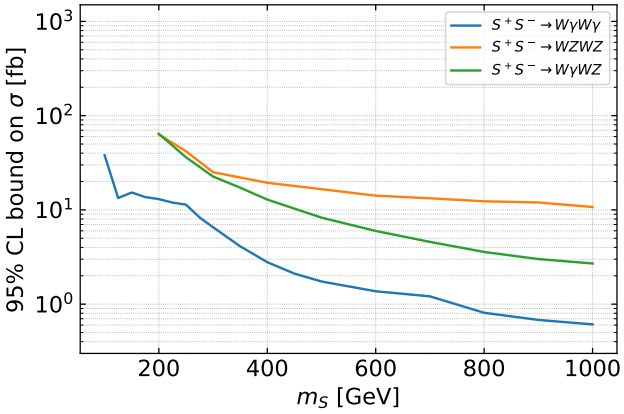

(c) S^+S^- with di-boson decays

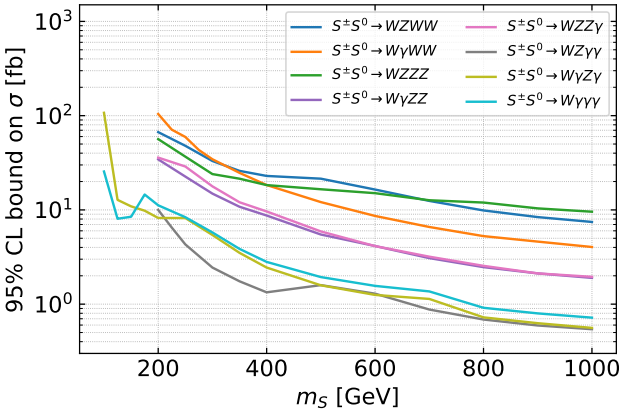

(d) $S^\pm S^0$ with di-boson decays

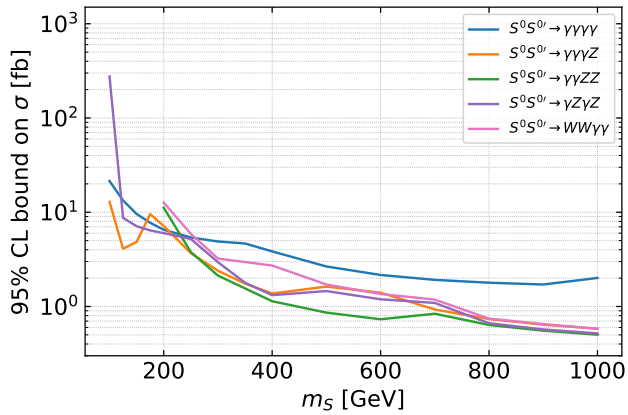

(e) $S^0S^{0\prime}$ with di-boson decays with ≥ 2 photons

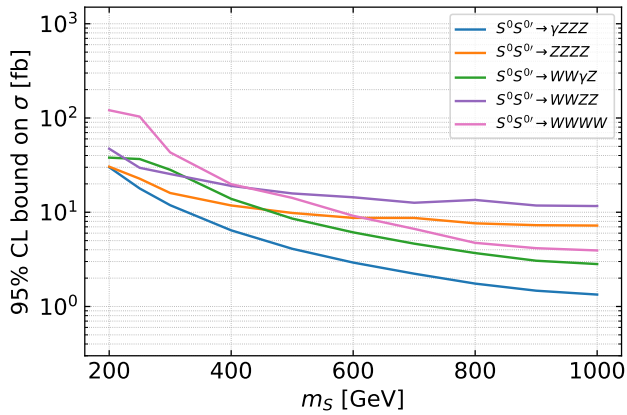

(f) $S^0S^{0\prime}$ with di-boson decays with ≤ 1 photons

Figure 4.7: Upper limits on the cross section of the di-scalar channels from Drell-Yan pair production. The scalars decay to (a) third generation quarks or (b)-(f) two vector bosons. Both scalars are assumed to have the same mass. The analyses contributing to the bounds are [121, 123, 124, 144, 153–164] (see Tab. C.1 and Tab. C.2 in Appendix C.3 for details). The numerical values of the limits are available on `https://github.com/manuelkunkel/scalarbounds`.

in Fig. 4.7 are derived from recasts of BSM searches or SM measurements. Therefore, the most important limitation of our results is that they are only based on searches and measurements by ATLAS, CMS, and LHCb, for which recasts are available in `MadAnalysis5`, `CheckMATE`, or `Rivet/Contur`. This is the case for only a fraction of LHC searches and measurements, with especially the latest and most advanced searches being underrepresented. Our bounds can certainly be improved by recasting additional searches. Performing all these recasts is beyond the scope of this work and instead requires a dedicated effort by the collider phenomenology community.

Another limitation of the simplified model approach lies in the fact that limits are extracted for each di-scalar channel separately. In a realistic model with an extended scalar sector however, there may well be several scalar states with the same charge, each of which have several possible decay channels, leading to a plethora of di-scalar channels. Applying the simplified model bounds is nontrivial in such a case. In the following, we therefore discuss how to extract reliable limits in several template scenarios which cover all possibilities.

Drell-Yan production, single scalar: We start with the case of DY production of a single particle, i.e. $S^{++}S^{--}$ or $S^{+}S^{-}$. There is a single relevant production cross section $\sigma(pp \to SS^*)$. If the scalar only has a single decay mode, the bound on the mass can immediately be obtained from Fig. 4.7 by drawing in $\sigma(pp \to SS^*)$ and reading off the intersection with the relevant bound. If the scalars have several decay channels, it is necessary to calculate $\sigma(pp \to SS^*) \times \mathrm{Br}(S \to XX^{(\prime)}) \times \mathrm{Br}(S \to YY^{(\prime)})$ for each matching di-scalar channel $XX^{(\prime)}YY^{(\prime)}$ and then compare each separately to the corresponding limit in Fig. 4.7. A conservative final result is the strongest of these bounds. As several of the channels may contribute to the same signal regions, the bound can be improved by performing a full simulation considering all decay channels simultaneously. An example for this case is an $\mathrm{SU}(2)_L$ singlet with $Y = 2$.

Drell-Yan production, unique scalar pair: The next complicated case is to add a multiplet where each charge eigenstate appears only once. DY production then leads to the scalar pairs listed in Eq. (4.25) (apart from $S^0 S^{0\prime}$) with only one contribution to each channel. In addition to $pp \to SS^*$, this case also contains the production $pp \to S_1 S_2$ with $S_1 \neq S_2$, leading to more di-scalar channels. A conservative bound on these new channels can be obtained analogously to the former case. An example of this case is the custodial quintuplet η_5 in the SU(5)/SO(5) coset discussed in Section 4.4.

The novel feature of this case is that there might be distinct channels leading to very similar signatures, e.g. $S^{\pm\pm}S^{\mp} \to W^{\pm}W^{\pm}W^{\mp}\gamma$ and $S^{\pm}S^{0} \to W^{\pm}\gamma W^{+}W^{-}$. As long as all scalars are close in mass, combining the two channels can lead to a more realistic bound. For example, we might sum up the cross sections times branching ratios of all di-scalar channels that contribute to the same signal region of a search. This is only valid as long as the acceptances are similar across all channels. We discuss an explicit example of this approach in Section 4.4.2.

Drell-Yan production, multiple scalar pairs: In a full model there may also be several states with the same electric charge, thus creating several contributions to at least some of the scalar pairs in Eq. (4.25). If all states are close to mass degenerate, the different contributions can be summed up as described in the previous paragraph. An example of this case is the bitriplet in the SU(5)/SO(5) coset.

Non Drell-Yan production and/or new decay channels: In models where the dominant pair production mode is not Drell-Yan but e.g. resonant production via a heavy resonance, the limits in Fig. 4.7 cannot be applied directly. Using bounds extracted from recasts plays in our favour here: The searches are not dedicated to the specific final state and production mechanism we apply them to, as they would be with a direct search. This gives us some leeway, since the different kinematics typically have a limited effect on the bounds. Considering the case of resonant production, the applicability naturally depends on the mass of the resonant particle: We can expect the limits in Fig. 4.7 to provide a good estimate for a moderate mass, while a multi-TeV resonance will lead to strongly boosted scalars which may alter acceptances significantly. In either case, a full simulation is needed to extract a reliable bound. Similarly, the limits in Fig. 4.7 may be partially applicable to different decay channels, such as cascade or three body decays.

4.4 Bounds on the SU(5)/SO(5) model

The simplified model approach taken in the previous section can be used to obtain conservative bounds for a large class of models. The generality comes at the cost of obtaining weaker bounds than a dedicated model study can provide. To quantify this effect we study a full model with an extended scalar sector in this section [1]. Of the three EW cosets present in the Ferretti models, we choose the SU(5)/SO(5) coset for this model specific investigation since it is the only one that contains a doubly charged scalar, thus covering the full breadth of the simplified model bounds. After summarising the model's phenomenology, we derive bounds on the full model and compare the results to the estimates obtained from the simplified model bounds in Fig. 4.7.

4.4.1 Phenomenology

The SU(5)/SO(5) model has been studied since the early days of composite Higgs models [25]. Within the context of the Ferretti models, early discussions of this real coset can be found in [165] and a first rough sketch of its LHC phenomenology is given in [32]. A thorough study of the model aspects has been performed in [105], which also includes a discussion of the phenomenology based on a few benchmark points. In this section we expand on the work of [105] and present a complete characterisation of the model's phenomenology.

We recall from Section 3.3.1 that the SU(5)/SO(5) coset contains 14 pNGBs: the Higgs

degrees of freedom, a singlet η, and an EW bitriplet that can be decomposed into a custodial fiveplet η_5, triplet η_3, and singlet η_1,

$$\eta_5 = (\eta_5^{++}, \eta_5^{+}, \eta_5^{0}, \eta_5^{-}, \eta_5^{--}), \quad \eta_3 = (\eta_3^{+}, \eta_3^{0}, \eta_3^{-}), \quad \eta_1 = \eta_1^{0} \tag{4.26}$$

which drive the BSM phenomenology of the model. We note that this superficially matches the Georgi-Machacek model [166, 167] with an additional singlet, but the scalars have different parities in the two models which significantly impacts the phenomenology [105]. The scalar potential induces a mixing among states of equal charge. We make the simplifying assumption that the mixing is negligibly small and take the custodial multiplets to have separate masses m_5, m_3, and m_1, but being mass degenerate within each multiplet. There will generically be mass splittings between the multiplets. Since they are caused by EWSB we expect the relative splitting to be of order v/m_i with the details depending on the scalar potential. In the following analysis we leave the mass differences as free parameters that can go up to 200 GeV.

All states in Eq. (4.26) are odd under a CP transformation, with the exception of η_3^0. In principle, the neutral triplet can therefore develop a VEV. The consequences of this are discussed in [105]. In this work we limit ourselves to the case $\langle \eta_3^0 \rangle = 0$. Finally, there is another parameter of the model: the pNGB decay constant f_ψ, which enters in cross sections and branching ratios through the combination $\sin\theta = v/f_\psi$. During our numerical studies we found that taking the simplifying limit $\theta \to 0$ has negligible effect on the phenomenology. We therefore employ it in all simulations in this section.

We recall from the discussion in Section 4.2 that the phenomenology of the pNGBs is determined by three types of couplings. The covariant derivative gives rise to couplings of two scalars to one (or two) EW gauge bosons, which determine the DY production cross sections as well as cascade decays in case of sufficiently large mass splittings; the S-S-V couplings for the SU(5)/SO(5) model are listed in Appendix C.1. The anomaly term couples all pNGBs (apart from the CP-even η_3^0) to two gauge bosons, and PC induces couplings of scalars to two third generation quarks. Whether the latter are generated depends on the embeddings of the top partners, see [105] for a classification.

In Fig. 4.8 we show the Drell-Yan production cross sections of all scalar pairs at the LHC at $\sqrt{s} = 13$ TeV. The cross sections were calculated at leading order and then multiplied with a flat K-factor of 1.15 to account for QCD corrections [168]. Depending on the channel, the cross section varies by about one order of magnitude. The signatures resulting from pair production depend strongly on whether the pNGBs couple to quarks or not. We will not make an explicit choice of top partner embeddings but follow the approach taken in Section 4.3 to separately consider a fermiophobic and a fermiophilic scenario.

We begin the discussion with the fermiophobic case. The di-boson branching ratios of the $\eta_{3,5}^{+}$ and the $\eta_{1,5}^{0}$ are shown as a function of mass in Figs. 4.4a and 4.4b, and can also be read off from the leftmost edges in the corresponding panels of Figs. 4.9 and 4.10 for $m_S = 600$ GeV.

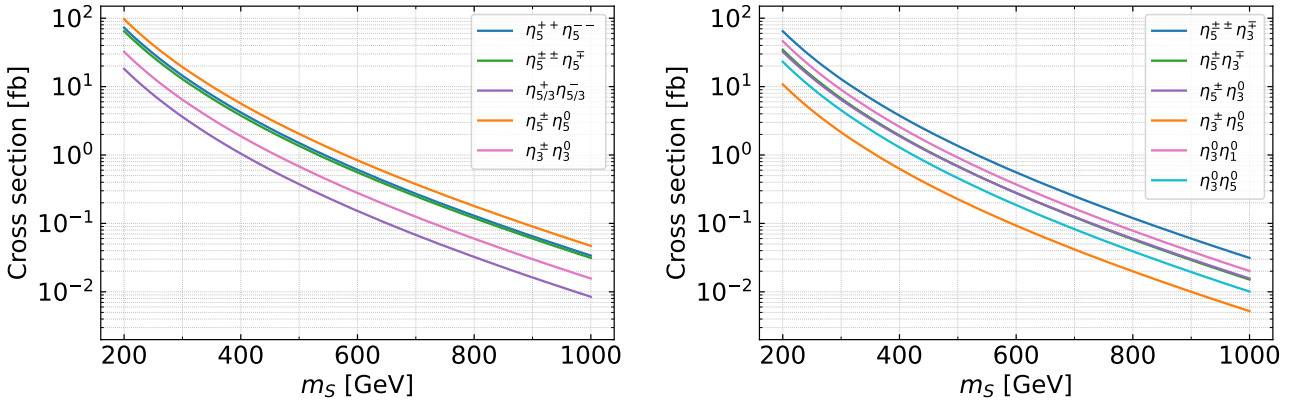

Figure 4.8: Cross sections for the Drell-Yan production of SU(5)/SO(5) pNGBs at the LHC with $\sqrt{s} = 13\,\text{TeV}$, assuming the same mass for all states of the custodial singlet, triplet, and quintuplet. Note that the $\eta_1^0\eta_5^0$ combination is not allowed as they are both CP-odd.

The singly charged states decay as

$$\eta_{3,5}^+ \to W^+\gamma,\, W^+Z. \tag{4.27}$$

The branching ratios for both states coincide (in the limit $\theta \to 0$) and we have $\text{Br}(\eta_{3,5}^+ \to W^+\gamma) \approx \cos^2\theta_W \approx 78\%$, as already pointed out in [105]. The neutral singlet and quintuplet decay as

$$\eta_{1,5}^0 \to \gamma\gamma,\, \gamma Z,\, ZZ \tag{4.28}$$

with comparable branching ratios. The channel $\eta_{1,5}^0 \to W^+W^-$ is strongly suppressed by $\sin^4\theta \sim 10^{-3}$ and thus completely negligible. The same suppression applies to the decay of the doubly charged scalar,

$$\eta_5^{++} \to W^+W^+. \tag{4.29}$$

However, since this is the only available decay channel, we cannot neglect it and we do not take $\sin\theta \to 0$ in its numerical treatment. We refer to the discussion around Eqs. (3.66) and (3.67) for an explanation of the hierarchies. Finally, we turn to the η_3^0 which is the odd one out due to the absence of anomaly couplings. Instead of di-boson channels, it therefore undergoes three body decays mediated by off-shell pNGBs:

$$\eta_3^0 \to W^+W^-\gamma,\, W^+W^-Z \quad \text{via } \eta_{3,5}^{\pm(*)} \tag{4.30}$$

$$\eta_3^0 \to Z\gamma\gamma,\, ZZ\gamma,\, ZZZ \quad \text{via } \eta_{1,5}^{0(*)} \tag{4.31}$$

The branching ratios of η_3^0 are shown in Figs. 4.10c and 4.10d for two mass hierarchies. As a result of the simplifications we have taken, a cancellation takes place among certain three body decay channels: When $\theta = 0$ and $m_3 = m_5$, the contributions to Eq. (4.30) cancel exactly, as do the ones in Eq. (4.31) if $m_1 = m_3 = m_5$. In this limit, the η_3^0 would be long lived and leave

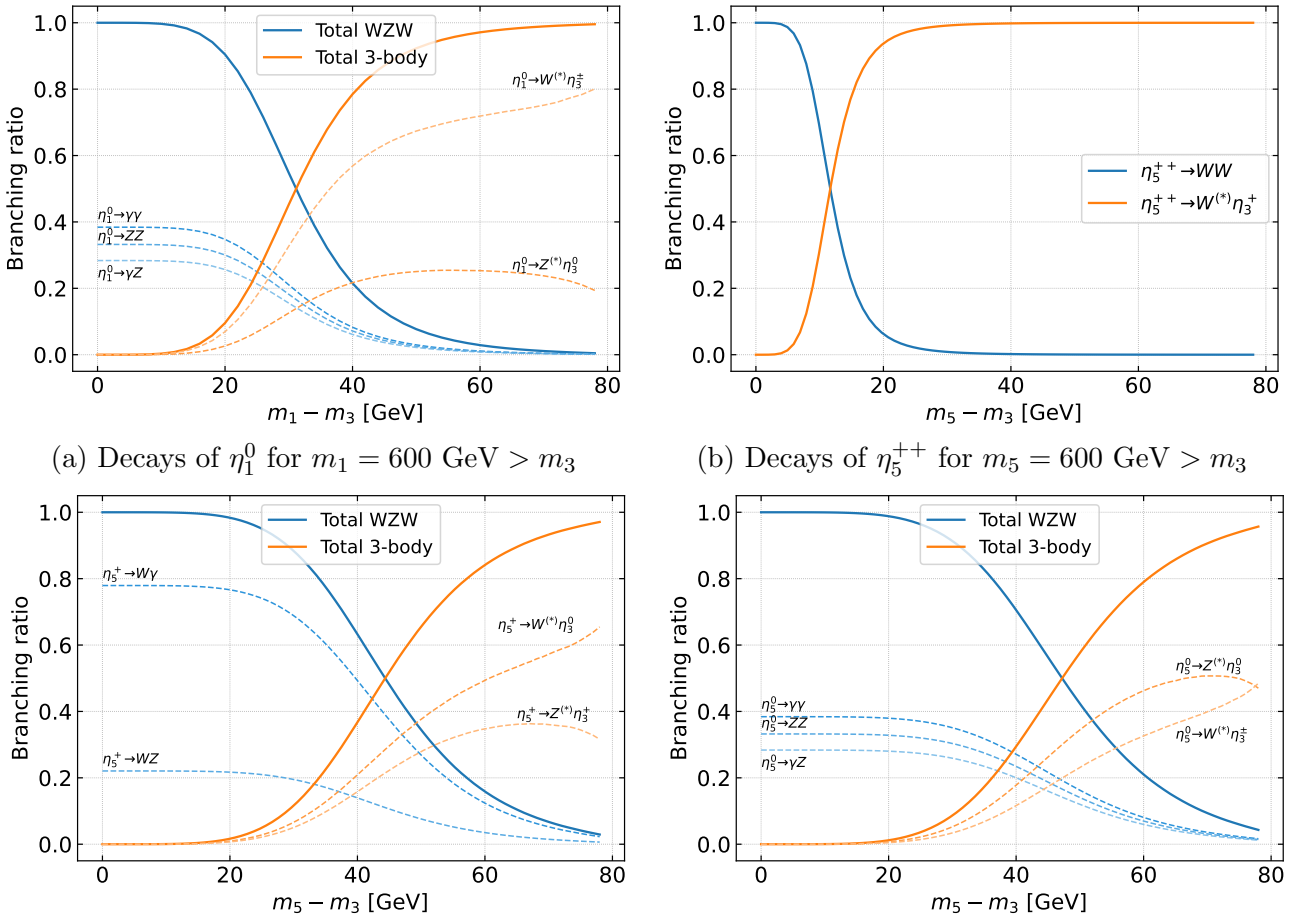

(a) Decays of η_1^0 for $m_1 = 600$ GeV $> m_3$

(b) Decays of η_5^{++} for $m_5 = 600$ GeV $> m_3$

(c) Decays of η_5^+ for $m_5 = 600$ GeV $> m_3$

(d) Decays of η_5^0 for $m_5 = 600$ GeV $> m_3$

Figure 4.9: Overview of the pNGB decays in the fermiophobic scenario. The mass of the decaying particles is set to 600 GeV. The heavier state decays either via the anomaly into di-boson final states or via an (off-shell) gauge boson into a lighter pNGB.

the detector before it decays. In practice however, we expect at least a small mass split, so η_3^0 decays promptly to three vector bosons. Still, the cancellation does have an impact on the phenomenology: it is the reason why the charged channels in Fig. 4.10d are strongly suppressed when $m_1 \gg m_5 \gtrsim m_3$. We explore this effect further in Section 4.4.3.

The decays discussed so far are always possible but may be subdominant if there is a lighter scalar multiplet that allows for cascade decays. For example, if $m_5 > m_3 > m_1$,

$$\eta_5^{++} \to W^{+(*)}\eta_3^+, \quad \eta_5^+ \to Z^{(*)}\eta_3^+, W^{+(*)}\eta_3^0, \quad \eta_5^0 \to W^{\pm(*)}\eta_3^\mp, Z^{(*)}\eta_3^0, \tag{4.32}$$

$$\eta_3^+ \to W^{+(*)}\eta_1^0, \quad \eta_3^0 \to Z^{(*)}\eta_1^0. \tag{4.33}$$

Note that $\eta_5 \to Z^{(*)}\eta_1^0$ is absent since both states are CP-odd. If the mass splitting lies below $m_{W/Z}$, the vector boson will be off-shell. The decays into an on-shell vector boson and an off-shell scalar are suppressed by the small anomaly couplings of the pNGBs. When the mass splitting is large enough to allow for a two body decay, the cascade decays will clearly dominate over the di-boson channels. To investigate the hierarchies for splittings below 80 GeV, we show the competing branching ratios in Figs. 4.9, 4.10a and 4.10b. We find that cascade and anomaly

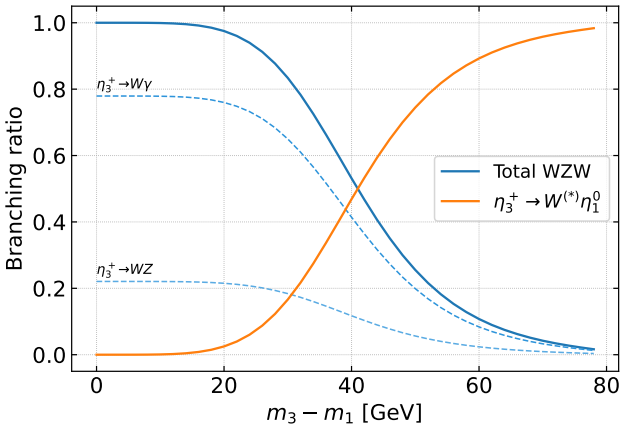

(a) Decays of η_3^+ for $m_5 \gg m_3 = 600$ GeV $> m_1$

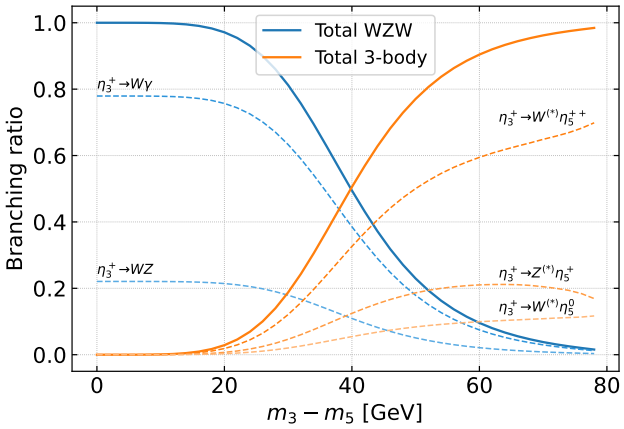

(b) Decays of η_3^+ for $m_1 \gg m_3 = 600$ GeV $> m_5$

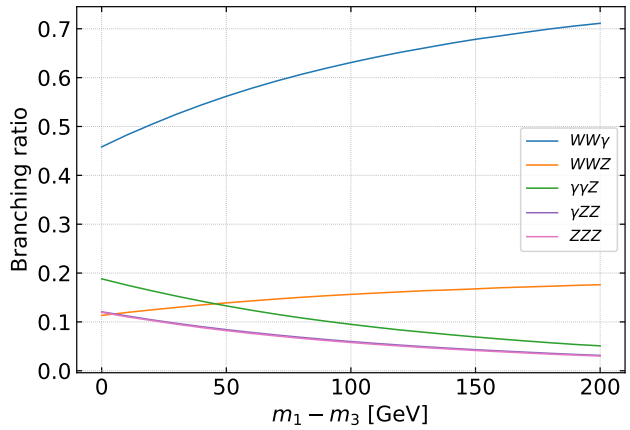

(c) Decays of η_3^0 for $m_5 \gg m_1 > m_3 = 600$ GeV

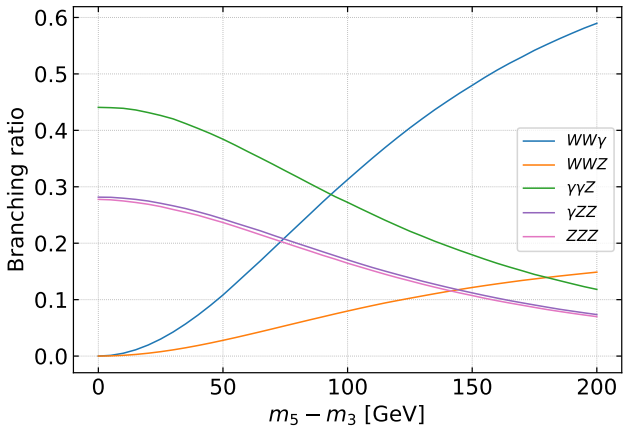

(d) Decays of η_3^0 for $m_1 \gg m_5 > m_3 = 600$ GeV

Figure 4.10: Overview of the pNGB decays in the fermiophobic scenario (continued from Fig. 4.9). The neutral triplet component decays into three gauge bosons, as it does not couple to the anomaly.

decays are comparable when the mass splitting is between 30 and 50 GeV. For larger splittings the cascade decays dominate. The two exceptions to this are the η_5^{++} (Fig. 4.9b) due to the suppressed anomaly coupling, and η_3^0 for which the cascade decays dominate over the anomaly-induced three body decays whenever they are open. In Fig. 4.11 we show a Feynman diagram for pNGB pair production that includes both cascade decays and the three body decay of η_3^0. This illustrates that the signatures in the full model can be significantly more complicated than the four vector boson channels studied in Section 4.3.

We now turn to the fermiophilic scenario. The couplings to quarks in Eq. (4.21) scale as

$$\kappa_t^{\eta_i^0} = c_t^i \frac{m_t}{f_\psi}, \quad \kappa_b^{\eta_i^0} = c_b^i \frac{m_b}{f_\psi}, \quad \kappa_{tb}^{\eta_j^+} = c_{tb}^j \frac{m_t}{f_\psi}. \tag{4.34}$$

For definiteness we set $f_\psi = 1$ TeV and all $c = 1$. While the anomaly couplings are still present, they are clearly subdominant to the quark couplings. We therefore have

$$\eta_{3,5}^+ \to t\bar{b} \tag{4.35}$$

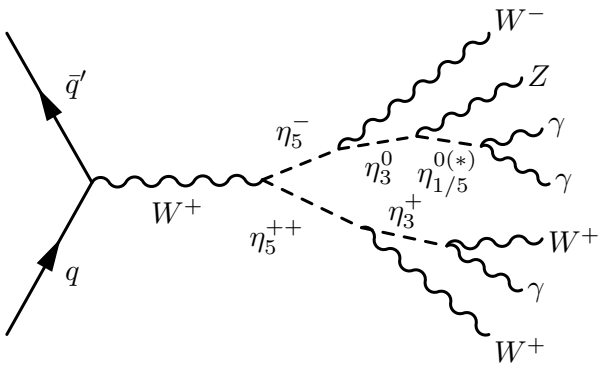

Figure 4.11: Example of Drell-Yan production of two pNGBs with cascade and anomaly decays. If the triplet is the lightest multiplet, the η_3^0 undergoes three-body decays via off-shell pNGBs.

and

$$\eta_{1,3,5}^0 \to b\bar{b} \quad \text{if } m_{\eta_i} < 2m_t, \tag{4.36}$$

$$\eta_{1,3,5}^0 \to t\bar{t} \quad \text{if } m_{\eta_i} > 2m_t. \tag{4.37}$$

For masses below but close to the $t\bar{t}$ threshold we also take decays into one on-shell and one off-shell top quark into account. The doubly charged scalar does not have a coupling to two quarks. Instead it can undergo three body decays via an off-shell $\eta_{3,5}^+$. The anomaly coupling of the η_5^{++} is not only loop induced but is further suppressed by a factor of $\sin^2\theta$. With the couplings listed above, it turns out that this suppression is strong enough for the decay

$$\eta_5^{++} \to W^+ t\bar{b} \tag{4.38}$$

to dominate over $\eta_5^{++} \to W^+W^+$ despite the reduced phase space. If there are mass differences between the multiplets, cascade decays as in Eq. (4.32) are opened up. However, in the fermiophilic case, they are not as competitive as in the fermiophobic case: For mass splits below the $m_{W/Z}$ thresholds the two body decays to quarks are dominant, while above the threshold the hierarchy depends on the c coefficients. Things are more complicated for η_5^{++}: for mass splits below 25 GeV the decay into quarks is dominant, while the cascade decay $\eta_5^{++} \to W^{+(*)}\eta_3^+$ becomes competitive around $\Delta m = 50$ GeV and dominates for larger splittings.

4.4.2 Application of simplified model bounds

Having detailed the model's phenomenology, we now set about determining constraints on the scalar masses. In a first step we apply the simplified model bounds derived in Section 4.3 to determine a baseline. The following discussion also serves to illustrate how to get the most out of the simplified model bounds. We focus only on the quintuplet η_5, thereby avoiding the complications of cascade and three body decays, and only consider the fermiophobic case. In Section 4.3 we saw that the di-scalar channels with at least two photons yield the strongest constraints. Within the quintuplet there are four such channels. In Fig. 4.12a, we compare the

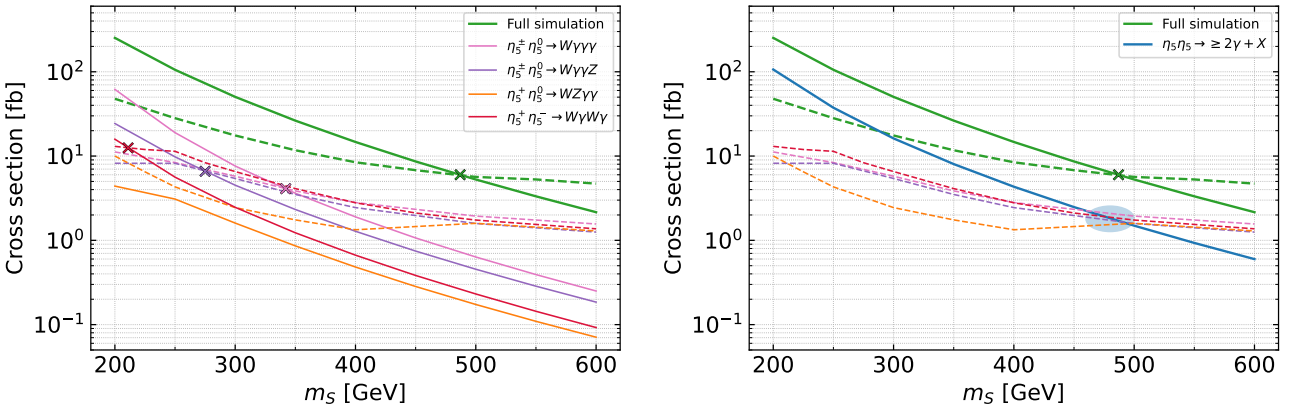

(a) Bounds from individual channels

(b) Bounds from sum of multiphoton channels

Figure 4.12: Application of the model independent bounds to a specific model: the custodial quintuplet η_5 from the SU(5)/SO(5) coset. In (a) we determine the bounds from the dominant individual channels by comparing the cross section time branching ratio from the model (solid) with the upper limits from Fig. 4.7 (dashed). In green we show the results of a full simulation. The blue line in (b) is the sum of the individual multi-photon cross sections shown in (a). Further details are given in the text.

cross section times branching ratio (solid lines) with the corresponding bounds from Fig. 4.7 (dashed lines). Three channels lead to a bound on m_S, with the strongest bound of 340 GeV stemming from $\eta_5^\pm\eta_5^0 \to W\gamma\gamma\gamma$. In order to assess the quality of the mass bound from the individual channels, we also perform a full simulation in which all states contained in the quintuplet are pair produced and decayed into di-bosons as discussed in the previous section. The solid green line denotes the sum of the pair production cross sections of all scalar pairs from the quintuplet and the dashed green line shows the corresponding upper limit at 95% CL. For the full model the upper limit is conceptually a bit different than for individual channels: given the convolution of pair productions with the corresponding decay channels, it is the upper limit on the overall cross section of these events. The bound obtained from the full simulation is $m_S \geq 485$ GeV, a significant improvement over the individual channels. The discrepancy between simplified model bounds and the full simulation was predictable: the latter collects all multiphoton contributions to the signal regions of constraining analysis [154] (listed in Tab. 4.4 for reference), while they are spread over three channels for the simplified model bounds. In fact, around $m_S \sim 500$ GeV, the signal region yielding the strongest limit is the same for all of the multiphoton channels (SRaaWH), and the limits are very close in magnitude. This allows us to perform a strong combination of bounds: we add up the cross section times branching ratio of all multiphoton channels, shown as a solid blue line in Fig. 4.12b, and compare it to the bounds on the individual channels. The resulting mass bound, indicated by the region shaded in blue, lies between 460 and 500 GeV, which is in agreement with the full simulation. This example highlights both the usefulness and limitations of the simplified model bounds.

4.4.3 Bounds in the fermiophobic case

We now turn to studying the full bitriplet with decays into vector bosons. In the previous section, we saw that the effective cross section of multiphoton production is of crucial importance for the mass bound, and how many scalar pairs ultimately lead to multiphoton final states depends on the mass hierarchies. To explore this further, we begin with several one dimensional mass scans with a single parameter m_S and fixed mass splits between the multiplets. Concretely, we study the following four scenarios:

$$\text{S-eq:} \quad m_3 = m_S - 2 \text{ GeV}, \quad m_5 = m_S, \quad m_1 = m_S + 2 \text{ GeV} \tag{4.39a}$$

$$\text{S-135:} \quad m_1 = m_S - 50 \text{ GeV}, \quad m_3 = m_S, \quad m_5 = m_S + 50 \text{ GeV} \tag{4.39b}$$

$$\text{S-531:} \quad m_5 = m_S - 50 \text{ GeV}, \quad m_3 = m_S, \quad m_1 = m_S + 50 \text{ GeV} \tag{4.39c}$$

$$\text{S-351:} \quad m_3 = m_S - 50 \text{ GeV}, \quad m_5 = m_S, \quad m_1 = m_S + 50 \text{ GeV} \tag{4.39d}$$

We chose mass splits of 50 GeV since they are expected to be a fraction of the Higgs VEV and we saw in Figs. 4.9 and 4.10 that around 50 GeV both cascade and anomaly decays are important. Each mass scenario has a different phenomenology: In S-eq, all particles decay via the anomaly and η_3^0 exhibits three body decays. We introduce a small mass split of 2 GeV to avoid a long lived η_3^0, see the discussion below Eq. (4.31). In S-351 we also have the triplet as the lightest states with the heavier ones decaying to η_3. In S-135 (S-531), it is the singlet (quintuplet) that decays exclusively via the anomaly.

The bounds on m_S in the four benchmark scenarios are shown in Fig. 4.13. The blue line shows the model cross section and the orange line indicates the upper limit σ_{95} on the convolution of production and decay channels. As discussed above, the strongest bounds come from the multiphoton plus jet search [154]. The kink in σ_{95} is due to a change in dominant signal region from SRaaWH to SRaaSH, see Tab. 4.4. The differences in mass bounds between the scenarios are a mixture of differences in cross section and in σ_{95}: Scenario S-531 has the largest cross section since the populous quintuplet is the lightest. However, this leaves many η_5^{++} after the cascade decays are done, which decay to W^+W^+ and therefore do not contribute to the signal regions of [154], leading to the weakest σ_{95} limits of the studied scenarios. The two effects combine in a way that gives the weakest mass bound, 640 GeV. On the other hand, the strongest bound of 720 GeV is obtained from scenario S-351, which trades a reduced cross section due to the heavier η_5 for the lightest multiplet η_3 having a large branching ratio into multiphoton channels. The scenario S-eq lies between them with $m_S \geq 660$ GeV.

Next, we study the dependence of the bounds on the mass splits between the multiplets. To this end we consider two benchmarks[2] where one of the multiplets is decoupled:

$$\text{S-31}: \quad m_5 \gg m_{3,1}, \qquad \text{S-35}: \quad m_1 \gg m_{3,5} \tag{4.40}$$

[2]Note that the case $m_3 \gg m_{1,5}$ is already covered by the discussion in Section 4.4.2 where we only considered the quintuplet since the η_5 and η_1 do not couple, reducing this case to $\eta_5\eta_5$ production.

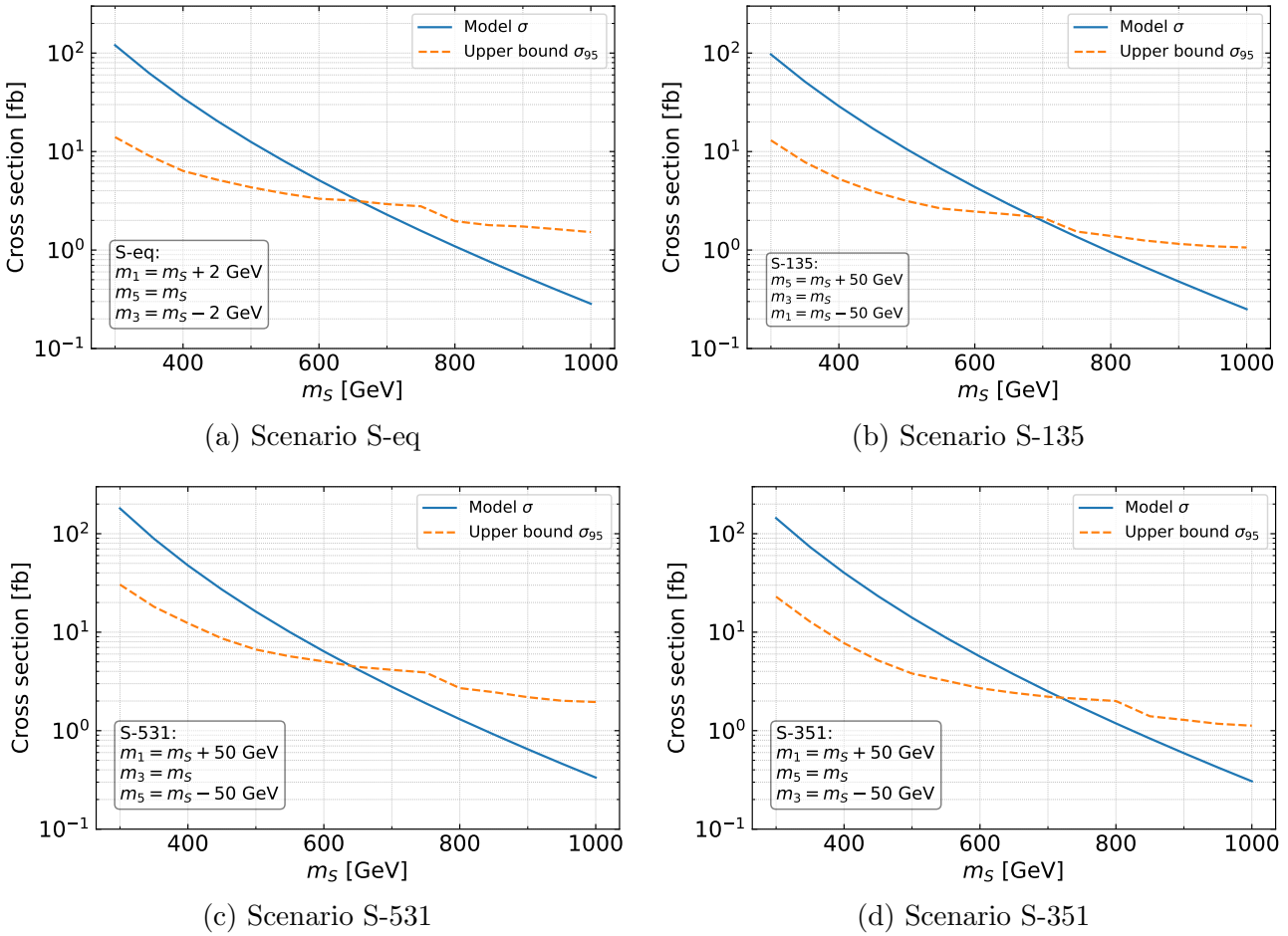

(a) Scenario S-eq

(b) Scenario S-135

(c) Scenario S-531

(d) Scenario S-351

Figure 4.13: Bounds on the pNGB masses for the Drell-Yan production of the full bi-triplet for multiple benchmark mass spectra defined in Eq. (4.39). In (a), all masses are approximately equal. In the remaining panels, there is a 50 GeV mass split between the multiplets.

We scan over the triplet mass and the mass split $\Delta m_{13} = m_1 - m_3$ or Δm_{53} in the range $|\Delta m| \leq 200$ GeV. For each point we simulate the DY production of all scalar pairs both within and across multiplets. Fig. 4.14 shows the results for scenario S-31. As solid lines we show the exclusion contours at 95% CL (black) and 68% CL (grey). Additionally, we show the total production cross section as a heatmap and dotted contours. This serves to identify interesting regions as those where the bound deviates from the cross section contour. We can identify three such regions by following the 95% CL bound: In the lower half of the plot, the singlet is the lightest state so the signatures are determined by the anomaly decays of η_1^0. The bounds weaken from $\Delta m_{13} = -200$ GeV to -100 GeV since the $V = W, Z$ from the $\eta_3 \to \eta_1 V$ decays get softer. This is followed by an increase in the bounds as the $\eta_3^+ \to W^+\gamma$ decay sets in towards $\Delta m_{13} = 0$. In the upper half of the plot the bounds decrease again as $\mathrm{Br}(\eta_3^0 \to \gamma\gamma Z)$ reduces with growing Δm_{13}. Finally we note the region at $m_3 = 700$ GeV where a few points are excluded at 68% CL despite being surrounded by allowed point. This is due to a switch in the dominant signal region from SRaaWL to SRaaSH analogous to the kinks in Fig. 4.13.

In Fig. 4.15 we repeat this analysis for scenario S-35. We again follow the 95% CL bound to understand the features, starting at $\Delta m_{53} = -200$ GeV where the quintuplet decays through

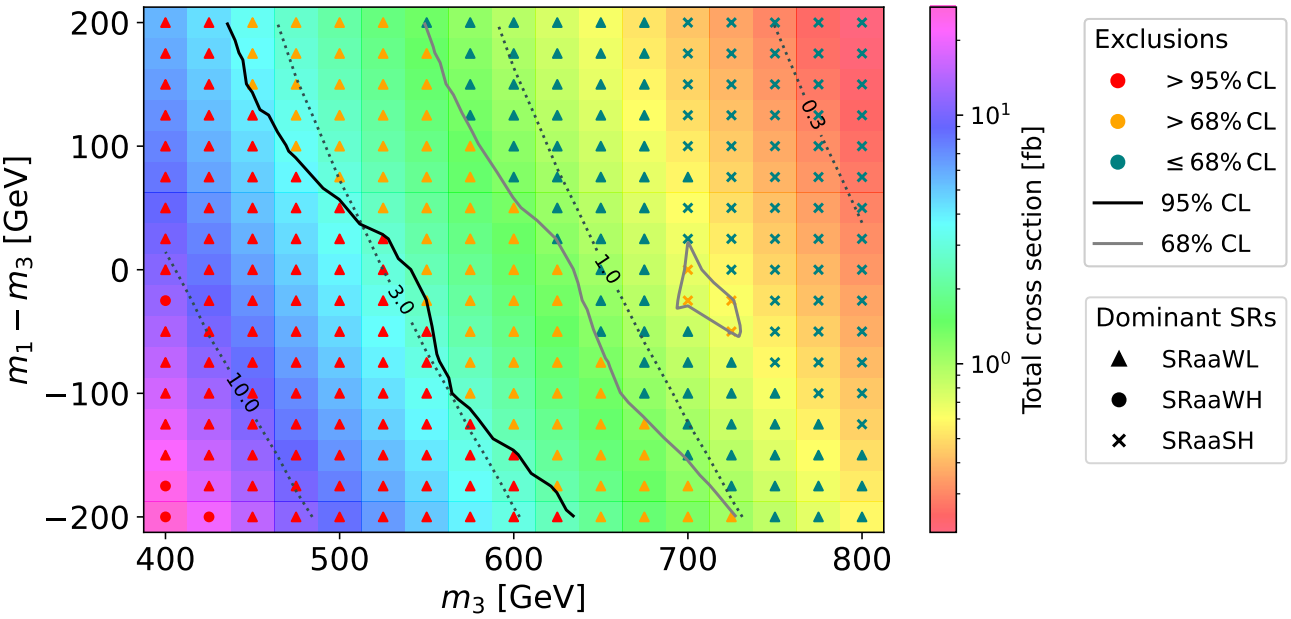

Figure 4.14: Bounds on the pNGB masses for the Drell-Yan production of the custodial triplet η_3 and singlet η_1 with the quintuplet η_5 decoupled (scenario S-31). Depending on the mass hierarchy, the pNGBs decay either into di-bosons or into one vector boson and a lighter pNGB. The heatmap and the dotted contours show the total cross section. The bounds are obtained from [154], with the dominant signal region indicated by the marker symbol (see Tab. 4.4 for details). The 95% and 68% CL exclusion contours are drawn in solid black and grey, respectively.

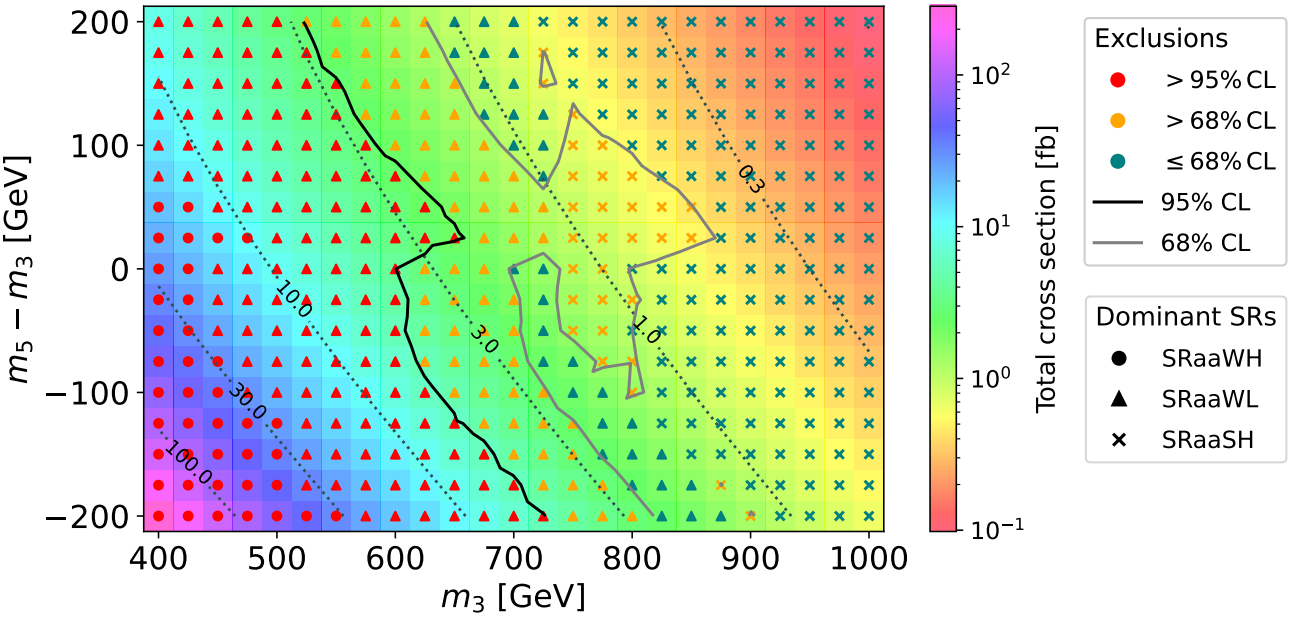

Figure 4.15: Bounds on the pNGB masses for the Drell-Yan production of the custodial triplet η_3 and quintuplet η_5 with the singlet η_1 decoupled (scenario S-35). Depending on the mass hierarchy, the pNGBs decay either into di-bosons or into one vector boson and a lighter pNGB. The heatmap and the dotted contours show the total cross section. The bounds are obtained from [154], with the dominant signal region indicated by the marker symbol (see Tab. 4.4 for details). The 95% and 68% CL exclusion contours are drawn in solid black and grey, respectively.

Signal region	SRaaWL	SRaaWH	SRaaSH
Number of photons	≥ 2	≥ 2	≥ 2
E_{T}^{γ} [GeV]	> 75	> 75	> 75
$E_{\mathrm{T}}^{\mathrm{miss}}$ [GeV]	> 150	> 250	> 250
H_{T} [GeV]	> 1500	> 1000	> 2000
$\Delta\phi_{\mathrm{min}}(\gamma, \mathrm{jet})$	> 0.5	> 0.5	> 0.5
$\Delta\phi_{\mathrm{min}}(\gamma, E_{\mathrm{T}}^{\mathrm{miss}})$	—	> 0.5	> 0.5

Table 4.4: Signal regions of [154] that are referenced in the text and in Figs. 4.14 and 4.15.

the anomaly. The dominant decay of the η_3^+ turns out to be into η_5^{++} which does not contribute any photons to the final state. As the η_3^+ anomaly decay becomes important around $\Delta m_{53} = -50$ GeV, we can therefore see the bounds increase relative to the cross section. This is followed by a rapid increase as Δm_{53} turns positive. This is due to the η_5^{++}: its suppressed anomaly coupling means that at $\Delta m_{53} = 25$ GeV the cascade decay into η_3^+ is already close to 100%. Combining this with the large production cross section of the η_5^{++} explains the sudden increase in photon production. Finally, with increasing Δm_{53} the bounds decrease again. This can be explained by the dependence of the η_3^0 three body decays on the mass split, see Fig. 4.10d. The channel $\gamma\gamma Z$ is enhanced for small Δm_{53} and decreases as the suppression of the channels $WW\gamma$ and WWZ lifts, thus decreasing the net number of multiphoton channels. And again, the unusual shape of the 68% CL line can be explained by a switch in the dominant signal region.

4.4.4 Bounds in the fermiophilic case

We now turn to the fermiophilic scenario where the pNGBs decay to third generation quarks. As discussed in Section 4.4.1, mass differences between the multiplets have a limited impact on the phenomenology in this case, so we limit ourselves to a one dimensional scan with all scalar masses equal to m_S. The results are shown in Fig. 4.16, where the blue line gives the sum of the DY cross sections of all scalar pairs and the orange lines indicate the upper limits on the convolution of production with all possible decays. The dominant bounds come from a search for R-parity-violating SUSY in final states with many jets and at least one lepton [121] which is implemented in `CheckMATE`. Using the default evaluation method of `CheckMATE` — selecting the most sensitive signal region as the one with the strongest expected bound and reporting the corresponding observed bound as the final result — yields the bound given by the solid orange line. However, this can lead to an unintuitive behaviour if the observed and expected bounds differ significantly, as is the case at $m_S = 325$ GeV and for $m_S \geq 450$ GeV in Fig. 4.16. The dashed orange line shows the limit obtained from a modified procedure where the strongest observed bound is chosen without reference to the expected bound. This would smooth out the line of σ_{95} and improve the mass bound to about 500 GeV. However, this is not a statistically sound approach. We discuss the differences of these two evaluation procedures

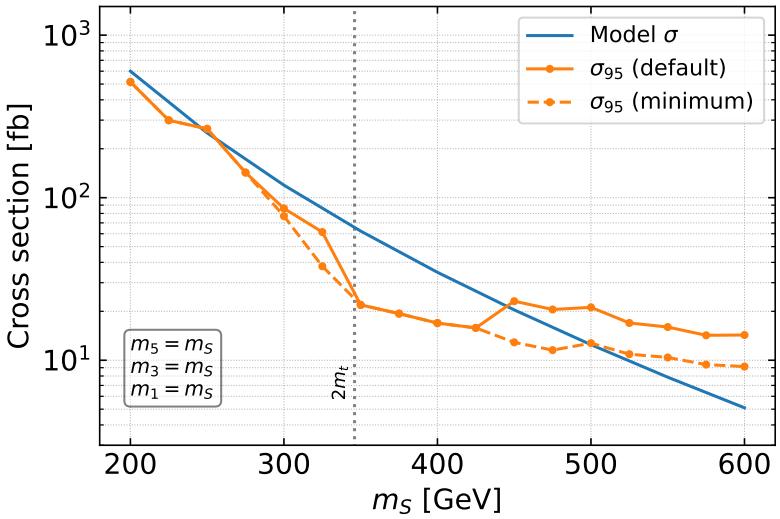

Figure 4.16: Bounds on the pNGB masses for the Drell-Yan production of the full bitriplet with decays to third generation quarks. All states are taken to be mass degenerate.

in Appendix C.2.

4.5 Deep learning-based search strategy for $pp \to S^{++}S^{--} \to W^+t\bar{b}W^-\bar{t}b$

In the previous sections we have performed a comprehensive survey of the current bounds on Drell-Yan pair production of electroweak pNGBs. The vast majority of the di-scalar channels under investigation have not been searched for at the LHC. We were therefore forced to base our bounds solely on analyses that have been recast, which imposes a twofold limitation. Firstly, a recast search is typically not optimised for the final state we are interested in, whereas a dedicated search can be very specifically designed. Secondly, only a fraction of the existing searches and measurements have been implemented in the public recasting tools. For the two di-scalar channels for which a direct search does exist [144], it provided significantly stronger bounds than the recasts. This underlines the need for further searches to fully utilise the LHC data to either discover or constrain EW pNGBs. In this section we contribute to that effort by proposing a search strategy for one of the di-scalar channels [2].

When choosing which channel to search for, there are multiple factors to consider. To maximise the chance of discovery, we look at channels with a large cross section and branching ratio (preferably 100%). The latter point suggests focusing on the fermiophilic scenario, where each state has one dominant decay channel. Another important consideration is the question of background processes. The fermiophilic di-scalar channels lead to final states with lots of hadronic activity, which implies large backgrounds at the LHC. A common method of reducing backgrounds is to focus on multilepton final states (lepton meaning electron or muon in this section). A same-sign lepton pair is particularly useful here since it cuts away the considerable

$t\bar{t}$ plus jets backgrounds. This rules out $S^+S^- \to tbtb$. In the end we decided on

$$pp \to S^{++}S^{--} \to W^+t\bar{b}W^-\bar{t}b \tag{4.41}$$

which is shown in Fig. 4.17a. We chose this channel because the three body decay channel of S^{++} had never been studied before, and because the signature mimics the production of four top quarks which has only recently been discovered [169, 170].

The goal in this section is to design an experimental search for Eq. (4.41). To evaluate our proposal, we will derive the expected cross sections that are needed for discovery or exclusion analogously to the simplified model bounds in Section 4.3. To assess the maximal reach of the LHC, we assume a centre-of-mass energy of $\sqrt{s} = 14$ TeV as well as an integrated luminosity of 3000 fb^{-1}, the dataset that is expected to be available after the HL-LHC phase has concluded [171]. While our results apply to any model featuring the process in Eq. (4.41), it is nonetheless useful to have a reference model from which we can derive concrete results. To this end we use the quintuplet from the SU(5)/SO(5) model for any model specific statements, i.e. we identify $S^{++} \to \eta_5^{++}$ and $S^+ \to \eta_5^+$.

Even while focusing on the same-sign lepton channel, the final state remains busy with multiple light and b-jets. This is a challenging scenario for a classic cut-and-count search due to limited b-tagging efficiencies and combinatorial difficulties in pairing jets to resonances. Thus, there is potential to improve upon cut-and-count searches with new approaches for handling final states with lots of hadronic activity. In recent years, deep learning techniques and in particular ideas from computer vision have been applied to particle physics with great success, e.g. to the task of differentiating jets originating from top quarks or QCD [172–174]. Inspired by these early successes, we designed a deep learning-based[3] search strategy for Eq. (4.41).

4.5.1 Process anatomy

We focus on the final state with two same-sign leptons (2SSL), i.e.

$$S^{++}S^{--} \to W^+t\bar{b}W^-\bar{t}b \to \ell^\pm\ell^\pm\, bbbb\, jjjj + p_T^{\text{miss}}. \tag{4.42}$$

A Feynman diagram for the full decay chain is shown in Fig. 4.17c. The conjugate process is also included in our analysis. The charged leptons can either directly come from W bosons, or from a τ through $W \to \tau\nu_\tau \to \ell\nu_\ell\nu_\tau$. Besides the 2SSL, the detector signature consists of missing transverse momentum due to the neutrinos, four b-tagged jets, and four light jets j.

Since the three body decay of S^{++} is mediated by an off-shell S^+, there must be a W-S^{++}-S^+ coupling, which implies that we can also produce $S^{\pm\pm}S^\mp$, see Fig. 4.17b. This channel can also yield 2SSL with a similar detector signature to our target process,

$$S^{\pm\pm}S^\mp \to Wtbtb \to \ell^\pm\ell^\pm\, bbbb\, jj + p_T^{\text{miss}} \tag{4.43}$$

[3] An overview of the basic concepts of deep learning is provided in Appendix D.

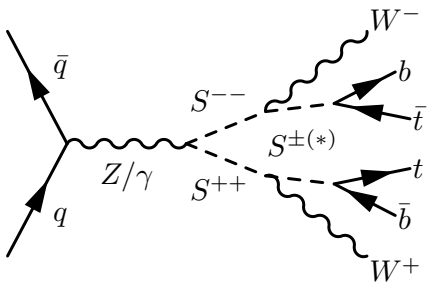

(a) $S^{++}S^{--} \to W^+t\bar{b}W^-\bar{t}b$

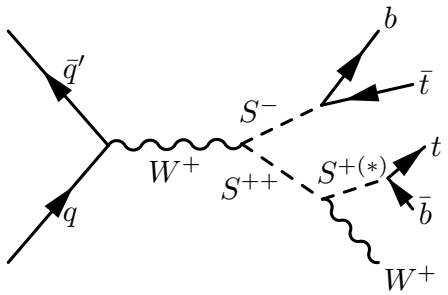

(b) $S^{\pm\pm}S^{\mp} \to Wtbtb$

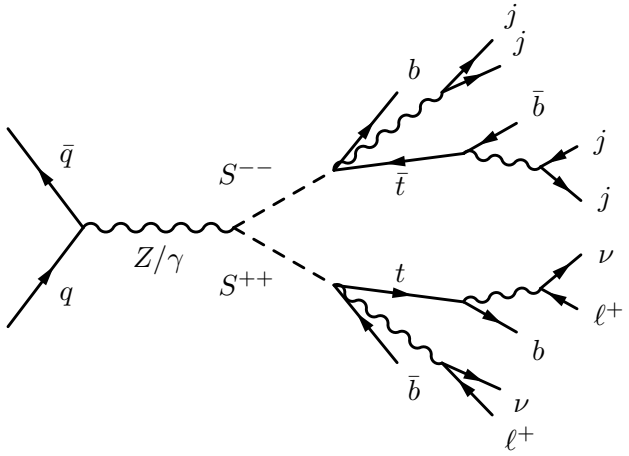

(c) Full decay chain of $S^{++}S^{--} \to W^+t\bar{b}W^-\bar{t}b$

Figure 4.17: Feynman diagrams for the processes studied in Section 4.5.

and will therefore contribute to our signal as well. In the following analysis we will look at two cases: (i) considering only the pair production of the doubly charged scalar and (ii) considering both the pair and the mixed production with the relative cross sections taken from the SU(5)/SO(5) quintuplet. There is a third process that warrants mentioning: the pair production of the singly charged state, $S^+S^- \to t\bar{b}\bar{t}b$. While it looks similar to Eq. (4.42) at first glance, its dilepton channel contains opposite-sign leptons, so it does not contribute to the signal.

4.5.2 Preselection and backgrounds

The core idea behind designing a search is to find a set of criteria by which to differentiate the signal process from its backgrounds. This is typically achieved by defining selection cuts which the signal largely passes while the background is significantly reduced. Here we use a two-stage approach: in a first step — the so-called preselection — we apply cuts on kinematic variables of the final state objects like a conventional cut-and-count analysis. The events that pass the preselection are then used to train a neural network (NN) classifier which provides the final discrimination between signal and background.

We have already mentioned one of our preselection criteria: we demand all events to have exactly two same-sign leptons. More precisely, we require two isolated leptons with equal

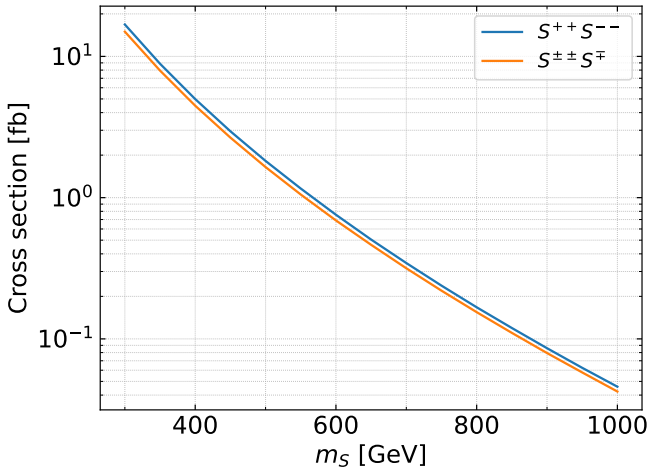

Figure 4.18: Drell-Yan production cross sections of $S^{++}S^{--}$ and $S^{\pm\pm}S^{\mp}$ in the SU(5)/SO(5) model at $\sqrt{s} = 14$ TeV.

charge but possibly different flavour that satisfy $p_T(\ell) > 20$ GeV, $|\eta(\ell)| < 2.5$, and the isolation criterium

$$\frac{p_T(\ell)}{p_T(\ell) + \sum_{i \in \mathcal{C}} p_{T,i}} > 0.7, \tag{4.44}$$

where the sum goes over particles in a cone $\mathcal{C}$ around the lepton ℓ defined by $\Delta R_{i\ell} < 0.3$ and we only count particles with $p_{T,i} > 0.5$ GeV. Besides the leptons, the target final state contains several light and b-tagged jets. While in principle we expect four of each, in practice the reconstruction of jets and especially the tagging of b-jets is not a perfect process, so by demanding the maximum number of jets we would cut away a lot of our signal. Instead, we apply the more inclusive cuts of $N(j) \geq 3$ and $N(b) \geq 3$, where both light and b-tagged jets are required to satisfy $|\eta| < 2.5$ and $p_T > 25$ GeV. Finally we apply two global cuts: to avoid final states which are too soft, we require the scalar sum S_T of the transverse momenta of all reconstructed jets and the two leptons to satisfy $S_T > 400$ GeV. And since the leptons in our signal process come from W bosons, we also require events to contain some missing transverse momentum, $p_T^{\text{miss}} > 20$ GeV.

Before presenting the results of the preselection, we describe our simulation setup, see Appendix B for details. We generate events with `MadGraph5_aMC@NLO` version 3.4.0 at a centre-of-mass energy of $\sqrt{s} = 14$ TeV with the `NNPDF` 2.3 set of PDFs using dynamical renormalisation and factorisation scales. The hard scattering events are showered and hadronised using `Pythia8` and then passed to `Delphes` v3.4.1 for detector simulation, reconstruction, and analysis. We use `Delphes` with modified ATLAS configurations as described in [175]. Jets are reconstructed using the anti-k_T algorithm with a cone radius of $r = 0.4$. For simplicity we assume a flat (i.e. η-independent) b-tagging efficiency of $\epsilon_{b\to b} = 0.8$, and a mistag rate for a c-jet (light-flavour jet) to be misidentified as a b-jet of $\epsilon_{c\to b} = 0.2$ ($\epsilon_{j\to b} = 0.01$), with values taken from [176].

For the generation of signal events we use the public `eVLQ` model implementation [113] in `FeynRules` to generate a UFO library. We generate leading order events of $S^{++}S^{--}$ and $S^{\pm\pm}S^{\mp}$

Process	Event generation	$\epsilon_{\text{Preselection}}$	σ_{fid} [fb]	Events at 3 ab^{-1}
$S^{++}S^{--}$	LO	9.87×10^{-3}	4.90×10^{-2}	147
$S^{\pm\pm}S^{\mp}$	LO	4.81×10^{-3}	2.87×10^{-3}	86
$t\bar{t}V$	NLO	1.70×10^{-4}	2.72×10^{-1}	816
$t\bar{t}h$	NLO	3.75×10^{-4}	2.10×10^{-1}	629
$t\bar{t}t\bar{t}$	LO	1.63×10^{-2}	1.91×10^{-1}	572
$t\bar{t}VV$	NLO	1.74×10^{-3}	3.29×10^{-2}	98
VVV	NLO	2.08×10^{-6}	1.05×10^{-3}	3

Table 4.5: Preselection results. For each process we indicate whether events were generated at leading or next-to-leading order, give the preselection efficiency, the fiducial cross section after the preselection cuts, and the expected number of events at the HL-LHC. For signal processes, we show results for a reference mass of $m_S = 400$ GeV.

production for m_S from 300 to 1000 GeV in steps of 50 GeV. We apply a flat K-factor of 1.15 to the cross sections to account for NLO effects [168]. The signal cross sections are shown in Fig. 4.18. For the background event generation we use the built-in SM implementation in `MadGraph5_aMC@NLO`. The irreducible background $t\bar{t}t\bar{t}$ is generated at leading order due to technical difficulties with the NLO event generation, but its cross section is rescaled to the NLO value of 11.7 fb. The remaining backgrounds are generated at NLO in QCD. In descending order of cross section, these are $t\bar{t}V$ (1.60 pb) where $V = W^{\pm}, Z$; $t\bar{t}h$ (560 fb); and $t\bar{t}VV$ (18.9 fb). Other background such as VVV (509 fb) turn out to be negligibly small once preselection efficiencies are taken into account.

We pass the generated events through the preselection as detailed above, leading to the results shown in Tab. 4.5. From the last column we can read off the expected total number of background events as $B = 2118$ compared to $S = 233$ signal events for a reference mass of $m_S = 400$ GeV. Using a crude approximation for the significance Z [177], we can estimate

$$Z \approx \frac{S}{\sqrt{B}} \approx 5. \tag{4.45}$$

This is a good first step: already after the first half of the analysis we have a discovery reach of up to 400 GeV. In the following sections we explore how far this can be extended using deep learning techniques.

4.5.3 Data representation

When preparing a machine learning analysis, one of the first questions that has to be addressed is how to represent the data. In our case, the raw data consists of `HepMC` files for the signal and background events. These are too large to use for machine learning and they contain a lot of redundant information that would hinder the learning process anyway. Instead, we should extract interesting features from the event data. A simple approach along those lines

is to construct high level kinematic variables from the reconstructed objects: by definition, each event that passes the preselection contains two leptons and at least three light and three b-tagged jets. If there are more than three jets, we only consider the three "leading" jets with the highest p_T and disregard the excess jets:

$$\mathcal{R} = \{\ell_1, \ell_2, j_1, j_2, j_3, b_1, b_2, b_3\} \tag{4.46}$$

The most basic properties of the reconstructed objects are their four momenta, which are however ill suited as neural network inputs [2]. Instead we use the four momenta to calculate higher level variables, such as the invariant mass and angular separation

$$M_{ij} = \sqrt{(p_i + p_j)^2}, \qquad \Delta R_{ij} = \sqrt{(\eta_i - \eta_j)^2 + (\phi_i - \phi_j)^2}, \qquad i, j \in \mathcal{R} \tag{4.47}$$

where p_i is the four momentum of object i. We also consider the transverse momentum $p_{T,i}$ of all reconstructed objects, as well as the global variables p_T^{miss} and S_T. All in all, the set of kinematic variables reads

$$\mathcal{K} = \bigcup_{i \neq j} M_{ij} \cup \bigcup_{i \neq j} \Delta R_{ij} \cup \bigcup_i p_{T,i} \cup \{p_T^{\text{miss}}, S_T\}. \tag{4.48}$$

Note that we make no attempt at pairing jets to reconstruct a resonance mass, nor employ any other involved variables. The point of the dataset $\mathcal{K}$ is rather to set a baseline for a simple deep learning analysis.

The final state under study features a lot of hadronic activity, the details of which cannot be captured by a few kinematic variables defined from the reconstructed jets. To get the full picture we have to look at lower level event data. A promising approach to this is the notion of jet images [172]: we imagine the calorimeter as a grid of towers. For each grid cell we sum up the p_T of each particle passing through it and project it into the η-ϕ-plane. The result is an image that shows the hadronic particle flow — a so-called jet image. Casting a physics event into an image allows it to be analysed with the quickly growing toolset of computer vision, including convolutional neural networks [178–180] as first explored in [173]. Early applications of jet images were in "jet tagging" [172, 173], the task of differentiating boosted jets from QCD jets. In fact, the tagging of top jets has become a benchmark problem for testing various neural network architectures [174, 181]. While jet tagging only considers images of a single (potentially fat) jet, there have also been efforts to use jet images of a full event to differentiate some signal process from its backgrounds [175, 182–186]. Our work is another contribution to that effort.

We construct jet images following the approach in [185], separating the particle flow into charged hadrons and neutral particles, the latter consisting of neutral hadrons and non-isolated photons. Leptons are removed from both channels. We descretise the η-ϕ-plane into 50×50 calorimeter cells covering the regions $-2.5 \leq \eta \leq 2.5$ and $-\pi \leq \phi \leq \pi$. We define the origin of the η-ϕ-plane to be the centre of the two isolated leptons, i.e. we shift the coordinates of all

particles by

$$\eta \to \eta - \eta_{\ell\ell}, \quad \eta_{\ell\ell} = \frac{1}{2}(\eta_{\ell_1} + \eta_{\ell_2}); \qquad \phi \to \phi - \phi_{\ell\ell}, \quad \phi_{\ell\ell} = \frac{1}{2}(\phi_{\ell_1} + \phi_{\ell_2}). \tag{4.49}$$

This may shift the ϕ of some particles out of the $[-\pi, \pi]$ region, so we enforce 2π-periodicity in ϕ-direction. While this is obvious for an angle, we also artificially impose periodicity in η rather than losing information or enlarging the images with mostly empty regions at the edges. We note that while the pseudorapidity is not actually periodic, there is no reason to require the jet images to be physical as long as they provide a useful data representation. The intensity of each pixel is the total transverse momentum of particles passing through that pixel, where we only consider hadrons with $p_T > 0.7$ GeV. Counter to common machine learning practices, we do not normalise the pixel intensities since the total intensity also holds information that can help differentiate signal from backgrounds, see Fig. 4.19. In addition to the charged and neutral particles, we also project the two leptons into the discretised η-ϕ-plane to obtain the "lepton jet images" which consist of only two non-zero pixels. We include the leptons to capture the full correlations between final state particles. All in all, the data structure of the jet images reads

$$\mathcal{I}_{CN\ell} = (3 \times 50 \times 50), \tag{4.50}$$

where the 3 represents the charged (C), neutral (N), and lepton (ℓ) channels.

We have yet to discuss one important caveat: the question of whether the jet images for the charged and neutral particles can be experimentally obtained in the first place. To answer this we have to discuss pileup effects. At the HL-LHC we expect $\mathcal{O}(200)$ collisions per bunch crossing [187] from which the actual hard scattering event has to be extracted. For charged particles the pileup can be cleaned up using longitudinal vertex information [188], but this is not possible for neutral particles. While there is ongoing experimental research to mitigate pileup for neutral particles [188, 189], an analysis based on $\mathcal{I}_{CN\ell}$ remains out of reach for now. We will therefore explore two scenarios: an optimistic case where advances in pileup mitigation make it possible to use the full $\mathcal{I}_{CN\ell}$ dataset, and a conservative analysis based on

$$\mathcal{I}_{C\ell} = (2 \times 50 \times 50), \tag{4.51}$$

which does not use the neutral images.

In Fig. 4.19 we show the distribution of the jet images of the (left three columns) background and (right three columns) signal processes for different masses. In each panel we overlay the jet images of all simulated events. The pixel intensity indicates the mean p_T per pixel. Comparing the jet images of the signal and background processes, we notice several differences: the signal images are generally "brighter" than the backgrounds, indicating a larger total p_T, as is to be expected from the decay products of a heavy resonance. The brightness further increases with m_S. Also the distributions differ significantly, with the leptons being centered around the

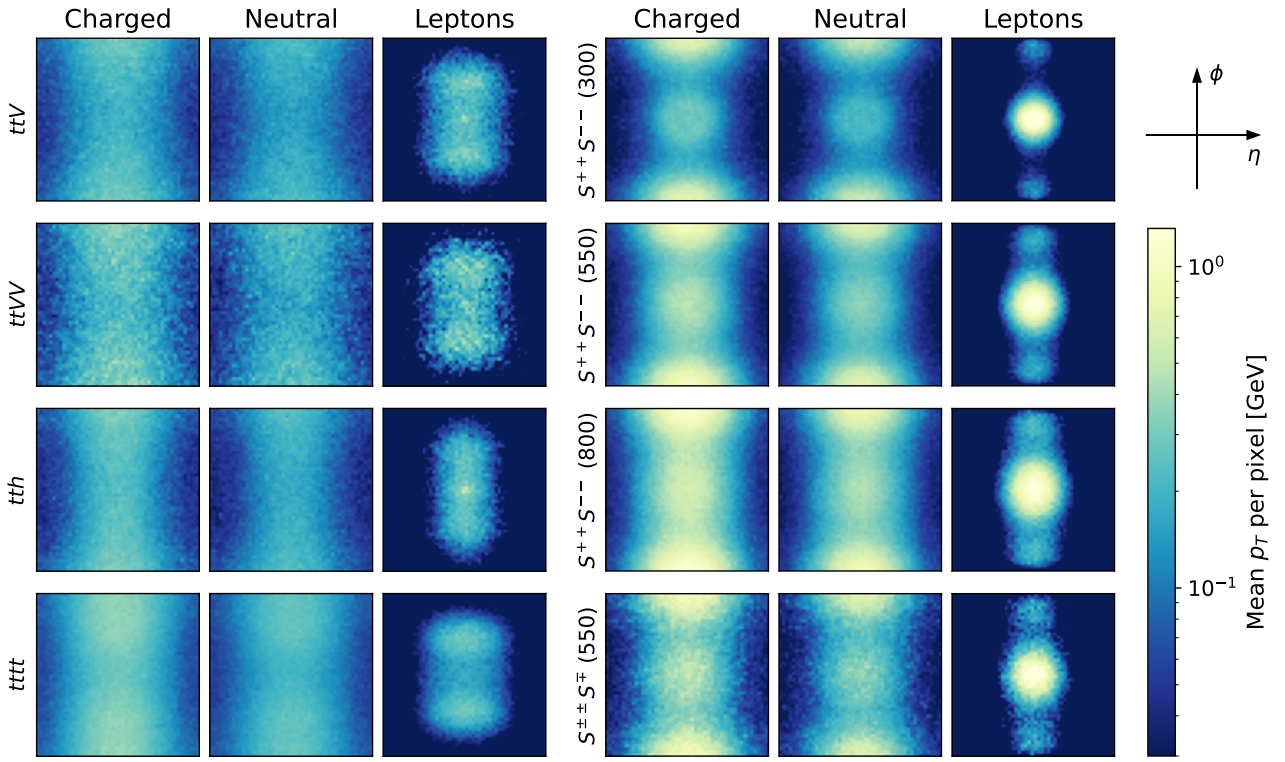

Figure 4.19: Distribution of jet and lepton images of (left) background and (right) signal processes, where the scalar mass in GeV is given in parentheses. The final state signatures are discretised into 50×50 calorimeter grids within a region of $-2.5 \leq \eta \leq 2.5$ and $-\pi \leq \phi \leq \pi$. The origin of the coordinate system is the centre of the two same-sign leptons. The columns show charged and neutral components of the jets, as well as isolated leptons, respectively. The colourbar indicates the mean p_T per pixel.

origin for the signal images but less focussed for the backgrounds. This can be understood by considering the decay chain: in the signal images both leptons come from the decay of the same particle, S^{++} or S^{--}, leading to a small angular separation between the leptons, whereas they are further apart for the backgrounds since they originate from different particles.

Just looking at the distributions in Fig. 4.19 may give a wrong impression about how easy signal and backgrounds are to separate. While the differences are obvious when overlaying many events, a separation by eye is impossible on an event-by-event basis. To illustrate this, we show some jet images for individual events in Fig. 4.20. Note also that the pixel intensities span more than two orders of magnitude.

4.5.4 Neural network architectures

We have extracted interesting features from the simulated events in the form of kinematic variables and jet images. The next step is to use the obtained data to train classifiers to differentiate signal from background events. We have designed three neural network architectures for this purpose, each using a different dataset. With a slight abuse of notation, we refer to the network architectures by the dataset they use:

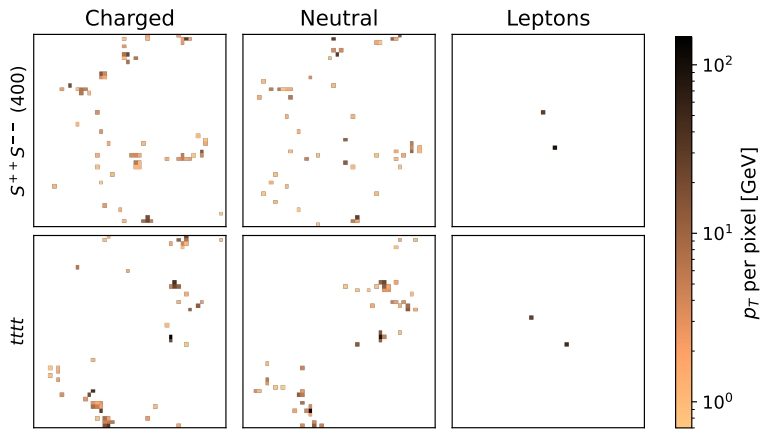

Figure 4.20: Example jet images for single events. The coordinates are chosen as in Fig. 4.19.

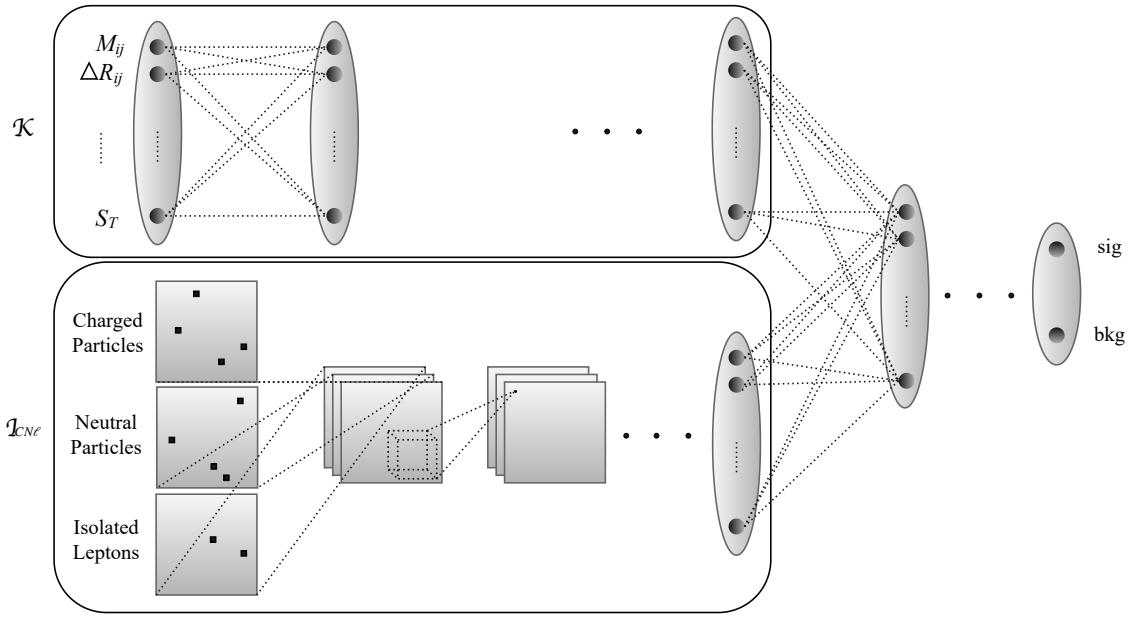

Figure 4.21: A schematic architecture of the neural networks used in this paper. We study both the multilayer perceptron and the convolutional neural network on their own as well as the combination shown here.

- $\mathcal{K}$: multilayer perceptron (MLP) using only kinematic data
- $\mathcal{I}_{C\ell}/\mathcal{I}_{CN\ell}$: convolutional neural network (CNN) using only jet images of charged (and neutral) hadrons and leptons
- $\mathcal{I}_{C\ell}+\mathcal{K}/\mathcal{I}_{CN\ell}+\mathcal{K}$: combination of a CNN using jet images and a MLP for the kinematic data. The flattened part of the CNN is interfaced with the MLP to produce one combined output, see Fig. 4.21.

By having some networks use only part of the available dataset we will be able to learn which data holds the strongest discriminatory power. Each network has two output nodes, the values of which can be interpreted as the probability of being a signal or background event as assigned by the network. In the following we refer to this probability of being a signal event as the

"NN score", i.e. an event with NN score close to 0 (1) is background-like (signal-like). We have implemented the networks in the `PyTorch` framework [190, 191]. Details of the network architectures and hyperparameters are given in Appendix D.1.

We train and evaluate the networks on a dataset consisting of about 130,000 events, which we split into training (64%), validation (16%), and a holdout test set (20%). The training and validation sets consist to equal parts of signal and background events. The signal events are a mixture of different mass hypotheses, with each mass from 300 GeV to 800 GeV in steps of 50 GeV present with the same weight. For the backgrounds, the number of events is proportional to the fiducial cross section in Tab. 4.5, thus weighting the background events by how often they are seen at the LHC. The training set is used to optimise the weights of the network with the `Adam` optimiser [192] such as to minimise the cross entropy loss function. During training we monitor the generalisation loss with the validation set and choose the best model parameters as those with the lowest validation loss. The final evaluation is performed on the test set, which is comprised of the same mix of background events as the training and validation sets but only contains signal events of a single mass.

There are many sources of systematic uncertainties in our proposed search: limited knowledge of the background cross sections in the relevant region of phase space, some processes have only been generated at leading order, different parton showering algorithms can lead to different jet images[4], a limited number of events in the dataset, and the stochastic nature of the training process, to name just a few. While a detailed study of the systematic uncertainties is beyond the scope of this work, we do have control over the systematics originating from the machine learning. The limited number of Monte Carlo events makes the results susceptible to statistical fluctuations. Furthermore, the random initialisation of the network parameters and the training with stochastic gradient descent both introduce uncertainties. To take these into account, we independently train 20 copies of each network and evaluate them separately. The results we present in the following are averaged over the 20 copies and the error bars indicate the 1σ variations across the samples.

4.5.5 Results

To assess how well our neural networks perform as classifiers, we compare the receiver operator characteristic (ROC) curves for several scalar masses in Fig. 4.22. The ROC curve displays how many background events can be successfully rejected for a given signal efficiency. The performance increases from $\mathcal{K}$ to $\mathcal{I}_{CN\ell} + \mathcal{K}$ in line with expectations that a network with more information should perform better. All networks perform better at higher m_S, which can be explained by the increased p_T of the final state particles. Also the boost in performance from adding the kinematic data to the jet images has an increased effect at higher mass, going from a negligible effect at $m_S = 300$ GeV to a significant improvement at 800 GeV.

[4]While we do not investigate this further, we emphasise that this may introduce sizable systematics for the results based on CNNs. The effect of different parton showers has been studied in [193] in the context of jet tagging.

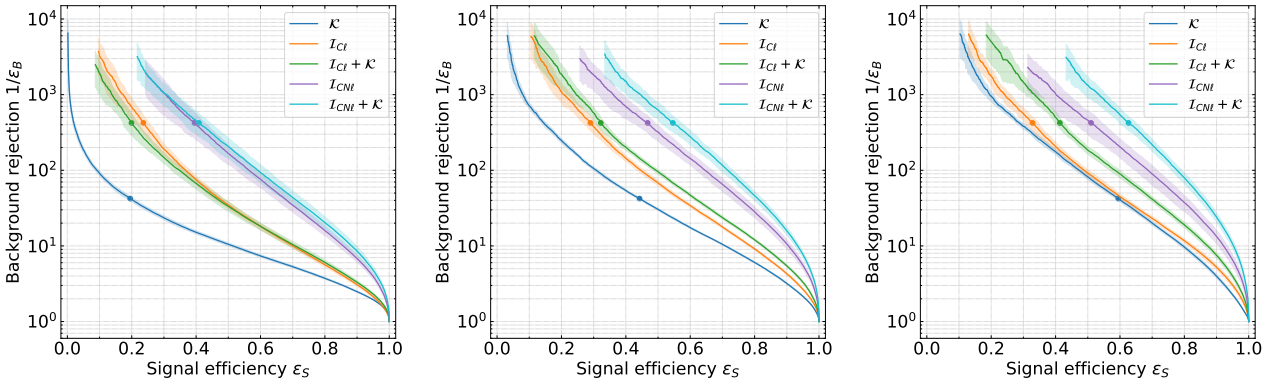

(a) $m_S = 300$ GeV (b) $m_S = 550$ GeV (c) $m_S = 800$ GeV

Figure 4.22: Comparison of network performances with ROC curves. The markers indicate the working points used in the following analysis.

We have now seen that our networks are effective at separating signal from background events, and we turn to the physics application. To this end we pick a working point on the ROC curve for each network. The chosen signal efficiency corresponds to a cut on the NN score, with each event with a NN score larger than the cut being designated as a signal event. Among the events passing the NN score cut, there are S true signal events and B background events that were misidentified as a signal. From these values we can calculate the significance of discovering the signal process as

$$Z_{\text{dis}} = \sqrt{-2 \ln \left(\frac{L(S+B|B)}{L(S+B|S+B)} \right)} \tag{4.52}$$

while the exclusion significance is given by

$$Z_{\text{excl}} = \sqrt{-2 \ln \left(\frac{L(B|S+B)}{L(B|B)} \right)}, \tag{4.53}$$

where

$$L(n|\lambda) = \frac{\lambda^n}{n!} e^{-\lambda} \tag{4.54}$$

is the likelihood of observing n events when λ events were expected [177, 194]. We are however not only interested in the significances assuming the cross sections from the SU(5)/SO(5) model, but rather in results that can be applied to any model featuring our signal process. To this end we replace $S \to \mu S$ and vary μ such that

$$Z_{\text{dis}}(S, B, \mu_{\text{dis}}) = 5, \qquad Z_{\text{excl}}(S, B, \mu_{\text{excl}}) = 1.64. \tag{4.55}$$

As final results we now obtain the expected discovery reach $\sigma_{5\sigma}$ required to discover the signal

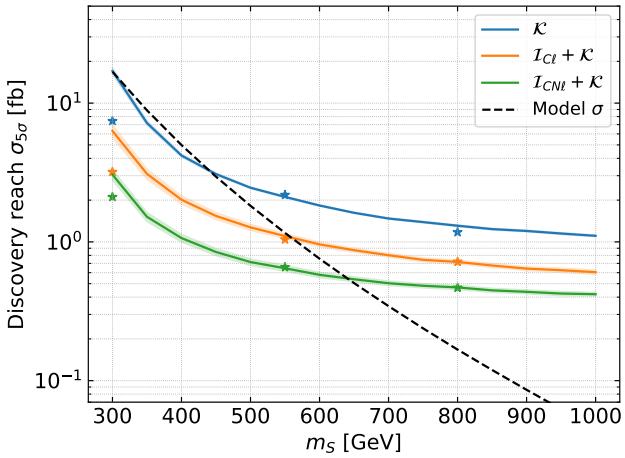

(a) Discovery reach of $S^{++}S^{--}$

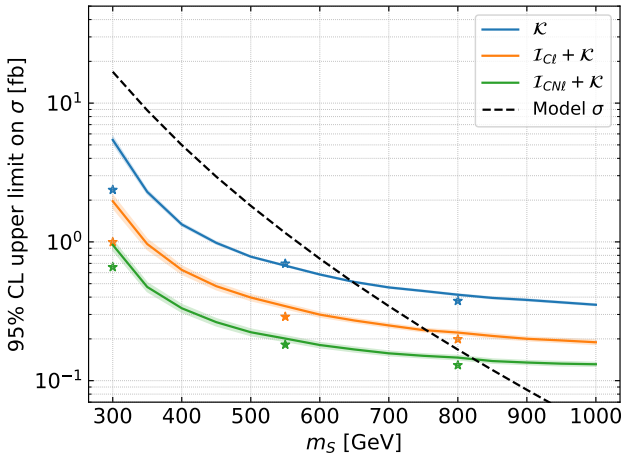

(b) Expected upper limit of $S^{++}S^{--}$

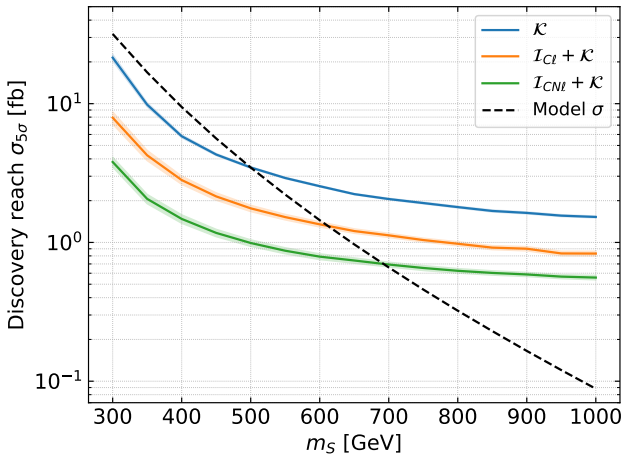

(c) Discovery reach of $S^{++}S^{--}$ and $S^{\pm\pm}S^{\mp}$

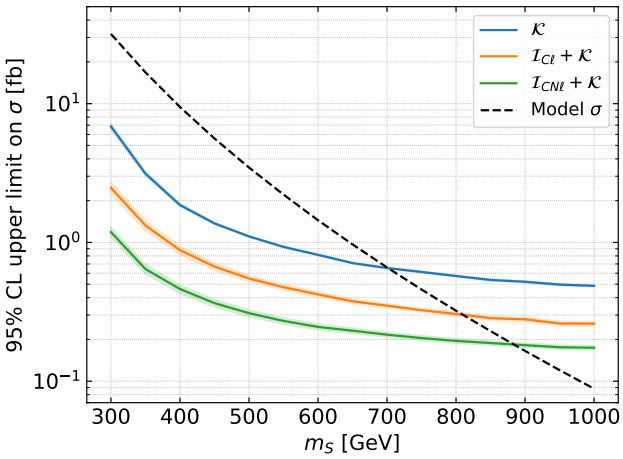

(d) Expected upper limit of $S^{++}S^{--}$ and $S^{\pm\pm}S^{\mp}$

Figure 4.23: Expected (left) discovery reach and (right) exclusion limit of S^{++} production at the HL-LHC (3 ab^{-1}) for different network architectures. In the first row, only $S^{++}S^{--}$ pair production is taken into account. The second row includes both $S^{++}S^{--}$ and $S^{\pm\pm}S^{\mp}$ production with $m_{S^{++}} = m_{S^+}$ and the corresponding cross sections from Fig. 4.18. The dashed lines indicate the 14 TeV reference cross sections in the SU(5)/SO(5) model of (top) $S^{++}S^{--}$ and (bottom) the sum of $S^{++}S^{--}$ and $S^{\pm\pm}S^{\mp}$ production. For the solid lines, the networks were trained on multiple masses simultaneously. The points marked by stars were trained using only the respective masses.

with 5σ significance and the upper limit σ_{95} required to exclude the signal at 95% CL as

$$\sigma_{5\sigma} = \mu_{\text{dis}}\,\sigma_{\text{ref}}, \qquad \sigma_{95} = \mu_{\text{excl}}\,\sigma_{\text{ref}}, \tag{4.56}$$

where σ_{ref} is the reference cross section from Fig. 4.18.

When setting the NN score cut, a common approach is to choose it such as to maximise Z_{dis}. For many of our networks however, the discrimination is so strong that this optimal cut regularly leaves fewer than 1 background event remaining, making the statistical treatment challenging. We therefore forgo the optimisation procedure and instead manually place the NN score cut at a fixed number of background events: $B = 5$ for the CNNs and $B = 50$ for

the network $\mathcal{K}$. We show in Appendix D.2 that this does not strongly affect the results. The selected working points are indicated by the markers in Fig. 4.22.

In Figs. 4.23a and 4.23b we show the expected discovery reaches and the upper limits derived from the networks $\mathcal{K}$, $\mathcal{I}_{C\ell} + \mathcal{K}$, and $\mathcal{I}_{CN\ell} + \mathcal{K}$, assuming an integrated luminosity of 3 ab^{-1}. The black dashed line shows the 14 TeV reference cross section for $S^{++}S^{--}$ production in the SU(5)/SO(5) model. The kinematic data in isolation is barely enough to discover the signal up to 440 GeV and exclude masses below 650 GeV. Combining the kinematic data with charged jet and lepton images brings a sizable improvement with a discovery reach up to 560 GeV and exclusion up to 750 GeV. This can be improved further if advances in pileup mitigation allow the usage of neutral jet images, in which case the signal can be discovered up to 640 GeV and masses below 820 GeV can be excluded.

For the solid lines in Fig. 4.23, the networks were trained on the dataset containing a mixture of signal masses. A priori we would expect the network to perform better if it is trained only on the mass that it is evaluated on. To investigate this, we retrained the networks with a single mass for $m_S = 300$, 550, and 800 GeV. The results are shown as star-shaped markers in Figs. 4.23a and 4.23b. For 300 GeV this leads to a considerable improvement, while the effect is negligible for the higher masses. This confirms that our approach of training with a mixed mass dataset only mildly affects the results while reducing the computation time significantly. More details on the choice of training dataset are provided in Appendix D.3.

In Figs. 4.23c and 4.23d, the mixed production $S^{\pm\pm}S^{\mp}$ is also taken into account. The discovery reach and upper limit cross sections now refer to the sum of pair and mixed production, as does the reference cross section from the quintuplet in the SU(5)/SO(5) model. Searching for both processes simultaneously increases both the discovery reach and exclusion limit by about 50 GeV for all three networks.

To properly assess our search strategy, we should compare it with a current search using the full Run-2 dataset. While our signal process has not yet been searched for, we can compare the upper limit derived from a recast of [121] in Section 4.3 with the exclusions our networks would provide. This comparison is shown in Fig. 4.24, where the network bounds were calculated for an integrated luminosity of 139 fb^{-1}. We note that the recast bounds were obtained for 13 TeV but the neural networks were trained on 14 TeV events, but this does not change the results qualitatively. Since we are comparing to a recast rather than a dedicated search, we cannot draw quantitative conclusions between the performances of cut-and-count vs deep learning searches. We can however see, that the recast performs similarly to the MLP, while the bounds are significantly stronger when jet images are included.

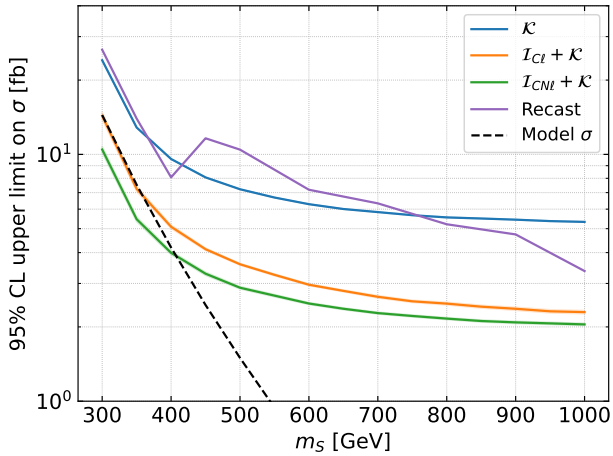

Figure 4.24: Expected exclusion limit of $S^{++}S^{--}$ pair production at the LHC with $\mathcal{L}_{\text{int}} = 139\ \text{fb}^{-1}$ for different network architectures. The recast bounds are taken from Fig. 4.7a and derived from [121]. The black line indicates the 13 TeV reference cross section in the SU(5)/SO(5) model.

5 | Phenomenology of spin-1/2 resonances

Modern CHMs tackle the problem of generating a large Yukawa coupling for the top quark by introducing a mixing between the elementary state and heavy top partners. As a consequence, the models contain heavy fermionic resonances with expected masses in the TeV range and thus accessible to the LHC. In this chapter we give an overview of the phenomenology of spin-1/2 resonances in the Ferretti models. We focus on the colour triplets, referred to as vector-like quarks (VLQs). Top partners with exotic colour charges have been studied in [107].

5.1 Simplified models for vector-like quarks

The Ferretti models contain the following VLQs

$$X_{8/3} \in \mathbf{3}_{8/3}, \quad X_{5/3} \in \mathbf{3}_{5/3}, \quad T \in \mathbf{3}_{2/3}, \quad B \in \mathbf{3}_{-1/3}, \quad Y \in \mathbf{3}_{-4/3} \tag{5.1}$$

expressed as eigenstates of $\mathrm{SU}(3)_c \times \mathrm{U}(1)_Q$. Note that any given model may contain only a subset of these as listed in Tab. 3.4. Furthermore, there may be several states with the same quantum numbers. For the purposes of this chapter, however, we do not consider the full VLQ content of a model but discuss general features of each VLQ on its own. To this end we employ simplified models [113]. For the charge-2/3 state for example,

$$\mathcal{L} = \frac{e}{\sqrt{2}s_W}\kappa^W_{T,L}\bar{T}\not{W}^+ P_L b + \frac{e}{2c_W s_W}\kappa^Z_{T,L}\bar{T}\not{Z}P_L t + \kappa^h_{T,L}h\bar{T}P_L t \tag{5.2}$$

$$+ \kappa^{S^0}_{T,L}S^0\bar{T}P_L t + \kappa^{S^+}_{T,L}S^+\bar{T}P_L b + (L \leftrightarrow R) + \text{h.c.}\,. \tag{5.3}$$

The interactions for the other VLQs are parameterised analogously. The relative sizes of the couplings in Eq. (5.2) are fixed by the underlying $\mathrm{SU}(2)_L$ representation. The T can originate from a doublet or a singlet, and it can be shown that

$$\text{singlet}: \qquad \mathrm{Br}(T \to W^+ b) : \mathrm{Br}(T \to Zt) : \mathrm{Br}(T \to ht) = 2:1:1 \tag{5.4}$$

$$\text{doublet}: \qquad \mathrm{Br}(T \to W^+ b) : \mathrm{Br}(T \to Zt) : \mathrm{Br}(T \to ht) = 0:1:1 \tag{5.5}$$

in the limit $m_T \to \infty$ [195, 196]. This can be understood by considering the $\mathrm{SU}(2)_L$ coupling structure: the Goldstone equivalance theorem [197] states that at high energies compared to the W mass the longitudinal degrees of freedom of the W and Z bosons are described by the NGBs. For the VLQ decays the longitudinal components turn out to be the dominant contribution [16]. We can therefore consider the couplings with the Higgs doublet, which for the case of a singlet/doublet top partner are

$$\text{singlet}: \qquad \tilde{H} \cdot \bar{q}_L T_R = \frac{1}{\sqrt{2}}(h - i\phi^0)\bar{t}_L T_R - \phi^- \bar{b}_L T_R \tag{5.6}$$

$$\text{doublet}: \qquad \tilde{H} \cdot \bar{Q}_L t_R = \frac{1}{\sqrt{2}}(h - i\phi^0)\bar{T}_L t_R - \phi^- \bar{B}_L t_R \tag{5.7}$$

where $Q_L = (T_L, B_L)^T$. This yields the branching ratios as quoted above. As a concrete example we consider the case of a singlet top partner, where the couplings scale as

$$\kappa^W_{T,L} = \kappa^Z_{T,L} = \frac{v}{m_T}\kappa, \quad \kappa^h_{T,L} = \kappa, \quad \kappa^i_{T,R} = 0 \tag{5.8}$$

and we assume dominant left handed couplings [198]. While the $X_{5/3}$ and Y only have one decay channel to two SM particles, the branching ratios of the B can be determined analogously to the T. In fact we can read off the doublet case from Eq. (5.7), and the analog to Eq. (5.6) yields:

$$\text{singlet}: \qquad \mathrm{Br}(B \to W^- t) : \mathrm{Br}(B \to Zb) : \mathrm{Br}(B \to hb) = 2 : 1 : 1 \tag{5.9}$$

$$\text{doublet}: \qquad \mathrm{Br}(B \to W^- t) : \mathrm{Br}(B \to Zb) : \mathrm{Br}(B \to hb) = 1 : 0 : 0 \tag{5.10}$$

5.2 Production and decay channels

As QCD coloured states the VLQs can be pair produced with a universal cross section depending only on the mass. This is shown in black in Fig. 5.2 for $\sqrt{s} = 13$ TeV calculated at NLO in QCD. We use the `NNPDF` 2.3 PDF set and fix the scales to $\mu_R = \mu_F = m_Q$. Besides pair production, the couplings discussed in the previous section also allow for single production, for which the cross section falls off less quickly with mass. When considering heavy VLQs it may therefore also be interesting to study single production. Both T and B can be produced through the diagrams in Fig. 5.1 (switching $t \leftrightarrow b$ for B) with the Higgs-channel being a subdominant contribution. For $X_{5/3}$ and Y, the W-channel is open while the $X_{8/3}$ cannot be singly produced. Fig. 5.2 also shows the single production cross sections of a singlet T, calculated with the same scale and PDF choices as above but at LO. The conjugate process is always included in the calculation. We parameterise the couplings as described in the previous section and set $\kappa = 1$. Note that the total cross sections are proportional to $|\kappa|^2$. The Tbj cross section is larger than Ttj for two reasons: firstly, the larger coupling to the W. Secondly, for Ttj a gluon must split into $t\bar{t}$, while Tbj only needs a $b\bar{b}$ pair, and the former is kinematically more costly due to the

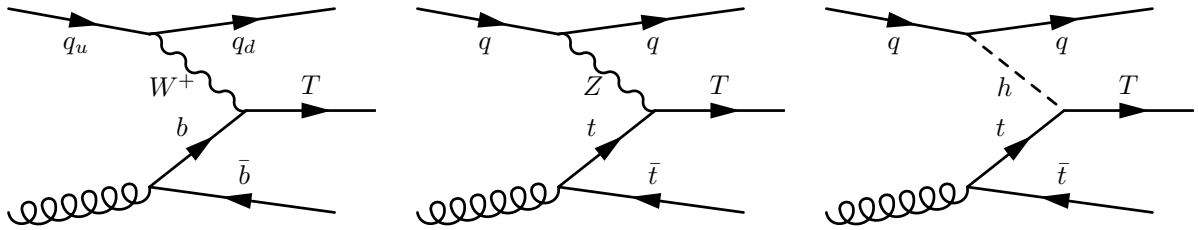

Figure 5.1: Feynman diagrams for the single production of T. Analogous diagrams exist for B. $X_{5/3}$ and Y can only be produced through the W-channel, and $X_{8/3}$ cannot be singly produced at all.

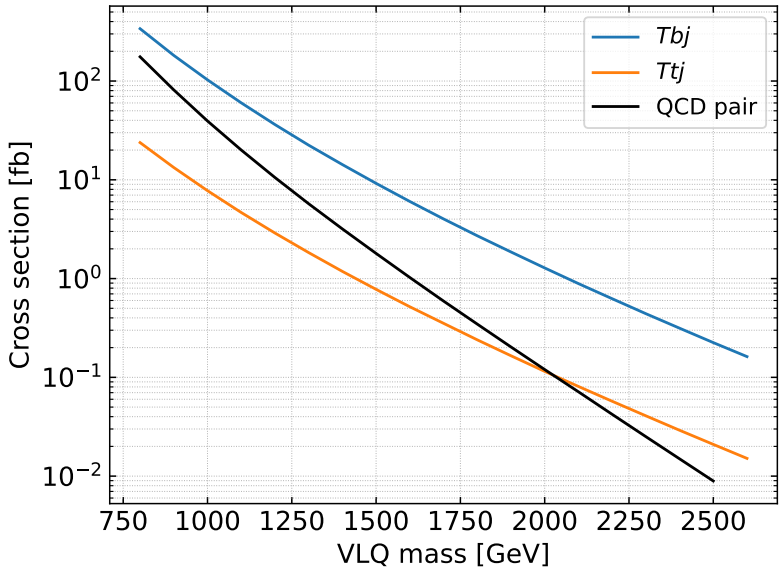

Figure 5.2: Cross sections for the pair and single production of VLQs at $\sqrt{s} = 13$ TeV. The former was calculated at NLO in QCD while for single production we show leading order results using the parameterisations from Section 5.1 with $\kappa = 1$.

large top mass. Finally, we note that a large single production cross section requires a large coupling which in turn leads to a large width compared to the mass. Large width effects in VLQ production have been studied in [199].

We now turn to the decays of the VLQs, which can be separated into two classes — standard channels and exotic channels. Under standard channels we collect the aforementioned decays of a VLQ into two SM particles,

$$X_{5/3} \to tW^+, \quad T \to bW^+, tZ, th, \quad B \to tW^-, bZ, bh, \quad Y \to bW^-. \tag{5.11}$$

These decays make use of the same couplings that allow for single production. Decays of a VLQ into a quark and a BSM scalar on the other hand are referred to as exotic decays. The decay widths are highly model dependent and we limit ourselves to listing the possibilities that

are allowed by colour and charge conservation:

$$X_{8/3} \to tS^{++} \tag{5.12}$$
$$X_{5/3} \to bS^{++},\, tS^{+}; \quad \bar{b}\pi_6^{4/3} \tag{5.13}$$
$$T \to tS^{0},\, bS^{+}; \quad t\pi_8,\, \bar{t}\pi_6^{4/3} \tag{5.14}$$
$$B \to bS^{0},\, tS^{-}; \quad b\pi_8,\, \bar{b}\pi_6^{-2/3}, \bar{b}\pi_3^{c} \tag{5.15}$$
$$Y \to bS^{-},\, tS^{--}; \quad \bar{t}\pi_6^{-2/3},\, \bar{t}\pi_3^{c} \tag{5.16}$$

Here we have further subdivided the exotic decays into ones featuring colour singlets $S^{\pm\pm,\pm,0}$ and coloured pNGBs π_r. While we expect the former to be relatively light, in Section 4.1 we have seen that the coloured states are already excluded as far as 1.5 TeV in mass, so the corresponding VLQ decay channels may be kinematically suppressed or even unavailable. We therefore focus on the decays into uncoloured pNGBs.

Naturally, the detector signatures further depend on the decays of the pNGBs, which have been discussed in Section 4.2. Starting from the pair production of two VLQs, all in all there are more than 150 distinct possible processes. Rather than listing them all out we instead discuss the general features that can be expected. Firstly, there will always be two third generation quarks from the primary decays, thus guaranteeing two b-jets with potentially additional W bosons. If the pNGBs decay into fermions, they will be joined by several further top and/or bottom quarks, for example

$$T\bar{T} \to tS^0\, \bar{t}S^0 \to 6t. \tag{5.17}$$

For the case of fermiophobic decays, we instead expect a number of W and Z bosons with the option of some hard photons as well.

5.3 Bounds on VLQ pair production

Pair production of VLQs with standard decay channels has been extensively searched for at the LHC, see [198] for a recent overview. The strongest bounds have been put on Y with masses below 1.70 TeV having been excluded by the ATLAS search [200]. The strongest bounds on T and B have been set by the CMS search [201], which excludes T_{doub}, T_{sing}, B_{doub}, and B_{sing} up to 1.48, 1.49, 1.47, and 1.56 TeV, respectively. Finally, the $X_{5/3}$ has been excluded up to 1.46 TeV by the ATLAS analysis [202]. In summary, the pair production of VLQs with standard decay channels currently yields bounds of about 1.5 TeV, with the exception of the more strongly constrained Y.

While a myriad of experimental searches have been performed for the standard decay channels, the exotic decays remain unexplored. Their inclusion is however crucial for a realistic image of VLQs since exotic decays are universally present in realistic CHMs. Even the models with the smallest scalar sectors, based on SU(4)/Sp(4), feature a neutral BSM scalar. Exotic

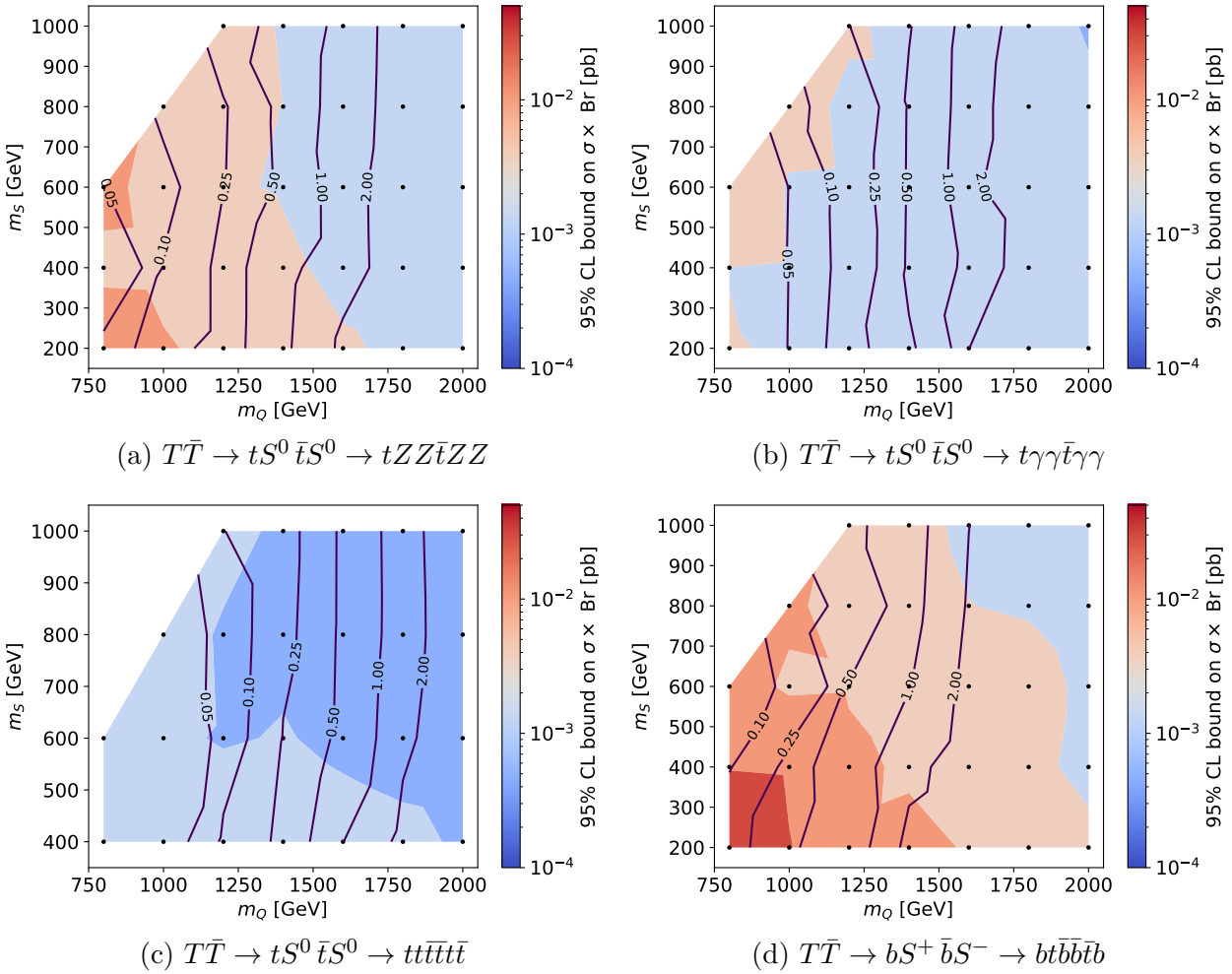

(a) $T\bar{T} \to tS^0\,\bar{t}S^0 \to tZZ\bar{t}ZZ$

(b) $T\bar{T} \to tS^0\,\bar{t}S^0 \to t\gamma\gamma\bar{t}\gamma\gamma$

(c) $T\bar{T} \to tS^0\,\bar{t}S^0 \to tt\bar{t}\bar{t}t\bar{t}$

(d) $T\bar{T} \to bS^+\,\bar{b}S^- \to bt\bar{b}\bar{b}t\bar{b}$

Figure 5.3: Bounds on the pair production of VLQs with exotic decays. The heatmap shows the upper limits on cross section times branching ratio. The solid lines indicate the mass bounds for a given total branching ratio, e.g. $\mathrm{Br}(T \to tS^0)^2 \times \mathrm{Br}(S^0 \to ZZ)^2$ in (a). There can be multiple VLQs contributing to a channel, so we also show a line for an effective branching ratio larger than 1.

VLQ decays have received more attention on the theoretical side [103, 133, 198, 203–205] including recast studies for a few processes, although only few recently. Also for us deriving recast bounds for all exotic channels is well beyond the scope of this work. Instead we will focus on a few benchmark processes, selected in order to cover a wide range of the possible signatures. From the channels with a fermiophobic scalar, we study the photon-less

$$T\bar{T} \to tS^0\,\bar{t}S^0 \to tZZ\,\bar{t}ZZ \tag{5.18}$$

and the multiphoton channel

$$T\bar{T} \to tS^0\,\bar{t}S^0 \to t\gamma\gamma\,\bar{t}\gamma\gamma. \tag{5.19}$$

From the fermiophilic channels, we consider one with a large number of top quarks,

$$T\bar{T} \to tS^0\,\bar{t}S^0 \to tt\bar{t}\,\bar{t}t\bar{t}, \tag{5.20}$$

and one with several bottom quarks,

$$T\bar{T} \to bS^+\,\bar{b}S^- \to bt\bar{b}\,\bar{b}t\bar{b}. \tag{5.21}$$

We present the bounds on these four processes in Fig. 5.3, where the heat map indicates the the upper limit on cross section times branching ratio. In this case branching ratio refers to the product of those for the VLQ decays and the scalar decays. For Fig. 5.3a for example,

$$\mathrm{Br}_{\mathrm{total}} = \mathrm{Br}(T \to tS^0)^2 \times \mathrm{Br}(S^0 \to ZZ)^2. \tag{5.22}$$

The upper limits are derived from recasts of [122, 156, 206] in Fig. 5.3a, [154] in Fig. 5.3b, [121,122] in Fig. 5.3c, and [206] in Fig. 5.3d, all of which have been implemented in `CheckMATE`. Besides the upper limits we also draw contours corresponding to mass bounds as solid lines. To this end we compare the NLO cross sections from Fig. 5.2 with the upper limits. We draw bounds for several values of the total branching ratio, including a value of 2. This is to be understood as several mass degenerate VLQs contributing to the same channel. The colours are chosen identically across the different processes. Fig. 5.3d is the weakest constrained and the $6t$ channel Fig. 5.3c the strongest. The upper limits depend weakly on the VLQ mass in Figs. 5.3b and 5.3c and more strongly in the other two. For all processes, the bounds are mostly vertical and therefore depend only weakly on the scalar mass.

The fact that for four quite different topologies we were able to derive largely competitive limits compared to the standard decay channels shows that the current recasting tools are well equipped for studying exotic VLQ decays. We leave a more detailed study for future work.

6 | Phenomenology of spin-1 resonances

The Ferretti models predict several heavy spin-1 resonances. Of those, the coloured states stand out through their large production cross section at hadron colliders. We will focus on them in this chapter and refer to [73, 106] for the EW states. In Chapter 3 we showed that every model has a colour octet vector $\mathcal{V}_8$ that mixes with the gluon and can therefore be singly produced at the LHC. We begin this chapter by describing the decay channels of the $\mathcal{V}_8$ and of the other spin-1 resonances and then turn to LHC bounds on $\mathcal{V}_8$. At the end we give an outlook for what signatures to expect at a future collider. Throughout this chapter we refer to the Ferretti models in terms of the colour sector classes C1-5 defined in Tab. 3.3. This chapter is based on [3].

6.1 Decay channels

We begin with the decays of the vector octet, for which we have

$$\mathcal{V}_8 \to q\bar{q},\, b\bar{b},\, t\bar{t},\, \pi_8\pi_8,\, \pi_6\pi_6^c,\, \pi_3\pi_3^c. \tag{6.1}$$

We list all possible decays across the models and leave it understood that only parts of them appear in any given model. The decays to light quarks $q = u, d, s, c$ are due solely to the mixing of the $\mathcal{V}_8$ with the gluon. The pNGB channels are also fixed by the hidden symmetry calculation. In fact, for fixed masses we have

$$\text{real}: \quad \frac{\text{Br}(\mathcal{V}_8 \to \pi_6\pi_6^c)}{\text{Br}(\mathcal{V}_8 \to \pi_8\pi_8)} = \frac{10}{3}\,, \qquad \text{pseudoreal}: \quad \frac{\text{Br}(\mathcal{V}_8 \to \pi_3\pi_3^c)}{\text{Br}(\mathcal{V}_8 \to \pi_8\pi_8)} = \frac{2}{3} \tag{6.2}$$

for models with real/pseudoreal cosets. The decays $\mathcal{V}_8 \to b\bar{b},\, t\bar{t}$ on the other hand have two contributions: one from the $\mathcal{V}_8$ mixing and one from partial compositeness couplings. The former we can calculate while the latter we cannot. For simplicity we assume right-handed PC couplings. In this case, the bottom quarks do not get an enhancement from PC and we include them in the q in the following. For the top quarks we neglect the left-handed part of the vector mixing and only take the right-handed coupling, i.e. $g^L_{\mathcal{V}tt} = 0$ and $g^R_{\mathcal{V}tt} \equiv c_{tt}$ in Eq. (3.172). We note that the couplings to top quarks originate from a coupling of the vector octet to two top

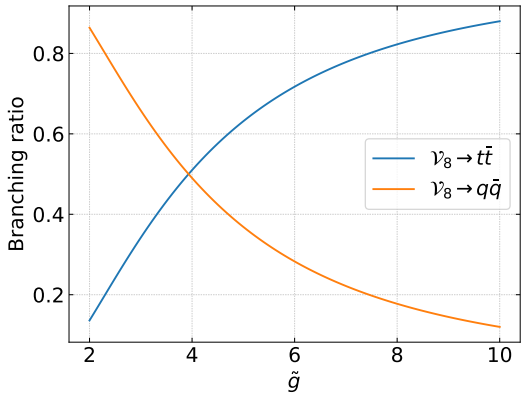

Figure 6.1: Branching ratios of the colour octet vector $\mathcal{V}_8$ when the pNGB decay channel is closed, $m_{\mathcal{V}_8} < 2m_\pi$. The branching ratios depend only on $\tilde{g}$ and the coupling to two top quarks which is fixed to $c_{tt} = 1$.

partners, which implies that

$$\mathcal{V}_8 \to T\bar{T},\, t\bar{T},\, \bar{t}T \tag{6.3}$$

are also possible. In the following we assume that the top partners are sufficiently heavy so that this decay can be safely ignored, which is the case for $m_T \gtrsim 2m_\pi$.

We recall from Section 3.4.6 that the hidden symmetry calculation leaves five independent parameters that fix all couplings,

$$\tilde{g}, \quad g_{\rho\pi\pi}, \quad m_{\mathcal{V}_8}, \quad \xi, \quad f_\chi, \tag{6.4}$$

which are the composite sector gauge coupling, the coupling scale of a vector to two pNGBs, the vector octet mass, the ratio of axial to vector octet mass, and the coloured pNGB decay constant, respectively. The branching ratios will further depend on the pion mass m_π and the top coupling c_{tt}. These are too many parameters for a grid scan so we make some simplifying assumptions. We take all pNGBs to have the same mass and fix it to $m_\pi = 1.6$ TeV to evade the bounds from Section 4.1. We further fix $f_\chi = 1$ TeV and $c_{tt} = 1$. The composite sector gauge coupling has to be $\tilde{g} > g_s$ but is otherwise only bounded by perturbativity, so it may be large. Similarly, we expect $g_{\rho\pi\pi} > 1$, being a composite sector coupling. Finally, both Lattice studies [88,91,93,100] and calculations employing gauge/gravity duality [80–83,85] suggest that the axial vectors are heavier than the vectors, i.e. $\xi > 1$.

We first briefly cover the case where the $\mathcal{V}_8$ is too light to decay into two pNGBs, which is shown in Fig. 6.1. The hierarchy between $\mathcal{V}_8 \to t\bar{t}$ and $\mathcal{V}_8 \to q\bar{q}$ then only depends on $\tilde{g}$ (and c_{tt}) and is universal for all cosets. The decay to light quarks is dominant for small $\tilde{g}$ while the top decay takes over for large $\tilde{g}$.

In Fig. 6.2 we give an overview of the branching ratios of the $\mathcal{V}_8$ with the vector mass well above the threshold for $\mathcal{V}_8 \to \pi\pi$, $m_{\mathcal{V}_8} = 4.5$ TeV. The figure is separated into three panels according to the coset. In each panel we consider $g_{\rho\pi\pi} \in \{1, 5\}$ and $\xi \in \{\frac{1}{2}, 1, 2\}$. For each

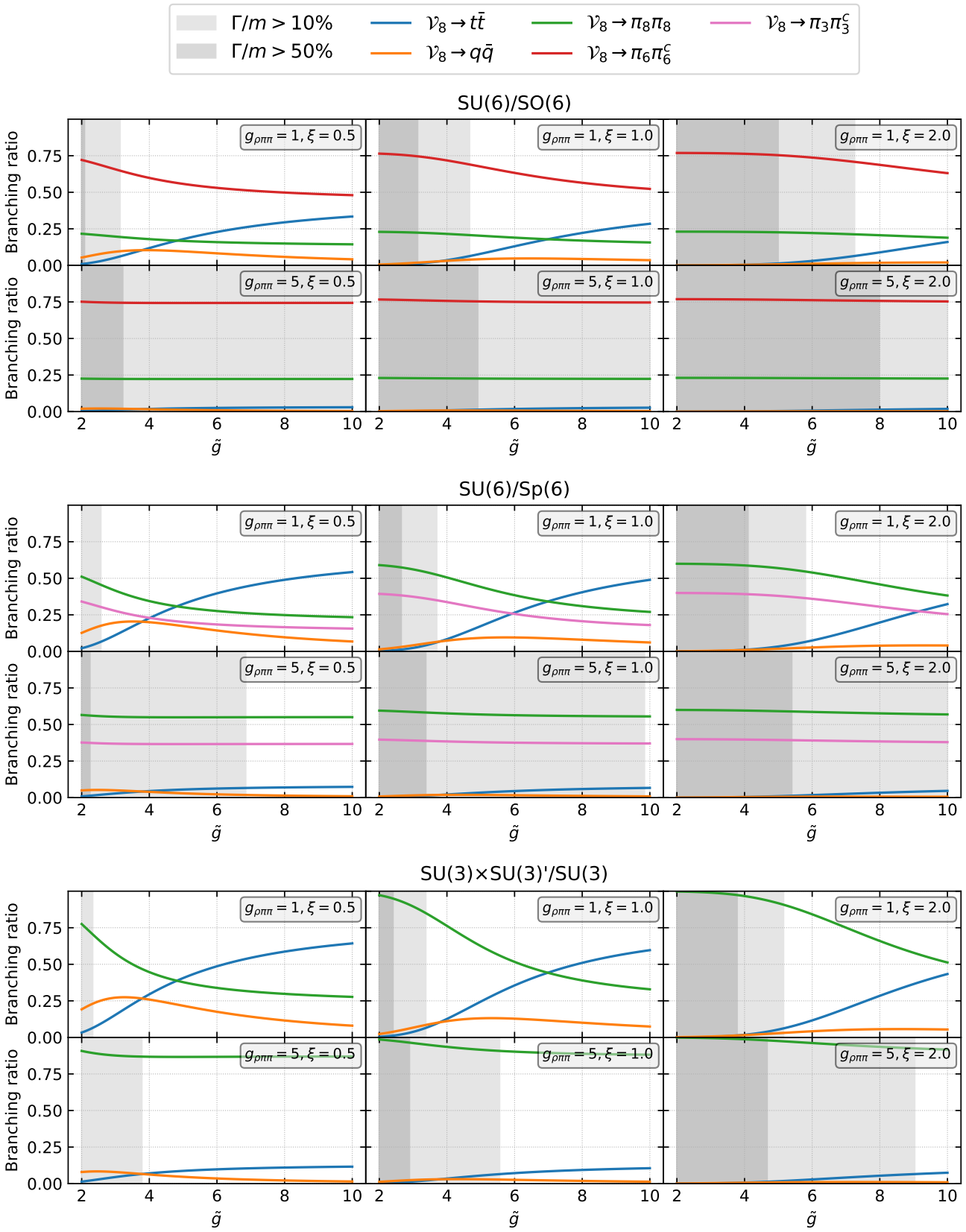

Figure 6.2: Branching ratios of the colour octet vector $\mathcal{V}_8$ for the three colour sector cosets. The light quarks $q = u, d, s, c, b$ include the bottom quark. The vector and pNGB masses are fixed to $m_{\mathcal{V}_8} = 4.5$ TeV and $m_\pi = 1.6$ TeV. The coupling to the top quark is $c_{tt} = 1$ and the pNGB decay constant is $f_\chi = 1$ TeV. The shaded areas indicate the regions of large width compared to the mass.

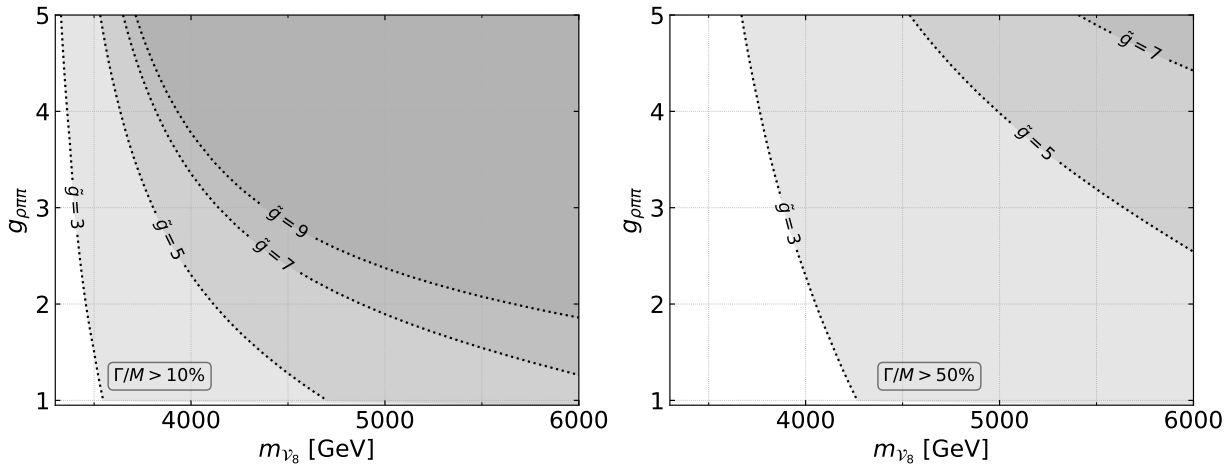

Figure 6.3: Contours of width over mass of the vector octet in the SU(6)/SO(6) coset using the same parameters as in Fig. 6.2. The shaded areas indicate the regions where the total width exceeds (left) 10% and (right) 50% of the mass.

combination we show the branching ratios as a function of $\tilde{g}$. We see that the decays into pNGBs tend to dominate while the light quarks are usually the weakest channel. The areas shaded in light (dark) grey indicate the regions where the total width of the $\mathcal{V}_8$ exceeds 10% (50%) of its mass. The former threshold marks the breakdown of the narrow width approximation (NWA), while a relative width of 50% calls even the interpretation as a resonance into question. The total width increases with $g_{\rho\pi\pi}$ and ξ but decreases with $\tilde{g}$. This is illustrated further by Fig. 6.3, where we show contours of $\Gamma/m_{\mathcal{V}_8}$. The shaded areas indicate the regions of large width. The dependence of the relative width on $g_{\rho\pi\pi}$ is low for small $\tilde{g}$ but quite strong for larger $\tilde{g}$.

We have discussed the first tier decays of the $\mathcal{V}_8$ but to see the detector signatures we need to combine this with the pNGB decays: $\pi_8 \to t\bar{t}$ (for simplicity we neglect the $\pi_8 \to gg$ decay here), $\pi_6 \to bb$ in C1 and $\pi_6 \to tt$ in C2, and $\pi_3 \to \bar{b}\bar{s}$ or $\pi_3 \to b\tau^+$, $t\bar{\nu}$ with equal branching ratios for the lepton channels, see Section 4.1 for details. For the different model classes, this yields

$$\text{C1}: \quad \mathcal{V}_8 \to q\bar{q},\, t\bar{t},\, \pi_8\pi_8(\to 4t),\, \pi_6\pi_6^c(\to 4b) \tag{6.5}$$

$$\text{C2}: \quad \mathcal{V}_8 \to q\bar{q},\, t\bar{t},\, \pi_8\pi_8(\to 4t),\, \pi_6\pi_6^c(\to 4t) \tag{6.6}$$

$$\text{C3}: \quad \mathcal{V}_8 \to q\bar{q},\, t\bar{t},\, \pi_8\pi_8(\to 4t),\, \pi_3\pi_3^c(\to \bar{b}\bar{s}bs \text{ or } q_3\bar{l}_3\bar{q}_3l_3) \tag{6.7}$$

$$\text{C4-5}: \quad \mathcal{V}_8 \to q\bar{q},\, t\bar{t},\, \pi_8\pi_8(\to 4t) \tag{6.8}$$

where $q_3 = b, t$ and $l_3 = \tau^-, \nu$.

We turn to the remaining coloured spin-1 states, starting with the vectors. We recall that $\mathbf{3} \times \mathbf{6} \times \mathbf{8} \supset \mathbf{1}$ in SU(3), so we can have $\mathcal{V}_3 \to \pi_8\pi_6^c$. In the class C2, the $\mathcal{V}_3$ can also couple to

two top quarks. All in all,

$$\text{C1}: \quad \mathcal{V}_3 \to \pi_8\pi_6^c \to t\bar{t}\bar{b}\bar{b}, \tag{6.9}$$

$$\text{C2}: \quad \mathcal{V}_3 \to \bar{t}\bar{t},\ \pi_8\pi_6^c(\to t\bar{t}\bar{t}\bar{t}). \tag{6.10}$$

The ditop channel in Eq. (6.10) is subleading, however, since its coupling is suppressed by $\sin\theta$, see Eq. (3.174). The sextet vector from C3 can analogously decay to

$$\text{C3}: \quad \mathcal{V}_6 \to \pi_8\pi_3^c \to t\bar{t}bs \text{ or } t\bar{t}\bar{b}\tau^-,\ t\bar{t}\bar{t}\nu. \tag{6.11}$$

The coupling to pNGBs is $g_{\rho\pi\pi}$, so we expect $\mathcal{V}_3$ and $\mathcal{V}_6$ to also have a large width.

Our calculation of the hidden symmetry Lagrangian in Section 3.4 showed that the lowest order coupling of axial vectors is to three pNGBs. There is an axial octet in all models, and colour allows

$$\text{C1}: \quad \mathcal{A}_8 \to \pi_8\pi_8\pi_8(\to 6t),\ \pi_8\pi_6\pi_6^c(\to 2t4b), \tag{6.12}$$

$$\text{C2}: \quad \mathcal{A}_8 \to \pi_8\pi_8\pi_8(\to 6t),\ \pi_8\pi_6\pi_6^c(\to 6t), \tag{6.13}$$

$$\text{C3}: \quad \mathcal{A}_8 \to \pi_8\pi_8\pi_8(\to 6t),\ \pi_8\pi_3\pi_3^c(\to t\bar{t}\bar{b}\bar{s}bs \text{ or } t\bar{t}q_3\bar{l}_3\bar{q}_3l_3), \tag{6.14}$$

$$\text{C4-5}: \quad \mathcal{A}_8 \to \pi_8\pi_8\pi_8(\to 6t). \tag{6.15}$$

Being three body decays, these channels are however subleading to

$$\mathcal{A}_8 \to t\bar{t} \tag{6.16}$$

which is induced by derivative couplings, see Eq. (3.74). The $\mathcal{A}_3$ only appears in C3 and can have

$$\text{C3}: \quad \mathcal{A}_3 \to \pi_8\pi_8\pi_3(\to t\bar{t}t\bar{t}\bar{b}\bar{s} \text{ or } t\bar{t}t\bar{t}q_3\bar{l}_3),\ \pi_3\pi_3^c\pi_3(\to \bar{b}\bar{s}bs\bar{b}\bar{s} \text{ or } q_3\bar{l}_3\bar{q}_3l_3q_3\bar{l}_3). \tag{6.17}$$

Finally, the axial sextet has a coupling to tt in C2 in addition to the pNGB decays. Thus,

$$\text{C1}: \quad \mathcal{A}_6 \to \pi_8\pi_8\pi_6(\to 4t2b),\ \pi_6\pi_6^c\pi_6(\to 6b), \tag{6.18}$$

$$\text{C2}: \quad \mathcal{A}_6 \to tt,\ \pi_8\pi_8\pi_6(\to 6t),\ \pi_6\pi_6^c\pi_6(\to 6t). \tag{6.19}$$

Due to the phase space suppression of the three body decays, the axial vectors are narrow resonances. The $\mathcal{A}_6 \to tt$ width is suppressed by $\sin^2\theta$ so it may be comparable with the three body decays.

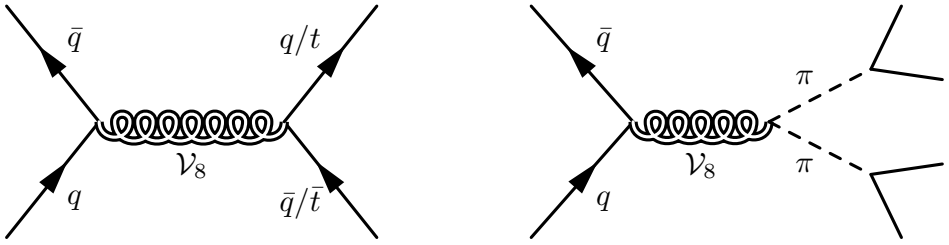

Figure 6.4: Feynman diagrams for the single production of $\mathcal{V}_8$ with decays into quarks or pNGBs.

6.2 LHC bounds from vector octet single production

The vector octet can be singly produced at the LHC via the Feynman diagrams shown in Fig. 6.4. The production cross section of $\mathcal{V}_8$ (assuming zero width) at $\sqrt{s} = 13$ TeV is shown as the background shading and dotted contours in Fig. 6.6. We use the `NNPDF` 2.3 PDF set and dynamical renormalisation and factorisation scales. Besides the mass, the cross section also depends on the vector-quark coupling and thereby on $\tilde{g}$, decreasing both with increasing mass and increasing $\tilde{g}$.

For the numerical simulations in this chapter we implemented a UFO library of the spin-1 resonances and pNGBs. The basis is formed by the publicly available models of top-philic resonances [129, 131] and sextet scalars [115, 116], which we extend by a vector and scalar triplet, a vector sextet, and the relevant interactions between the states. We then generate one combined UFO model at LO.

Each of the decay channels of the $\mathcal{V}_8$ allows us to constrain the parameter space. We first consider the region below the pNGB threshold, $m_{\mathcal{V}_8} < 2m_\pi$, where the universal branching ratios are given by Fig. 6.1 assuming a coupling to top quarks of $c_{tt} = 1$. The two decay channels are covered by experimental searches for high mass di-jet resonances [207] and $t\bar{t}$ resonances [142]. In Fig. 6.5 we compare the cross sections for both processes with the upper limits for $m_{\mathcal{V}_8} = 2m_\pi = 3.2$ TeV. We choose the highest possible mass which corresponds to the smallest cross section, but we have verified that the following statements holds for the full mass range: the top quark channel provides the stronger bounds and excludes the full $\tilde{g}$ range.

Next we consider the case where the pNGB channel is open. The decays into pNGBs have not been searched for, so we derive recast bounds for them using the simulation setup described in Appendix B assuming a narrow width. In all cases the most sensitive searches turn out to be recasts of SUSY searches [122, 156, 206] that are implemented in `CheckMATE`. We show the bounds on the vector mass and $\tilde{g}$ in Fig. 6.6, where we assume 100% branching ratio into the respective channels. The pNGB decays are weighted by the branching ratios in Eq. (6.2). Looking at Fig. 6.2, above the $\pi\pi$ threshold the most important decays are into a top pair and into pNGBs. The bounds on these turn out to be quite similar. In the model classes C2-5, vector masses up to 4 and 5.5 TeV are excluded for large and small $\tilde{g}$, respectively. In C1, the

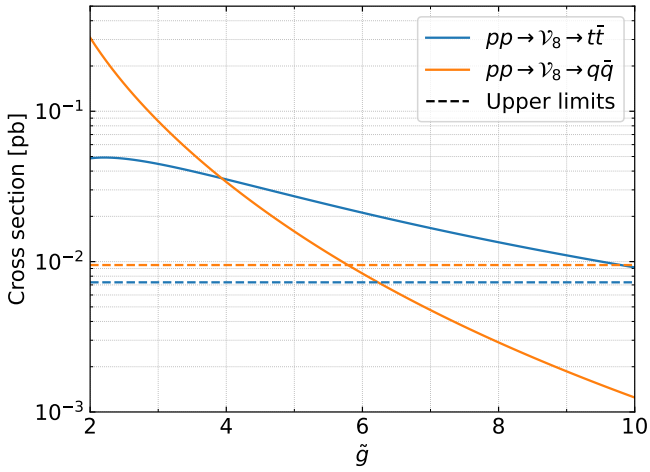

Figure 6.5: Bounds on vector octet single production for $m_{\mathcal{V}_8} = 3.2$ TeV, just below the threshold for the decay into pNGBs, with upper limits from [142, 207].

limit at large $\tilde{g}$ is reduced to 3.5 TeV due to the less strongly constrained $4b$ final state. Note that the region of small $\tilde{g}$ has to be treated with care as the NWA is likely not valid here.

We have claimed multiple times throughout this work that the phenomenology of the spin-1 states at the LHC is driven by single production of the vector octet, despite $\mathcal{V}_8$ pair production always being possible. We can now justify this statement: we have shown that the $\mathcal{V}_8$ must have a mass of at least 3.5 TeV, for which the pair production cross section is 3.8×10^{-7} pb — clearly negligible compared to single production.

6.3 Pair production at future colliders

While pair production of heavy vectors is out of reach for the LHC, it may be accessible to future colliders. In Fig. 6.7 we show the LO pair production cross sections of colour octet, sextet, and triplet vectors for the often discussed case of a 100 TeV pp-collider [208, 209]. The cross sections were calculated with the `NNPDF` 2.3 PDF set with the scales fixed to $\mu_R = \mu_F = m_{\mathcal{V}}$ and apply both to vector and axial vector states. The sextets have the largest cross section as expected from the large Casimir while the triplets have the smallest. Naturally, single production will also be enhanced by the increased centre-of-mass energy. Fig. 6.7 shows that even for a large $\tilde{g}$, single production overtakes octet pair production at $m_{\mathcal{V}_8} = 4$ TeV.

Nevertheless, vector pair production will definitely be detectable at a 100 TeV collider, and we discuss the expected signatures in this section. To simplify the discussion we assume that one class of decays always dominate: light quarks, top quarks, or pNGBs. In all models we can have

$$\mathcal{V}_8\mathcal{V}_8 \to 4q,\ 4t,\ 4\pi_8(\to 8t). \tag{6.20}$$

Of those, the light quark decay is likely subdominant, see Fig. 6.2, while either of the other channels may dominate. In the model classes C1-3 we get additional contributions from the

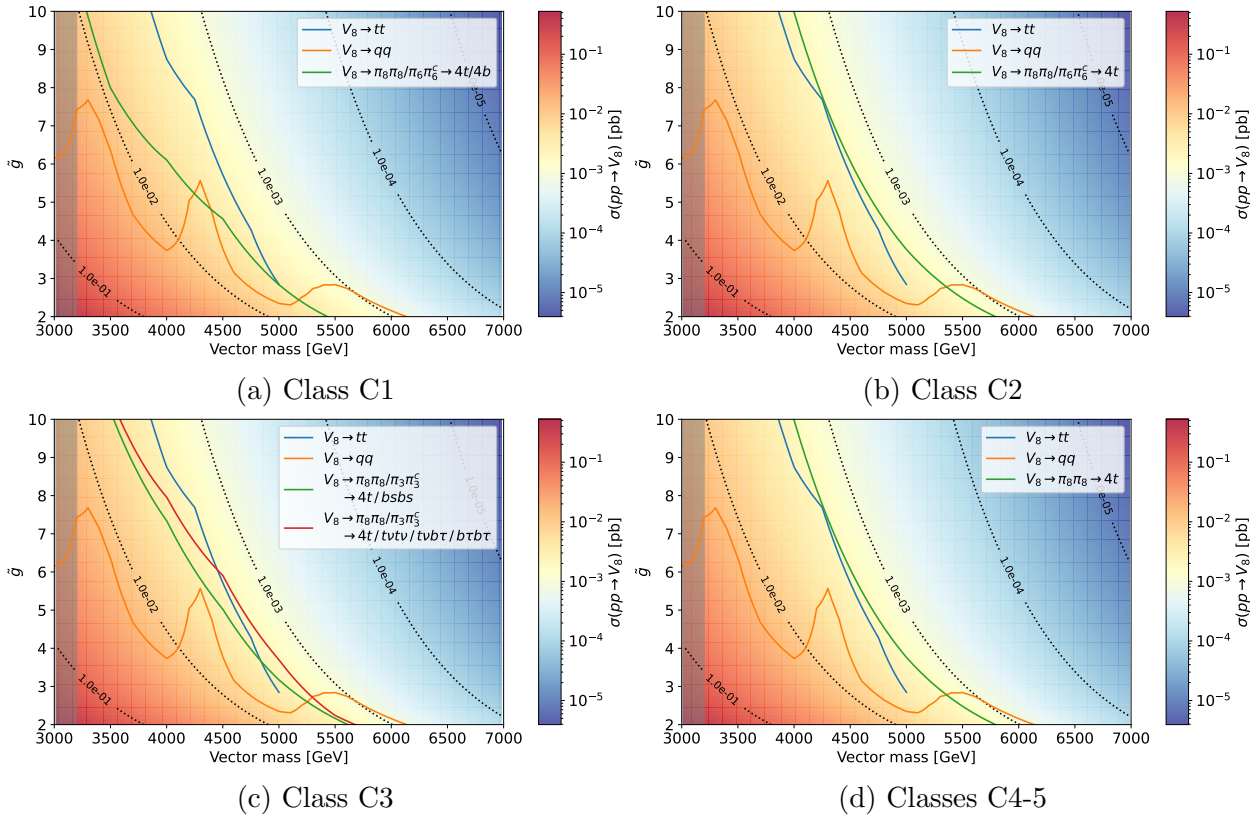

(a) Class C1

(b) Class C2

(c) Class C3

(d) Classes C4-5

Figure 6.6: Bounds on vector octet single production with $m_\pi = 1.6$ TeV. The heat map and the dotted contours indicate the single production cross section. The region to the left and below the coloured lines is excluded, as is the region shaded in grey. The bounds are determined assuming 100% branching ratio into the indicated channel. For the decays in pNGBs, the branching ratios in Eq. (6.2) are taken into account.

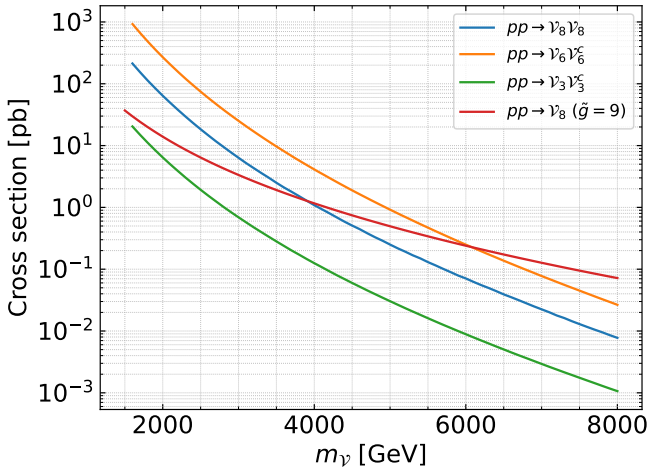

Figure 6.7: Pair production cross section of spin-1 resonances at a $\sqrt{s} = 100$ TeV pp-collider. The values also apply to axial vectors. For comparison we show the single production cross section for $\tilde{g} = 9$.

pNGBs,

$$\text{C1}: \quad \mathcal{V}_8\mathcal{V}_8 \to 4\pi_6(\to 8b),\ 2\pi_8 2\pi_6(\to 4t4b), \tag{6.21}$$

$$\text{C2}: \quad \mathcal{V}_8\mathcal{V}_8 \to 4\pi_6(\to 8t),\ 2\pi_8 2\pi_6(\to 8t), \tag{6.22}$$

$$\text{C3}: \quad \mathcal{V}_8\mathcal{V}_8 \to 4\pi_3(\to 4b4s \text{ or } 4l_3 4q_3),\ 2\pi_8 2\pi_3(\to 4t2b2s \text{ or } 4t2l_3 2q_3). \tag{6.23}$$

From the triplet vector we get

$$\text{C1}: \quad \mathcal{V}_3\mathcal{V}_3^c \to 2\pi_8 2\pi_6 \to 4t4b, \tag{6.24}$$

$$\text{C2}: \quad \mathcal{V}_3\mathcal{V}_3^c \to 2\pi_8 2\pi_6 \to 8t, \tag{6.25}$$

where we neglect the suppressed $\mathcal{V}_3 \to \overline{tt}$ channel. The $\mathcal{V}_6$ from C3 yields

$$\mathcal{V}_6\mathcal{V}_6^c \to 2\pi_8 2\pi_3 \to 4t2b2s \text{ or } 4t2l_3 2q_3. \tag{6.26}$$

Note that we expect the decay widths of the vectors to be large relative to the mass, thus requiring dedicated search strategies.

Next we turn to the axial vectors. We again have the universal octet which has the dominant channel

$$\mathcal{A}_8\mathcal{A}_8 \to 4t, \tag{6.27}$$

with the subleading contributions

$$\text{C1}: \quad \mathcal{A}_8\mathcal{A}_8 \to 6\pi_8(\to 12t),\ 2\pi_8 4\pi_6(\to 4t8b),\ 4\pi_8 2\pi_6(\to 8t4b), \tag{6.28}$$

$$\text{C2}: \quad \mathcal{A}_8\mathcal{A}_8 \to 6\pi_8(\to 12t),\ 2\pi_8 4\pi_6(\to 12t),\ 4\pi_8 2\pi_6(\to 12t), \tag{6.29}$$

$$\text{C3}: \quad \mathcal{A}_8\mathcal{A}_8 \to 6\pi_8(\to 12t),\ 2\pi_8 4\pi_3(\to 4t4b4s \text{ or } 4t4l_3 4q_3),\ 4\pi_8 2\pi_3(\to 8t2b2s \text{ or } 8t2l_3 2q_3). \tag{6.30}$$

The pair production of the axial sextets yields

$$\text{C1}: \quad \mathcal{A}_6\mathcal{A}_6^c \to 4\pi_8 2\pi_6(\to 8t4b),\ 2\pi_8 4\pi_6(\to 4t8b),\ 6\pi_6(\to 12b), \tag{6.31}$$

$$\text{C2}: \quad \mathcal{A}_6\mathcal{A}_6^c \to 4t,\ 4\pi_8 2\pi_6(\to 12t),\ 2\pi_8 4\pi_6(\to 12t),\ 6\pi_6(\to 12t). \tag{6.32}$$

Finally, the triplet from C3 leads to

$$\mathcal{A}_3\mathcal{A}_3^c \to 4\pi_8 2\pi_3(\to 8t2b2s \text{ or } 8t2q_3 2l_3),\ 6\pi_3(\to 6b6s \text{ or } 6q_3 6l_3). \tag{6.33}$$

The axial vectors will have a narrow width and decay promptly.

To summarise, pair production of spin-1 resonances leads to exotic signatures with large multiplicities of top and bottom quarks. Through the ubiquitous octets, every model can

produce four and eight top quarks. In C1 this is supplemented by decays into multiple bottom quarks. The triplet pNGB in C3 leads to more diverse signatures: mixtures of light jets, bottom jets, and potentially top quarks in the baryon number violating case; and third generation quarks with large missing transverse momentum and tau leptons if lepton number violating interactions are added.

7 | Conclusions and outlook

In this thesis we explored the collider phenomenology of realistic composite Higgs models in the context of the Ferretti model class [31–33]. The Ferretti models are characterised by an underlying fermionic description with two species of hyperquarks in distinct irreps of the hypercolour gauge group. After defining the Ferretti models we presented the relevant particle content, highlighted the kinds of interactions in the models, and calculated the Lagrangian that determines the phenomenology of the coloured spin-1 resonances.

We then turned to studying the phenomenology of this model class, beginning with the pseudo Nambu-Goldstone bosons. Starting with the coloured pNGBs, we collected the bounds on QCD pair production where direct searches have been performed and derived recast bounds where no searches were available. To our knowledge, we were able to set the strongest bounds on the production of two octet (sextet) pNGBs decaying to $t\bar{t}$ (tt) so far, excluding masses below 1375 (1510) GeV. Next we considered the pNGBs emerging from the EW sector. We began with a model agnostic approach, setting upper limits on production cross section times branching ratio on the DY pair production of pNGBs in the context of simplified models. We studied all decay channels that can occur within the Ferretti models, providing a comprehensive overview. This showed that multiphoton channels especially are very strongly constrained. In comparison, the bounds on decay channels with multiple W/Z bosons or third generation quarks are considerably weaker. We then studied the bounds on a full model, choosing the SU(5)/SO(5) coset for its rich particle content. We first applied the simplified model bounds and then performed a full simulation of the model. For the case where all pNGBs are mass degenerate and decay into EW gauge bosons, the model is excluded up to 660 GeV; the bound on decays into third generation quarks is 450 GeV. With a few exceptions, none of these Drell-Yan pair production processes have been directly searched for. To contribute to that effort, we proposed a search technique for the process $pp \to S^{++}S^{--} \to W^+t\bar{b}W^-\bar{t}b$ making use of deep learning methods. We trained deep neural networks to differentiate the signal process from the dominant SM backgrounds. The best performing network was a combination of a convolutional neural network using jet images and a multilayer perceptron based on kinematic observables. This would allow for a discovery/exclusion of up to 640/820 GeV at the HL-LHC.

Next we considered the vector-like quarks. We discussed the standard and exotic decay channels, summarised the current bounds on the former and derived recast bounds for some select exotic channels. This revealed that several different final state topologies can be con-

strained quite strongly, showing that the current recasting tools are well equipped for a more systematic study of VLQs.

Finally, we made use of the aforementioned calculation of the spin-1 Lagrangian to study the phenomenology of the coloured vector resonances. These contain a vector octet $\mathcal{V}_8$ that mixes with the gluon. This state dominates the LHC phenomenology through its single production channel. We discussed the relative strengths of the possible decay channels and derived bounds in the mass-coupling-plane. The bounds lie between 3.5 to 5.5 TeV. We also showed that the $\mathcal{V}_8$ may well have a large relative width $> 10\%$ or even 50%, requiring a specialised search technique. As an outlook for future colliders we finally summarised the signatures expected from pair production of two spin-1 states, where multi top processes are common, featuring as many as 12 top quarks.

While we have made an effort to shine some light on the phenomenology of the Ferretti models in this work, a lot remains to explore. We have touched on the VLQs, but given their prominence they deserve further attention. This is a challenging topic: setting upper limits on all VLQ pair production channels, similar to what we did for the EW pNGBs, would require recasting for more than 150 processes in a mass-mass-plane. This requires significant resources, both in terms of computation time and manual work. It might be more efficient to first perform a preselection to identify the most important processes and then target these. For example, one might focus on processes that are available in a large number of models rather than very specific ones. This information can be combined with the branching ratios for the fermiophobic decays of the scalars, considering only common processes with a large expected branching ratio. Besides the VLQs, the Ferretti models also feature fermionic resonances of different colour representations. The sextets stand out by their large pair production cross section. They have not been studied before, so an exploration of their phenomenology is needed. Furthermore, while we have thoroughly covered the coloured spin-1 states, a corresponding study of the EW vectors should be performed. In fact, we are currently working on applying the approach in Chapter 6 to the EW sector [106].

A different direction for extending our work is regarding the application of deep learning in the search for new physics. One possibility is to focus on the methodological aspects, for example trying to find better neural network architectures. We highlight [210] as a step in that direction. The approach can also be improved to be closer to experiment, for example by including pileup effects. Besides that we highlight that our approach can also be used to study different BSM processes.

A | Colour sector embeddings

At several points throughout this work we embed QCD coloured states into two-index irreps of Sp(6). In this appendix we summarise these embeddings and collect some identities that are useful for the corresponding calculations.

We label the generators of $\mathrm{SU}(3)_c$ as $t^a_{\mathbf{r}}$ where $\mathbf{r}$ is the irrep they are acting on. For example,

$$t^a_{\mathbf{3}} = \frac{1}{2}\lambda^a \tag{A.1}$$

with the Gell-Mann matrices λ^a satisfying $\mathrm{Tr}\big(\lambda^a\lambda^b\big) = 2\delta^{ab}$. From the product identity [211]

$$\lambda^a\lambda^b = \frac{2}{3}\delta^{ab}\mathbb{1}_3 + (d^{abc} + if^{abc})\lambda^c \tag{A.2}$$

follows the useful trace

$$\mathrm{Tr}\big(\lambda^a\lambda^b\lambda^c\big) = 2(d^{abc} + if^{abc}). \tag{A.3}$$

Before turning to Sp(6), we review how to express several SU(3) irreps as 3×3 matrices. Following the notation of [212], we write

$$\boldsymbol{\phi}_1 = \phi_1\mathbb{1}_3, \quad \boldsymbol{\phi}_3 = \phi^i_3 L^i, \quad \boldsymbol{\phi}_6 = \phi^s_6 K^s, \quad \boldsymbol{\phi}_8 = \phi^a_8 t^a_{\mathbf{3}} \tag{A.4}$$

for a generic field $\phi_{\mathbf{r}}$ of irrep $\mathbf{r}$. The triplet and sextet matrices are symmetric and antisymmetric, respectively, with

$$[L^i]^{jk} = \frac{1}{\sqrt{2}}\epsilon^{ijk} \tag{A.5}$$

and

$$K^1 = \begin{pmatrix} 1 & 0 & 0 \\ 0 & 0 & 0 \\ 0 & 0 & 0 \end{pmatrix}, \quad K^2 = \frac{1}{\sqrt{2}}\begin{pmatrix} 0 & 1 & 0 \\ 1 & 0 & 0 \\ 0 & 0 & 0 \end{pmatrix}, \quad K^3 = \begin{pmatrix} 0 & 0 & 0 \\ 0 & 1 & 0 \\ 0 & 0 & 0 \end{pmatrix}, \tag{A.6}$$

$$K^4 = \frac{1}{\sqrt{2}}\begin{pmatrix} 0 & 0 & 0 \\ 0 & 0 & 1 \\ 0 & 1 & 0 \end{pmatrix}, \quad K^5 = \begin{pmatrix} 0 & 0 & 0 \\ 0 & 0 & 0 \\ 0 & 0 & 1 \end{pmatrix}, \quad K^6 = \frac{1}{\sqrt{2}}\begin{pmatrix} 0 & 0 & 1 \\ 0 & 0 & 0 \\ 1 & 0 & 0 \end{pmatrix}. \tag{A.7}$$

They are normalised as

$$\mathrm{Tr}\big(L^i L^j\big) = -\delta^{ij}, \qquad \mathrm{Tr}\big(K^s K^t\big) = \delta^{st}. \tag{A.8}$$

In the main text we make use of the fact that [212]

$$\mathrm{Tr}\big(L^i L^j t^a_{\mathbf{3}}\big) = \frac{1}{2}[t^a_{\mathbf{3}}]^{ij}, \qquad \mathrm{Tr}\big(K^t K^s t^a_{\mathbf{3}}\big) = \frac{1}{2}[t^a_{\mathbf{6}}]^{st}. \tag{A.9}$$

In the Ferretti models, the $\mathrm{SU}(3)_c$ is a subgroup of the unbroken global symmetry group, for example Sp(6). States appear in the **14** and **21** of Sp(6), which decompose as

$$\mathbf{14} \to \mathbf{8}_0 + \mathbf{3}_{2/3} + \bar{\mathbf{3}}_{-2/3}, \tag{A.10}$$

$$\mathbf{21} \to \mathbf{8}_0 + \mathbf{6}_{-2/3} + \bar{\mathbf{6}}_{2/3} + \mathbf{1}_0 \tag{A.11}$$

under $\mathrm{Sp}(6) \to \mathrm{SU}(3)_c \times \mathrm{U}(1)_X$. Embedding the $\mathrm{SU}(3)_c$ into Sp(6) by

$$T^a = \frac{1}{\sqrt{2}} \begin{pmatrix} t^a_{\mathbf{3}} & 0 \\ 0 & -(t^a_{\mathbf{3}})^T \end{pmatrix}, \tag{A.12}$$

we can embed the $\mathrm{SU}(3)_c$ irreps by [107]

$$\boldsymbol{\phi}_{14} = \frac{1}{\sqrt{2}} \begin{pmatrix} \boldsymbol{\phi}_8 & \boldsymbol{\phi}_3^\dagger \\ \boldsymbol{\phi}_3 & \boldsymbol{\phi}_8^T \end{pmatrix}, \tag{A.13}$$

$$\boldsymbol{\phi}_{21} = \frac{1}{\sqrt{2}} \begin{pmatrix} \boldsymbol{\phi}_8 + \frac{1}{\sqrt{6}}\boldsymbol{\phi}_1 & \boldsymbol{\phi}_6 \\ \boldsymbol{\phi}_6^\dagger & -\boldsymbol{\phi}_8^T - \frac{1}{\sqrt{6}}\boldsymbol{\phi}_1 \end{pmatrix}. \tag{A.14}$$

They are normalised such that

$$\mathrm{Tr}\Big(\boldsymbol{\phi}_{14}^\dagger \boldsymbol{\phi}_{14}\Big) = \frac{1}{2}\phi_8^a \phi_8^a + \phi_3^{*,i}\phi_3^i, \tag{A.15}$$

$$\mathrm{Tr}\Big(\boldsymbol{\phi}_{21}^\dagger \boldsymbol{\phi}_{21}\Big) = \frac{1}{2}\phi_1\phi_1 + \phi_6^{*,s}\phi_6^s + \frac{1}{2}\phi_8^a\phi_8^a. \tag{A.16}$$

Finally we discuss a normalisation subtlety in the field strength tensor of the vector resonances, which we would like to have the form

$$\mathcal{V}^A_{\mu\nu} = \partial_\mu \mathcal{V}^A_\nu - \partial_\nu \mathcal{V}^A_\mu + \tilde{g} f^{ABC} \mathcal{V}^B_\mu \mathcal{V}^C_\nu \tag{A.17}$$

where A, B, C are adjoint indices of the unbroken subgroup H. We included a $1/\sqrt{2}$ in the definition of the T^a above, but this has the side effect that

$$[T^a, T^b] = \frac{1}{2} \begin{pmatrix} [t^a_{\mathbf{3}}, t^b_{\mathbf{3}}] & 0 \\ 0 & [t^{a,T}_{\mathbf{3}}, t^{b,T}_{\mathbf{3}}] \end{pmatrix} = \frac{1}{\sqrt{2}} i f^{abc} T^c. \tag{A.18}$$

To counteract this we need an additional $\sqrt{2}$ in front of the commutator in

$$\boldsymbol{\mathcal{V}}_{\mu\nu} = \partial_\mu \boldsymbol{\mathcal{V}}_\nu - \partial_\nu \boldsymbol{\mathcal{V}}_\mu - \sqrt{2} i \tilde{g} [\boldsymbol{\mathcal{V}}_\mu, \boldsymbol{\mathcal{V}}_\nu]. \tag{A.19}$$

B | Simulation setup

In the main text we present a variety of numerical results obtained from simulating particle physics events. This appendix provides a comprehensive summary of the utilised tools and evaluation methods.

Our first step to simulating BSM events is to implement the model under study in the `FeynRules` framework [213] and generate a UFO library [214]. The UFO is then read by the Monte Carlo event generator `MadGraph5_aMC@NLO` [215], which allows to calculate cross sections and generate hard scattering events of arbitrary processes at leading or next-to-leading order. Unless stated otherwise, we run `MadGraph5` with the default dynamical renormalisation and factorisation scale choices and use the `NNPDF` 2.3 set of PDFs [216] provided by `LHAPDF6` [217]. The events are then passed to `Pythia8` [218], which performs the decays of unstable SM particles (top quarks, W/Z bosons etc.), then showers and hadronises the events, and finally saves them in the `HepMC` format [219]. This is a universal format that can be read by many analysis tools.

Despite the extensive search program for physics beyond the SM being carried out by the ATLAS and CMS collaborations, it is impossible for them to search for every signature of every model. Furthermore, from theorists proposing a new model to a corresponding search being published it can take years. In response to this issue, the theoretical community has developed several tools that allow model builders to quickly determine which parts of the parameter space are still viable — so-called recasting tools. The basic idea of them is to reimplement the cuts of a given search, then run simulated BSM events through the cuts, compare the number of events that pass the cuts with the observed number of events in the search, and finally compute an exclusion value with the CL_s prescription [220]. Such routines are implemented in `MadAnalysis5` [221–224] and `CheckMATE` [225, 226]. Both tools use `Delphes 3` [227] for detector simulation and event reconstruction, and jets are clustered with the anti-k_T algorithm [228] implemented in `FastJet` [229]. While `MadAnalysis5` and `CheckMATE` focus on recasts of searches, a similar procedure can be applied to SM measurements. The tool of choice for this purpose is `Rivet` [230], where a large quantity of measurements have been implemented, in particular differential cross section measurements. Monte Carlo events are analysed with `Rivet` and the results passed to `Contur` [231, 232] for statistical evaluation. We list the version of each tool that was used in the various simulations in the main text in Tab. B.1. In practice we used these tools within framework of the `scangen` program which is documented in Appendix E.

Section	MadGraph5	MadAnalysis5	CheckMATE	Rivet	Contur
Section 4.1	v3.5.1	v1.10.9beta	commit 1cb3f7	v3.1.8	v2.2.4
Sections 4.3 and 4.4	v3.3.2*	v1.9.60	commit 8952e7	v3.1.5	v2.2.1
Section 4.5	v3.4.0	—	—	—	—
Chapter 5	v3.5.1	v1.10.9beta	commit 1cb3f7	v3.1.8	v2.2.4
Chapter 6	v3.5.3	v1.10.9beta	commit 1cb3f7	v3.1.8	v2.2.4

Table B.1: Tool versions used in the simulations in the main text. v3.3.2* consists of v3.3.2 along with several patches that were later published in v3.4.0.

In this work, we use recasting tools to answer two related but different questions:

1. Given a signal process, is a given parameter point excluded or still viable?
2. Given a signal process, what does its cross section have to be to exclude it at 95% CL?

Answering question 1 is straightforward as this is arguably what the recasting tools are designed to do: after supplying hadronised signal events and the corresponding cross section, all three tools calculate an exclusion value. The approach to question 2, calculating an upper limit σ_{95} on the cross section, depends on the tool [1]:

- `MadAnalysis5` performs the necessary calculation internally and outputs an expected (`sig95exp`) and an observed (`sig95obs`) upper limit for every signal region. We use the observed limit from the most sensitive signal region as indicated by the `best` column in the output file.
- `CheckMATE` quotes upper limits on the number of signal events obtained from the recast search, S_{95}^{exp} (expected) and S_{95}^{obs} (observed). We can combine these with the number of signal events S that passed the cuts and the input cross section σ_{in} to calculate the upper limit as

$$\sigma_{95} = \frac{S_{95}^{\text{obs}}}{S}\,\sigma_{\text{in}}. \tag{B.1}$$

  We use the observed bound to calculate the final result but choose the signal region with the strongest expected bound, which is the default procedure employed by `CheckMATE`.
- `Contur` does not have any features to facilitate calculating σ_{95}. Instead we rerun the evaluation multiple times and update the input cross section dynamically until we reach $\text{CL}_s = 0.05 \pm 0.01$.

We determine the results from all three tools and implemented analyses and then report the overall strongest exclusion/upper limit as the final result. We do not attempt any statistical combination of results beyond what is implemented in the tools.

C | Details on bounds on EW pNGBs

In Sections 4.3 and 4.4 we derive bounds on the Drell-Yan pair production of EW pNGBs. In this appendix we provide some supplemental information on this: we list the couplings in the SU(5)/SO(5) model that determine the production cross section, discuss a technical point about extracting bounds from `CheckMATE`, and provide a list detailling which searches contribute to which simplified model bounds [1].

C.1 Couplings for Drell-Yan pair production

In this appendix we list the couplings emerging from the kinetic term of the pNGBs in the SU(5)/SO(5) coset which have been presented in [113]. In the notation of Eq. (4.19), they read

	$K_W^{S_i^0 S_j^+}$		$K_W^{S_i^- S_j^{++}}$
	η_3^+	η_5^+	η_5^{++}
h	0	0	
η_3^0	$-\frac{i}{2}$	$\frac{c_\theta}{2}$	
η_5^0	$-\frac{c_\theta}{2\sqrt{3}}$	$\frac{i\sqrt{3}}{2}$	$-$
η_1^0	$\sqrt{\frac{2}{3}}c_\theta$	0	
η	0	0	
η_3^-			$\frac{c_\theta}{\sqrt{2}}$
η_5^-	$-$		$-\frac{i}{\sqrt{2}}$

	$K_Z^{S_i^0 S_j^0}$					$K_Z^{S_i^+ S_j^-}$		$K_Z^{S_i^{++} S_j^{--}}$
	h	η_3^0	η_5^0	η_1^0	η	η_3^-	η_5^-	η_5^{--}
h	0	0	0	0	0			
η_3^0		0	$\frac{ic_\theta}{\sqrt{3}}$	$i\sqrt{\frac{2}{3}}c_\theta$	0			
η_5^0			0	0	0	$-$		$-$
η_1^0				0	0			
η					0			
η_3^+						$-\frac{c_{2w}}{2}$	$-\frac{ic_\theta}{2}$	
η_5^+			$-$				$-\frac{c_{2w}}{2}$	
η_5^{++}				$-$				$-c_{2w}$

where $c_\theta = \cos\theta$ with $\sin\theta = v/f_\psi$ and $c_{2w} = \cos 2\theta_W$ with the Weinberg angle θ_W.

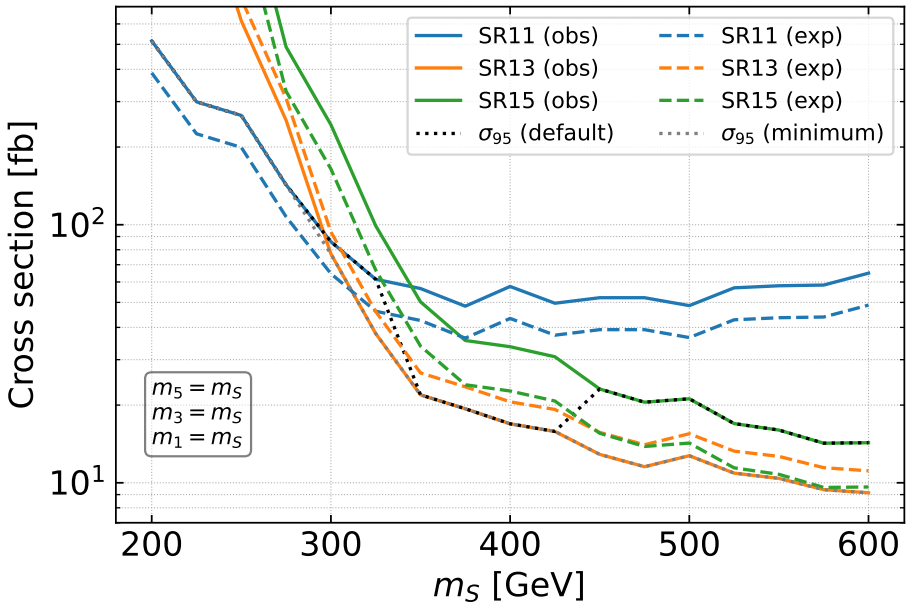

Figure C.1: Bounds on the pNGB masses for the Drell-Yan production of the full bitriplet with decays to third generation quarks.

C.2 Choosing the best signal region

In Section 4.4 we determined the bounds on the SU(5)/SO(5) model assuming all pNGBs to be mass degenerate. This was done for both fermiophobic (Fig. 4.13a) and fermiophilic (Fig. 4.16) decays of the pNGBs. In both cases the upper limit on the cross section shows a distinctive kink — towards stronger bounds for the former, but weakening the bounds in the second case. The kinks are due to a change in the dominant signal region. However, we usually expect the upper limits to grow stronger with mass since the final state objects grow harder. Seeing a weakening bound is therefore worthy of further examination.

We show all relevant limits in Fig. C.1. There are three relevant signal regions — SR11 in blue, SR13 in orange, and SR15 in green — and for each we show the expected (dashed) and observed (solid) upper limits. As mentioned in the previous appendix, `CheckMATE` uses the expected limit to select the most sensitive signal region but then reports the observed limit as the result. This method leads to the total upper limit shown as a black dotted line. To contrast, the grey dotted line shows the limit that is obtained by disregarding the expected limit and only choosing the strongest of all observed limits. At low masses, SR11 is clearly the strongest signal region. A first discrepancy occurs at $m_S = 300$ GeV where SR13 overtakes SR11 in the observed but not yet the expected bound, the latter catching up around 330 GeV. The major difference that motivated this investigation occurs at 450 GeV: The expected bound of SR15 slightly overtakes SR13. The observed bound of SR15, however, is considerably weaker than that of SR13, leading to a decreased bound. Given that the difference between expected limits is marginal, one might be tempted to ignore it and simply choose the stronger observed bound. This would not be statistically sound, however. Once an evaluation procedure has been chosen we cannot pick another one based on the results. Otherwise we tend to inflate our bounds by

a look-elsewhere effect. We therefore take the black dotted line in Fig. C.1 as our result.

C.3 List of dominant analyses

In Section 4.3 we give an overview of DY production of EW pNGBs, presenting simplified model bounds for a variety of decay channels. Besides the bounds themselves, another purpose of this work is as an assessment of the sensitivity of the searches currently implemented in recast tools to a variety of final states. This appendix gives more information to this end. In Tab. C.1 we go through all processes and list the searches that provide the dominant bound for at least one mass point, separated by the tool they are implemented in. An even finer breakdown showing also which mass points the searches were dominant for, along with the numerical upper limits, can be found at `https://github.com/manuelkunkel/scalarbounds`. Additionally, Tab. C.2 provides a brief overview of these searches and lists the internal name under which they are implemented in the recasting tools.

Production	Channel	MadAnalysis5	CheckMATE	Rivet/Contur
$S^{++}S^{--}$	$WWWW$	[153]	[164]	
$S^{\pm\pm}S^{\mp}$	$WWWZ$	[153]	[164]	
	$WWW\gamma$			[161, 162]
$S^{+}S^{-}$	$WZWZ$		[164]	
	$WZW\gamma$			[161, 162]
	$W\gamma W\gamma$		[154, 159]	
$S^{\pm}S^{0}$	$WZWW$	[153]	[164]	
	$W\gamma WW$			[161, 162]
	$WZZZ$		[164]	
	$(W\gamma)(ZZ)$			[160–162]
	$(WZ)(Z\gamma)$			[161, 162]
	$(WZ)(\gamma\gamma)$		[154]	
	$(W\gamma)(Z\gamma)$		[154, 159]	
	$W\gamma\gamma\gamma$		[123, 154, 159]	
$S^{0}S'^{0}$	$WWWW$	[153]	[164]	
	$WWZZ$		[164]	
	$WW\gamma Z$			[161, 162]
	$WW\gamma\gamma$		[154]	
	$ZZZZ$		[164]	[160]
	γZZZ			[160–162]
	$(\gamma Z)(\gamma Z)$		[154, 159]	[160, 161]
	$(\gamma\gamma)(ZZ)$		[154]	
	$\gamma\gamma\gamma Z$		[154, 159]	
	$\gamma\gamma\gamma\gamma$		[123]	[155]
$S^{++}S^{--}$	$WtbWtb$		[121]	
$S^{\pm\pm}S^{\mp}$	$Wtbtb$		[121]	
$S^{+}S^{-}$	$tbtb$		[121, 156]	
$S^{\pm}S^{0}$	$tbtt$		[121]	
	$tbbb$	[157]	[121, 123, 124, 156]	
$S^{0}S'^{0}$	$tttt$		[121]	
	$ttbb$	[158]	[121, 156]	
	$bbbb$	[158]	[123]	

Table C.1: Experimental analyses contributing to the simplified model bounds in Fig. 4.7. More details are available on `https://github.com/manuelkunkel/scalarbounds`.

Analysis	Description	Recast
ATLAS JHEP [144] 139 fb^{-1}	$S^{++}S^{--} \to 4W$, $S^{++}S^{-} \to WWWZ$; 2, 3 or 4 leptons, MET and jets	_
CMS PAS EXO-19-002 [153] 137 fb^{-1}	Type-III seesaw and light scalars; at least 3 charged leptons	`MadAnalysis5` `cms_exo_19_002`
ATLAS PRD 97 [154] 36.1 fb^{-1}	Gauge mediated SUSY breaking; (multi)photon and jets	`CheckMATE` `atlas_1802_03158`
ATLAS JHEP [155] 139 fb^{-1}	Measurement of prompt photon-pair production	`Rivet/Contur` `ATLAS_2021_I1887997`
ATLAS EPJ C 81 [121] 139 fb^{-1}	RPV SUSY; many jets, ≥ 1 leptons and 0 or ≥ 3 b-jets	`CheckMATE` `atlas_2106_09609`
ATLAS EPJ C 81 [156] 139 fb^{-1}	Squarks and gluinos; 1 lepton, jets and MET	`CheckMATE` `atlas_2101_01629`
ATLAS EPJ C 79 [123] 3.2 fb^{-1}	General search for new phenomena	`CheckMATE` `atlas_1807_07447`
ATLAS JHEP [124] 139 fb^{-1}	Bottom-squark pair production; no leptons, ≥ 3 b-jets and MET	`CheckMATE` `atlas_1908_03122`
CMS PAS SUS-19-006 [157] 137 fb^{-1}	Gluinos and squarks; no leptons, multiple jets and MET	`MadAnalysis5` `cms_sus_19_006`
CMS-SUS-16-033 [158] 35.9 fb^{-1}	Gluinos and stops; no leptons, multiple jets and MET	`MadAnalysis5` `cms_sus_16_033`
ATLAS JHEP [159] 139 fb^{-1}	Chargino-neutralino production; MET and $h \to \gamma\gamma$	`CheckMATE` `atlas_2004_10894`
ATLAS JHEP [160] 139 fb^{-1}	Measurements of four-lepton differential cross sections	`Rivet/Contur` `ATLAS_2021_I1849535`
ATLAS JHEP [161] 139 fb^{-1}	Measurement of the $Z(\to \ell^+\ell^-)\gamma$ production cross section	`Rivet/Contur` `ATLAS_2019_I1764342`
ATLAS JHEP [162] 36.1 fb^{-1}	Measurement of the $Z(\to \nu\bar{\nu})\gamma$ production cross section	`Rivet/Contur` `ATLAS_2018_I1698006`
ATLAS-CONF-2016-096 [163] 13.3 fb^{-1}	Electroweakino production; 2 to 3 leptons, MET and no jets	`CheckMATE` `atlas_conf_2016_096`
CMS PAS SUS-16-039 [164] 35.9 fb^{-1}	Electroweakino production; ≥ 2 leptons and MET	`CheckMATE` `cms_sus_16_039`

Table C.2: Summary of the analyses that contribute to the simplified model bounds in Fig. 4.7.

D | Deep learning

In this appendix we give further information on the technical aspects of our search proposal in Section 4.5. We begin with a general overview of the fundamentals of deep learning. We then provide justification for our choice of training set and evaluation method [2].

D.1 A brief introduction to deep learning

This section contains the necessary background on the neural networks (NNs) employed in Section 4.5. A thorough introduction to deep learning is beyond the scope of this work, so we will focus only on the basics. We mostly follow [233]. For more elementary introductions see e.g. [234, 235].

We begin with some nomenclature: A *machine learning* (ML) algorithm is anything where a program autonomously learns patterns from data. A simple example is a linear regression which, while undeniably useful, is quite limited in the tasks it can solve. *Deep learning* is a subset of ML algorithms that employs deep neural networks. This approach has seen tremendous success in recent years both in science and in everyday life, and we have applied it to particle physics in this work.

The simplest network is the *multilayer perceptron* (MLP) which consists of an input layer, an output layer, and a number of hidden layers. The hidden layers transfer information through the network and consist of several nodes which we can think of as forming a vector of numbers $\vec{l}_i$. To calculate the output layer from the input data (performing a *forward pass*), we work our way from left to right by chaining affine transformations,

$$\vec{l}_{n+1} = W_{n+1}\vec{l}_n + \vec{b}_{n+1}. \tag{D.1}$$

The matrix W_{n+1} is often called weight matrix and $\vec{b}$ is the bias vector. In the following we refer to the elements of the weight matrices and the bias vectors collectively as *weights*. Due to the presence of the weight matrix, every node of the next layer is connected to every node of the previous layer; the network is *fully connected*. One detail is still missing: concatenating two affine transformations is again an affine transformation, so we need to introduce non-linearity via a so-called *activation function* for the network to be able to learn non-linear behavior. In

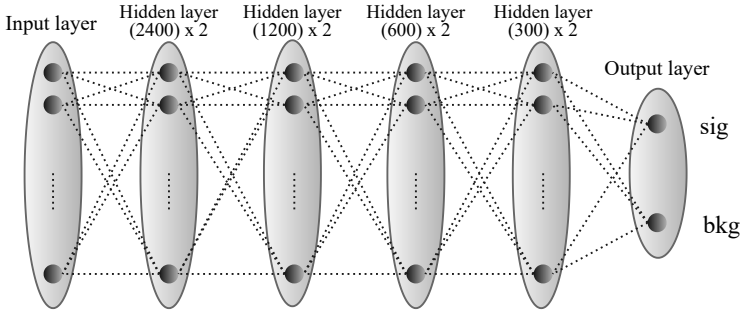

Figure D.1: Neural network architecture of the MLP used in the main text. A ReLU activation function is used between each layer. $(2400) \times 2$ indicates two consecutive hidden layers with 2400 nodes each.

this work we always use the rectified linear unit (ReLU), which is defined as

$$\mathrm{ReLU}(x) = \max(0, x). \tag{D.2}$$

To move from one layer to the next, we therefore have

$$\vec{l}_{n+1} = \mathrm{ReLU}\left(W_{n+1}\vec{l}_n + \vec{b}_{n+1}\right). \tag{D.3}$$

In this work we are interested in classification tasks, specifically differentiating signal from background events. We therefore present the network with data corresponding to a physics event and ask it to predict whether it is a signal or background. To this end, the output layer of our network contains only two nodes $z_{1,2}$. After normalisation with the softmax function

$$\mathrm{softmax}(z_i) = \frac{e^{z_i}}{\sum_j e^{z_j}} \tag{D.4}$$

their values correspond to the probability of the event being signal p_S or background p_B as assigned by the network. In the following we refer to p_S as the *NN score*. We present the MLP network architecture used in the main text in Fig. D.1, which consists of a sequence of fully connected layers with a ReLU activation function between each layer.

Once a network architecture is defined, we have to train it. To this end we need a metric for how well the network has classified an event. It can be shown [233] that the optimal loss function for a classification task is the *cross entropy loss*, which in our case reads

$$L_{\mathrm{CE}} = -\left(p_{S,\mathrm{true}} \log p_S + p_{B,\mathrm{true}} \log p_B\right) = \begin{cases} -\log p_S, & \text{true signal event} \\ -\log p_B, & \text{true background event} \end{cases} \tag{D.5}$$

for a given event, where $p_{S/B}$ are the model's predictions and $p_{S,\mathrm{true}} = 1$ if it is in fact a signal event and $p_{S,\mathrm{true}} = 0$ otherwise. The loss function is then used to optimise the network by iteratively adjusting the weights θ_i by a method called *gradient descent*: Each optimisation step we run over the dataset and pass the events through the network. We then calculate the

Network	Batch size	Learning rate	Weight decay
$\mathcal{K}$	20	5×10^{-7}	2×10^{-9}
$\mathcal{I}_{C\ell}$	20	5×10^{-4}	3×10^{-4}
$\mathcal{I}_{CN\ell}$	20	3×10^{-4}	3×10^{-4}
$\mathcal{I}_{C\ell} + \mathcal{K}$	20	3×10^{-4}	2×10^{-4}
$\mathcal{I}_{CN\ell} + \mathcal{K}$	20	5×10^{-4}	3×10^{-4}

Table D.1: Hyperparameters of the networks used in the main text.

loss functions and the gradients with respect to the weights, average over the gradients, and finally update the weights to reduce the loss:

$$\theta_i^{t+1} = \theta_i^t - \lambda \left\langle \frac{\partial L^t}{\partial \theta_i} \right\rangle \tag{D.6}$$

The step size λ is called the *learning rate*. The networks in this work were not trained with pure gradient descent but with the `Adam` optimiser [192], a more advanced algorithm based on the same principle.

In practice we cannot use the whole dataset for training. Rather, we split it into three parts: one for training, one for validation, and a holdout test set only to be used at the very end for a final evaluation. The training set is used as outlined above while the validation set serves to monitor the training progress and optimise the network architecture without introducing biases into the evaluation. A full pass over the training set is called an *epoch*. However, updating the weights only once per epoch turns out to be computationally inefficient. We rather divide the training set into minibatches, then evaluate the mean gradient and take the optimisation step after each minibatch. The number of samples in a minibatch is called the *batch size*.

A common issue with gradient descent learning is that the network might overfit on the training set, i.e. it performs very well on this training set but badly on unseen data. One of the purposes of the validation set is to monitor this by regularly evaluating the network on data it has not been trained on. To further combat overfitting we can apply *regularisation* methods. A common practice is to add the square sum of all weights to the loss function [234],

$$L \to L + \frac{1}{2}\alpha \sum_i \theta_i^2, \tag{D.7}$$

where the parameter α is known as *weight decay*.

The learning rate, weight decay, batch size, and in fact the full network architecture are external parameters that are not optimised during training. Rather one starts with an initial guess, fully trains the network, and then varies the parameter and retrains to see if the performance improved or not. The performance measure for this task is the loss evaluated on the validation set. In Tab. D.1 we list the most important hyperparameters of the networks used in the main text.

Neural networks tend to learn best on normalised data. A popular way to ensure that

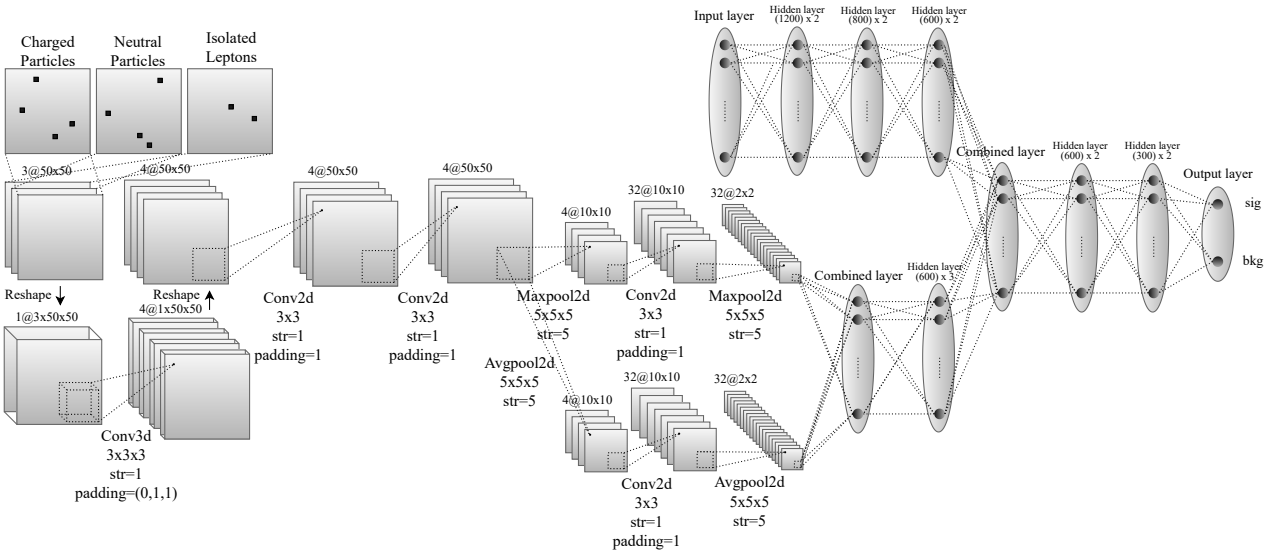

Figure D.2: Neural network architecture of the CNN used in the main text. For the networks $\mathcal{I}_{C(N)\ell} + \mathcal{K}$ the CNN output is interfaced with a separate MLP using kinematic data, shown in the top right. 4@50 × 50 denotes 4 feature maps of size 50 × 50. A batch normalisation layer is included after every convolutional layer.

normalisation is maintained throughout the network is with *batch normalisation* layers [236]. Given a minibatch of samples x_i with $i = 1, \ldots, N_{\text{batch size}}$, we calculate the mean $\langle x_i \rangle$ and variance σ^2 and then define normalised values $\hat{x}_i$ by

$$\hat{x}_i = \frac{x_i - \langle x_i \rangle}{\sqrt{\sigma^2 + \epsilon}} \tag{D.8}$$

where ϵ is a small number to avoid dividing by zero. Finally, the output of the batch normalisation is a rescaled and shifted $\hat{x}_i$,

$$\text{BN}_{\gamma,\beta}(x_i) = \gamma \hat{x}_i + \beta, \tag{D.9}$$

where γ and β are trainable parameters.

Besides the simple MLP we also employ a more advanced architecture, a so-called *convolutional neural network* (CNN) [178–180]. These networks were developed in the context of computer vision and as such the input is usually image data — in our case jet images. Our full architecture is shown in Fig. D.2. The core of a CNN is the convolution operation, which constructs a new image x'_{ij} by convolving the old image x_{ij} with a filter matrix W. Mathematically [233],

$$x'^{(k)}_{ij} = \sum_{l=1}^{n_f} \sum_{r,s} W^{(kl)}_{rs} x^{(l)}_{i+r,j+s} + b^{(k)}, \qquad k = 1, \ldots, n_f, \tag{D.10}$$

where we take n_f copies of the image, called *feature maps*. Each convolution is characterised by a kernel size (the range of r and s), the stride (the step size at which the kernel moves across

the image), and the padding (adding a full line of zeroes around the image). To keep the image size fixed during a convolution, we use a stride of 1 and a padding of 1.

In the end we have to reduce the image information down to only two output nodes. In a first step we condense the images with *pooling* operations which combine multiple pixels into only one pixel in the next layer. We use both average and max pooling which respectively replace the input with the average or maximum value, for example

$$\begin{bmatrix} 1 & 3 \\ 6 & 8 \end{bmatrix} \xrightarrow{\text{AvgPool}} \frac{9}{2}, \qquad \begin{bmatrix} 1 & 3 \\ 6 & 8 \end{bmatrix} \xrightarrow{\text{MaxPool}} 8. \tag{D.11}$$

In our network in Fig. D.2 we have two branches, one using average and one max pooling. After two pooling steps they are flattened and combined into a MLP which eventually reduces the information down to the two output nodes.

Besides the pure MLP and CNN we also use a combined network which starts out as a CNN and a separate MLP, see the right side of Fig. D.2. Once the CNN has been flattened we interface it with the MLP by concatenating the outputs from the two fully connected chains followed by a combined MLP with two output nodes.

D.2 Details on the evaluation

To derive physical results from the networks we evaluate them on the test set. This yields a NN score associated with each event, where a score close to 1 indicates that the network thinks the event is signal-like whereas 0 is background-like. While the NN score distribution contains the most information, our goal is to calculate discovery reaches and exclusion limits. This requires the calculation of significances, for which we need to place a cut on the NN score which defines everything with a larger score as being identified as a signal. A common way to place this cut is to find the cut that maximises the significance. However, our networks are such strong classifiers that this approach regularly yielded results with less than 1 expected background event [2]. This calls into question if this approach is statistically sound.

We therefore employed a different approach to the NN score cut. In Fig. D.3 we show the discovery reach as a function of the number of background events (which corresponds one-to-one to the NN score cuts) for each mass we evaluate at. We see that especially for high masses a very strict cut is preferred. On the whole, however, the discovery reach is relatively flat. Rather than dynamically determining the cut, we therefore decided on picking it manually to ensure a certain number of background events — 5 for the CNNs and 50 for the MLP. For the latter the dynamical approach would have been fine but for consistency we also fix it manually. These cutoffs were chosen ad hoc to get sufficient statistics while not overly diminishing the discovery reach.

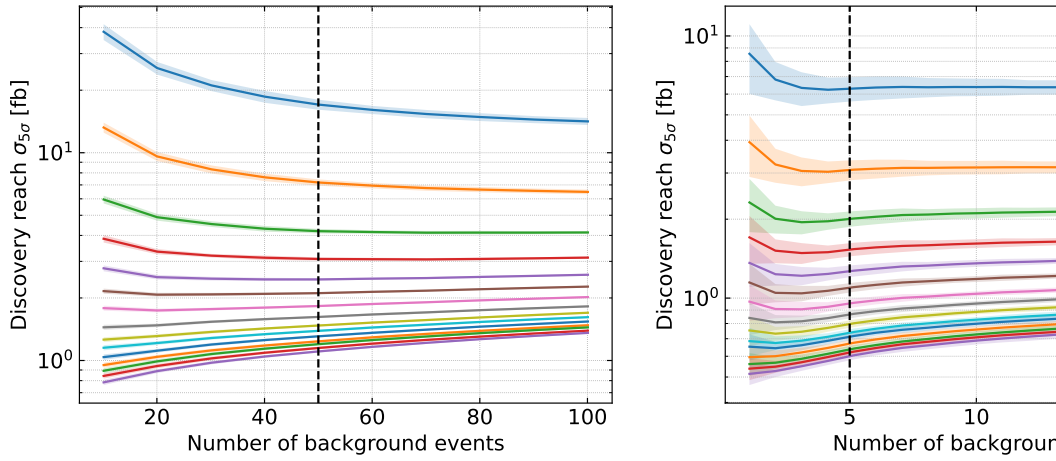

(a) Network $\mathcal{K}$

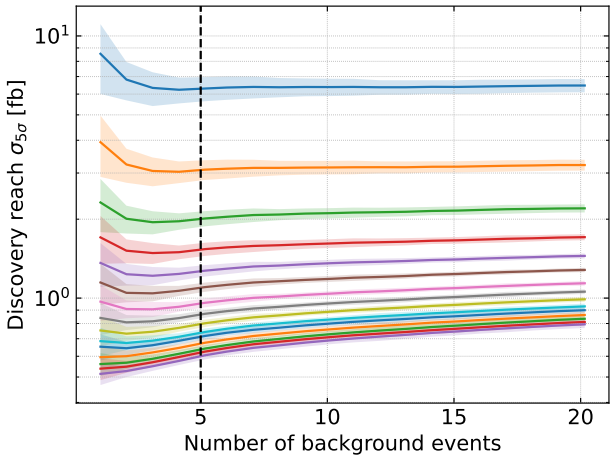

(b) Network $\mathcal{I}_{C\ell} + \mathcal{K}$

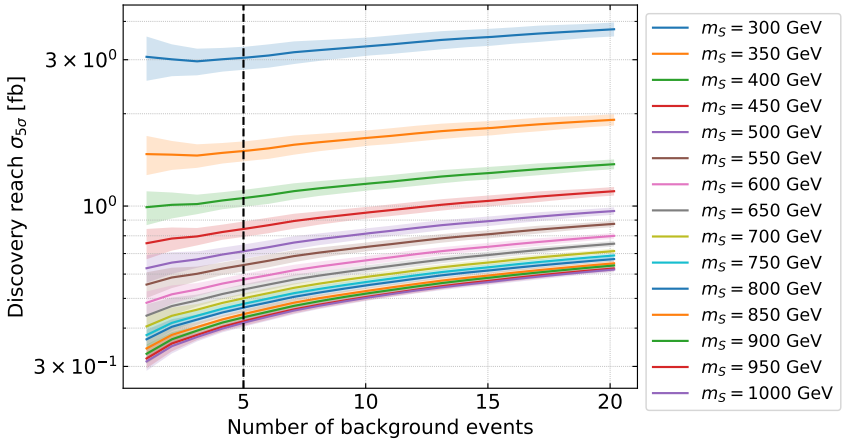

(c) Network $\mathcal{I}_{CN\ell} + \mathcal{K}$

Figure D.3: Discovery reach as a function of number of background events, i.e. the NN score cut.

D.3 Details on the training dataset

In the main text we described the makeup of our dataset: it is divided into training (64%), validation (16%), and test (20%). Each part is further divided into 50% signal events and 50% backgrounds. The latter are always constituted according to the cross section after the preselection cuts. For the training dataset we instead combine several signal mass hypotheses, taking events from $m_S = 300$ GeV to 800 GeV in steps of 50 GeV with equal weight. The motivation for this was mainly to save on computational resources by not having to train separately for each mass. It raises the question, however, if the results would have been better with a more focused training set. To investigate this, we have also trained the networks with a training set consisting of events of only one mass [2]. As benchmark masses we chose 300 GeV, 550 GeV, and 800 GeV. We have already shown a part of these results in the main text: the star shaped markers in Figs. 4.23a and 4.23b show the discovery reach and exclusion limit when the network is trained with the same mass where it is evaluated. This showed a significant boost in performance at 300 GeV but hardly any effect at higher masses. We now take a closer look

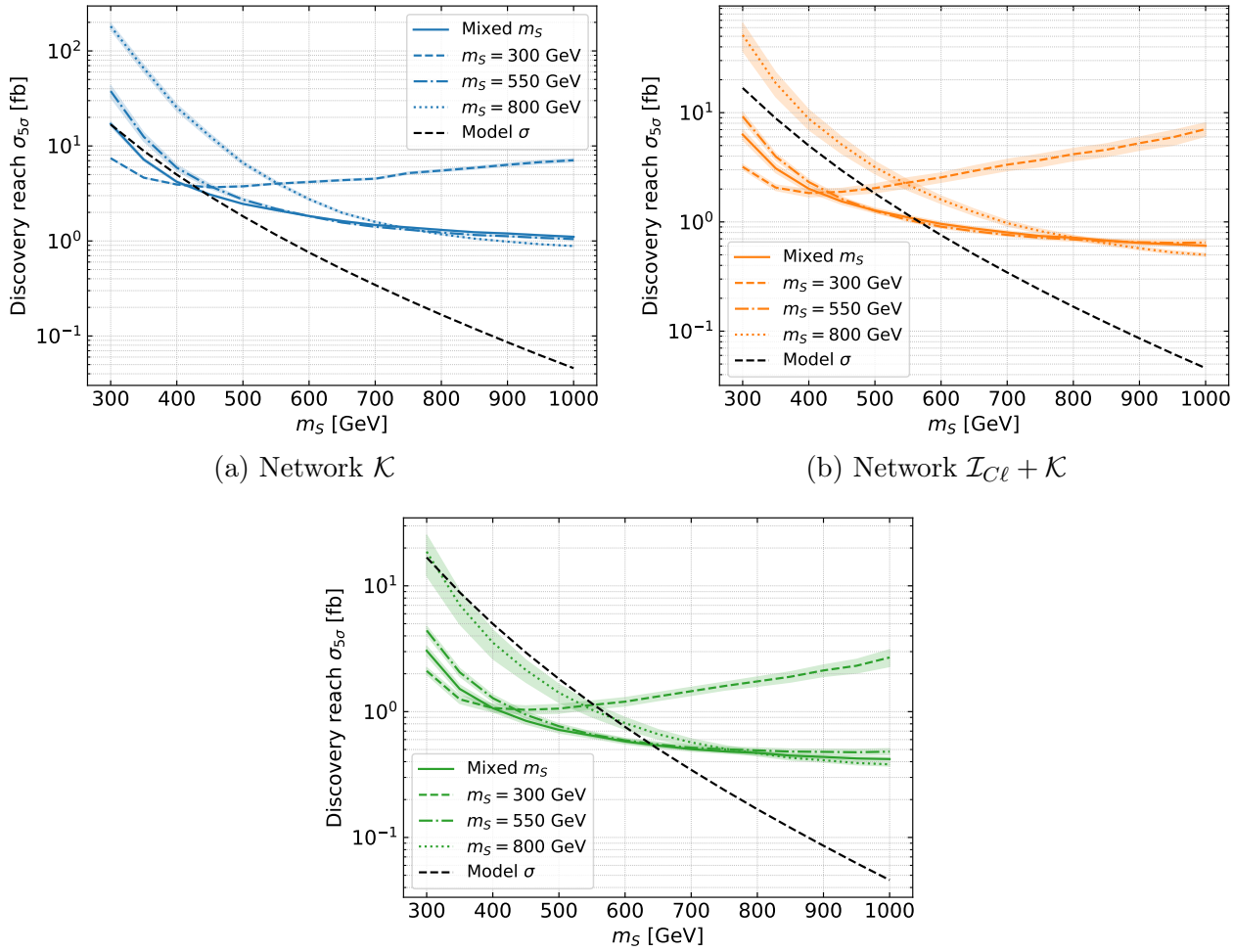

(a) Network $\mathcal{K}$

(b) Network $\mathcal{I}_{C\ell} + \mathcal{K}$

(c) Network $\mathcal{I}_{CN\ell} + \mathcal{K}$

Figure D.4: Comparison of networks trained on a single fixed mass.

at the dependence on the training set. To this end we compare the full results of training with a fixed mass versus the mixed training set in Fig. D.4. For the fixed masses, the error bands indicate the 1σ variation across 10 independent training runs. The effects qualitatively coincide for all three networks. We find that indeed at low masses the best performance is achieved by training on 300 GeV. However, it is quickly overtaken by the network trained on 550 GeV and the mixed dataset, the two having comparable performances across most of the mass range. At masses above 800 GeV there is a marginal advantage to using the network trained on the high mass.

To summarise, the mixed dataset is performing well and we are justified in using it for our evaluations in the main text. Given the additional computational costs, training on each mass point separately seems unnecessary for the expected gains. Only at small masses can we expect a significant improvement. A hybrid approach might be the best solution: training two networks, one for $m_S \leq 400$ GeV and one for $m_S > 400$ GeV. For the latter, either a mixed dataset can be used or a single midrange mass point, e.g. 550 GeV.

E | Documentation of `scangen`

Some of the simulations performed in this work — recasting studies for a large number of processes and scans over large parameter grids — are quite complex and time consuming to set up. To help with this we have developed a tool, dubbed `scangen`, that automates a lot of the manual work. The purpose of this appendix is to give an overview of its features and show its usefulness on a few examples. Both making the code public and publishing a detailed documentation is planned for the near future.

The first step towards setting up simulations is to have a functioning toolchain. To simplify this, `scangen` comes with installation scripts[1] for all relevant tools which can either be used to install them locally or build up a `singularity` container environment [237]. The latter is especially useful because it is portable and can be used both on local machines and on a high performance cluster. Specifically, we install

- `ROOT` [238], a software for scientific computing that is a requirement of `CheckMATE` and `MadAnalysis5`,
- `HepMC` and `Delphes`, external installations of which are required for `CheckMATE`,
- the recasting tools `CheckMATE`, `MadAnalysis5`, `Rivet`, and `Contur`,
- and `MadGraph5_aMC@NLO` as our event generator of choice.

For the `singularity` container, these tools are installed in a Debian 11 environment.

The idea for `scangen` came from an attempt to build a unified framework for all recasting tools. `Contur` comes with a great tool for setting up parameter scans, `contur-batch`, so `scangen` started as a collection of bash scripts around `contur-batch`. Over time, it became clear that the features we wanted to add required building up a new tool from scratch — this is the `scangen` used in this work. Due to this history, our naming conventions and directory structure closely follows the ones of `Contur`. This has the advantage that a `Contur` recasting study performed within `scangen` can still be evaluated with pure `Contur`.

To perform a simple scan, say to calculate cross sections of top partner pair production, three things must be provided: a UFO, a steering file for `MadGraph5`, and a file defining the parameter ranges, in this case the top partner mass. The latter two must be placed in a directory called `input/`. Example files for top partner pair production are

[1] Thanks to Yang Liu for providing me with a first version of these.

```
$ cat input/param_file.dat
[Parameters]
[[mass]]
mode = LIST
values = [1000, 1500, 2000]
```

and

```
$ cat input/mg.txt
import model ../../../SimpleVLQ_UFO
generate p p > tp tp~
output mgevents
launch
shower=OFF
set param_card mtp {mass}
```

To prepare the scan, we run

```
$ scangen -e 14 -n 10000 -i 3
```

which sets the centre-of-mass energy to 14 TeV, generates 10000 events per point and ensures that all three parameter points are run in parallel. The `scangen` call creates a directory called `myscan00` that contains the steering scripts and the runareas for the parameter points. For example,

```
$ ls myscan00/14TeV/0000
mg.txt  params.dat  runpoint.sh
```

where `mg.txt` is the file shown above except that the parameters in curly braces have been replaced with the value listed in `params.txt` and the number of events and beam energy have been added to the bottom. That is,

```
$ cat runarea/14TeV/0000/params.dat
mtp = 1000.0
```

and

```
$ cat runarea/14TeV/0000/mg.txt
import model ../../../SimpleVLQ_UFO
generate p p > tp tp~
output mgevents
launch
shower=OFF
set param_card mtp 1000.0
```

```
set run_card nevents 10000
set run_card ebeam1 7000.0
set run_card ebeam2 7000.0
```

Finally, `runpoint.sh` contains the commands to start the run in the container environment. The user can now start the run with

```
$ scangen-run
```

and then evaluate it by calling

```
$ scangen-get-xs
point   mass   xs(pb)
0000 1000.0 0.044525
0001 1500.0 0.002367
0002 2000.0 0.000194
```

In the simple example above we only calculated cross sections. Let us now discuss a more advanced use case: determining recast bounds on the process

$$pp \to T\bar{T} \to tS^0\bar{t}S^0 \to 6t. \tag{E.1}$$

To this end we provide files in the style of MadAnalysis5's `recasting_card.dat` that can be used to conveniently specify which search from which tool should be turned on for this run. We again consider $m_T = 1.0, 1.5, 2.0$ TeV and fix $m_S = 400$ GeV. To set up the scan, we run

```
scangen -e 13 -n 10000 -i 3 --ma --cm --ct
```

and again start it with `scangen-run`. As for the cross sections there is a convenient readout script:

```
$ scangen-eval
Point 0000
* Parameters
    * mvlq = 1000.0
    * ms = 400.0
* Cross section: 0.037845 pb
* Results:
tool          analysis/pool       sr/analysis            sig95exp    sig95obs    exclusion
------------  ------------------  --------------------  ----------  ----------  -----------
MadAnalysis5  atlas_susy_2018_17  SR-12ij50-2ib            0.00441     0.00444      1.00000
Contur        CombinedExclusion   CombinedDATABG         inf         inf            0.44530
Contur        ATLAS_13_JETS       ATLAS_2019_I1724098    inf         inf            0.33130
Contur        ATLAS_13_TTHAD      ATLAS_2022_I2077575    inf         inf            0.31605
Contur        CMS_13_JETS         CMS_2018_I1682495      inf         inf            0.00668
Contur        CMS_13_TTHAD        CMS_2019_I1753720      inf         inf            0.00000
Contur        LHCB_13_L1L2B       LHCB_2018_I1662483     inf         inf            0.00000
```

```
CheckMATE     atlas_2106_09609    SR1                     0.00970     0.00962      1.00000

Point 0001
* Parameters
    * mvlq = 1500.0
    * ms = 400.0
* Cross section: 0.0017456 pb
* Results:
tool          analysis/pool       sr/analysis            sig95exp    sig95obs    exclusion
------------  ------------------  --------------------  ----------  ----------  -----------
MadAnalysis5  atlas_susy_2018_17  SR-10ij50-1ib-MJ500     0.00334     0.00238      0.87100
Contur        CombinedExclusion   CombinedDATABG         inf         inf          0.06440
Contur        ATLAS_13_TTHAD      ATLAS_2022_I2077575    inf         inf          0.06110
Contur        ATLAS_13_JETS       ATLAS_2019_I1724098    inf         inf          0.02031
Contur        CMS_13_JETS         CMS_2018_I1682495      inf         inf          0.00123
Contur        CMS_13_TTHAD        CMS_2019_I1753720      inf         inf          0.00000
Contur        LHCB_13_L1L2B       LHCB_2018_I1662483     inf         inf          0.00000
CheckMATE     atlas_2106_09609    SR4                     0.00092     0.00132      0.98924

Point 0002
* Parameters
    * mvlq = 2000.0
    * ms = 400.0
* Cross section: 0.00011714 pb
* Results:
tool          analysis/pool       sr/analysis            sig95exp    sig95obs    exclusion
------------  ------------------  --------------------  ----------  ----------  -----------
MadAnalysis5  atlas_susy_2018_17  SR-12ij50-2ib           0.00241     0.00241      0.08580
Contur        CombinedExclusion   CombinedDATABG         inf         inf          0.00640
Contur        ATLAS_13_TTHAD      ATLAS_2022_I2077575    inf         inf          0.00626
Contur        ATLAS_13_JETS       ATLAS_2019_I1724098    inf         inf          0.00132
Contur        CMS_13_JETS         CMS_2016_I1459051      inf         inf          0.00016
Contur        CMS_13_TTHAD        CMS_2019_I1753720      inf         inf          0.00000
Contur        LHCB_13_L1L2B       LHCB_2018_I1662483     inf         inf          0.00000
CheckMATE     atlas_2106_09609    SR10                    0.00124     0.00132      0.14250
```

For brevity only a few searches have been activated for this example. The expected and observed upper limits on the cross section, `sig95exp` and `sig95obs`, are determined as detailed in Appendix B. As explained there, these values are not automatically calculated by `Contur` and a more involved iterative procedure is required to determine them, which is why they are listed as `inf` above. Including them amounts to adding the flag `--xs95` to the `scangen` call and providing a file with initial guesses for the iteration.

The example above was a simple one dimensional scan. If we instead performed a scan over both masses we could implement the kinetic constraint of the T decay by including

```
[Restrictions]
require {mtp} > {ms} + MT
```

in the parameter definition. The user can now specify a square grid and the points that violate the requirement are automatically removed.

List of abbreviations

2SSL two same-sign leptons

ABJ Adler-Bell-Jackiw

BSM beyond the Standard Model

CCWZ Callan, Coleman, Wess, and Zumino

CHM composite Higgs model

CL confidence level

CNN convolutional neural network

CP charge-parity

DY Drell-Yan

EFT effective field theory

ETC extended technicolor

ggF gluon-gluon-fusion

EW electroweak

EWSB electroweak symmetry breaking

FCNC flavour-changing neutral currents

HC hypercolour

HL-LHC high-luminosity LHC

IR infrared

irrep irreducible representation

LHC Large Hadron Collider

LO leading order

LQ leptoquark

MAC maximally attractive channel

ML machine learning

MLP multilayer perceptron

NGB Nambu-Goldstone boson

NLO next-to-leading order

NN neural network

NNLL next-to-next-to-leading log

NNLO next-to-next-to-leading order

NWA narrow width approximation

PC partial compositeness

PDF parton distribution function

pNGB pseudo NGB

QCD quantum chromodynamics

QED quantum electrodynamics

ReLU rectified linear unit

RG renormalisation group

ROC receiver operator characteristic

SM Standard Model

SSB spontaneous symmetry breaking

SUSY supersymmetry

TC technicolor

UFO Universal FeynRules Output

VBF vector boson fusion

VEV vacuum expectation value

VLQ vector-like quark

WZW Wess-Zumino-Witten

Acknowledgments

The physics is done, and it's time to reflect on the past three years. This thesis could not have come about without the support of many people, and ~~we~~ I would like to take some time to thank them.

Chief among them is my supervisor, Prof. Werner Porod. Both in terms of physics — for introducing me to and getting me excited about particle phenomenology; for always having an open door for physics discussions and being incredibly generous with your time; for your confidence that it would lead to something useful when I checked out to work on my latest tool for a couple of months — and personally — for accommodating my Covid anxiety and health issues with maximal flexibility; for enabling several formative trips to France and South Korea; for believing in me when I sometimes did not — I could not have asked for a better supervisor. Thank you.

I would also like to thank my second supervisor, Prof. Raimund Ströhmer, for his valuable inputs about experimental details I had overlooked. Another thanks goes to Prof. Johanna Erdmenger for agreeing to join my examination committee.

While my PhD began three years ago, my path towards theoretical particle physics started long before that. I want to acknowledge Profs. Harald Lesch and Leonard Susskind for getting me interested in physics and theoretical physics in the first place through their online lectures. I further want to thank Profs. Ansgar Denner and Thorsten Ohl for two invaluable QFT lectures.

Next I would like to thank my collaborators[2], especially Leonard Schwarze (for suffering through many and long debugging sessions with me and making *the* figure with me — yes, that one), Thomas Flacke (our IRL discussions planning out new projects were genuinely some of the most fun things in my PhD), and Giacomo Cacciapaglia (for his unending expertise in model building). I also want to thank Jeong Han Kim and Jun Seung Pi for introducing me to deep learning in particle physics and for being exceptional hosts on my two visits. Finally a shoutout to the rest of the Snowmass gang — Avik Banerjee, Diogo Buarque Franzosi, Aldo Deandrea, Gabriele Ferretti, Benjamin Fuks, and Luca Panizzi — for the interesting discussions and the fun times at the conferences in Lyon and Mainz.

I have benefited from a great research environment in Prof. Porod's working group. I want to thank Rosy Caliri, Jan Hadlik, and Manuel Schmidt for many interesting discussions. A special thanks also to Yang Liu, from whose experience I have benefited from many times. Finally, I

[2]I'll dispense with the titles from here on — they are all decorated experts ;)

want to thank Alexandre Alvarez, Amitayus Banik, Konrad Becker, Ricardo Cepedello, Andreas Karle, Moritz Schnelke, and Deepali Singh for the lively discussions in our group meetings.

Now comes the paragraph for the non-physicists, so allow me to make a strained analogy. A mathematical statement, say "37 is a prime number", can either be true or false. But it is meaningless without the framework of Mathematics to define what a number is, how multiplication works etc. Analogously, I have spent the past years working on specific particle physics models, but they can only exist within the framework of quantum field theory. Mum and Dad, Tim and Tess, you are the quantum field theory to my model.

References

[1] G. Cacciapaglia, T. Flacke, M. Kunkel, W. Porod, and L. Schwarze, "Exploring extended Higgs sectors via pair production at the LHC," JHEP **12** (2022) 087, arXiv:2210.01826 [hep-ph].

[2] T. Flacke, J. H. Kim, M. Kunkel, P. Ko, J. S. Pi, W. Porod, and L. Schwarze, "Uncovering doubly charged scalars with dominant three-body decays using machine learning," JHEP **11** (2023) 009, arXiv:2304.09195 [hep-ph].

[3] G. Cacciapaglia, A. Deandrea, M. Kunkel, and W. Porod, "Coloured spin-1 states in composite Higgs models," JHEP **06** (2024) 092, arXiv:2404.02198 [hep-ph].

[4] **UA1** Collaboration, G. Arnison et al., "Experimental Observation of Isolated Large Transverse Energy Electrons with Associated Missing Energy at $\sqrt{s} = 540$ GeV," Phys. Lett. B **122** (1983) 103–116.

[5] **UA2** Collaboration, M. Banner et al., "Observation of Single Isolated Electrons of High Transverse Momentum in Events with Missing Transverse Energy at the CERN anti-p p Collider," Phys. Lett. B **122** (1983) 476–485.

[6] **UA1** Collaboration, G. Arnison et al., "Experimental Observation of Lepton Pairs of Invariant Mass Around 95 GeV/c^2 at the CERN SPS Collider," Phys. Lett. B **126** (1983) 398–410.

[7] **UA2** Collaboration, P. Bagnaia et al., "Evidence for $Z^0 \to e^+e^-$ at the CERN $\bar{p}p$ Collider," Phys. Lett. B **129** (1983) 130–140.

[8] S. L. Glashow, "Partial Symmetries of Weak Interactions," Nucl. Phys. **22** (1961) 579–588.

[9] S. Weinberg, "A Model of Leptons," Phys. Rev. Lett. **19** (1967) 1264–1266.

[10] A. Salam, p. 367 of *Elementary Particle Physics*. ed. N. Svartholm, Almquist and Wiksell, Stockholm, 1969.

[11] F. Englert and R. Brout, "Broken Symmetry and the Mass of Gauge Vector Mesons," Phys. Rev. Lett. **13** (1964) 321–323.

[12] P. W. Higgs, "Broken Symmetries and the Masses of Gauge Bosons," Phys. Rev. Lett. **13** (1964) 508–509.

[13] G. S. Guralnik, C. R. Hagen, and T. W. B. Kibble, "Global Conservation Laws and Massless Particles," Phys. Rev. Lett. **13** (1964) 585–587.

[14] **ATLAS** Collaboration, G. Aad et al., "Observation of a new particle in the search for the Standard Model Higgs boson with the ATLAS detector at the LHC," Phys. Lett. B **716** (2012) 1–29, arXiv:1207.7214 [hep-ex].

[15] **CMS** Collaboration, S. Chatrchyan et al., "Observation of a New Boson at a Mass of 125 GeV with the CMS Experiment at the LHC," Phys. Lett. B **716** (2012) 30–61, arXiv:1207.7235 [hep-ex].

[16] G. Panico and A. Wulzer, The Composite Nambu-Goldstone Higgs, vol. 913 of Lect. Notes Phys. Springer, 2016. arXiv:1506.01961 [hep-ph].

[17] G. 't Hooft, "Naturalness, chiral symmetry, and spontaneous chiral symmetry breaking," NATO Sci. Ser. B **59** (1980) 135–157.

[18] J. Wess and B. Zumino, "A Lagrangian Model Invariant Under Supergauge Transformations," Phys. Lett. B **49** (1974) 52.

[19] J. Wess and B. Zumino, "Supergauge Transformations in Four-Dimensions," Nucl. Phys. B **70** (1974) 39–50.

[20] S. Weinberg, "Implications of Dynamical Breaking," Phys. Rev. D **13** (1976) 974–996. [Addendum: Phys.Rev.D 19, 1277–1280 (1979)].

[21] L. Susskind, "Dynamics of Spontaneous Symmetry Breaking in the Weinberg-Salam Theory," Phys. Rev. D **20** (1979) 2619–2625.

[22] R. Contino, "The Higgs as a Composite Nambu-Goldstone Boson," in Theoretical Advanced Study Institute in Elementary Particle Physics: Physics of the Large and the Small, pp. 235–306. 2011. arXiv:1005.4269 [hep-ph].

[23] D. B. Kaplan and H. Georgi, "SU(2) x U(1) Breaking by Vacuum Misalignment," Phys. Lett. B **136** (1984) 183–186.

[24] D. B. Kaplan, H. Georgi, and S. Dimopoulos, "Composite Higgs Scalars," Phys. Lett. B **136** (1984) 187–190.

[25] M. J. Dugan, H. Georgi, and D. B. Kaplan, "Anatomy of a Composite Higgs Model," Nucl. Phys. B **254** (1985) 299–326.

[26] Y. Nambu, "Quasiparticles and Gauge Invariance in the Theory of Superconductivity," Phys. Rev. **117** (1960) 648–663.

[27] J. Goldstone, "Field Theories with Superconductor Solutions," Nuovo Cim. **19** (1961) 154–164.

[28] J. Goldstone, A. Salam, and S. Weinberg, "Broken Symmetries," Phys. Rev. **127** (1962) 965–970.

[29] D. B. Kaplan, "Flavor at SSC energies: A New mechanism for dynamically generated fermion masses," Nucl. Phys. B **365** (1991) 259–278.

[30] K. Agashe, R. Contino, and A. Pomarol, "The Minimal composite Higgs model," Nucl. Phys. B **719** (2005) 165–187, arXiv:hep-ph/0412089.

[31] G. Ferretti and D. Karateev, "Fermionic UV completions of Composite Higgs models," JHEP **03** (2014) 077, arXiv:1312.5330 [hep-ph].

[32] G. Ferretti, "Gauge theories of Partial Compositeness: Scenarios for Run-II of the LHC," JHEP **06** (2016) 107, arXiv:1604.06467 [hep-ph].

[33] A. Belyaev, G. Cacciapaglia, H. Cai, G. Ferretti, T. Flacke, A. Parolini, and H. Serodio, "Di-boson signatures as Standard Candles for Partial Compositeness," JHEP **01** (2017) 094, arXiv:1610.06591 [hep-ph]. [Erratum: JHEP 12, 088 (2017)].

[34] K. D. Lane, "Technicolor," NATO Sci. Ser. B **352** (1996) 609–621, arXiv:hep-ph/9501249.

[35] S. Dimopoulos and L. Susskind, "Mass Without Scalars," Nucl. Phys. B **155** (1979) 237–252.

[36] E. Eichten and K. D. Lane, "Dynamical Breaking of Weak Interaction Symmetries," Phys. Lett. B **90** (1980) 125–130.

[37] C. T. Hill and E. H. Simmons, "Strong Dynamics and Electroweak Symmetry Breaking," Phys. Rept. **381** (2003) 235–402, arXiv:hep-ph/0203079. [Erratum: Phys.Rept. 390, 553–554 (2004)].

[38] **Particle Data Group** Collaboration, S. Navas et al., "Review of particle physics," Phys. Rev. D **110** no. 3, (2024) 030001.

[39] B. Holdom, "Techniodor," Phys. Lett. B **150** (1985) 301–305.

[40] T. Akiba and T. Yanagida, "Hierarchic Chiral Condensate," Phys. Lett. B **169** (1986) 432–435.

[41] T. W. Appelquist, D. Karabali, and L. C. R. Wijewardhana, "Chiral Hierarchies and the Flavor Changing Neutral Current Problem in Technicolor," Phys. Rev. Lett. **57** (1986) 957.

[42] K. Yamawaki, M. Bando, and K.-i. Matumoto, "Scale Invariant Technicolor Model and a Technidilaton," Phys. Rev. Lett. **56** (1986) 1335.

[43] T. Appelquist and L. C. R. Wijewardhana, "Chiral Hierarchies and Chiral Perturbations in Technicolor," Phys. Rev. D **35** (1987) 774.

[44] T. Appelquist and L. C. R. Wijewardhana, "Chiral Hierarchies from Slowly Running Couplings in Technicolor Theories," Phys. Rev. D **36** (1987) 568.

[45] K. Lane, "Two Lectures on Technicolor," `arXiv:hep-ph/0202255`.

[46] T. Plehn, "Lectures on LHC Physics," Lect. Notes Phys. **844** (2012) 1–193, `arXiv:0910.4182 [hep-ph]`.

[47] H. Georgi and D. B. Kaplan, "Composite Higgs and Custodial SU(2)," Phys. Lett. B **145** (1984) 216–220.

[48] G. Cacciapaglia and F. Sannino, "Fundamental Composite (Goldstone) Higgs Dynamics," JHEP **04** (2014) 111, `arXiv:1402.0233 [hep-ph]`.

[49] S. R. Coleman, J. Wess, and B. Zumino, "Structure of phenomenological Lagrangians. 1.," Phys. Rev. **177** (1969) 2239–2247.

[50] C. G. Callan, Jr., S. R. Coleman, J. Wess, and B. Zumino, "Structure of phenomenological Lagrangians. 2.," Phys. Rev. **177** (1969) 2247–2250.

[51] B. Gripaios, A. Pomarol, F. Riva, and J. Serra, "Beyond the Minimal Composite Higgs Model," JHEP **04** (2009) 070, `arXiv:0902.1483 [hep-ph]`.

[52] R. Feger, T. W. Kephart, and R. J. Saskowski, "LieART 2.0 – A Mathematica application for Lie Algebras and Representation Theory," Comput. Phys. Commun. **257** (2020) 107490, `arXiv:1912.10969 [hep-th]`.

[53] J. Wess and B. Zumino, "Consequences of anomalous Ward identities," Phys. Lett. B **37** (1971) 95–97.

[54] E. Witten, "Global Aspects of Current Algebra," Nucl. Phys. B **223** (1983) 422–432.

[55] E. Witten, "Current Algebra, Baryons, and Quark Confinement," Nucl. Phys. B **223** (1983) 433–444.

[56] R. A. Bertlmann, Anomalies in Quantum Field Theory. International Series of Monographs on Physics. Oxford University Press, 1996.

[57] S. L. Adler, "Axial vector vertex in spinor electrodynamics," Phys. Rev. **177** (1969) 2426–2438.

[58] J. S. Bell and R. Jackiw, "A PCAC puzzle: $\pi^0 \to \gamma\gamma$ in the σ model," Nuovo Cim. A **60** (1969) 47–61.

[59] K. Fujikawa, "Path Integral Measure for Gauge Invariant Fermion Theories," Phys. Rev. Lett. **42** (1979) 1195–1198.

[60] K. Fujikawa, "Path Integral for Gauge Theories with Fermions," Phys. Rev. D **21** (1980) 2848. [Erratum: Phys.Rev.D 22, 1499 (1980)].

[61] J. Davighi, Topological effects in particle physics phenomenology. PhD thesis, Cambridge U., DAMTP, 2020.

[62] S. L. Adler and W. A. Bardeen, "Absence of higher order corrections in the anomalous axial vector divergence equation," Phys. Rev. **182** (1969) 1517–1536.

[63] O. Kaymakcalan, S. Rajeev, and J. Schechter, "Nonabelian Anomaly and Vector Meson Decays," Phys. Rev. D **30** (1984) 594.

[64] E. Cremmer and B. Julia, "The N=8 Supergravity Theory. 1. The Lagrangian," Phys. Lett. B **80** (1978) 48.

[65] A. P. Balachandran, A. Stern, and C. G. Trahern, "Nonlinear models as gauge theories," Phys. Rev. D **19** (1979) 2416.

[66] E. Cremmer and B. Julia, "The SO(8) Supergravity," Nucl. Phys. B **159** (1979) 141–212.

[67] S. J. Gates, M. T. Grisaru, M. Rocek, and W. Siegel, Superspace Or One Thousand and One Lessons in Supersymmetry, vol. 58 of Frontiers in Physics. 1983. `arXiv:hep-th/0108200`.

[68] M. Bando, T. Kugo, and K. Yamawaki, "Composite Gauge Bosons and 'Low-energy Theorems' of Hidden Local Symmetries," Prog. Theor. Phys. **73** (1985) 1541.

[69] M. Bando, T. Kugo, and K. Yamawaki, "Nonlinear Realization and Hidden Local Symmetries," Phys. Rept. **164** (1988) 217–314.

[70] R. Casalbuoni, S. De Curtis, D. Dominici, and R. Gatto, "Effective Weak Interaction Theory with Possible New Vector Resonance from a Strong Higgs Sector," Phys. Lett. B **155** (1985) 95–99.

[71] M. Bando, T. Kugo, S. Uehara, K. Yamawaki, and T. Yanagida, "Is the ρ Meson a Dynamical Gauge Boson of Hidden Local Symmetry?," Phys. Rev. Lett. **54** (1985) 1215.

[72] R. Casalbuoni, S. De Curtis, D. Dominici, F. Feruglio, and R. Gatto, "Vector and Axial Vector Bound States From a Strongly Interacting Electroweak Sector," Int. J. Mod. Phys. A **4** (1989) 1065.

[73] D. Buarque Franzosi, G. Cacciapaglia, H. Cai, A. Deandrea, and M. Frandsen, "Vector and Axial-vector resonances in composite models of the Higgs boson," JHEP **11** (2016) 076, arXiv:1605.01363 [hep-ph].

[74] R. Contino, Y. Nomura, and A. Pomarol, "Higgs as a holographic pseudoGoldstone boson," Nucl. Phys. B **671** (2003) 148–174, arXiv:hep-ph/0306259.

[75] F. Caracciolo, A. Parolini, and M. Serone, "UV Completions of Composite Higgs Models with Partial Compositeness," JHEP **02** (2013) 066, arXiv:1211.7290 [hep-ph].

[76] D. Marzocca, A. Parolini, and M. Serone, "Supersymmetry with a pNGB Higgs and Partial Compositeness," JHEP **03** (2014) 099, arXiv:1312.5664 [hep-ph].

[77] J. Barnard, T. Gherghetta, and T. S. Ray, "UV descriptions of composite Higgs models without elementary scalars," JHEP **02** (2014) 002, arXiv:1311.6562 [hep-ph].

[78] K. Agashe, R. Contino, L. Da Rold, and A. Pomarol, "A Custodial symmetry for $Zb\bar{b}$," Phys. Lett. B **641** (2006) 62–66, arXiv:hep-ph/0605341.

[79] S. Raby, S. Dimopoulos, and L. Susskind, "Tumbling Gauge Theories," Nucl. Phys. B **169** (1980) 373–383.

[80] J. Erdmenger, N. Evans, W. Porod, and K. S. Rigatos, "Gauge/gravity dynamics for composite Higgs models and the top mass," Phys. Rev. Lett. **126** no. 7, (2021) 071602, arXiv:2009.10737 [hep-ph].

[81] J. Erdmenger, N. Evans, W. Porod, and K. S. Rigatos, "Gauge/gravity dual dynamics for the strongly coupled sector of composite Higgs models," JHEP **02** (2021) 058, arXiv:2010.10279 [hep-ph].

[82] D. Elander, M. Frigerio, M. Knecht, and J.-L. Kneur, "Holographic models of composite Higgs in the Veneziano limit. Part I. Bosonic sector," JHEP **03** (2021) 182, arXiv:2011.03003 [hep-ph].

[83] D. Elander, M. Frigerio, M. Knecht, and J.-L. Kneur, "Holographic models of composite Higgs in the Veneziano limit. Part II. Fermionic sector," JHEP **05** (2022) 066, arXiv:2112.14740 [hep-ph].

[84] J. Erdmenger, N. Evans, Y. Liu, and W. Porod, "Holographic Non-Abelian Flavour Symmetry Breaking," Universe **9** no. 6, (2023) 289, arXiv:2304.09190 [hep-th].

[85] J. Erdmenger, N. Evans, Y. Liu, and W. Porod, "Holography for Sp($2N_c$) gauge dynamics: from composite Higgs to technicolour," JHEP **07** (2024) 169, arXiv:2404.14480 [hep-ph].

[86] V. Ayyar, T. DeGrand, M. Golterman, D. C. Hackett, W. I. Jay, E. T. Neil, Y. Shamir, and B. Svetitsky, "Spectroscopy of SU(4) composite Higgs theory with two distinct fermion representations," Phys. Rev. D **97** no. 7, (2018) 074505, arXiv:1710.00806 [hep-lat].

[87] E. Bennett, D. K. Hong, J.-W. Lee, C. J. D. Lin, B. Lucini, M. Piai, and D. Vadacchino, "Sp(4) gauge theory on the lattice: towards SU(4)/Sp(4) composite Higgs (and beyond)," JHEP **03** (2018) 185, arXiv:1712.04220 [hep-lat].

[88] V. Ayyar, T. Degrand, D. C. Hackett, W. I. Jay, E. T. Neil, Y. Shamir, and B. Svetitsky, "Baryon spectrum of SU(4) composite Higgs theory with two distinct fermion representations," Phys. Rev. D **97** no. 11, (2018) 114505, arXiv:1801.05809 [hep-ph].

[89] V. Ayyar, T. DeGrand, D. C. Hackett, W. I. Jay, E. T. Neil, Y. Shamir, and B. Svetitsky, "Partial compositeness and baryon matrix elements on the lattice," Phys. Rev. D **99** no. 9, (2019) 094502, arXiv:1812.02727 [hep-ph].

[90] V. Ayyar, T. DeGrand, D. C. Hackett, W. I. Jay, E. T. Neil, Y. Shamir, and B. Svetitsky, "Finite-temperature phase structure of SU(4) gauge theory with multiple fermion representations," Phys. Rev. D **97** no. 11, (2018) 114502, arXiv:1802.09644 [hep-lat].

[91] E. Bennett, D. K. Hong, J.-W. Lee, C.-J. D. Lin, B. Lucini, M. Mesiti, M. Piai, J. Rantaharju, and D. Vadacchino, "$Sp(4)$ gauge theories on the lattice: quenched fundamental and antisymmetric fermions," Phys. Rev. D **101** no. 7, (2020) 074516, arXiv:1912.06505 [hep-lat].

[92] V. Ayyar, M. F. Golterman, D. C. Hackett, W. Jay, E. T. Neil, Y. Shamir, and B. Svetitsky, "Radiative Contribution to the Composite-Higgs Potential in a Two-Representation Lattice Model," Phys. Rev. D **99** no. 9, (2019) 094504, arXiv:1903.02535 [hep-lat].

[93] E. Bennett, D. K. Hong, J.-W. Lee, C. J. D. Lin, B. Lucini, M. Piai, and D. Vadacchino, "Sp(4) gauge theories on the lattice: $N_f = 2$ dynamical fundamental fermions," JHEP **12** (2019) 053, arXiv:1909.12662 [hep-lat].

[94] E. Bennett, J. Holligan, D. K. Hong, J.-W. Lee, C. J. D. Lin, B. Lucini, M. Piai, and D. Vadacchino, "Color dependence of tensor and scalar glueball masses in Yang-Mills theories," Phys. Rev. D **102** no. 1, (2020) 011501, arXiv:2004.11063 [hep-lat].

[95] M. Golterman, W. I. Jay, E. T. Neil, Y. Shamir, and B. Svetitsky, "Low-energy constant L_{10} in a two-representation lattice theory," Phys. Rev. D **103** no. 7, (2021) 074509, arXiv:2010.01920 [hep-lat].

[96] E. Bennett, J. Holligan, D. K. Hong, J.-W. Lee, C. J. D. Lin, B. Lucini, M. Piai, and D. Vadacchino, "Glueballs and strings in $Sp(2N)$ Yang-Mills theories," Phys. Rev. D **103** no. 5, (2021) 054509, arXiv:2010.15781 [hep-lat].

[97] E. Bennett, D. K. Hong, H. Hsiao, J.-W. Lee, C. J. D. Lin, B. Lucini, M. Mesiti, M. Piai, and D. Vadacchino, "Lattice studies of the Sp(4) gauge theory with two fundamental and three antisymmetric Dirac fermions," Phys. Rev. D **106** no. 1, (2022) 014501, arXiv:2202.05516 [hep-lat].

[98] E. Bennett et al., "Symplectic lattice gauge theories in the grid framework: Approaching the conformal window," Phys. Rev. D **108** no. 9, (2023) 094508, arXiv:2306.11649 [hep-lat].

[99] E. Bennett, D. K. Hong, H. Hsiao, J.-W. Lee, C. J. D. Lin, B. Lucini, M. Piai, and D. Vadacchino, "Lattice investigations of the chimera baryon spectrum in the Sp(4) gauge theory," Phys. Rev. D **109** no. 9, (2024) 094512, arXiv:2311.14663 [hep-lat].

[100] E. Bennett, J. Holligan, D. K. Hong, J.-W. Lee, C. J. D. Lin, B. Lucini, M. Piai, and D. Vadacchino, "Spectrum of mesons in quenched Sp(2N) gauge theories," Phys. Rev. D **109** no. 9, (2024) 094517, arXiv:2312.08465 [hep-lat].

[101] A. Hasenfratz, E. T. Neil, Y. Shamir, B. Svetitsky, and O. Witzel, "Infrared fixed point and anomalous dimensions in a composite Higgs model," Phys. Rev. D **107** no. 11, (2023) 114504, arXiv:2304.11729 [hep-lat].

[102] G. Cacciapaglia, G. Ferretti, T. Flacke, and H. Serôdio, "Light scalars in composite Higgs models," Front. in Phys. **7** (2019) 22, arXiv:1902.06890 [hep-ph].

[103] G. Cacciapaglia, T. Flacke, M. Park, and M. Zhang, "Exotic decays of top partners: mind the search gap," Phys. Lett. B **798** (2019) 135015, arXiv:1908.07524 [hep-ph].

[104] D. Buarque Franzosi, G. Cacciapaglia, X. Cid Vidal, G. Ferretti, T. Flacke, and C. Vázquez Sierra, "Exploring new possibilities to discover a light pseudo-scalar at LHCb," Eur. Phys. J. C **82** no. 1, (2022) 3, arXiv:2106.12615 [hep-ph].

[105] A. Agugliaro, G. Cacciapaglia, A. Deandrea, and S. De Curtis, "Vacuum misalignment and pattern of scalar masses in the SU(5)/SO(5) composite Higgs model," JHEP **02** (2019) 089, arXiv:1808.10175 [hep-ph].

[106] R. Caliri, J. Hadlik, M. Kunkel, W. Porod, and C. Verollet, "Electroweak spin-1 resonances in Composite Higgs models," arXiv:2412.08720 [hep-ph].

[107] G. Cacciapaglia, T. Flacke, M. Kunkel, and W. Porod, "Phenomenology of unusual top partners in composite Higgs models," JHEP **02** (2022) 208, arXiv:2112.00019 [hep-ph].

[108] M. Kunkel, "LHC phenomenology of top partners in models with SU(6)/Sp(6)." 2021. Master thesis, University of Würzburg.

[109] A. R. Zerwekh, "On the Quantum Chromodynamics of a Massive Vector Field in the Adjoint Representation," Int. J. Mod. Phys. A **28** (2013) 1350054, arXiv:1207.5233 [hep-ph].

[110] G. Cacciapaglia, A. Deandrea, T. Flacke, and A. M. Iyer, "Gluon-Photon Signatures for color octet at the LHC (and beyond)," JHEP **05** (2020) 027, arXiv:2002.01474 [hep-ph].

[111] A. Belyaev, R. Rosenfeld, and A. R. Zerwekh, "Tevatron potential for technicolor search with prompt photons," Phys. Lett. B **462** (1999) 150–157, arXiv:hep-ph/9905468.

[112] G. Cacciapaglia, H. Cai, A. Deandrea, T. Flacke, S. J. Lee, and A. Parolini, "Composite scalars at the LHC: the Higgs, the Sextet and the Octet," JHEP **11** (2015) 201, arXiv:1507.02283 [hep-ph].

[113] A. Banerjee et al., "Phenomenological aspects of composite Higgs scenarios: exotic scalars and vector-like quarks," arXiv:2203.07270 [hep-ph]. contribution to Snowmass 2021.

[114] C. Degrande, B. Fuks, V. Hirschi, J. Proudom, and H.-S. Shao, "Automated next-to-leading order predictions for new physics at the LHC: the case of colored scalar pair production," Phys. Rev. D **91** no. 9, (2015) 094005, arXiv:1412.5589 [hep-ph].

[115] J. Alwall and C. Duhr, "FeynRules model SextetDiquarks.fr" https://feynrules.irmp.ucl.ac.be/wiki/Sextets. Accessed 30.10.2024.

[116] T. Han, I. Lewis, and T. McElmurry, "QCD Corrections to Scalar Diquark Production at Hadron Colliders," JHEP **01** (2010) 123, arXiv:0909.2666 [hep-ph].

[117] W. Beenakker, C. Borschensky, R. Heger, M. Krämer, A. Kulesza, and E. Laenen, "NNLL resummation for stop pair-production at the LHC," JHEP **05** (2016) 153, arXiv:1601.02954 [hep-ph].

[118] W. Beenakker, C. Borschensky, M. Krämer, A. Kulesza, and E. Laenen, "NNLL-fast: predictions for coloured supersymmetric particle production at the LHC with threshold and Coulomb resummation," JHEP **12** (2016) 133, arXiv:1607.07741 [hep-ph].

[119] **LHC SUSY Cross Section Working Group** Collaboration, A. Kulesza and C. Borschensky. https://twiki.cern.ch/twiki/bin/view/LHCPhysics/SUSYCrossSections13TeVstopsbottom. Accessed 16.09.2024.

[120] **CMS** Collaboration, A. Tumasyan et al., "Search for resonant and nonresonant production of pairs of dijet resonances in proton-proton collisions at $\sqrt{s} = 13$ TeV," JHEP **07** (2023) 161, arXiv:2206.09997 [hep-ex].

[121] **ATLAS** Collaboration, G. Aad et al., "Search for R-parity-violating supersymmetry in a final state containing leptons and many jets with the ATLAS experiment using $\sqrt{s} = 13$ TeV proton–proton collision data," Eur. Phys. J. C **81** no. 11, (2021) 1023, arXiv:2106.09609 [hep-ex].

[122] **ATLAS** Collaboration, G. Aad et al., "Search for supersymmetry in final states with missing transverse momentum and three or more b-jets in 139 fb^{-1} of proton–proton collisions at $\sqrt{s} = 13$ TeV with the ATLAS detector," Eur. Phys. J. C **83** no. 7, (2023) 561, arXiv:2211.08028 [hep-ex].

[123] **ATLAS** Collaboration, M. Aaboud et al., "A strategy for a general search for new phenomena using data-derived signal regions and its application within the ATLAS experiment," Eur. Phys. J. C **79** no. 2, (2019) 120, arXiv:1807.07447 [hep-ex].

[124] **ATLAS** Collaboration, G. Aad et al., "Search for bottom-squark pair production with the ATLAS detector in final states containing Higgs bosons, b-jets and missing transverse momentum," JHEP **12** (2019) 060, arXiv:1908.03122 [hep-ex].

[125] **ATLAS** Collaboration, G. Aad et al., "Search for a scalar partner of the top quark in the all-hadronic $t\bar{t}$ plus missing transverse momentum final state at $\sqrt{s} = 13$ TeV with the ATLAS detector," Eur. Phys. J. C **80** no. 8, (2020) 737, arXiv:2004.14060 [hep-ex].

[126] **ATLAS** Collaboration, G. Aad et al., "Search for new phenomena in pp collisions in final states with tau leptons, b-jets, and missing transverse momentum with the ATLAS detector," Phys. Rev. D **104** no. 11, (2021) 112005, arXiv:2108.07665 [hep-ex].

[127] **ATLAS** Collaboration, G. Aad et al., "Search for pair production of third-generation leptoquarks decaying into a bottom quark and a τ-lepton with the ATLAS detector," Eur. Phys. J. C **83** no. 11, (2023) 1075, arXiv:2303.01294 [hep-ex].

[128] **ATLAS** Collaboration, G. Aad et al., "Combination of searches for pair-produced leptoquarks at s=13 TeV with the ATLAS detector," Phys. Lett. B **854** (2024) 138736, arXiv:2401.11928 [hep-ex].

[129] B. Fuks and L. Darme, "FeynRules model top-philic resonances," https://feynrules.irmp.ucl.ac.be/wiki/TopHeavyRes. Accessed 30.10.2024.

[130] L. Darmé, B. Fuks, and M. Goodsell, "Cornering sgluons with four-top-quark events," Phys. Lett. B **784** (2018) 223–228, arXiv:1805.10835 [hep-ph].

[131] L. Darmé, B. Fuks, and F. Maltoni, "Top-philic heavy resonances in four-top final states and their EFT interpretation," JHEP **09** (2021) 143, arXiv:2104.09512 [hep-ph].

[132] **ATLAS** Collaboration, G. Aad et al., "Search for $t\bar{t}H/A \to t\bar{t}t\bar{t}$ production in proton-proton collisions at $\sqrt{s} = 13$ TeV with the ATLAS detector," arXiv:2408.17164 [hep-ex].

[133] A. Banerjee, D. B. Franzosi, and G. Ferretti, "Modelling vector-like quarks in partial compositeness framework," JHEP **03** (2022) 200, arXiv:2202.00037 [hep-ph].

[134] S. Dittmaier, M. Kramer, M. Spira, and M. Walser, "Charged-Higgs-boson production at the LHC: NLO supersymmetric QCD corrections," Phys. Rev. D **83** (2011) 055005, arXiv:0906.2648 [hep-ph].

[135] **LHC Higgs Cross Section Working Group** Collaboration, https://twiki.cern.ch/twiki/bin/view/LHCPhysics/CERNYellowReportPageBSMAt13TeV. Accessed 31.10.2024.

[136] **LHC Higgs Cross Section Working Group** Collaboration, D. de Florian et al., "Handbook of LHC Higgs Cross Sections: 4. Deciphering the Nature of the Higgs Sector," arXiv:1610.07922 [hep-ph].

[137] **CMS** Collaboration, A. M. Sirunyan et al., "Search for a charged Higgs boson decaying into top and bottom quarks in events with electrons or muons in proton-proton collisions at $\sqrt{\mathrm{s}} = 13$ TeV," JHEP **01** (2020) 096, arXiv:1908.09206 [hep-ex].

[138] **ATLAS** Collaboration, G. Aad et al., "Search for charged Higgs bosons decaying into a top quark and a bottom quark at $\sqrt{\mathrm{s}} = 13$ TeV with the ATLAS detector," JHEP **06** (2021) 145, arXiv:2102.10076 [hep-ex].

[139] **ATLAS** Collaboration, G. Aad et al., "Search for $t\bar{t}H/A \to t\bar{t}t\bar{t}$ production in the multilepton final state in proton–proton collisions at $\sqrt{s} = 13$ TeV with the ATLAS detector," JHEP **07** (2023) 203, arXiv:2211.01136 [hep-ex].

[140] **ATLAS** Collaboration, M. Aaboud et al., "Search for heavy particles decaying into top-quark pairs using lepton-plus-jets events in proton–proton collisions at $\sqrt{s} = 13$ TeV with the ATLAS detector," Eur. Phys. J. C **78** no. 7, (2018) 565, arXiv:1804.10823 [hep-ex].

[141] **CMS** Collaboration, A. M. Sirunyan et al., "Search for resonant $\mathrm{t\bar{t}}$ production in proton-proton collisions at $\sqrt{s} = 13$ TeV," JHEP **04** (2019) 031, arXiv:1810.05905 [hep-ex].

[142] **ATLAS** Collaboration, G. Aad et al., "Search for $t\bar{t}$ resonances in fully hadronic final states in pp collisions at $\sqrt{s} = 13$ TeV with the ATLAS detector," JHEP **10** (2020) 061, arXiv:2005.05138 [hep-ex].

[143] **ATLAS** Collaboration, G. Aad et al., "Search for resonances decaying into photon pairs in 139 fb^{-1} of pp collisions at $\sqrt{s}$=13 TeV with the ATLAS detector," Phys. Lett. B **822** (2021) 136651, arXiv:2102.13405 [hep-ex].

[144] **ATLAS** Collaboration, G. Aad et al., "Search for doubly and singly charged Higgs bosons decaying into vector bosons in multi-lepton final states with the ATLAS detector using proton-proton collisions at $\sqrt{s}$ = 13 TeV," JHEP **06** (2021) 146, arXiv:2101.11961 [hep-ex].

[145] **CMS** Collaboration, A. Tumasyan et al., "Search for Higgs Boson Pair Production in the Four b Quark Final State in Proton-Proton Collisions at $\sqrt{s} = 13$ TeV," Phys. Rev. Lett. **129** no. 8, (2022) 081802, arXiv:2202.09617 [hep-ex].

[146] **CMS** Collaboration, A. Tumasyan et al., "Search for Nonresonant Pair Production of Highly Energetic Higgs Bosons Decaying to Bottom Quarks," Phys. Rev. Lett. **131** no. 4, (2023) 041803, arXiv:2205.06667 [hep-ex].

[147] **CMS** Collaboration, A. Tumasyan et al., "Search for Higgs boson pairs decaying to WW*WW*, WW*$\tau\tau$, and $\tau\tau\tau\tau$ in proton-proton collisions at $\sqrt{s} = 13$ TeV," JHEP **07** (2023) 095, arXiv:2206.10268 [hep-ex].

[148] **ATLAS** Collaboration, G. Aad et al., "Search for nonresonant pair production of Higgs bosons in the $b\bar{b}b\bar{b}$ final state in pp collisions at $\sqrt{s} = 13$ TeV with the ATLAS detector," Phys. Rev. D **108** no. 5, (2023) 052003, arXiv:2301.03212 [hep-ex].

[149] **ATLAS** Collaboration, M. Aaboud et al., "Search for pair production of Higgs bosons in the $b\bar{b}b\bar{b}$ final state using proton–proton collisions at $\sqrt{s} = 13$ TeV with the ATLAS detector," Phys. Rev. D **94** no. 5, (2016) 052002, arXiv:1606.04782 [hep-ex].

[150] **ATLAS** Collaboration, M. Aaboud et al., "Search for Higgs boson pair production in the $\gamma\gamma WW^*$ channel using pp collision data recorded at $\sqrt{s} = 13$ TeV with the ATLAS detector," Eur. Phys. J. C **78** no. 12, (2018) 1007, arXiv:1807.08567 [hep-ex].

[151] **ATLAS** Collaboration, M. Aaboud et al., "Search for Higgs boson pair production in the $WW^{(*)}WW^{(*)}$ decay channel using ATLAS data recorded at $\sqrt{s} = 13$ TeV," JHEP **05** (2019) 124, arXiv:1811.11028 [hep-ex].

[152] **CMS** Collaboration, A. Tumasyan et al., "Search for new particles in an extended Higgs sector with four b quarks in the final state at $\sqrt{s} = 13$ TeV," Phys. Lett. B **835** (2022) 137566, arXiv:2203.00480 [hep-ex].

[153] **CMS** Collaboration, "Search for new physics in multilepton final states in pp collisions at $\sqrt{s} = 13$ TeV,". CMS PAS EXO-19-002.

[154] **ATLAS** Collaboration, M. Aaboud et al., "Search for photonic signatures of gauge-mediated supersymmetry in 13 TeV pp collisions with the ATLAS detector," Phys. Rev. D **97** no. 9, (2018) 092006, arXiv:1802.03158 [hep-ex].

[155] **ATLAS** Collaboration, G. Aad et al., "Measurement of the production cross section of pairs of isolated photons in pp collisions at 13 TeV with the ATLAS detector," JHEP **11** (2021) 169, arXiv:2107.09330 [hep-ex].

[156] **ATLAS** Collaboration, G. Aad et al., "Search for squarks and gluinos in final states with one isolated lepton, jets, and missing transverse momentum at $\sqrt{s} = 13$ TeV with the ATLAS detector," Eur. Phys. J. C **81** no. 7, (2021) 600, arXiv:2101.01629 [hep-ex]. [Erratum: Eur.Phys.J.C 81, 956 (2021)].

[157] **CMS** Collaboration, "Search for supersymmetry in proton-proton collisions at 13 TeV in final states with jets and missing transverse momentum,". CMS PAS SUS-19-006.

[158] **CMS** Collaboration, A. M. Sirunyan et al., "Search for supersymmetry in multijet events with missing transverse momentum in proton-proton collisions at 13 TeV," Phys. Rev. D **96** no. 3, (2017) 032003, arXiv:1704.07781 [hep-ex].

[159] **ATLAS** Collaboration, G. Aad et al., "Search for direct production of electroweakinos in final states with missing transverse momentum and a Higgs boson decaying into photons in pp collisions at $\sqrt{s} = 13$ TeV with the ATLAS detector," JHEP **10** (2020) 005, arXiv:2004.10894 [hep-ex].

[160] **ATLAS** Collaboration, G. Aad et al., "Measurements of differential cross-sections in four-lepton events in 13 TeV proton-proton collisions with the ATLAS detector," JHEP **07** (2021) 005, arXiv:2103.01918 [hep-ex].

[161] **ATLAS** Collaboration, G. Aad et al., "Measurement of the $Z(\to \ell^+\ell^-)\gamma$ production cross-section in pp collisions at $\sqrt{s} = 13$ TeV with the ATLAS detector," JHEP **03** (2020) 054, arXiv:1911.04813 [hep-ex].

[162] **ATLAS** Collaboration, M. Aaboud et al., "Measurement of the $Z\gamma \to \nu\overline{\nu}\gamma$ production cross section in pp collisions at $\sqrt{s} = 13$ TeV with the ATLAS detector and limits on anomalous triple gauge-boson couplings," JHEP **12** (2018) 010, arXiv:1810.04995 [hep-ex].

[163] **ATLAS** Collaboration, "Search for supersymmetry with two and three leptons and missing transverse momentum in the final state at $\sqrt{s} = 13$ TeV with the ATLAS detector,". ATLAS-CONF-2016-096.

[164] **CMS** Collaboration, A. M. Sirunyan et al., "Search for electroweak production of charginos and neutralinos in multilepton final states in proton-proton collisions at $\sqrt{s} =$ 13 TeV," JHEP **03** (2018) 166, arXiv:1709.05406 [hep-ex].

[165] G. Ferretti, "UV Completions of Partial Compositeness: The Case for a SU(4) Gauge Group," JHEP **06** (2014) 142, arXiv:1404.7137 [hep-ph].

[166] H. Georgi and M. Machacek, "Doubly charged Higgs bosons," Nucl. Phys. B **262** (1985) 463–477.

[167] M. S. Chanowitz and M. Golden, "Higgs Boson Triplets With $M_W = M_Z \cos\theta_W$," Phys. Lett. B **165** (1985) 105–108.

[168] B. Fuks, M. Klasen, D. R. Lamprea, and M. Rothering, "Precision predictions for electroweak superpartner production at hadron colliders with Resummino," Eur. Phys. J. C **73** (2013) 2480, arXiv:1304.0790 [hep-ph].

[169] **ATLAS** Collaboration, G. Aad et al., "Observation of four-top-quark production in the multilepton final state with the ATLAS detector," Eur. Phys. J. C **83** no. 6, (2023) 496, arXiv:2303.15061 [hep-ex]. [Erratum: Eur.Phys.J.C 84, 156 (2024)].

[170] **CMS** Collaboration, A. Hayrapetyan et al., "Observation of four top quark production in proton-proton collisions at s=13TeV," Phys. Lett. B **847** (2023) 138290, arXiv:2305.13439 [hep-ex].

[171] I. Béjar Alonso et al., eds., High-luminosity Large Hadron Collider (HL-LHC): Technical design report. 2020. CERN-2020-010.

[172] J. Cogan, M. Kagan, E. Strauss, and A. Schwartzman, "Jet-Images: Computer Vision Inspired Techniques for Jet Tagging," JHEP **02** (2015) 118, arXiv:1407.5675 [hep-ph].

[173] L. de Oliveira, M. Kagan, L. Mackey, B. Nachman, and A. Schwartzman, "Jet-images — deep learning edition," JHEP **07** (2016) 069, arXiv:1511.05190 [hep-ph].

[174] A. Butter et al., "The Machine Learning landscape of top taggers," SciPost Phys. **7** (2019) 014, arXiv:1902.09914 [hep-ph].

[175] J. H. Kim, M. Kim, K. Kong, K. T. Matchev, and M. Park, "Portraying Double Higgs at the Large Hadron Collider," JHEP **09** (2019) 047, arXiv:1904.08549 [hep-ph].

[176] **ATLAS** Collaboration, "Technical Design Report for the ATLAS Inner Tracker Pixel Detector," Tech. Rep. ATLAS-TDR-030, 2017.

[177] G. Cowan, K. Cranmer, E. Gross, and O. Vitells, "Asymptotic formulae for likelihood-based tests of new physics," Eur. Phys. J. C **71** (2011) 1554, arXiv:1007.1727 [physics.data-an]. [Erratum: Eur.Phys.J.C 73, 2501 (2013)].

[178] K. Fukushima, "Neocognitron: A hierarchical neural network capable of visual pattern recognition," Neural networks **1** no. 2, (1988) 119–130.

[179] Y. LeCun, L. Bottou, Y. Bengio, and P. Haffner, "Gradient-based learning applied to document recognition," Proceedings of the IEEE **86** no. 11, (1998) 2278–2324.

[180] A. Krizhevsky, I. Sutskever, and G. E. Hinton, "Imagenet classification with deep convolutional neural networks," Advances in neural information processing systems **25** (2012) .

[181] **ATLAS** Collaboration, "Constituent-Based Top-Quark Tagging with the ATLAS Detector,". ATL-PHYS-PUB-2022-039.

[182] W. Bhimji, S. A. Farrell, T. Kurth, M. Paganini, Prabhat, and E. Racah, "Deep Neural Networks for Physics Analysis on low-level whole-detector data at the LHC," J. Phys. Conf. Ser. **1085** no. 4, (2018) 042034, arXiv:1711.03573 [hep-ex].

[183] **CMS** Collaboration, M. Andrews, M. Paulini, S. Gleyzer, and B. Poczos, "Exploring End-to-end Deep Learning Applications for Event Classification at CMS," EPJ Web Conf. **214** (2019) 06031.

[184] S. Diefenbacher, H. Frost, G. Kasieczka, T. Plehn, and J. M. Thompson, "CapsNets Continuing the Convolutional Quest," SciPost Phys. **8** (2020) 023, arXiv:1906.11265 [hep-ph].

[185] L. Huang, S.-b. Kang, J. H. Kim, K. Kong, and J. S. Pi, "Portraying double Higgs at the Large Hadron Collider II," JHEP **08** (2022) 114, arXiv:2203.11951 [hep-ph].

[186] J. Kim et al., "Large-Scale Deep Learning for Multi-Jet Event Classification," arXiv:2207.11710 [hep-ex].

[187] **ATLAS** Collaboration, "Expected performance of the ATLAS detector at the High-Luminosity LHC,". ATL-PHYS-PUB-2019-005.

[188] D. Bertolini, P. Harris, M. Low, and N. Tran, "Pileup Per Particle Identification," JHEP **10** (2014) 059, arXiv:1407.6013 [hep-ph].

[189] **CMS** Collaboration, A. M. Sirunyan et al., "Pileup mitigation at CMS in 13 TeV data," JINST **15** no. 09, (2020) P09018, arXiv:2003.00503 [hep-ex].

[190] A. Paszke, S. Gross, S. Chintala, G. Chanan, E. Yang, Z. DeVito, Z. Lin, A. Desmaison, L. Antiga, and A. Lerer, "Automatic differentiation in pytorch," arXiv:1701.02617 [cs.IR].

[191] A. Paszke, S. Gross, et al., "Pytorch: An imperative style, high-performance deep learning library," Advances in neural information processing systems **32** (2019) , arXiv:1912.01703 [cs.LG].

[192] D. P. Kingma and J. Ba, "Adam: A method for stochastic optimization," arXiv:1412.6980 [cs.LG].

[193] J. Barnard, E. N. Dawe, M. J. Dolan, and N. Rajcic, "Parton Shower Uncertainties in Jet Substructure Analyses with Deep Neural Networks," Phys. Rev. D **95** no. 1, (2017) 014018, arXiv:1609.00607 [hep-ph].

[194] N. Craig, F. D'Eramo, P. Draper, S. Thomas, and H. Zhang, "The Hunt for the Rest of the Higgs Bosons," JHEP **06** (2015) 137, arXiv:1504.04630 [hep-ph].

[195] J. A. Aguilar-Saavedra, "Identifying top partners at LHC," JHEP **11** (2009) 030, arXiv:0907.3155 [hep-ph].

[196] A. De Simone, O. Matsedonskyi, R. Rattazzi, and A. Wulzer, "A First Top Partner Hunter's Guide," JHEP **04** (2013) 004, arXiv:1211.5663 [hep-ph].

[197] M. S. Chanowitz and M. K. Gaillard, "The TeV Physics of Strongly Interacting W's and Z's," Nucl. Phys. B **261** (1985) 379–431.

[198] A. Banerjee, E. Bergeaas Kuutmann, V. Ellajosyula, R. Enberg, G. Ferretti, and L. Panizzi, "Vector-like quarks: status and new directions at the LHC," arXiv:2406.09193 [hep-ph].

[199] A. Deandrea, T. Flacke, B. Fuks, L. Panizzi, and H.-S. Shao, "Single production of vector-like quarks: the effects of large width, interference and NLO corrections," JHEP **08** (2021) 107, arXiv:2105.08745 [hep-ph]. [Erratum: JHEP 11, 028 (2022)].

[200] **ATLAS** Collaboration, G. Aad et al., "Search for pair-production of vector-like quarks in lepton+jets final states containing at least one b-tagged jet using the Run 2 data from the ATLAS experiment," Phys. Lett. B **854** (2024) 138743, arXiv:2401.17165 [hep-ex].

[201] **CMS** Collaboration, A. Tumasyan et al., "Search for pair production of vector-like quarks in leptonic final states in proton-proton collisions at $\sqrt{s} = 13$ TeV," JHEP **07** (2023) 020, arXiv:2209.07327 [hep-ex].

[202] **ATLAS** Collaboration, G. Aad et al., "Search for pair-produced vector-like top and bottom partners in events with large missing transverse momentum in pp collisions with the ATLAS detector," Eur. Phys. J. C **83** no. 8, (2023) 719, arXiv:2212.05263 [hep-ex].

[203] R. Benbrik et al., "Signatures of vector-like top partners decaying into new neutral scalar or pseudoscalar bosons," JHEP **05** (2020) 028, arXiv:1907.05929 [hep-ph].

[204] K.-P. Xie, G. Cacciapaglia, and T. Flacke, "Exotic decays of top partners with charge 5/3: bounds and opportunities," JHEP **10** (2019) 134, arXiv:1907.05894 [hep-ph].

[205] A. Banerjee, V. Ellajosyula, and L. Panizzi, "Heavy vector-like quarks decaying to exotic scalars: a case study with triplets," JHEP **01** (2024) 187, arXiv:2311.17877 [hep-ph].

[206] **ATLAS** Collaboration, G. Aad et al., "Search for squarks and gluinos in final states with same-sign leptons and jets using 139 fb^{-1} of data collected with the ATLAS detector," JHEP **06** (2020) 046, arXiv:1909.08457 [hep-ex].

[207] **CMS** Collaboration, A. M. Sirunyan et al., "Search for high mass dijet resonances with a new background prediction method in proton-proton collisions at $\sqrt{s} = 13$ TeV," JHEP **05** (2020) 033, arXiv:1911.03947 [hep-ex].

[208] **FCC** Collaboration, A. Abada et al., "FCC-hh: The Hadron Collider: Future Circular Collider Conceptual Design Report Volume 3," Eur. Phys. J. ST **228** no. 4, (2019) 755–1107.

[209] J. Tang, Y. Zhang, Q. Xu, J. Gao, X. Lou, and Y. Wang, "Study Overview for Super Proton-Proton Collider," arXiv:2203.07987 [hep-ex]. contribution to Snowmass 2021.

[210] M. Schmidt, "Machine Learning Methods for (semi-)hadronic final-states at the LHC." 2024. Master thesis, University of Würzburg.

[211] M. Böhm, A. Denner, and H. Joos, Gauge Theories of the Strong and Electroweak Interaction. B. G. Teubner, 2001.

[212] L. M. Carpenter, T. Murphy, and T. M. P. Tait, "Phenomenological cornucopia of SU(3) exotica," Phys. Rev. D **105** no. 3, (2022) 035014, arXiv:2110.11359 [hep-ph].

[213] A. Alloul, N. D. Christensen, C. Degrande, C. Duhr, and B. Fuks, "FeynRules 2.0 - A complete toolbox for tree-level phenomenology," Comput. Phys. Commun. **185** (2014) 2250–2300, arXiv:1310.1921 [hep-ph].

[214] C. Degrande, C. Duhr, B. Fuks, D. Grellscheid, O. Mattelaer, and T. Reiter, "UFO - The Universal FeynRules Output," Comput. Phys. Commun. **183** (2012) 1201–1214, arXiv:1108.2040 [hep-ph].

[215] J. Alwall, R. Frederix, S. Frixione, V. Hirschi, F. Maltoni, O. Mattelaer, H. S. Shao, T. Stelzer, P. Torrielli, and M. Zaro, "The automated computation of tree-level and next-to-leading order differential cross sections, and their matching to parton shower simulations," JHEP **07** (2014) 079, arXiv:1405.0301 [hep-ph].

[216] R. D. Ball et al., "Parton distributions with LHC data," Nucl. Phys. B **867** (2013) 244–289, arXiv:1207.1303 [hep-ph].

[217] A. Buckley, J. Ferrando, S. Lloyd, K. Nordström, B. Page, M. Rüfenacht, M. Schönherr, and G. Watt, "LHAPDF6: parton density access in the LHC precision era," Eur. Phys. J. C **75** (2015) 132, arXiv:1412.7420 [hep-ph].

[218] T. Sjöstrand, S. Ask, J. R. Christiansen, R. Corke, N. Desai, P. Ilten, S. Mrenna, S. Prestel, C. O. Rasmussen, and P. Z. Skands, "An introduction to PYTHIA 8.2" Comput. Phys. Commun. **191** (2015) 159–177, arXiv:1410.3012 [hep-ph].

[219] M. Dobbs and J. B. Hansen, "The HepMC C++ Monte Carlo event record for High Energy Physics," Comput. Phys. Commun. **134** (2001) 41–46.

[220] A. L. Read, "Presentation of search results: The CL_s technique," J. Phys. G **28** (2002) 2693–2704.

[221] E. Conte, B. Fuks, and G. Serret, "MadAnalysis 5, A User-Friendly Framework for Collider Phenomenology," Comput. Phys. Commun. **184** (2013) 222–256, arXiv:1206.1599 [hep-ph].

[222] E. Conte, B. Dumont, B. Fuks, and C. Wymant, "Designing and recasting LHC analyses with MadAnalysis 5," Eur. Phys. J. C **74** no. 10, (2014) 3103, arXiv:1405.3982 [hep-ph].

[223] B. Dumont, B. Fuks, S. Kraml, S. Bein, G. Chalons, E. Conte, S. Kulkarni, D. Sengupta, and C. Wymant, "Toward a public analysis database for LHC new physics searches using MADANALYSIS 5," Eur. Phys. J. C **75** no. 2, (2015) 56, arXiv:1407.3278 [hep-ph].

[224] E. Conte and B. Fuks, "Confronting new physics theories to LHC data with MADANALYSIS 5," Int. J. Mod. Phys. A **33** no. 28, (2018) 1830027, arXiv:1808.00480 [hep-ph].

[225] M. Drees, H. Dreiner, D. Schmeier, J. Tattersall, and J. S. Kim, "CheckMATE: Confronting your Favourite New Physics Model with LHC Data," Comput. Phys. Commun. **187** (2015) 227–265, arXiv:1312.2591 [hep-ph].

[226] D. Dercks, N. Desai, J. S. Kim, K. Rolbiecki, J. Tattersall, and T. Weber, "CheckMATE 2: From the model to the limit," Comput. Phys. Commun. **221** (2017) 383–418, arXiv:1611.09856 [hep-ph].

[227] **DELPHES 3** Collaboration, J. de Favereau, C. Delaere, P. Demin, A. Giammanco, V. Lemaître, A. Mertens, and M. Selvaggi, "DELPHES 3, A modular framework for fast simulation of a generic collider experiment," JHEP **02** (2014) 057, arXiv:1307.6346 [hep-ex].

[228] M. Cacciari, G. P. Salam, and G. Soyez, "The anti-k_t jet clustering algorithm," JHEP **04** (2008) 063, arXiv:0802.1189 [hep-ph].

[229] M. Cacciari, G. P. Salam, and G. Soyez, "FastJet User Manual," Eur. Phys. J. C **72** (2012) 1896, arXiv:1111.6097 [hep-ph].

[230] C. Bierlich et al., "Robust Independent Validation of Experiment and Theory: Rivet version 3," SciPost Phys. **8** (2020) 026, arXiv:1912.05451 [hep-ph].

[231] J. Butterworth, "BSM constraints from model-independent measurements: A Contur Update," J. Phys. Conf. Ser. **1271** no. 1, (2019) 012013, arXiv:1902.03067 [hep-ph].

[232] A. Buckley et al., "Testing new physics models with global comparisons to collider measurements: the Contur toolkit," SciPost Phys. Core **4** (2021) 013, arXiv:2102.04377 [hep-ph].

[233] T. Plehn, A. Butter, B. Dillon, T. Heimel, C. Krause, and R. Winterhalder, "Modern Machine Learning for LHC Physicists," arXiv:2211.01421 [hep-ph].

[234] I. Goodfellow, Y. Bengio, and A. Courville, Deep Learning. MIT Press, 2016. http://www.deeplearningbook.org.

[235] I. Pointer, Programming PyTorch for Deep Learning: Creating and Deploying Deep Learning Applications. O'Reilly Media, Incorporated, 2019.

[236] S. Ioffe, "Batch normalization: Accelerating deep network training by reducing internal covariate shift," arXiv:1502.03167 [cs.LG].

[237] G. M. Kurtzer, V. Sochat, and M. W. Bauer, "Singularity: Scientific containers for mobility of compute," PLOS ONE **12** no. 5, (05, 2017) 1–20.

[238] R. Brun and F. Rademakers, "Root—an object oriented data analysis framework," Nuclear instruments and methods in physics research section A: accelerators, spectrometers, detectors and associated equipment **389** no. 1-2, (1997) 81–86.